# REPORT DOCUMENTATION PAGE

AFRL-SR-BL-TR-98-

⊙372

| 1. AGENCY USE ONLY (Leave Blank) | 2. REPORT DATE <br> May 1997 | 3. REPORT ... AND DATES COVERED <br> Final |
|---|---|---|

**4. TITLE AND SUBTITLE**
Turbulent Coagulation of Particles Smaller than the Length Scales of Turbulence and Equilibrium Sorption of Phenanthrene to Clay: Implications for Pollutant Transport in the Estuarine Water Column

**5. FUNDING NUMBERS**

**6. AUTHORS**
Brett Kenneth Brunk

**7. PERFORMING ORGANIZATION NAME(S) AND ADDRESS(ES)**
Cornell University

**8. PERFORMING ORGANIZATION REPORT NUMBER**

**9. SPONSORING/MONITORING AGENCY NAME(S) AND ADDRESS(ES)**
AFOSR/NI
110 Duncan Avenue, Room B-115
Bolling Air Force Base, DC 20332-8080

**10. SPONSORING/MONITORING AGENCY REPORT NUMBER**

**11. SUPPLEMENTARY NOTES**

**12a. DISTRIBUTION AVAILABILITY STATEMENT**
Approved for Public Release

**12b. DISTRIBUTION CODE**

**13. ABSTRACT** *(Maximum 200 words)*
See attachment

**14. SUBJECT TERMS**

**15. NUMBER OF PAGES**

**16. PRICE CODE**

| 17. SECURITY CLASSIFICATION OF REPORT <br> Unclassified | 18. SECURITY CLASSIFICATION OF THIS PAGE <br> Unclassified | 19. SECURITY CLASSIFICATION OF ABSTRACT <br> Unclassified | 20. LIMITATION OF ABSTRACT <br> UL |
|---|---|---|---|

DTIC QUALITY INSPECTED 3

# TURBULENT COAGULATION OF PARTICLES SMALLER THAN THE LENGTH SCALES OF TURBULENCE AND EQUILIBRIUM SORPTION OF PHENANTHRENE TO CLAY: IMPLICATIONS FOR POLLUTANT TRANSPORT IN THE ESTUARINE WATER COLUMN

A Dissertation

Presented to the Faculty of the Graduate School

of Cornell University

in Partial Fulfillment of the Requirements for the Degree of

Doctor of Philosophy
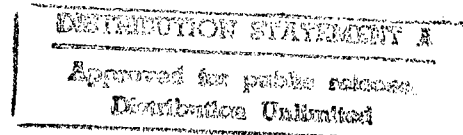
19980430 053

by

Brett Kenneth Brunk

May 1997

# TURBULENT COAGULATION OF PARTICLES SMALLER THAN THE LENGTH SCALES OF TURBULENCE AND EQUILIBRIUM SORPTION OF PHENANTHRENE TO CLAY: IMPLICATIONS FOR POLLUTANT TRANSPORT IN THE ESTUARINE WATER COLUMN

Brett Kenneth Brunk, Ph.D.

Cornell University 1997

Pollutant and particle transport in estuaries is affected by a multitude of physical, chemical and biological processes. In this research the importance of equilibrium sorption and turbulent coagulation were studied.

Sorption in estuaries was modeled using phenanthrene, bacterial extracellular polymer and kaolinite clay as surrogates for a hydrophobic organic pollutant, dissolved organic matter and inorganic suspended sediment, respectively. Experiments over a range of estuarine salinities showed that ionic strength had the largest effect on the extent of sorption, while the effect of extracellular polymer coatings on the mineral surfaces was insignificant. Further calculations using typical estuarine suspended sediment concentrations indicated that equilibrium sorption could not fully account for the solid/solution phase distribution of hydrophobic organic compounds in the estuarine water column.

For particles that are small compared to the length scales of turbulence, the rate of coagulation is related to the dynamics of the smallest turbulent eddies since they have the highest shear rate. Experimental and theoretical effort focused on determining the coagulation rate of spherical

particles in isotropic turbulence. A pair diffusion approximation valid for rapidly fluctuating flows was used to calculate the rate of coagulation in a randomly varying isotropic linear flow field. Dynamic simulations of particle coagulation in Gaussian turbulence were computed over a range of representative values of particle-particle interactions (i.e, hydrodynamic interactions and van der Waals attraction) and total strain (i.e., the product of the strain rate and its time scale). The computed coagulation rates for isotropic turbulence differed from analytical approximations valid at large and small total strain. As expected, particle interactions were found to be significant. Experimental measurements of coagulation in grid-generated turbulence were obtained by measuring the loss of singlet particles from an initially monodisperse suspension as a function of turbulence intensity. Model predictions based on the particle Hamaker constant and spatial distribution of turbulence in the reactor agreed well with the experiments without the use of any fitting parameters. The close agreement of simulations and observations indicate the numerical model has successfully captured the relevant physics that governs the aggregation of colloidal particles in turbulent flows. This work is the first successful description of turbulent coagulation. Given the ubiquity of turbulent suspensions in engineered and natural systems, the ability to quantitatively describe particle behavior under these conditions is expected to have considerable utility.

## BIOGRAPHICAL SKETCH

Brett Brunk began his engineering education at the Colorado School of Mines. While there amidst the foothills of the Rockies, the heady smells of the neighboring Coors Brewery and his future wife, Brett pursued an undergraduate degree in Chemical Engineering. After being told by more than one campus recruiter that he should go to graduate school, Brett applied to graduate school and law school. The outrage of Brett's undergraduate advisor over the law school applications was enough to send Brett running for cover to the ivy-strewn halls of Cornell University. Since August 1992 Brett has been working towards his doctorate degree in Chemical Engineering with the help of Professor Leonard W. Lion.

*To Debra and Chesney*

# ACKNOWLEDGMENT

It is only right to start my acknowledgment with a thank you to my wife, Debra Brunk. Her continuous support and encouragement has been the foundation upon which I have built this dissertation.

I thank all my official and unofficial academic advisors: Prof. Leonard Lion, Prof. Don Koch, Prof. Gerhard Jirka, Prof. Jim Gossett, Dr. Monroe Weber-Shirk and Anna Jensen. Len Lion was all one could hope for in an advisor. I appreciated having the opportunity to direct my own research and was comforted by his unflagging confidence in me and his enthusiasm for research. To Don Koch I owe another large debt of gratitude. Without his help, tensors and fluid dynamics would not be my friends. Thank you Monroe for our many long conversations about the direction my research should take. Anna Jensen has been a wonderfully entertaining and intelligent officemate — the likes of which I will probably never experience again.

In addition I would like to recognize the hard work of three undergraduate researchers. I thank Amy Wazenegger for her taking on some of the misery of sorption experiments. I enjoyed our many conversations while she was here and appreciate the hard work that she did. Joye Thaller's investigations of clay flocculation helped me gain insight into the behavior of natural particles as opposed to the polystyrene beads I predominately used. Lastly, I thank Damaris Santos for bringing a bit of Puerto Rican sunshine to cloud-covered Ithaca. I enjoyed "learning"

Spanish and the mysteries of Puerto Rican "Goat Suckers." Her diligence and meticulously performed coagulation experiments were a time saver.

A number of additional people helped me along the way. I want to thank the Civil & Environmental Engineering staff, Cameron Willkens and Lee Virtue for making the paperwork and the experiments run smoothly.

# TABLE OF CONTENTS

# LIST OF TABLES

# LIST OF FIGURES

# CHAPTER 1:

## INTRODUCTION

Understanding anthropogenic impacts on the environment lies at the heart of much of the research interest that is focused on estuaries. There at the boundary between rivers and the ocean, spatial and temporal changes in the physical, biological, and chemical characteristics of the aqueous phase lead to a complex network of competing transport and transformation processes that govern the fate of pollutants and particles (see for example, O'Melia, 1995; McCave, 1984; Rogers, 1993; Officer & Lynch, 1989). This research focuses on two of these processes: hydrophobic organic pollutant equilibrium sorption onto colloidal solids in the estuarine water column and turbulent shear-induced coagulation of colloids.

Depending on the relative strength of tidal forces compared with river discharge, a variety of saline structures can develop in estuaries. Systems with weak tidal mixing are highly stratified as freshwater discharged from the river flows over the more dense marine water. As tidal energy increases, the vertical salinity gradients decrease and the estuary becomes partially mixed and eventually vertically homogeneous (Fischer et al., 1979). Stratified estuaries such as that depicted in Figure 1.1 provide a conceptual starting point for this work. In Figure 1.1 fresh water flows on top of a marine water intrusion. A sharp salinity gradient or

1
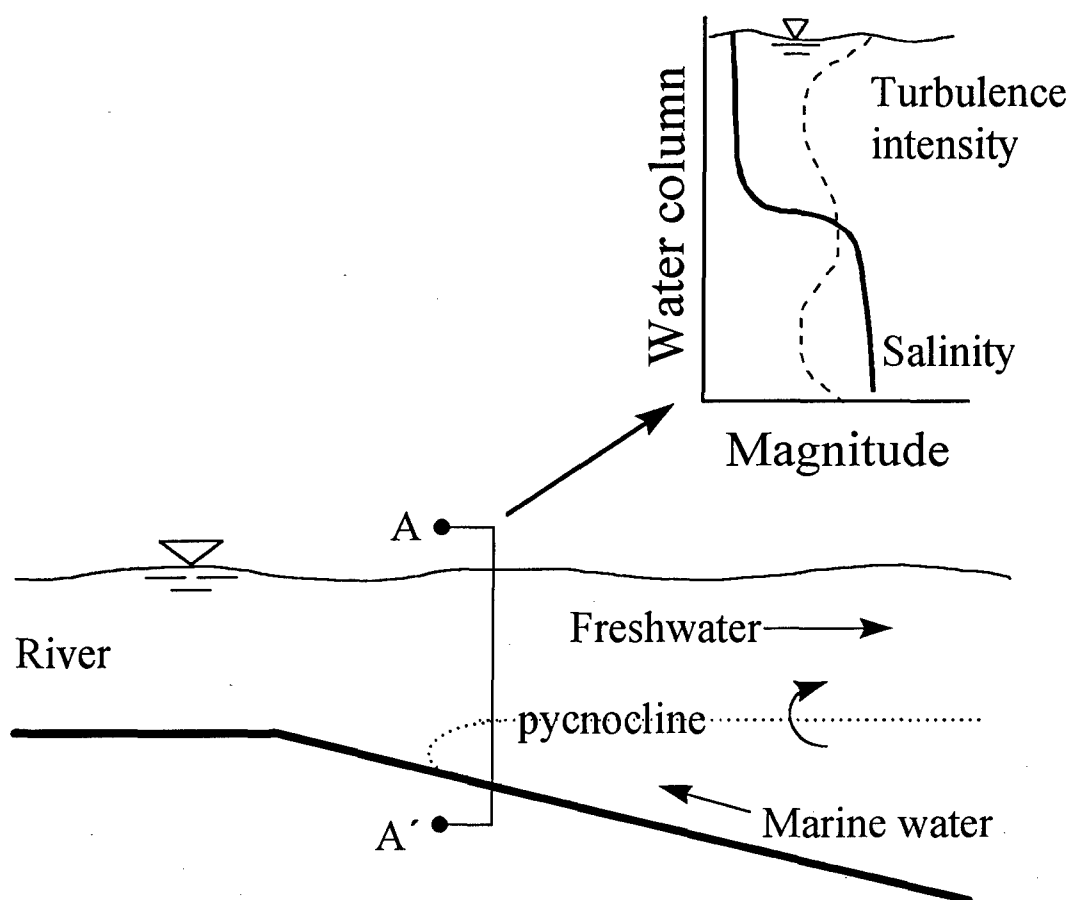
**Figure 1.1**: Sketch of a stratified estuary. The cross-sectional profile (denoted A-A′) shows the typical vertical distribution of salinity (solid line) and turbulence intensity (dashed line) found in stratified estuaries.

pycnocline separates the two fluid layers. Turbulence in the stratified estuary is generated in the freshwater layer by wind mixing, in the saline layer by tidal motions and/or bottom roughness and at the pycnocline through shear instabilities. The turbulence leads to mixing and entrainment of salt water across the pycnocline; therefore, the salinity of the upper layer increases with distance toward the ocean.

Estuaries are frequently contaminated with anthropogenic pollutants since they are often the locations of concentrated industrial development, coastal cities and ports. Both inorganic pollutants, such as heavy metals, and organic chemicals, such as the polycyclic aromatic hydrocarbons (PAHs) examined in this study, contaminate the estuarine environment. While there is a consensus that estuaries serve as a sink for pollutants and particles (Bates et al., 1987; Murphy et al., 1988; Sagemann et al., 1996), the combinations of physical and chemical processes that govern the rate and extent of estuarine particle and pollutant trapping are inadequately understood.

A well-known example of the coupling between physical and chemical processes is the relationship between fresh water/marine water mixing and coagulation of colloids (O'Melia, 1995). Since colloidal particles in natural systems are typically negatively charged (Hunter & Liss, 1979), the low ionic strength of fresh water leads to a diffuse cationic double layer that produces a significant particle repulsion when two particles approach one another. Because of the significant double layer repulsion, fresh water particles are usually stable or resistant to aggregation. Colloid stability decreases substantially when salt water, with

its high ionic strength, is mixed into the fresh water and compression of the double layer occurs. Hence, as fresh water mixes with sea water in the estuary, particle-particle repulsion is reduced allowing coagulation reactions to transfer suspended sediment from the non-settling colloidal fraction to large flocs that can settle out of the water column at appreciable rates. In summary, alterations in solution ionic strength brought on by mixing at the fresh/salt water interface ultimately lead to enhanced deposition of coagulated riverine suspended sediment.

Chemical reactions such as hydrophobic organic compound sorption are also strongly influenced by changes in salinity (Rogers, 1993). In this case, high salinity promotes "salting out" of hydrophobic compounds as their aqueous activity coefficients increase (Karickhoff, 1984). Finally, the presence of plankton and algal blooms in estuaries can alter the phase distribution of pollutants (Prahl & Carpenter, 1979) and, in turn, the abundance and distribution of the biota are regulated by the chemistry and circulation patterns of the estuary (Eldridge & Sieracki, 1993).

Spatial variation in rates of mixing, flow intensity and salinity can clearly alter the fate of dissolved and suspended material in the estuary. While the interplay between chemical, biological and physical processes is grossly understood, a mechanistic understanding of many of these interactions remains elusive. This work attempts to improve our understanding of two abiotic processes affecting pollutant and particle transport, namely, equilibrium sorption to suspended inorganic sediment and turbulent shear coagulation. Equilibrium sorption in the water column is evaluated for the case of hydrophobic organic compounds (more

specifically for the polycyclic aromatic hydrocarbon compound, PAH, phenanthrene) and the importance of sorption in controlling the distribution of pollutants between the particulate and aqueous phase is deduced as a function of salinity and the presence of dissolved organic matter. Particle coagulation due to turbulent shear is expected to be a critical step leading to the formation of flocs that settle to the estuarine sediments. In this thesis, a combination of theory, experiments and simulations are used to investigate rates of turbulent shear coagulation for an ideal isotropic turbulent flow.

## 1.1 Processes affecting pollutant and particle fate in estuaries

A number of processes, some of which are illustrated in Figure 1.2, control the fate and transport of pollutants in an estuary. These include transport mechanisms such as turbulent diffusion, particle settling, mean advection to the ocean and, entrainment, as well as reactions, such as coagulation and sorption. In this subsection results from dimensional analysis and physical arguments are used to estimate the time scales of these transformation processes so that their relative importance can be assessed. Using the scaling arguments as a foundation, a two-step process is proposed to control the trapping of hydrophobic organic compounds introduced into the aqueous phase of the estuary. In this process organic pollutants are rapidly sorbed to suspended particulates and these particles undergo coagulation and subsequent settling because of changes in the solution ionic strength.
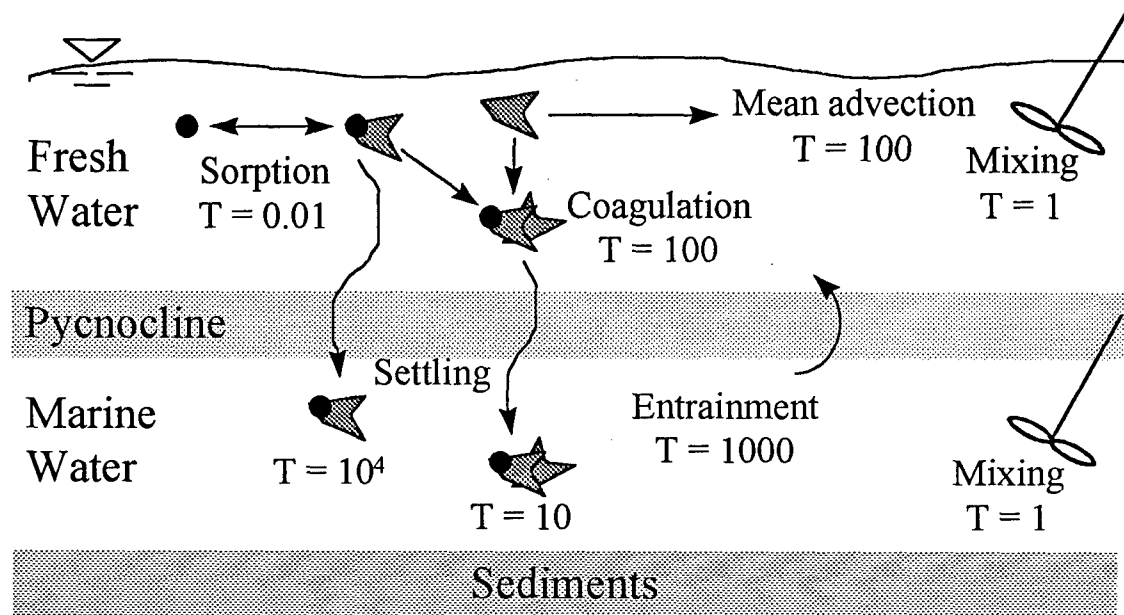
**Figure 1.2**: : Schematic illustrating the major processes affecting pollutant and particle transport in stratified estuaries. The characteristic time for each process is shown normalized to the time for bulk mixing in the top and bottom fluid layers.

Consider a stratified estuary scenario in which an initially dissolved hydrophobic organic pollutant and colloidal solids are introduced by riverine flow into the upper freshwater layer. As the estuary widens, the mean flow slows and the vertical particle flux increases. Wind mixing in the estuary provides energy input generating turbulent surface waters that promote particle contact and entrain the deeper and more dense salt water layer into the freshwater layer. The entrainment of salt water increases the solution ionic strength and that destabilizes the particles and further enhances the rate of aggregation. The large particles that subsequently form rapidly settle to the estuarine bottom.

Figure 1.2 summarizes the characteristic times of the pollutant transport mechanisms relative to turbulent transport in the fresh or salt water layer. For this analysis we consider typical estuarine turbulence conditions where the turbulent dissipation rates range from 0.002 to 0.7 $cm^2/s^3$ and root mean square (rms) turbulent velocity varies between 1 and 7 cm/s (Krone, 1978). In the analysis, suspended sediment diameters range from 1 to 100 μm, their density is assumed to be 2 $g/cm^3$ (McCave, 1984) and the particle concentration is 1 g/L (Campbell & Spinrad, 1987; Gibbs, 1977; Rogers, 1993). Partitioning of hydrophobic organic compounds between an aqueous phase and an inorganic colloid is generally governed by a physical sorption process. Barring significant mass transport limitations, physical sorption is typically a rapid reaction that occurs on times scales of milliseconds to seconds (Weber et al., 1991). Consequently, pollutant sorption to suspended sediment is expected to be

orders of magnitude faster than bulk mixing (see Figure 1.2) suggesting that the sorption process can be treated as if it is at equilibrium.

The stable density interface in the estuary acts as an impedance to freshwater/salt water mixing. The rate of salt water entrainment into a turbulent freshwater layer is related to the local value of the Richardson number:

$$Ri = \frac{\Delta \rho g L}{\bar{\rho} u'^2}$$  (1.1)

where $\Delta \rho / \bar{\rho}$ is the density difference between the fresh and salt water layers divided by the average density, g is the acceleration due to gravity, $u'$ is the root mean square (rms) velocity of turbulence and, L is the integral length scale of turbulence. The integral length scale of turbulence is the characteristic size of the largest turbulent eddies within the turbulent fluid. The relative importance of entrainment compared with turbulent transport is given by (Breidenthal, 1992):

$$\frac{T_{entrainment}}{T_{mixing}} \propto Ri^{3/2}$$  (1.2)

For fresh water ($\approx 0$ ppt salinity) over sea water ($\approx 36$ ppt salinity), this leads to a relatively slow time scale for entrainment as shown in Figure 1.2.

Settling is the other important transport process and the ratio of the rms turbulent velocity to the particle settling velocity describes the relative importance of particle settling. In this analysis spherical particles are assumed, so Stokes settling velocity may be used. For small particles with

diameters near 1 μm, settling is very slow; however, since the relative importance of settling increases with the square of the particle diameter, it can become significant for particles on the order of 10 to 100 μm in diameter.

Mean advection to the ocean varies widely and it depends primarily on the length of the estuary and magnitude of the mean velocity. These order of magnitude calculations assume a estuary length to depth ratio of 100-1000 (see for instance, Bates et al., 1987).

Brownian motion, turbulent shear, and differential settling are all mechanisms that can lead to colloid aggregation. Using the coagulation rate expressions provided by Pearson et al. (1984) the importance of these coagulation mechanisms is compared with bulk mixing. Whatever the dominant coagulation mechanism, coagulation is a weak process that occurs about 100 times slower than turbulent mixing of the stratified fluid layer. The coagulation mechanism that controls the coagulation rate changes across the particle size spectrum with Brownian motion being important for diameters near 1 μm, turbulent shear controlling for 1 to 10 μm diameter particles and differential settling becoming dominant for size particles larger than about 10 μm in diameter and with a characteristic size difference of 10 μm.

Considering these transformation processes permits the development of a sequence of plausible mechanisms that control particle and pollutant trapping in a stratified estuary. Pollutants and particles in the fresh water phase rapidly come to chemical equilibrium and are mixed throughout the freshwater layer. In general, colloidal particles are too fine to settle

appreciably; thus coagulation followed by sedimentation of the large flocs is likely to be the dominant particle removal pathway. Entrainment of salt from the estuarine bottom water layer destabilizes colloidal particles allowing them to aggregate into large flocs with significant settling velocities. As a first step, Brownian motion causes the coagulation of submicron particles. Floc size is further increased via the mechanism of turbulent shear coagulation. Eventually, the particle aggregates become large enough to sweep out smaller particles via differential settling flocculation.

Jensen (1997) provides an experimental example illustrating how coagulation can augment suspended sediment vertical flux. In this work, a two-layer stratified fluid was created in a laboratory water column containing vertically spaced oscillating grids for turbulence generation (see Chapter 5 for details on the design of the experimental apparatus). A particle slurry was introduced into the upper freshwater layer and the evolution of the suspended sediment concentration was monitored as a function of time, turbulence intensity and particle size. Mixing in the upper fresh water layer was fast compared with settling so the experiments reproduced the relative rates shown in Figure 1.2. Model predictions for the evolution of suspended sediment concentration in the well-mixed upper layer were based on a mass balance that incorporated the effect of particle settling through the pycnocline. Shown in Figure 1.3 are experimental and model results for coagulating and non-coagulating suspensions. Plotted in Figure 1.3 is the relative concentration ($C/C_0$) versus time, in which the time has been normalized with the characteristic settling time of the
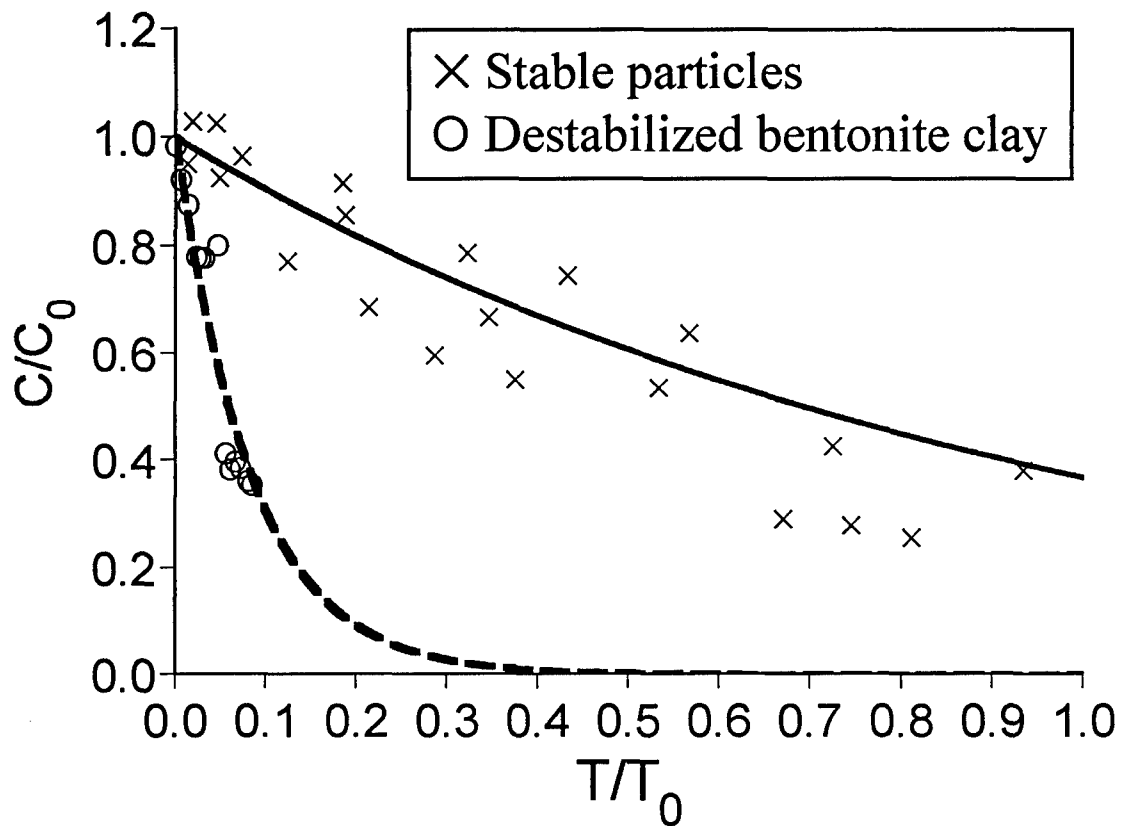
**Figure 1.3**: Evolution of the suspended sediment concentration in the upper layer of a stratified system. The particle concentration relative to the initial value is plotted against the normalized time. $T_0 = V/Aw$ is the characteristic settling time of the primary (non-aggregated) particles where V is the upper layer volume, A is the horizontal cross sectional area and w is the particle settling velocity (after Jensen, 1997).

primary particles: $T_0 = V/wA$ where V is the tank volume, A is the reactor horizontal cross sectional area and w is the settling velocity of the primary particles. The crosses represent experimental measurements for non-cohesive sediment and the solid line is the model prediction. The circles are data collected for kaolinite, a coagulating clay with an initial diameter of 1.5 μm. The relative concentration of the coagulating particles decreased more rapidly than the stable suspension indicating that coagulation created large flocs that fell faster than the non-coagulated particles. As shown in Figure 1.3, the concentration of the destabilized particles reached 40% of its initial value ten times faster than the non-coagulating sediment. Clearly, coagulation can dramatically alter the vertical flux of sediment in the estuarine environment. Fitting the kaolinite data with a mass balance modified to reflect the size of the floc particles (shown by the dashed line) suggested that the effective mean particle diameter had to increase about 3.5 times for the particles to settle at the observed rate.

## 1.2 Research Objectives

Estuaries are purported to be sinks for river-borne pollutants. Given the time scales discussed above, a two-fold mechanism for pollutant trapping, including equilibrium sorption of pollutants to suspended sediment followed by the coagulation and settling of the particulates, is proposed to control estuarine pollutant fate. This research addresses both the issues of sorption and coagulation by:

- Investigating the role of equilibrium sorption in controlling the phase distribution of hydrophobic pollutants in the estuarine water column.

- Investigating coagulation due to turbulent shear through theory, experiments and computer simulations.

### 1.2.1 *Equilibrium sorption*

In Chapter 2 the role of equilibrium sorption in the estuarine environment is considered using a three-component equilibrium sorption model consisting of a hydrophobic sorbate, suspended sediment and dissolved organic matter (DOM). Model surrogates were chosen to mimic actual estuarine materials. The polycyclic aromatic hydrocarbon, phenanthrene, represented the hydrophobic pollutant, two types of clay minerals were used as surrogates for the suspended sediment, and several recalcitrant organic compounds were selected to mimic DOM.

An experimental program was developed to study the effects of salinity and DOM coatings on phenanthrene sorption. Past work conducted predominately by Tipping and coworkers (Tipping, 1981; Tipping & Heaton, 1983) suggested that DOM will bind to solids as the concentration of divalent cations such as $Ca^{+2}$ is increased. The DOM coating on the particles would result in a higher effective organic carbon content, and since the extent of hydrophobic organic compound sorption is strongly correlated with the sorbent organic carbon content (Karickhoff, 1984), sorption of phenanthrene to the sediment is expected to increase.

Field measurements of phenanthrene in estuarine sediments imply that the pollutant is predominantly associated with the solid phase (McGroddy & Farrington, 1995; McGroddy et al., 1996). Using

experimental sorption data collected for several simulated estuarine pollutant/sediment/DOM systems, as well as additional sorption studies from the literature, the role of sorption in controlling pollutant phase distribution was examined.

### 1.2.2 *Turbulent coagulation*

The discussion in Section 1.2 highlights the importance of turbulent coagulation as the mechanism that transforms non-settling, stable colloids into larger flocs with appreciable settling fluxes in estuarine environments. Unfortunately, current models for turbulent coagulation have been incompletely validated and in some cases are formulated based upon incorrect assumptions about the turbulent flow field. A major component of this thesis is focused on developing a physically based model for turbulent coagulation that can be used to obtain *a priori* predictions.

In Chapter 3, coagulation in an isotropic random flow is examined in the limit of small total strain where relative particle transport and coagulation by the fluctuating flow field can be represented with a pair diffusion coefficient. While the pair diffusion method only approximates coagulation in turbulent flows, it can be used as a baseline to which more realistic simulations of turbulent shear-induced coagulation can be compared. In addition, the pair diffusion formulation outlined in Chapter 3 was made sufficiently general to have application in other random flows such as chaotic laminar flows.

Simulations of coagulation in Gaussian isotropic turbulence are presented in Chapter 4 as a function of the turbulent flow time scales and the importance of viscous resistance to motion and van der Waals

attractions is examined. The model assumes that the flow field in the neighborhood of a pair of coagulating particles controls the rate of aggregation. Equations of motion that include the effects of a random linear flow field, hydrodynamic interactions and interparticle forces are derived. A temporal Fourier series is used to represent the fluctuating velocity gradient field and particle trajectories calculated in this random flow are used to compute the coagulation rate.

In the last phase of this research (Chapter 6), the model simulations presented in Chapter 4 are compared with experimental measurements of coagulation in grid-stirred turbulence. First the turbulence generating apparatus is described and characterized (Chapter 5). Steady-state sediment and turbulence profiles obtained in the apparatus are measured and successfully compared with theory. These measurements give confidence that the grid-stirred apparatus can produce nearly homogeneous turbulence. In Chapter 6 the initial turbulent coagulation rate of monodisperse polystyrene particles is presented and compared with model simulations. The spatial distribution of turbulent shear is measured so the observed coagulation rate can be related to the local distribution of coagulation rates within the reactor. The coagulation rate of monodisperse polystyrene particles are measured at several turbulent intensities and separate Brownian coagulation experiments are used to find the magnitude of the van der Waals attraction for the polystyrene beads for use in the numerical model. Conclusions based on the turbulent coagulation and sorption studies described in Chapters 2 through 6 are summarized in Chapter 7.

This thesis utilizes concepts and terminology from a variety of scientific fields, including: fluid mechanics, hydraulics, turbulence, colloids and surface science, and surface reactions. The reader is referred to Appendix A for a listing of general textbooks that can aid in comprehending the material in this thesis. Also included in Appendix A are definitions of common fluid mechanics terms used throughout the chapters.

# REFERENCES

BATES, T. S., MURPHY, P. P., CURL, H. C. & FEELY, R. A. 1987 Hydrocarbon distributions and transport in an urban estuary. *Env. Sci. & Tech.* **21**, 193-198.

BREIDENTHAL, R. E. 1992 Entrainment at thin stratified interfaces: the effects of Schmidt, Richardson, and Reynolds numbers. *Phys. Fluids A* **4**(10), 2141-2144.

ELDRIDGE, P. M. & SIERACKI, M. E. 1993 Biological and hydrodynamic regulation of the microbial food web in a periodically mixed estuary. *Limnol. Oceanogr.* **38**(8), 1666-1679.

CAMPBELL, D. E. & SPINRAD, R. W. 1987 The relationship between light attenuation and particle characteristics in a turbid estuary. *Est. Coast. Shlf Sci.* **25**, 53-65.

FISCHER, H. B., LIST, E. J., KOH, R. C. Y., IMBERGER, J. & BROOKS, N. H. 1979 *Mixing in Inland and Coastal Waters*, pp. 229-240. Academic Press.

GIBBS, R. J. 1977 Suspended sediment transport and the turbidity maximum. In *Estuaries, Geophysics and the Environment* (ed. National Research Council). National Academy of Sciences.

HUNTER, K. A. & LISS, P. S. 1979 The surface charge of suspended particles in estuarine and coastal waters. *Nature* **282**, 823-825.

JENSEN, A. S. 1997 Experiments and modeling of turbulence, salinity and sediment concentration interactions in a simulated estuarine water column. MS Thesis. School of Civil & Environmental Engineering, Cornell University.

KARICKHOFF, S. W. 1984 Organic pollutant sorption in aquatic systems. *J. Hydr. Eng.* **110**, 707-735.

KRONE, R. B. 1978 Aggregation of sediment particles in estuaries. In *Estuarine Transport Processes* (ed. B. Kferfve). Univ. South Caroline Press.

McCAVE, I. N. 1984 Size spectra and aggregation of suspended particles in the deep ocean. *Deep Sea Res.* **31**(4), 329-352.

McGRODDY, S. E. & FARRINGTON, J. W. 1995 Sediment porewater partitioning of polycyclic aromatic hydrocarbons in three cores from Boston Harbor Massachusetts. *Env. Sci. & Tech.* **29**, 1542-1550.

McGRODDY, S. E., FARRINGTON, J. W. & GSCHWEND, P. M. 1996 Comparison of *in situ* and desorption sediment-water partitioning of polycyclic aromatic hydrocarbons and polychlorinated biphenyls. *Env. Sci. & Tech.* **30**, 172-177.

MURPHY, P. P., BATES, T. S., CURL, H. C., FEELY, R. A. & BURGER, R. S. 1988 The transport and fate of particulate hydrocarbons in an urban fjord-like estuary. *Est. Coast. & Shlf. Sci.* **27**, 461-482.

O'MELIA, C. R. 1995 From Algae to Aquifers. In *Aquatic Chemistry Interfacial and Interspecies Processes* (eds. C. P. Huang, C. R. O'Melia & J. J. Morgan), pp. 333-336. American Chemical Society.

OFFICER, C. B. & LYNCH, D. R. Bioturbation, sedimentation and sediment-water exchanges. *Est. Coast. & Shlf. Sci.* **28**(1), 1-12.

PEARSON, H. J., VALIOULIS, I. A. & LIST, E. J. 1984 Monte Carlo simulation of coagulation in discrete particle-size distributions. *J. Fluid Mech.* **143**, 367-385.

PRAHL, F. G. & CARPENTER, R. 1979 The role of zooplankton fecal pellets in the sedimentation of polycyclic aromatic hydro-carbons in Dabob Bay, Washington. *Geochim. et Coscmochim. Acta* **43**, 1959-1972.

ROGERS, H.R. 1993 Speciation and partitioning of priority organic contaminants in estuarine waters. *Coll. Surf. A* **73**, 229-235.

SAGEMANN, J., SKOWRONKE, F., DAHMKE, A., SCHULZ, H. D. 1996 Pore-water response on seasonal environmental changes in intertidal sediments of the Weser Estuary, Germany. *Env. Geo.* **27**, 326-369.

TIPPING, E. 1981 Adsorption by geothite (alpha-FeOOH) of humic substances from three different lakes. *Chem. Geo.* **33**, 81-89.

TIPPING, E. & HEATON, M. J. 1983 The adsorption of aquatic humic substances by two oxides of manganese. *Geochim. et Cosmochim. Acta.* **47**, 1393-1397.

WEBER, W. J. JR., MCGINLEY, P. M. & KATZ, L. E. 1991 Sorption phenomena in subsurface systems: concepts, models and effects on contaminant fate and transport. *Wat. Res.* **25**(5), 499-528.

# CHAPTER 2:
## EFFECTS OF SALINITY CHANGES AND THE FORMATION OF DISSOLVED ORGANIC MATTER COATINGS ON THE SORPTION OF PHENANTHRENE: IMPLICATIONS FOR POLLUTANT TRAPPING IN ESTUARIES*

## 2.1 Introduction

Estuaries are particularly susceptible to environmental abuse since industrial activity is often concentrated near them. Water quality management in the estuarine zone, including the assessment and remediation of contaminated areas, requires techniques to predict the fate of pollutants discharged into estuaries. Understanding the factors that affect pollutant trapping within the estuary is an important first step toward developing comprehensive plans for managing and remediating these delicate aquatic environments (NRC, 1989).

Studies investigating hydrophobic pollutant transport within estuaries show that these compounds are not flushed out to sea, but are transferred to estuarine sediments (Bates et al., 1987, Bouloubassi &

Saliot, 1994; Murphy et al., 1988). Bates et al. (1987) and Murphy et al. (1988) examined suspended sediment concentrations of polycyclic aromatic hydrocarbons (PAHs) in a fjord-like estuary near Seattle, Washington. Large horizontal PAH concentration gradients led Bates et al. (1987) to conclude that vertical transport dominated PAH distribution. Similarly, Murphy et al.(1988) concluded that more than 90% of sediment bound hydrocarbons remained within the estuary. Neither of these investigations examined the mechanisms that led to the observed pollutant trapping.

For hydrophobic pollutants, sorption onto particulate matter is one of the dominate phase-transfer processes affecting their movement and fate in the aquatic environment (Shian-chee & Gschwend, 1986). Dramatic changes in sorptive behavior caused by increases in sorbate and sorbent hydrophobicity brought on through increases in salinity are one possible explanation for the pollutant trapping observed in estuaries. High ionic strengths "salt out" hydrophobic compounds causing their effective sorption coefficients to increase. A recent study of PAH sorption to harbor sediment found the increase in sorption attributable to increases in ionic strength to be about 22% (Hegemen et al., 1995), which agrees with theoretical estimates (Karickhoff, 1984). The effect of ionic strength on hydrophobic organic compound binding to dissolved macromolecules (such as humic acid) is more difficult to predict. The magnitude and direction of the "salt effect" has been observed to be a complicated function of pH, divalent ion concentration and of the specific organic macromolecule

studied (Carter & Suffet, 1982; Schlautman & Morgan, 1993; Murphy et al., 1994).

The formation of hydrophobic dissolved organic matter (DOM) coatings on suspended sediment in response to solution chemistry changes might lead to increased pollutant sorption. Studies have shown that at low ionic strengths (1-30 mM) the addition of divalent cations, such as $Mg^{+2}$ and $Ca^{+2}$, enhanced sorption of DOM to solid surfaces (Dempsey & O'Melia, 1983; Tipping, 1981; Tipping & Heaton, 1983). If these results are extrapolated to the high salinities, and therefore high ionic strengths, seen in the estuarine system one might surmise that the removal of DOM from the dissolved to particulate phase would be enhanced significantly by the increased concentration of $Ca^{+2}$ and $Mg^{+2}$ found in seawater. This coating of sediment by DOM would effectively raise the organic carbon content associated with the solid phase and, since the distribution coefficients of nonionic organic compounds are highly correlated with the organic content of the sorbent (Karickhoff, 1984), sorption of the hydrophobic pollutant might be expected to increase.

Using batch isotherm experiments, this research simulated equilibrium sorptive phenomena in the estuarine environment to better understand the interplay between hydrophobic pollutants, DOM and suspended sediment as a function of salinity. Model surrogates were chosen to simulate actual estuarine materials. The PAH, phenanthrene, was used as a representative hydrophobic pollutant, DOM was modeled with an extracellular polymer from a soil bacterial isolate and kaolinite clay was used as the experimental surrogate for suspended sediment.

Information gathered from this three-component system was integrated into a model of pollutant sorption within an estuary. Model calculations were used to ascertain the effects of salinity and DOM coatings on phenanthrene sorption and to provide evidence for the relative importance of sorptive mechanisms in estuarine pollutant trapping.

## 2.2 Theory

Under many conditions the sorption of hydrophobic pollutants can be successfully described with a linear equilibrium distribution coefficient:

$$[Sorbate]_s = K_d [Sorbate]_a \qquad (2.1)$$

where $[]_s$ denotes solid phase concentrations (g/g solid), $[]_a$ represents aqueous phase concentrations (g/ml) and $K_d$ is the distribution coefficient (ml/g). In the literature, the treatment of sorption to colloidal material has been handled as both a separate sorbent phase and lumped with the sorbent in the aqueous phase (see for instance, Bergen et al., 1993; Backhus & Gschwend, 1990; Allen-King et al., 1995). In this work the sorptive effects of colloidal suspended sediment and the bulk solid phase are combined; care has been taken in the experiments so that sorption onto sediment and onto colloidal material are considered together.

To elucidate the underlying mechanisms leading to enhanced sorption, a three component equilibrium model (Magee et al., 1991) was used to represent the PAH (phenanthrene), DOM (extracellular polymer), solid (kaolinite clay) system. Figure 2.1 shows the three sorption pathways relating the estuarine surrogates. In this model, sorption of PAH to free
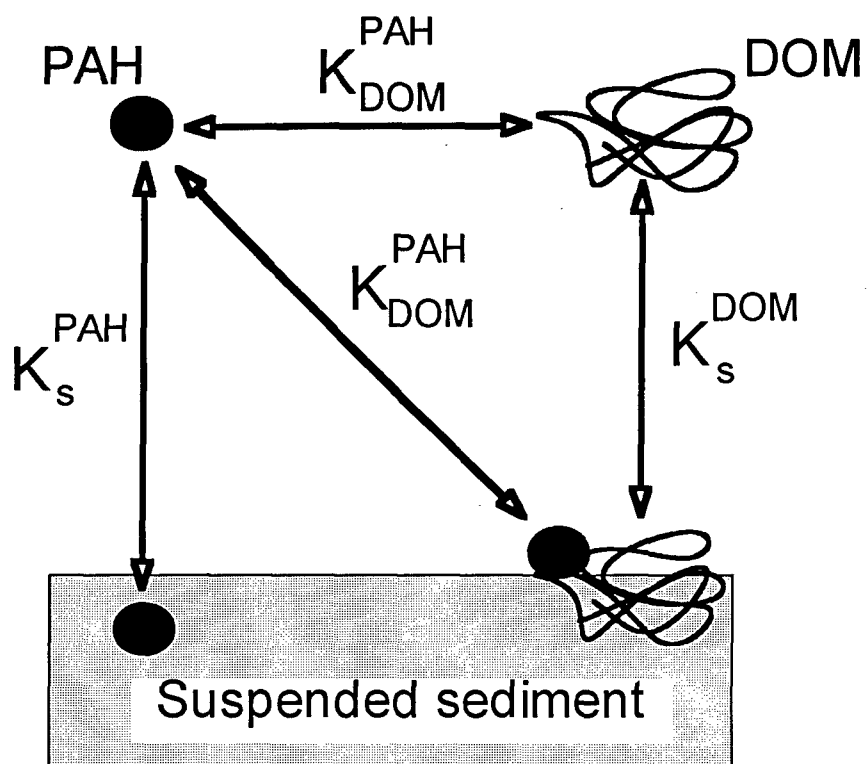
**Figure 2.1**: Schematic of the three component sorption equilibrium model for a PAH, DOM and solid phase. Arrows indicate sorptive equilibrium reactions. It was assumed that the PAH would sorb to both free and clay-bound DOM to the same extent.

and clay-bound DOM was assumed to be identical. The experimentally defined sorption coefficients for the binary interactions between PAH, DOM and solid, were used to derive an "effective" overall sorption coefficient,$K_O$, for the distribution of PAH between the aqueous and solid phases:

$$K_O = \frac{[PAH]_s^T}{[PAH]_a^T} \qquad (2.2)$$

The superscript T indicates that these concentrations include the free PAH plus the DOM-bound PAH. Combining Equation 2.2 with the equilibrium distribution relations suggested in Figure 2.1 leads to an expression for $K_O$:

$$K_O = \frac{K_s^{PAH} + K_{DOM}^{PAH} K_s^{DOM} [DOM]_a}{1 + K_{DOM}^{PAH} [DOM]_a} \qquad (2.3)$$

where $K_s^{PAH} = [PAH]_s / [PAH]_a$, $K_{DOM}^{PAH} = [PAH]_{DOM} / [PAH]_a$, $K_s^{DOM} = [DOM]_s / [DOM]_a$, and $[]_{DOM}$ denotes concentrations on the DOM (ex., g/g extracellular polymer). From Equation 2.3, one can observe that increases in $K_s^{DOM}$ caused by cation effects (Dempsey & O'Melia, 1983; Tipping, 1981; Tipping & Heaton, 1983) could lead to higher overall PAH sorption than that seen without DOM.

The degree of hydrophobic pollutant sorption is linked to its activity in the aqueous phase. As the activity coefficient of a pollutant increases in response to increases in ionic strength, pollutant sorption rises (Karickhoff,

1984). The effect of ionic strength on pollutant hydrophobicity is generally incorporated into the pollutant's aqueous activity coefficient using an empirical salting coefficient model (Garrels & Christ, 1965; Whitehouse, 1985):

$$\gamma = 10^{k_s I} \qquad (2.4)$$

where $\gamma$ is the activity coefficient, $k_s$ is the salting coefficient (L/mol) and I is the ionic strength (mol/L). The value of the salting coefficient depends on the composition of the ionic medium which is taken to be an artificial saline solution (see Section 2.3) in this chapter. Combining Equations 2.1 and 2.4 results in an expression describing the change in the sorption coefficient as a function of ionic strength:

$$K_d = K_d^0 10^{k_s I} \qquad (2.5)$$

where the superscript 0 signifies the freshwater (zero ionic strength) sorption coefficient. Analogous expressions for $K_s^{PAH}$, $K_{DOM}^{PAH}$, $K_s^{DOM}$ were used to include "salting out" in Equation 2.3. The resulting equation for the overall sorption coefficient as a function of solution ionic strength is:

$$K_O = \frac{K_s^{PAH,0} 10^{k_s^{PAH,S} I} + K_{DOM}^{PAH,0} K_s^{DOM,0} 10^{(k_s^{PAH,DOM} + k_s^{DOM,S}) I} [DOM]_a}{1 + K_{DOM}^{PAH,0} 10^{k_s^{PAH,DOM} I} [DOM]_a} \qquad (2.6)$$

where the superscripts for the salting coefficients refer to the sorbate and sorbent, respectively.

The experiments described in this chapter were conducted in aqeuous environments ranging from fresh to marine saline levels. Salinities in this chapter are reported in ppt. The empirical relation: I = 0.01986(Salinity), converts from salinity in ppt to ionic strength in mol/L for the artificial sea water solution used in this work.

It is convenient to consider the sorbed fraction when appraising the impact of sorption on pollutant trapping in estuaries. The sorbed fraction, $f_s$, is a ratio of the mass of contaminant sorbed to the suspended sediment to the total mass in the system and it is related to the overall distribution coefficient by:

$$f_s = \frac{K_O[suspended\ sediment]_a}{K_O[suspended\ sediment]_a + 1} \qquad (2.7)$$

Values of $f_s$ greater than 0.5 would suggest that the pollutant was being trapped since most of the contaminant would be associated with the suspended sediment phase.

## 2.3 Experimental Methods

### 2.3.1 Materials

Phenanthrene was chosen as a model hydrophobic pollutant since it has been isolated and monitored in field studies that examined pollutant distributions in estuaries (Bates et al., 1987; Hegemen & Weijden, 1995). Radiolabeled phenanthrene (9-^{14}C, specific activity = 13.1 mCi/mmol,

Sigma Chemical Co, St. Louis, MO) was placed in a saturater similar to that designed by Burris and MacIntyre (1985) and dissolved in distilled deionized water containing 5 mM $CaSO_4$ and 0.25 wt% $NaN_3$. The $CaSO_4$ was added to represent a background riverine electrolyte and the $NaN_3$ was used to inhibit bacterial degradation. Isotope purity was verified by the manufacturer through HPLC analysis and it was found to be greater than 98% pure.

Commercially available kaolinite (trade name Hydrite 121-S, Dry Branch Kaolin Co., Dry Branch, GA) was dried at 105°C for at least 24 hours and used without further preparation. The average particle size of this non-swelling clay was 1.5 μm as determined from analysis with a Coulter Multisizer II (Coulter Corp., FL) and the organic carbon content of the kaolinite was determined to be 0.076% ± 0.015% (n = 5) as measured by high temperature combustion (Lecco induction furnace model 777-500, Lecco Corp.). Bentonite (Aldrich Chemical Co., Milwaukee, WI) was used for some experiments. This swelling clay was dried at 105°C for 24 hours before use. The organic carbon content was 2.03% ± 0.3% (n = 5), and the average particle diameter was 1.5 μm.

Solutions with salinities ranging from 0 to 30 ppt were made using an artificial seawater solution described by Hsieh et al. (1985). In this research the bacterial growth factors included by Hsieh et al. were omitted and the pH was adjusted to 8.

Many bacteria produce high molecular weight polymers and excrete them into the environment. These extracellular polymers are resistant to biodegradation and are a ubiquitous constituent of DOM in natural aquatic

systems (Chudoba et al., 1986; Underwood et al., 1995). A bacterium isolated from soil (designated as isolate 9702-M4) was obtained from the culture collection of Prof. W. C. Ghiorse (Section of Microbiology, Cornell University). Madsen et al. (1993) describe the coal tar waste site from which the bacterium was isolated. The isolate is of the *Rhizobiaceae* genus (Jenkins, 1996), and it produces a high-molecular-weight amorphous polysaccharide that has previously been found to interact strongly with phenanthrene (Dohse & Lion, 1994). To obtain extracellular polymer, the 9702-M4 isolate was grown in a glucose-based growth medium following the procedure described by Czajka (1995). Dissolved polymer was separated by centrifugation, purified by dialysis against distilled deionized water using a 5000 MWCO membrane and freeze-dried. For studies of polymer sorption to kaolinite, $^{14}$C-labeled polymer was produced by adding $^{14}$C-glucose (uniformly labeled, specific activity = 9.1 μCi/μmol, ICN Biomedicals, Irvine, CA) to the nutrient broth. Dried polymer was stored at -20°C until use. For isotherm studies, concentrated polymer solutions were prepared by dissolving the freeze dried polymer into a pH = 8 solution containing 5 mM $CaSO_4$ and 0.25 wt% $NaN_3$. Additional experiments were performed with tannic acid (Aldrich Chemical Co., Milwaukee, WI) and alginic acid (Aldrich Chemical Co., Milwaukee, WI) as surrogates for DOM. Stock solutions of tannic acid were prepared with 5 mM $CaSO_4$ and 0.25 wt% $NaN_3$ and adjusted to a pH of 8. Solutions of alginic acid were only sparingly soluble in $Ca^{+2}$ electrolyte and were prepared in distilled deionized water.

Further characterization of the materials used may be found in Table B.1 of Appendix B.

2.3.2 *Isotherm experiments.*

Equilibrium batch sorption isotherms were used to characterize the sorption coefficients of phenanthrene to a solid substrate with and without DOM and to characterize the sorption coefficient of DOM to the solid phase. The techniques used to obtain the sorption isotherms, examples of which are shown in Figure 2.2, are briefly described below. The reader is directed to the supplementary material in Appendix B for additional details.

2.3.2.1 Dialysis Technique

A modified dialysis technique (Carter & Suffet, 1982; Allen-King et al., 1995) was used to obtain the distribution coefficient for phenanthrene onto kaolinite clay, $K_s^{PAH}$. This procedure eliminated the difficulty of separating the kaolinite clay from the aqueous solution and hence circumvented what has been termed the "solids effect" (Gschwend & Shian-chee, 1985). In these experiments, phenanthrene in aqueous and clay slurry phases was allowed to equilibrate across a dialysis membrane. A series of long-term experiments performed over 18 days showed that a 6-day equilibration time was more than sufficient to reach stable phenanthrene concentrations. After equilibration, radioactive phenanthrene in samples from the aqueous and clay slurry phases was counted on a Beckman LS9800 liquid scintillation counter (Irvine, CA). By assuming all phenanthrene sinks were at equilibrium, the relative concentration difference of phenanthrene between the aqueous phase and the clay slurry

**Figure 2.2**: Example sorption isotherms. (a) Phenanthrene sorption to kaolinite clay as determined by the dialysis technique for salinities of 0 (O) and 30 (□) ppt. (b) Extracellular polymer sorption to kaolinite using the centrifugation technique at 8.2 ppt salinity. (c) Isotherms for sorption of phenanthrene to extracellular polymer at 0 (O) and 30 (□) ppt as obtained from fluorescence quenching experiments.

(a)

$K_s^{PAH} = 2.21$ ml/g

$K_s^{PAH} = 1.48$ ml/g

[Phenanthrene]$_s$ (ng/g)

[Phenanthrene]$_a$ (ng/ml)

(b)

[Polymer]$_s$ (DPM/g)

$K_s^{DOM} = 7.65$ ml/g

[Polymer]$_a$ (DPM/ml)

(c)

$F_O/F$

$K_{DOM}^{PAH} = 3170$ ml/g

$K_{DOM}^{PAH} = 1944$ ml/g

[Polymer]$_a$ (mg/l)
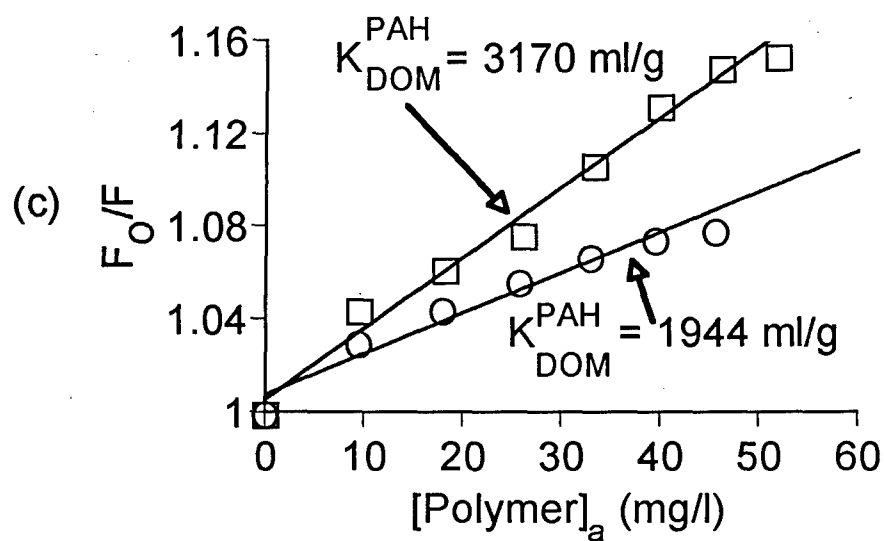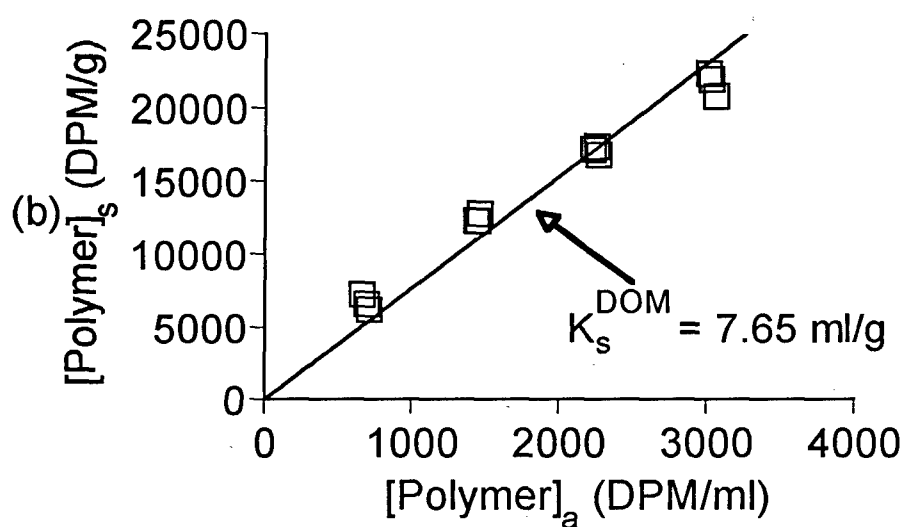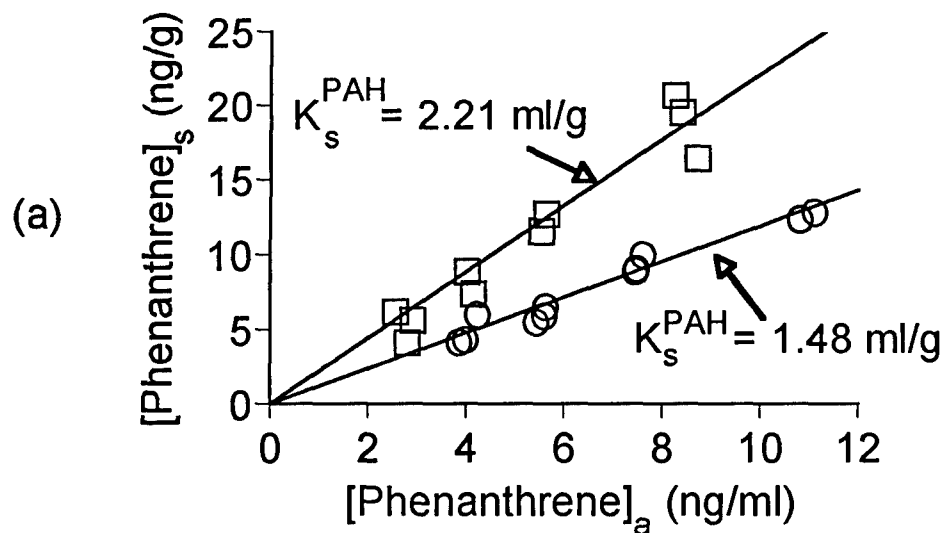
gave the sorption distribution coefficient. The presence of clay slurry within the counting samples was shown not to affect the scintillation results.

Generally, each isotherm experiment consisted of 3 replicates at 4 solids concentrations. Figure 2.2(a) shows typical results obtained at salinities of 0 and 30 ppt. The slope of a best fit line through the data yielded the distribution coefficient, $K_s^{PAH}$.

2.3.2.2 Centrifugation Technique

The dialysis procedure could not be used in experiments that included the extracellular polymer because the molecular weight cutoff of the dialysis tubing was too small to allow the polymer to pass freely. Particle separation by centrifugation offered an alternative, albeit a possibly inaccurate one due to incomplete solid/aqueous phase separation (Gschwend & Wu, 1985). This method was used to ascertain the equilibrium distribution coefficient for extracellular polymer sorption to kaolinite clay and to observe sorption of phenanthrene to clay in the presence of DOM surrogates. The procedure used followed that of Lion et al. (1990). Slow desorption of the phenanthrene from the polymer was found to affect the isotope levels measured by the scintillation counter; therefore, liquid scintillation counting was repeated daily until the phenanthrene activity remained constant between successive measurements. The equilibrium sorption coefficient was obtained from a mass balance equation which was modified to include corrections for sorptive bottle losses (Lion et al., 1990).

Typically, each isotherm utilized 3 replicates of 4 radiolabeled phenanthrene concentrations. Figure 2.2(b) shows example results for the sorption of polymer to kaolinite at a salinity of 8.2 ppt. The effect of incomplete solids separation was ascertained by comparing phenanthrene to kaolinite distribution coefficients obtained with the centrifugation protocol to those obtained with the dialysis technique. Results from the two methods were not significantly different (see Figure 2.3).

2.3.2.3 Fluorescence quenching

Fluorescence quenching experiments (Backhus & Gschwend, 1990; Gauthier et al., 1986) were used to elucidate the distribution coefficient between phenanthrene and the extracellular polymer. The procedure followed that given by Gauthier et al. (1986) with controls to correct for extracellular polymer fluorescence, inner filter effects, dilution and photo-bleaching. After equilibration the fluorescence of the phenanthrene was recorded using an SLM Aminco 8000 spectrofluorimeter with excitation and emission wavelengths of 288 nm and 364 nm, respectively.

Loss of phenanthrene to container walls was not observed and significant volatilization of the phenanthrene was not expected over the time frame of the analysis since the cuvettes were fitted with Teflon® caps. The Stern-Volmer equation was used to relate the ratio of the fluorescence intensity to the distribution coefficient for phenanthrene sorbing to extracellular polymer (Gauthier et al., 1986). Figure 2.2(c) shows example results at 0 and 30 ppt salinity.
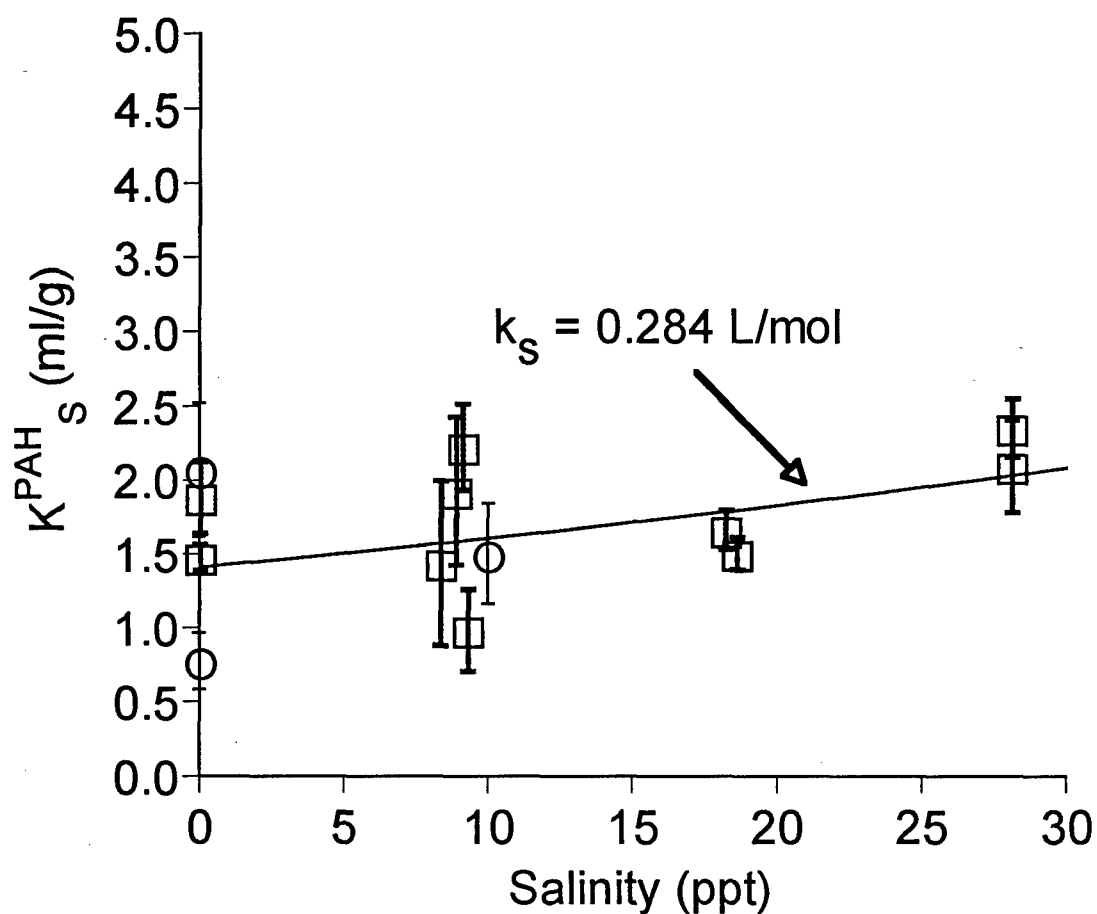
**Figure 2.3**: The effect of salinity on the distribution coefficient for phenanthrene sorption to kaolinite clay. Distribution coefficients obtained with both the dialysis (□) and centrifugation (O) techniques are shown. Error bars represent 95% confidence intervals and the fitted exponential curve is based upon the empirical salting coefficient model (Equation 2.5).

## 2.4 Results And Discussion

### 2.4.1 *Characterization of the overall sorption coefficient for the phenanthrene - polymer - kaolinite system*

2.4.1.1 Phenanthrene to kaolinite equilibrium distribution coefficient

Figure 2.3 shows the effect of salinity on $K^{PAH}_s$ from isotherms obtained via the dialysis and centrifugation technique. As expected, the distribution coefficient increased with salinity, ranging from an average value of 1.41 ml/g at 0 ppt salinity to 2.08 ml/g at 30 ppt salinity. Liljestrand and Shimizu (1991) measured the sorption coefficient for anthracene (a structural isomer of phenanthrene) to kaolinite at pH = 7.08 and observed a value of 1.97 ml/g, in agreement with the results reported here. Nonlinear regression was used to fit the data to an exponential curve based upon the "salting" coefficient model for the activity coefficient (Equation 2.5). The calculated salting coefficient was 0.284 L/mol; however, variability in the data was such that the regressed coefficient was not statistically different from 0.0. The magnitude of the empirical "salting" coefficient was, however, similar to the values reported by Whitehouse (1985) for phenanthrene at 25.3°C ($k_s = 0.269 \pm 0.066$ L/mol) and within the range of salting coefficients that can be calculated from data collected by Hegeman et al. on phenanthrene sorption to Rotterdam Harbor sediment (1995).

2.4.1.2 Phenanthrene to extracellular polymer equilibrium distribution coefficient

Results from the fluorescence quenching experiments are summarized in Figure 2.4. The distribution coefficient ranged from 2060 ml/g to 3290 ml/g at 0 and 30 ppt, respectively. Sorption of phenanthrene to the extracellular polymer was about an order of magnitude smaller (on a sorbent mass basis) than reported values for PAH sorption to humic acids (Schlautman & Morgan, 1993; Gauthier et al., 1986; Liljestrand & Shimizu, 1991).

An exponential curve fit through the data resulted in a salting coefficient of 0.341 L/mol. Based on the experimental values, phenanthrene sorption to extracellular polymer would increase about 60% as phenanthrene is transported from a fresh to marine environment.

Other researchers (Carter & Suffet, 1982; Schlautman & Morgan, 1993) have investigated the effects of small additions of divalent cations on hydrophobic pollutant sorption to DOM surrogates. Schlautman and Morgan (1993) studied the effect of ionic strength on anthracene sorption to International Humic Substances Society humic acid at pH = 7. As $Ca^{+2}$ was added to increase the ionic strength from 0.001 to 0.1 mol/L, these investigators observed that the PAH distribution coefficient remained nearly constant (Schlautman & Morgan, 1993). An ionic strength of 0.1 mol/L corresponds to a salinity of about 5 ppt and, based on the regressed salting coefficient model, a change in salinity from 0 to 5 ppt would change $K^{PAH}_{DOM}$ by 8%. Given reasonable experimental errors, an 8% change would be difficult to detect. Carter and Suffet (1982) saw increases in
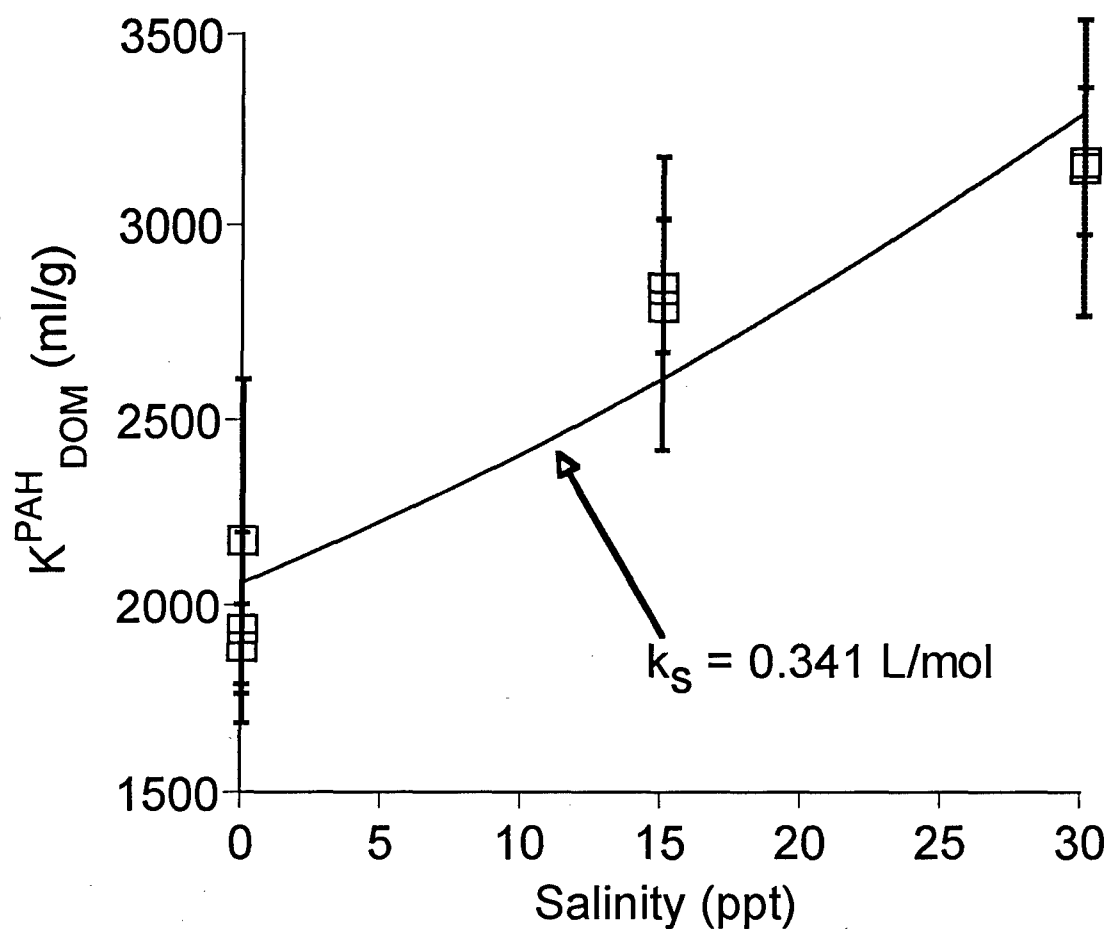
**Figure 2.4**: The effect of salinity on the distribution coefficient for phenanthrene sorption to 9702-M4 extracellular polymer. The exponential curve fit is based upon an empirical salting coefficient model (Equation 2.5) and the error bars denote 95% confidence intervals.

DDT binding to humic substances with small $Ca^{+2}$ additions (20 mg/L), but they reported that their results were not statistically significant.

2.4.1.3 Extracellular polymer to kaolinite equilibrium distribution coefficient

The effect of salinity on $K^{DOM}_s$ is shown in Figure 2.5. The data does not show any systematic trends and it is believed that batch-to-batch variability in the extracellular polymer was the likely cause of the scatter. Regression to obtain a salting coefficient was not attempted and, for modeling purposes, the sorption coefficient was assumed to be constant at the average value of 7.5 ml/g as shown in Figure 2.5.

The lack of an ionic strength effect on polymer sorption would appear to be at variance with the work of several investigators who examined the effects of divalent cations on humic acid sorption to solids (Dempsey & O'Melia, 1983; Tipping, 1981; Tipping & Heaton, 1983). At ionic strengths ranging from 1 to 30 mM these researchers observed that the addition of divalent cations significantly enhanced humic sorption to solid surfaces (Tipping & Heaton, 1983). The ionic strengths used in their work were smaller than the background riverine electrolyte solution employed in this research (i.e., 5 mM $CaSO_4$). Tipping and Heaton (1983) note that the effects of $Ca^{+2}$ have been attributed to bridging between the solid surface and the humic acid. Since the specific surface area of the solid and/or binding capacity of the organic matter would limit the number of bridging sites available, it would appear reasonable to expect that once all the sites have been filled, additional increases in $Ca^{+2}$ concentration would not result in an incremental increase in the sorption coefficient. In
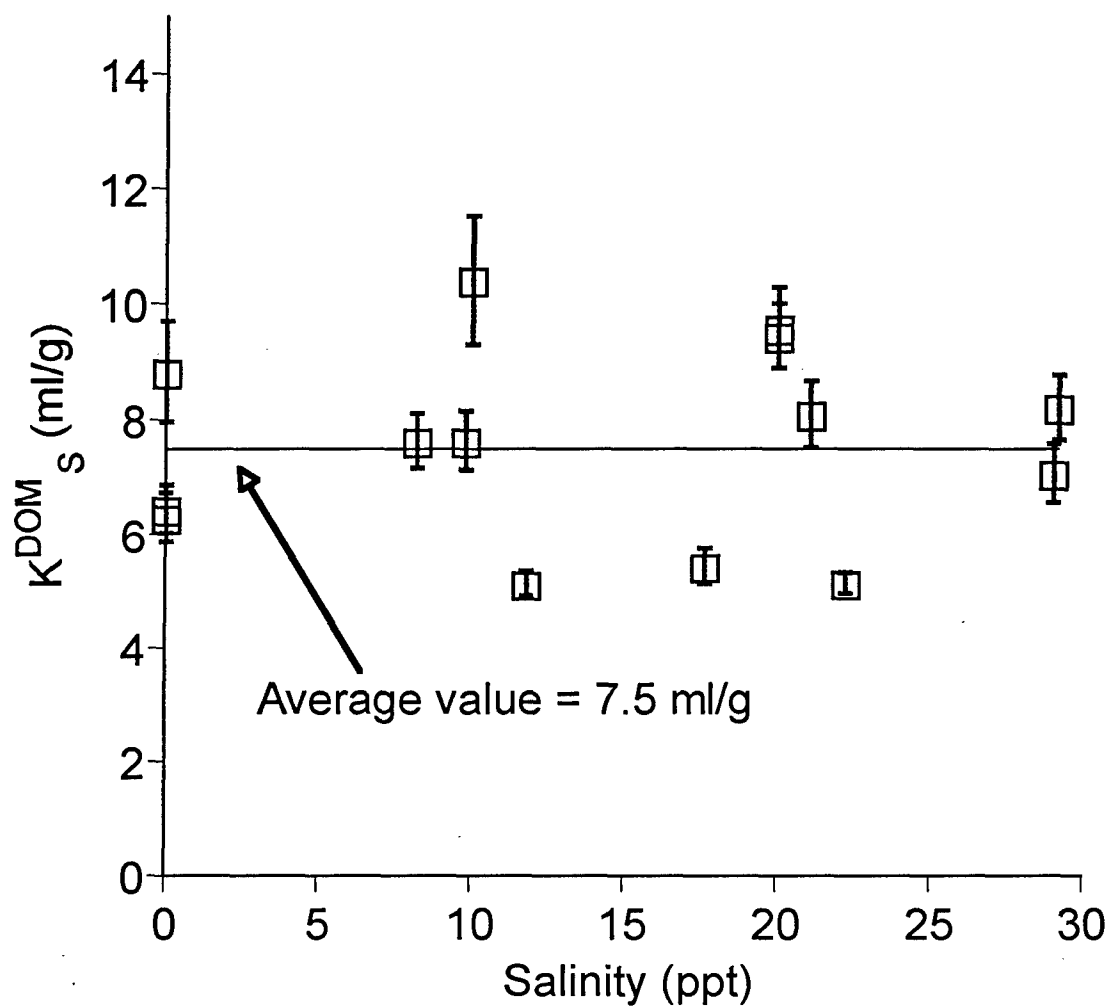
**Figure 2.5**: The effect of salinity on extracellular polymer sorption to kaolinite clay. The experimentally obtained distribution coefficients are shown with 95% confidence intervals. The horizontal line represents the average of the data.

this research observed values of $K^{DOM}_s$ were insensitive to salinity changes, supporting the conclusion that the effect of divalent cations on sorption of DOM is limited to low ionic strengths. At ionic strengths typical for estuaries, the expectation of a significant additional influence on DOM sorption caused by increases in the concentration of $Ca^{+2}$ and other divalent cations may not be reasonable.

Differences in the physical/chemical composition of the extracellular polymer used in this research and the humic acids used by other investigators might explain the contradictory observations concerning the effect of ionic strength on DOM sorption. However, both extracellular polymer and humic acid are high molecular weight polydisperse poly-functional compounds (Tipping, 1981; Jenkins, 1996) found as recalcitrant components of natural DOM (Chudoba et al., 1986; Underwood et al., 1995). It seems likely that their response to changes in solution chemistry would be correlated. Regardless of chemical differences in the DOM constituents examined, the significant increases in sorption coefficient seen by Tipping and others (Dempsey & O'Melia, 1983; Tipping, 1981; Tipping & Heaton, 1983) are unlikely to be sustainable as the ionic strength continues to increase beyond riverine levels.

2.4.2 *Simulating sorption in the estuary with a three component equilibrium sorption model*

2.4.2.1 System parameters

Two criteria must be met for equilibrium sorption to explain trapping of pollutants in estuaries. The pollutant sorption coefficient must: 1) be large enough to cause a significant fraction of the pollutant to be bound to

suspended sediment and 2) if it is not sufficiently large under fresh water conditions the sorption coefficient must increase considerably when the pollutant is exposed to elevated salinities.

A simulation of phenanthrene sorption in the estuarine environment was calculated for typical estuarine conditions at the turbidity maximum. The turbidity maximum is a location of high salinity gradient where alluvial particles are hypothesized to coagulate and settle; hence, it is likely to be a prime location for pollutant trapping within an estuary. Typical sediment concentrations in this region range from about 10 to 600 mg/L (Campbell & Spinrad, 1987; Gibbs, 1977). Although sediment concentrations as high as 2.5 g/L have been reported (Rogers, 1993), it is likely that such extreme concentrations are not reasonable for the majority of the world's estuaries. Since large sediment concentrations increase the sorbed fraction (see Equation 2.7), a conservatively high value of 0.6 g/L was chosen when calculating the feasible extent of pollutant trapping. Dissolved organic matter concentrations also vary widely in estuaries depending on local organic matter sources; a value of 10 mg/L (Liss, 1976) would mimic an estuary polluted by anthropogenic DOM sources and result in a suspended sediment:DOM weight ratio of 60. Sorption coefficients used for the model calculations discussed below are summarized in Table 2.1.

2.4.2.2 Enhanced sorption: salinity effects and coatings of suspended sediment with DOM

Figure 2.6 shows how the overall sorption coefficient for phenanthrene might be expected to change as the salinity increases from

**Table 2.1:** Summary of overall distribution coefficients, $K_O$, used in the pollutant trapping analysis for [suspended sediment]$_a$ = 600 mg/L, [DOM]$_a$ = 10 mg/L.

| Sorption System | $K_O$ (ml/g) 0 ppt | 30 ppt | Ref. |
|---|---|---|---|
| Phenanthrene + | | | |
| extracellular polymer + kaolinite | 1.51 | 2.27 | this work |
| tannic acid + kaolinite[a] | 8.44 | 12.4 | this work |
| alginic acid + kaolinite[a] | 14.5 | 21.1 | this work |
| tannic acid + bentonite[a] | 473 | 570 | this work |
| alginic acid + bentonite[a] | 745 | 798 | this work |
| humic acid + kaolinite | | 67 | this work |
| Boston Harbor lab results[b] | | 1000 | Chin & Gschwend, 1992 |
| Boston Harbor field results[b] | | 29400 | McGroddy & Farrington, 1995 |

[a]Results are reported at a suspended sediment:DOM weight ratio of 50.
[b]For a sediment organic carbon content of 5%.
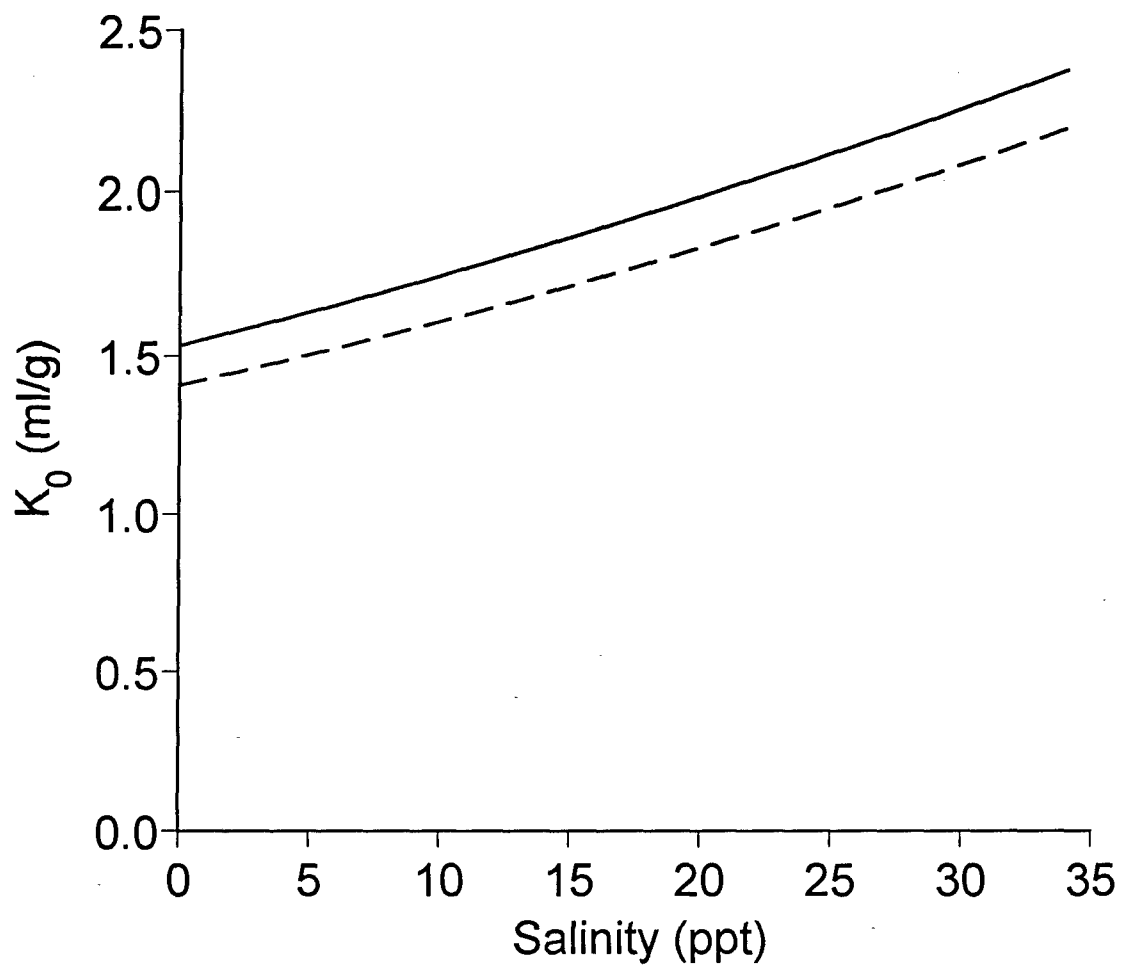
**Figure 2.6**: Results from calculations with the three component sorption equilibrium model are plotted as the overall sorption coefficient, $K_O$, versus salinity. Model predictions are shown with (—) and without (--) the inclusion of 10 mg/L DOM, to illustrate the impact of the surrogate DOM.

riverine to marine levels. Model results are provided with and without the influence of DOM so that the importance of enhanced sorption via increased DOM coatings can be discerned. The predictions for the overall distribution coefficient rose from a value of 1.51 ml/g at 0 ppt salinity to a value of 2.27 ml/g at 30 ppt. The deposition of DOM coatings increased $K_O$ by 9% at all salinities while increases due to "salting" out resulted in a 55% increase in $K_O$. The low enhancement to sorption by DOM coatings is a result of the observed insensitivity of $K^{DOM}_s$ to changes in salinity.

Combining the "salt" and DOM mediated effects on phenanthrene sorption yielded an overall increase in the $K_O$ of about 65% in the transition from fresh to marine water. While the magnitude of this increase is significant, for the typical estuarine parameters used in this analysis a 900% increase in the overall sorption coefficient would be required to go from a sorbed fraction of 10% to 50%. Given the assumptions in the model calculations, equilibrium sorption appears to be relatively insensitive to estuarine salinity changes, and hence is unlikely to be a dominant mechanism leading to increased pollutant association with suspended solids in the transition from a fresh to marine environment.

To generalize the conclusions about DOM sorption under estuarine conditions, additional DOM/suspended sediment surrogates were screened for enhanced sorption effects. Screening experiments were performed with the low organic carbon content kaolinite clay used in prior experiments and a higher organic content bentonite clay. Extracellular polymer, tannic acid and alginic acid were all considered as DOM surrogates. The overall sorption coefficient for phenanthrene was obtained using the centrifugation

method. Experiments were performed at fresh (0 ppt) and marine (30 ppt) conditions with sediment:DOM weight ratios of ∞, 10,000, 50 and 10. Table 2.1 summarizes of the sorption coefficients obtained with a sediment:DOM weight ratio of 50 and Table B.2 in Appendix B provides sorption coefficients for the other weight ratios tested. In agreement with the relative hydrophobicities of alginic and tannic acid (Merck, 1976), sorption coefficients for phenanthrene in the presence of alginic acid were consistently 60% higher than those observed with tannic acid. Changing the sorbent from kaolinite to bentonite increased the overall sorption coefficient by a factor of 50. For all the sediment and DOM combinations studied, except for phenanthrene sorption to kaolinite in the presence of extracellular polymer, the DOM caused a weak enhancement to the phenanthrene sorption that reached about 25% at a sediment:DOM weight ratio of 10. For most cases, the extent of DOM enhancement to phenanthrene sorption decreased with increasing sediment:DOM weight ratio. Details of these results are summarized in Figures B.1 to B.3 of Appendix B. In similar work, Murphy et al. (1994) studied hydrophobic organic compound sorption to mineral bound humic acid at ionic strengths comparable to salinities ranging from 0 to 5 ppt. In support of the results of this research, they observed that changes in the ionic strength had little influence on hydrophobic organic compound sorption. The results of the screening tests also corroborate data obtained from the three component equilibrium sorption model for phenanthrene, extracellular polymer and kaolinite.

For the sorption paradigm to explain pollutant trapping, large increases in pollutant binding in response to elevated salinities are needed; however, the aggregated experimental evidence obtained for extracellular polymer, alginic acid and tannic acid sorption to kaolinite and bentonite indicate that increases in salinity did not cause a significant increase in DOM sorption. Furthermore, this work suggests that the considerable increases in DOM binding to solid surfaces seen by previous investigators at low ionic strengths (Dempsey & O'Melia, 1983; Tipping, 1981; Tipping & Heaton, 1983) cannot necessarily be extrapolated to salinity levels encountered in the estuary.

### 2.4.2.3 Implications for pollutant trapping

Using the data obtained for the phenanthrene, kaolinite, extracellular polymer system, the sorbed fraction, $f_s$ (Equation 2.7) was found to be 0.1% signifying that 99.9% of the phenanthrene would be expected to remain dissolved. The DOM/sediment screening experiments previously described were also used to estimate the extent of pollutant trapping. Observed and experimentally obtained $K_O$'s for fresh and seawater are summarized in Table 2.1 and sorbed fractions are compared to other calculations (detailed below) in Figure 2.7. The calculated fraction sorbed to sediment (Equation 2.7) ranged from 0.9% to 32% with the phenanthrene, alginic acid, bentonite system providing the highest level of trapping. The evidence garnered in these experiments show that the observed sorption coefficients are not large enough to account for pollutant trapping (i.e., $f_s > 0.5$). Using Equation 2.7 at the point where the sorbed fraction is one-half, indicates that $K_O$ would have to be larger than 1667

**Figure 2.7:** Comparison of PAH trapping observed in the field and calculated in this paper for typical estuarine conditions. Results are reported as the sorbed fraction which is a ratio of the amount of phenanthrene sorbed to suspended sediment to the total amount in the system. In all cases, laboratory sorption measurements cannot achieve the level of trapping seen in the field. Boston harbor field and laboratory results were derived from McGroddy and Farrington (1995) and Chin and Gschwend (1992), respectively.

Fraction of phenanthrene associated with
suspended sediment under estuarine conditions
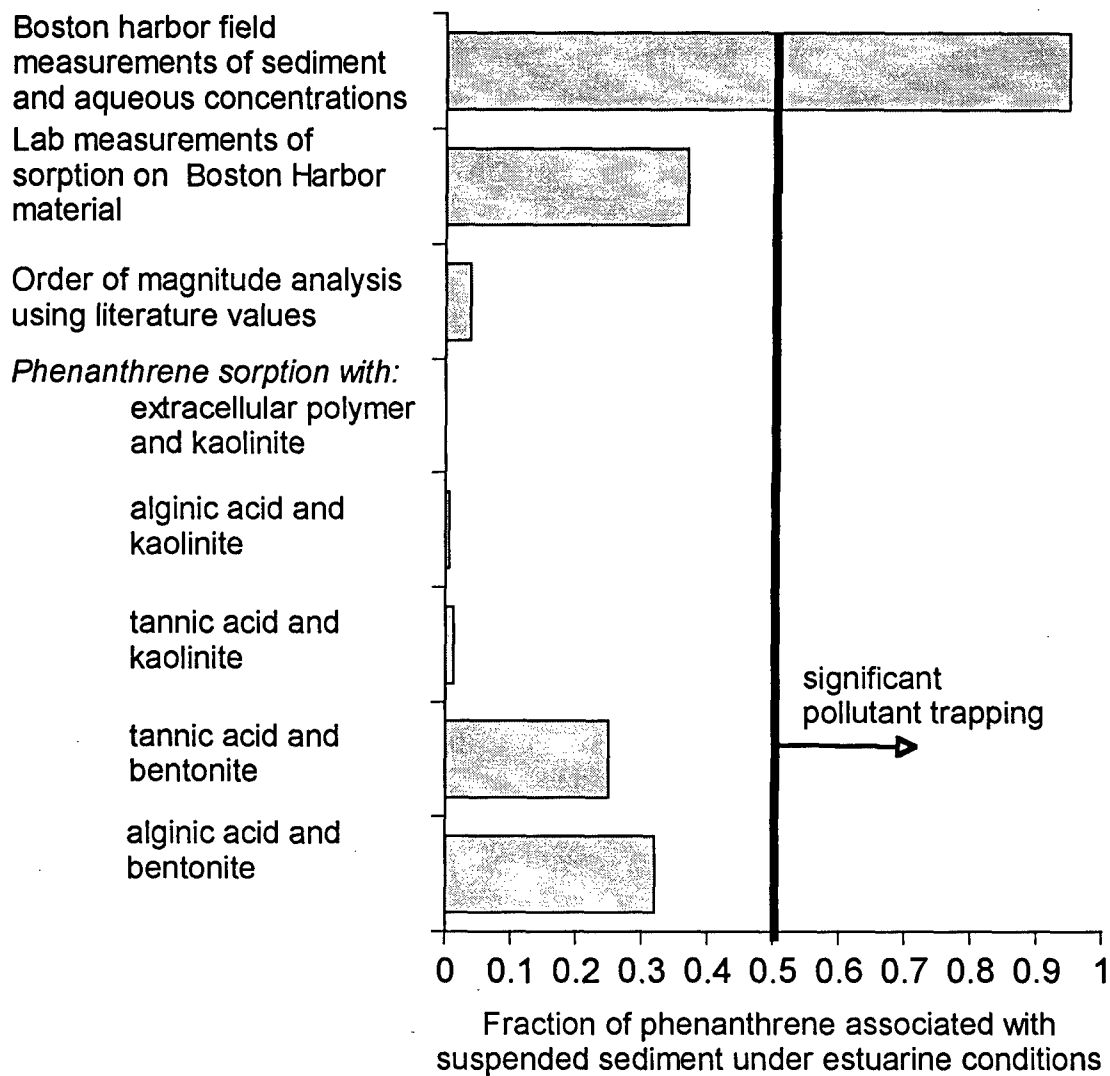
ml/g for the sorption mechanism to result in greater than 50% trapping to sediments. A $K_O$ greater than 15,000 ml/g would be needed to explain a 90% level of pollutant trapping. A possible rationale for the low results obtained using the sorption model is that the experimental surrogates were not representative of the DOM found in estuaries. To test this hypothesis, a thought experiment was performed using humic acid, a very hydrophobic DOM constituent. Representative values of 15,000 ml/g and 500 ml/g were chosen for $K^{PAH}_{DOM}$ and $K^{DOM}_s$, respectively (See Table B.3 in Appendix B for a list of sources consulted). With these values the resulting estimate for $f_s$ was only 3.9%.

It is worth noting that the high $K_O$ values necessary to explain pollutant trapping have been reported in some field studies (McGroddy & Farrington, 1995; McGroddy et al., 1996). McGroddy and Farrington (1995) directly measured solid and aqueous phase concentrations of phenanthrene in Boston Harbor. Using a 5% organic carbon content for the solid phase, a $K_O$ of approximately 29,400 ml/g was estimated from their data, leading to an $f_s$ of 95%. However, Chin and Gschwend (1992) performed laboratory sorption experiments on the same Boston Harbor sediments used by McGroddy and Farrington (1995) and significantly lower $K_O$'s were obtained from their data. Their sorption coefficient was roughly 30 times smaller than the field observations, indicating that sorption contributed about 3.4% to the observed phase distribution coefficient based on sediment and water analysis in the field. The $K_O$ obtained by Chin and Gschwend (1992) would lead to an estimated sorbed fraction of 37%. This value is considerably lower than that based upon the

measured phase distributions and is within the range of the values seen for the model systems examined in this research.

A comparison of $f_s$ from field, laboratory and scaling analysis is illustrated in Figure 2.7. Field levels of PAH trapping ($f_s > 0.5$) were not found for the experimental surrogates even though conservatively high estimates for the suspended sediment concentration (600 mg/L) and DOM concentration (10 mg/L) in estuaries were used. The extent of trapping summarized in Figure 2.7 is based on the suspended sediment concentrations assumed and the validity of phenanthrene as a representative hydrophobic pollutant. Although this analysis considered the high end of the typical suspended sediment concentrations, unusually high solids loading could result in sorbed fractions greater than 50%. In addition, the overall sorption coefficient is highly sensitive to pollutant hydrophobicity (Karickhoff, 1984), so that $f_s$ calculated using more hydrophobic pollutants might be larger than 50% for some suspended sediment/DOM combinations. It is, however, unlikely that either of these effects would increase the sorption coefficient enough to achieve the sorbed fractions seen in field measurements (McGroddy & Farrington, 1995; McGroddy et al., 1996).

Sorptive equilibrium data analyzed in this research resulted in levels of pollutant trapping of less than 50%, at variance with field measurements done in the Boston Harbor (McGroddy & Farrington, 1995). Yet, the sorption coefficients obtained with the model systems were in agreement with laboratory sorption experiments done on the same Boston Harbor sediment, suggesting that suitable surrogates for studying sorption in

estuaries have been used. The disparity between distribution coefficients based on sorptive uptake and those based upon phase distribution of contaminants in the field lead to the conclusion that some sediment bound phenanthrene, perhaps associated with atmospheric soot particulates, may not be available for aqueous phase equilibrium distribution (McGroddy & Farrington, 1995; McGroddy et al., 1996). From the model calculations presented herein it can be inferred that sorptive equilibrium is likely to play a minor role in controlling phenanthrene trapping within the estuary.

# REFERENCES

ALLEN-KING, R. M., GROENEVELT, H. & MACKAY, D. M. 1995 Analytical method for sorption of hydrophobic organic pollutants in clay-rich materials. *Env. Sci. Tech.* **29**, 148-153.

BACKHUS, D. A. & GSCHWEND, P. M. 1990 Fluorescent polycyclic aromatic hydrocarbons as probes for studying the impact of colloids on pollutant transport in groundwater. *Env. Sci. & Tech.* **24**, 1214-1223.

BATES, T. S., MURPHY, P. P., CURL, H. C. JR. & FEELY, R. A. 1987 Hydrocarbon distributions and transport in an urban estuary. *Env. Sci. & Tech.* **21**, 193-198.

BERGEN, B. J., NELSON, W. G. & PRUELL, R. J. 1993 Partitioning of polychlorinated biphenyl congeners in the seawater of New Bedford Harbor, Massachusetts. *Env. Sci. & Tech.* **27**, 936-942.

BOULOUBASSI, I. & SALIOT, A. 1994 Implications of a multi-layered nepheloid system for hydrocarbon distributions and transport in a microtidal Mediterranean estuary. *Marine Chem.* **46**, 101-117.

Burris, D.R. & MacIntyre, W.G. 1985 Water solubility behavior of binary hydrocarbon mixtures. *Env. Toxicol. Chem.* **4**, 371-377.

CAMPBELL, D. E. & SPINRAD, R. W. 1987 The relationship between light attenuation and particle characteristics in a turbid estuary. *Est. Coast. Shlf Sci.* **25**, 53-65.

CARTER, C. W. & SUFFET, I. H. 1982 Binding of DDT to dissolved humic materials. *Env. Sci. & Tech.* **16**, 735-740.

CHIN, Y.-P. & GSCHWEND, P. M. 1992 Partitioning of polycyclic aromatic hydrocarbons to marine porewater organic colloids. *Env. Sci. & Tech.* **26**, 1621-1626.

CHUDOBA, J., HEJZLAR, J. & DOLEŽAL, M. 1986 Microbial polymers in the aquatic environment -- III. Isolation from river, potable and underground water and analysis. *Wat. Res.* **20**, 1223-1227.

CZAJKA, D. R. 1995 Application of bacterial extracellular polymers for treatment of metal contaminated solids: polymer persistence, mobility and the influence of lead. MS Thesis, School of Civil & Environmental Engineering, Cornell University.

DEMPSEY, B.A. & O'MELIA, C.R. 1983 Proton and Calcium Complexation of Four Fulvic Acid Fractions. In *Aquatic and Terrestrial Humic Materials* (eds. R.F. Christman & C.R. O'Melia.). Ann Arbor Sci.

DOHSE, D. M. & LION, L. W. 1994 Microbially facilitated transport of polynuclear aromatic hydrocarbons in low-carbon aquifer materials. *Env. Sci. & Tech.* **28**, 541-548.

GARRELS, R. M. & CHRIST, C. L. 1965 *Solutions, Minerals and Equilibria*, Harper & Row, New York.

GAUTHIER, T. D., SHANE, E. C., GUERIN, W. F., SELTZ, W. R. & GRANT, C. L. 1986 Fluorescence quenching method for determining equilibrium constants for polycyclic aromatic hydrocarbons binding to dissolved humic materials. *Env. Sci. & Tech.* **20**, 1162-1166.

GIBBS, R. J. 1977 Suspended sediment transport and the turbidity maximum. In *Estuaries, Geophysics and the Environment* (ed. National Research Council). National Academy of Sciences.

GSCHWEND, P. M. & WU, S.-C.. 1985 On the constancy of sediment-water partition coefficients of hydrophobic organic pollutants. *Env. Sci. & Tech.* **19**, 90-96.

HEGEMEN, W. J. M., VAN DER WEIJDEN, C. H. & LOCH, J. P. G. 1995 Sorption of benzo[a]pyrene and phenanthrene on suspended harbor sediment as a function of suspended sediment concentration and salinity: a laboratory study using the cosolvent partition coefficient. *Env. Sci. & Tech.* **29**, 363-371.

HSIEH, K. M., LION, L. W. & SCHULER, M. L. 1985 Bioreactor for the study of defined interactions of toxic metals and biofilms. *Appl. Env. Microbio.* **50**, 1155-1161.

JENKINS, M. 1996 Personal communication. Section of Microbiology, Cornell University, Ithaca, NY.

KARICKHOFF, S. W. 1984 Organic pollutant sorption in aquatic systems. *J. Hydr. Eng.* **110**, 707-735.

LILJESTRAND, H.M. & SHIMIZU, Y. 1991 Sorption of organic pollutants onto natural solid components in aquatic environments. In *Water Pollution: Modelling, Measuring and Prediction* (eds. L.C. Wrobel and C.A. Brebbia.). Computational Mechanics Publications.

LION, L. W., STAUFFER, T. B. & MACINTYRE, W. G. 1990 Sorption of hydrophobic compounds in aquifer materials: analysis methods and the effects of organic carbon. *J. Cont. Hydr.* **5**, 215-234.

LISS, P. S. 1976 Conservative and non-conservative behavior of dissolved constituents during estuarine mixing. In *Estuarine Chemistry* (eds. J.D. Burton & P.S. Liss). Academic Press.

MADSEN, E. L., WINDING, A., MALACHOWSKY, K., THOMAS, C. T. & GHIORSE, W. C. 1993 Contrasts between subsurface microbial communities and their metabolic adaptation to polycyclic aromatic hydrocarbons at a forested and an urban coal tar disposal site. *Microb. Ecol.* **24**, 199-213.

MAGEE, B. R., LION, L. W. & LEMLEY, A. T. 1991 Transport of dissolved organic macromolecules and their effect on the transport of phenanthrene in porous media. *Env. Sci. Tech.* **25**, 323-331.

MCGRODDY, S. E. & FARRINGTON, J. W. 1995 Sediment porewater partitioning of polycyclic aromatic hydrocarbons in three cores from Boston Harbor, Massachusetts. *Env. Sci. & Tech.* **29**, 1542-1550.

McGRODDY, S. E., FARRINGTON, J. W. & GSCHWEND, P. M. 1996 Comparison of the in situ and desorption sediment-water partitioning of polycyclic aromatic hydrocarbons and polychlorinated biphenyls. *Env. Sci. & Tech.* **30**, 172-177.

MERCK. 1976 *Merck Index*, 9th ed., (ed. Susan Budavari). Merck.

MURPHY, E. M., ZACHARA, J. M., SMITH, S. C., PHILLIPS, J. L. & WIETSMA, T. W. 1994 Interaction of hydrophobic organic compounds with mineral-bound humic substances. *Env. Sci. & Tech.* **28**, 1291-1299.

MURPHY, P. P., BATES, T. S., CURL, H. C. JR., FEELY, R. A.& BURGER, R. S. 1988 The transport and fate of particulate hydrocarbons in an urban fjord-like estuary. *Est. Coast. Shlf Sci.* **27**, 461-482.

NRC. 1989 *Contaminated marine sediments -- assessment and remediation.* pp. 1-19. National Academy of Sciences.

ROGERS, H.R. 1993 Speciation and partitioning of priority organic contaminants in estuarine waters. *Coll. Surf. A* **73**, 229-235.

SCHLAUTMAN, M. A. & MORGAN, J. J. 1993 Effects of aqueous chemistry on the binding of polycyclic aromatic hydrocarbons by dissolved humic materials. *Env. Sci. & Tech.* **27**, 961-969.

TIPPING, E. 1981 Adsorption by geothite (alpha-FeOOH) of humic substances from three different lakes. *Chem. Geo.* **33**, 81-89.

TIPPING, E. & HEATON, M. J. 1983 The adsorption of aquatic humic substances by two oxides of manganese. *Geochimica et Cosmo. Acta.* **47**, 1393-1397.

UNDERWOOD, G. J. C., PATERSON, D. M. & PARKES, R. J. 1995 The measurement of microbial carbohydrate exopolymers from intertidal sediments. *Limnol. Oceanogr.* **40**, 1243-1253.

WHITEHOUSE, B. G.  1985 Observation of abnormal solubility behavior of aromatic hydrocarbons in seawater. *Marine Chem.* **17**, 277-284.

WU, S.-C. & GSCHWEND, P. M. 1986 Sorption kinetics of hydrophobic organic Compounds to natural sediments and soils. *Env. Sci. & Tech.* **20**, 717-725.

# CHAPTER 3:

# HYDRODYNAMIC PAIR DIFFUSION IN ISOTROPIC RANDOM VELOCITY FIELDS WITH APPLICATION TO TURBULENT COAGULATION*

3.1 <u>Introduction</u>

Coagulation and colloidal stability depend on the detailed hydrodynamics and interparticle forces that affect the particle collision rate. Fluid motion and van der Waals attraction increase the aggregation rate while fluid drag and interparticle forces, such as double layer repulsion, resist particle-particle contact (Russel et al., 1989). The mechanisms leading to colloidal aggregation have been previously investigated with the goal of either preventing or promoting particle aggregation. Long term colloidal stability is important in the production of paints, while flocculation tanks used in wastewater treatment plants rely on fluid shear to promote aggregation and subsequent settling of undesirable particulate matter (Appiah & O'Melia, 1990). Coagulation processes are also important in natural systems where they may govern pollutant fate and transport. In estuaries, suspended sediment aggregation in response to the

---

58

destabilizing influence of salinity gradients is an important mechanism leading to the deposition of contaminated sediments (O'Melia, 1980).

Flow type can have a profound influence on the level of coagulation observed in natural and engineered systems. For instance, coagulation rates in steady laminar flows are influenced by the specific linear flow considered (Greene et al., 1994); flows containing significant rotational components, like simple shear, lead to slower coagulation compared with irrotational flows such as uniaxial extension (i.e., stagnation flow) (Greene et al., 1994).

In each of the practical examples noted above, the colloidal particles experience a spatially and temporally complex fluid environment. Turbulent flows are probably the most prevalent class of complex flows encountered. Analytical expressions valid in the large total strain limit (i.e., when the product of the velocity gradient and the time scale over which the gradient changes is large) have been proposed for modeling turbulent coagulation of particles in the absence of interparticle forces (Delichatsios & Probstein, 1973; Camp & Stein, 1943; Saffman & Turner, 1956). As yet, the complicated stochastic structure of turbulence and other complex flows has eluded detailed analysis of particle collision dynamics when interparticle potentials and hydrodynamic interactions are incorporated. In spite of the importance of coagulation in complex flows such as turbulence, prior calculations of coagulation rates in the presence of colloidal forces and hydrodynamic resistance have been limited to simple stationary linear flows (Greene et al., 1994; van de Ven & Mason, 1977; Zeichner & Schowalter, 1977; Adler, 1981), Brownian diffusion

(Spielman, 1970; Valioulis & List, 1984) and gravitational settling (Davis, 1984). The applicability of coagulation results gleaned from computations in steady linear flows to turbulence is uncertain.

In many aqueous solutions the particle based Reynolds number is small even for 100 μm particles and therefore the turbulent flow in the neighborhood of colliding particles behaves like a random laminar flow. Important advances have been made in the study of coagulation in two-dimensional chaotic laminar flows such blinking vortex flow (i.e., a flow produced by the periodic application of two corotating point vortices separated by a fixed distance) (Ottino et al., 1992; Ottino, 1991). Results from these numerical studies may provide insight into floc formation for more realistic complex flows.

The investigations of aggregation in blinking vortex (Muzzio & Ottino, 1988; Bidkar & Khakhar, 1990) and other chaotic flows (Danielson et al., 1991) are limited to non-interacting particles. In steady non-chaotic flows characterized by the high vorticity that exists in blinking vortex flow, coagulation at long times is hindered by non-crossing, closed streamlines because particles on adjacent streamlines are prevented from coagulating with each other. This confinement is largely removed when considering chaotic flows (Ottino et al., 1992; Muzzio & Ottino, 1988). Dynamical simulations of coagulation in chaotic flows of moderate strain show that, compared to regular flows having the same vorticity, chaotic flows lead to higher coagulation rates (Ottino, 1991). For moderate strain rates, the initial collision rate in a chaotic blinking vortex flow was found to be a

monotonically increasing function of total strain (see Figure 5 of Bidkar & Khakhar, 1990).

In agreement with the chaotic flow work, this chapter shows that the rate of coagulation is a linearly increasing function of total strain in the limit when the product of the characteristic rate of strain and the strain rate correlation time is small. As a result of the dependence on total strain, the coagulation rate in the diffusion limit can be significantly lower than that calculated for the steady linear flow. This rate decrease is exacerbated with the inclusion of interparticle forces and hydrodynamic interactions. In Section 3.3.3 hydrodynamic drag is established to have increased importance in randomly fluctuating flows which can lead to increased suspension stability.

The coagulation process is considered for a general three-dimensional isotropic random flow that can be linearized on scales comparable to the particle radius. Results of the colloid aggregation analysis in this generalized fluctuating flow serve as a prototype for a broad class of flows in which the imposed randomly varying velocity field leads to relative particle motions that are diffusive in character. The flow is taken to be a statistically stationary velocity field with separate strain and rotation time scales. (N.B. One might imagine constructing a chaotic flow with these specifications by considering an aperiodic three-dimensional combination of the H/E-flow studied by Danielson et al., 1991. Statistically stationary is used here to mean that the statistics of the randomly varying velocity field do not change with time.)

The approach is to consider the limit where the relative particle motion can be written statistically in terms of a probability conservation equation containing a pair diffusion coefficient that embodies the kinematics of the flow field. The pair diffusion paradigm is restricted to flows exhibiting small total strain so that particle movement over distances comparable to the particle radius is the result of many uncorrelated velocity field fluctuations.

The diffusion model has been previously used to treat polymer stretch in turbulent flows (Jhon et al., 1987) and in fixed beds (Shaqfeh & Koch, 1992). The diffusion equation for the pair probability is derived by time averaging over many velocity fluctuation events. The resulting conservation equation given in Section 3.2 contains a pair diffusion coefficient and a "drift" velocity. The "drift" velocity is shown to result in a non-uniform steady-state pair probability distribution when hydrodynamic interactions are included.

Using the pair diffusion approximation an analytical expression is derived for coagulation in the absence of interparticle forces that depends on the strain rate correlation time. Correlation time is used here and below to mean the time scale over which the variable of interest is correlated to subsequent values (i.e., the integral of the autocorrelation coefficient as shown in Equation 3.2 below). Inclusion of interparticle forces and hydrodynamic interactions into the diffusion model leads to a non-analytic integral for the stability factor, W, where W is the ratio of the coagulation rate without consideration of interparticle interactions to the rate with interparticle interactions. The analysis of W for random flows is greatly

simplified by using the diffusion approach because W can be obtained from a one-dimensional numerical integration rather than by computing ensembles of relative particle trajectories. Stability factors are calculated (Section 3.4) for coagulation of different size particles in the presence of van der Waals attraction, electrostatic repulsion and hydrodynamic interactions.

These colloid stability results are applied to the problem of coagulation in a turbulent flow for particles that are small compared with the Kolmogorov length scale, i.e., the length scale of the smallest turbulent eddies (Section 3.5). As estimates for the strain and rotation rate correlation times at the Kolmogorov scale of turbulence, results have been taken from the direct numerical simulations (DNS) of Pope and coworkers (Yeung & Pope, 1989; Girimaji & Pope, 1990; Pope, 1990).

3.2 Derivation of the pair probability conservation equation

Consider an incompressible, locally linear velocity field that fluctuates randomly with time and is characterized by different rotation and strain rate correlation times. The magnitude of the fluctuations in the shear are assumed to be large compared to the mean shear on length scales comparable to the particle radius, so only the fluctuating motions are dynamically important in determining particle movement and coagulation. As a consequence of the above assumptions, the relative velocity between two material points in the flow can be written as:

$$u_i = \Gamma_{ij}(t) r_j \qquad\qquad (3.1)$$

where $u_i$ is the relative velocity, $\Gamma_{ij}(t)$ is the statistically-stationary fluctuating velocity gradient, and $r_j$ is the relative position vector between the particles. The characteristic velocity gradient is defined as $\Gamma = (<\Gamma_{ij}\Gamma_{ij}>)^{\frac{1}{2}}$ where the brackets indicate ensemble averaging over independent realizations of the fluctuating velocity gradient. The velocity gradient is decomposed into its strain and rotational components and the times scales of the strain and rotation rate are assumed to be decoupled. The strain rate correlation time, $\tau_s$, is defined as:

$$\tau_s = \int_0^\infty f^s(t/\tau_s)dt = \int_0^\infty \frac{<S_{ik}(0)S_{jl}(t)>}{<S_{ik}(0)S_{jl}(0)>}dt \qquad (3.2)$$

where $S_{ij}(t)$ is the strain rate defined as $\frac{1}{2}(\Gamma_{ij} + \Gamma_{ji})$, and $f^s(t/\tau_s)$ represents the correlation coefficient between the strain rate at two different times, i.e., the two-time strain rate correlation coefficient. The integral in Equation 3.2 is assumed to converge and the terms in brackets are not tensors but components of the strain rate covariance matrix. The rotation rate correlation time, $\tau_R$, can be written with an analogous expression by replacing all S's in Equation 3.2 with R's and noting that $R_{ij} = \frac{1}{2}(\Gamma_{ij} - \Gamma_{ji})$. The characteristic strain, S, and rotation rates, R, are defined analogously to $\Gamma$ and are subject to the constraint that $\Gamma^2 = S^2 + R^2$.

Consider a dilute suspension of particles immersed in a randomly varying isotropic flow field such that only encounters between pairs of particles are significant. The total strain, defined as the product of the characteristic velocity gradient, $\Gamma$, and the strain (or rotation) rate correlation time ($\tau_S$ or $\tau_R$) is assumed to be small. Since the flow is

stochastic, it is convenient to describe the distribution of particles using a pair probability density function (pdf), P(r,t), that describes the probability of finding particles separated by the vector r at time t. For particles immersed in this flow, the influence of a singlet random velocity fluctuation is minor. That is, the response of the relative particle position is small over the correlation time of the flow; therefore, a diffusive process characterizes the relative particle motion. In the absence of hydrodynamic interactions, colloidal forces and aggregation, this relative diffusion randomizes the particle positions making all relative separations equally likely.

Hydrodynamic interactions, however, lead to a nonsolenoidal relative velocity (i.e., the particle velocities are compressible.). The compressibility of the relative trajectories leads to a net drift of pairs toward small interparticle separations. This velocity may be rationalized in terms of the variations in the amplitude of the velocity fluctuations with relative position. When hydrodynamic interactions are included, the relative velocity between two particles is a non-linear function of the particle separation; thus, the response of the particle pair to a random velocity event will depend on its current position. At large particle separations a velocity fluctuation has a comparably large influence on the pair probability compared to small separations. Therefore a zero net particle flux at steady state requires a non-uniform pair probability distribution. The particle flux, given by the product of the relative velocity and concentration, will be equal at all positions if the concentration at small separations is higher than at large separations. The accumulation of

particles at small separations is manifested by the presence of a "drift" velocity in the pair probability conservation equation.

The presence of a hydrodynamic drift for the pair probability in a random linear flow is analogous to the phenomena of thermophoresis observed for Brownian particles in a temperature gradient. Since the Brownian diffusion coefficient is proportional to the temperature, the particle flux is higher in the hot region than in the cold. Therefore, to have zero flux at steady-state, the particles must be concentrated in the colder region. The accumulation of particles in the cold regions indicates that there was a "drift" of particles from the hot region.

The equation governing the pair probability is derived below and analytical expressions for the pair diffusion coefficient are obtained. In the derivations presented in this section, particle coagulation will be ignored. The methodology employed to obtain an equation for P(r,t) follows the techniques used by Shaqfeh & Koch (Shaqfeh & Koch, 1988) for the orientation probability of axisymmetric particles flowing through a dilute fixed bed and used by Koch & Shaqfeh (Koch & Shaqfeh, 1991) for the pair probability of sedimenting particles influenced by a distant third particle. An alternative derivation of the pair diffusivity and drift velocity in terms of the time rate of change of the first and second moments of the pair separation is presented in Appendix C to this thesis.

The pair probability, $\Omega(\mathbf{r},t)$, satisfies the conservation equation:

$$\frac{\partial \Omega}{\partial t} + \nabla_r \cdot [\dot{r}\Omega] = 0 \qquad (3.3)$$

where $\nabla_r$ is the del operator, and the overdot indicates a time derivative. $\Omega(r,t)$ is influenced by the details of the velocity fluctuations governing the rleative motion of the pair at the present time t. To obtain a pair probability that only experiences the average effects of the velocity fluctuations, $P(r,t)$ is defined as the time average of $\Omega(r,t)$:

$$P(r,t) = \int_{t-\tau_P}^{t+\tau_P} \Omega(r,t')dt' \qquad (3.4)$$

where the time, $\tau_P$ is much larger than the relaxation times, $\tau_S$ and $\tau_R$ for the stochastic flow field. The validity of this time average implies that a separation of time scales exists so that P varies due to hydrodynamic diffusion on a time scale $\tau_Q$ which is much larger than $\tau_P$. This assumption will be validated at the conclusion of the derivation.

The fluctuating pair probability, p is defined as the difference between the pair probability and its time averages:

$$p = \Omega - P \qquad (3.5)$$

Since p arises solely due to the velocity fluctuations occurring over the previous time period $\tau_S(\tau_R)$ and $\Gamma\tau_S(\Gamma\tau_R) \ll 1$, the perturbation to the pair probability is small, i.e., $|p| \ll |P|$. In the forthcoming analysis it will become apparent that p scales in proportion to $(S\tau_S)P$.

Taking the average of Equation 3.3 over a time interval $(t - \tau_P, t + \tau_P)$ gives the evolution equation for P:

$$\frac{\partial P}{\partial t} + \nabla_r \cdot \langle \dot{r} \Omega \rangle_t = 0 \qquad (3.6)$$

Time averaging over $\tau_P \gg \tau_S, \tau_R$ is equivalent to sampling over many realizations of the random velocity field; therefore, the time average is equivalent to an ensemble average and it is denoted by $<>$. Substituting the perturbation expansion for $\Omega$ (Equation 3.5) into the convection term in Equation 3.6 gives:

$$\frac{\partial P}{\partial t} + \nabla_r \cdot \left[ \langle \dot{r} P \rangle_t + \langle \dot{r} p \rangle \right] = 0 \qquad (3.7)$$

It will be seen that P varies over time scales much large than $\tau_P$; therefore; P can be taken out of the time average in Equation 3.7. The mean relative velocity of the particles is zero due to the isotropy of the flow; thus, Equation 3.7 simplifies to:

$$\frac{\partial P}{\partial t} + \nabla_r \cdot \langle \dot{r} p \rangle = 0 \qquad (3.8)$$

This result shows that the pair probability comes from the convection of the fluctuating probability. Ultimately, the p transport term in Equation 3.8 will give rise to a diffusion coefficient that characterizes the underlying random flow as shown below.

To continue the analysis, an expression for p is needed. The fluctuating probability is the incremental response of particles to a singlet

velocity fluctuation. The conservation equation for p is found by substituting Equation 3.5 into Equation 3.3 to yield:

$$\frac{\partial P}{\partial t} + \frac{\partial p}{\partial t} + \nabla_r \cdot [\dot{r} P + \dot{r} p] = 0 \qquad (3.9)$$

$\partial P/\partial t$ scales like $P/\tau_Q$ while $\partial p/\partial t$ is proportional to $P(\tau_S S)/\tau_S$ so that $\partial P/\partial t$ is order $(S\tau_Q)^{-1}$ smaller than $\partial p/\partial t$ and the time derivative of P can be neglected. [*A posteriori* analysis shows that $\tau_S/\tau_Q \sim (\tau_S S)^2$.] In addition since $|p| \ll |P|$ the advection term involving p in Eq. (9) is negligible compared with the advection term involving P. The solution to Eq. (9) is found by integrating over time.

$$p = - \int\limits_{-\infty}^{t} \nabla_r \cdot [\dot{r} P] dt' \qquad (3.10)$$

Because $\dot{r}$ remains correlated for $\tau_S$ and $\tau_P \gg \tau_S$ the lower limit of integration can be replaced with $-\infty$ without affecting the value of the integral. After substituting Equation 3.10 into Equation 3.8, the pair probability conservation equation becomes:

$$\frac{\partial P}{\partial t} + \frac{\partial}{\partial r_i} \left[ V_i^f P - D_{ij}^f \frac{\partial P}{\partial r_j} \right] = 0 \qquad (3.11)$$

where the drift velocity, $V_i^f$ and the pair diffusivity, $D_{ij}^f$ are given by:

$$V_i^f = - \int\limits_{-\infty}^{t} \left\langle \dot{r}_i(t) \frac{\partial \dot{r}_j}{\partial r_j}(t') \right\rangle dt' \qquad (3.12)$$

As expected the pair diffusion coefficient is found by integrating the two time relative velocity correlation. The drift velocity comes from temporal

$$D_{ij}^{f} = \int_{-\infty}^{t} \left\langle \dot{r}_i(t) \dot{r}_j(t') \right\rangle dt' \qquad (3.13)$$

correlations between the relative velocity and its divergence. Below explicit expressions for $D_{ij}^{f}$ and $V_i^{f}$ are given for the random linear flow considered in this work.

### 3.2.1 Hydrodynamic pair diffusion coefficient

The particle separation is assumed to be small compared with the characteristic length of the imposed flow so that the relative velocity in Equation 3.13 can be expanded as a linear function of position:

$$D_{ij}^{f} = \int_{0}^{t} \left\langle \Gamma_{ik}(t') r_k(t') \Gamma_{jl}(t) r_l(t) \right\rangle dt' \qquad (3.14)$$

Since the analysis considers flows in which the total velocity gradient is small, $\Gamma \tau_s$ (and $\Gamma \tau_R$) $\ll 1$, particle positions do not change much over the velocity gradient correlation time. Under this constraint, the relative position vectors are approximately independent of the random velocity gradient field and can be removed from the ensemble average:

$$D_{ij}^{f} = r_k r_l \int_{0}^{t} \left\langle \Gamma_{ik}(t') \Gamma_{jl}(t) \right\rangle dt' \qquad (3.15)$$

Furthermore, if t » $\tau_S$ (and $\tau_R$) the lower limit of integration can be replaced with -∞ without changing the value of the integral. Letting t" = t'-t and assuming the system is statistically stationary in time so that the process depends only on time differences, t", yields:

$$D_{ij}^f = r_k r_l \int_{-\infty}^{0} \left\langle \Gamma_{ik}(t'')\Gamma_{jl}(0) \right\rangle dt'' \qquad (3.16)$$

which relates the turbulent diffusivity to the integral of the covariance of the velocity gradient at time, t = 0 and time t = t"(i.e., the Lagrangian velocity gradient autocorrelation function). The Lagrangian velocity gradient autocorrelation function may be decomposed into its strain and rotation components to yield:

$$D_{ij}^f = r_k r_l \int_{-\infty}^{0} \left[ S_{ikjl} f^s(t/\tau_s) + R_{ikjl} f^r(t/\tau_r) \right] dt'' \qquad (3.17)$$

where $S_{ikjl} = <S_{ik}(t)S_{jl}(t)>$, $R_{ikjl} = <R_{ik}(t)R_{jl}(t)>$ and cross terms such as $<S_{ik}(t)R_{jl}(t)>$ are zero due to isotropy.

To complete this derivation, tensor expressions for the covariance of the velocity gradient tensors need to be inserted into Equation 3.17. Tensor relations for $S_{ikjl}$ and $R_{ikjl}$ in the assumed isotropic linear flow field are obtained by writing $S_{ikjl}$ and $R_{ikjl}$ as fourth order isotropic tensors that depend on three scalar coefficients. For the strain rate tensor, the numerical coefficients are evaluated by applying symmetry, $S_{ikjl} = S_{kijl}$; continuity, $S_{iijl} = S_{ikjj} = 0$; and, defining the magnitude of the strain to be $S_{ijij} = S^2$. The final form for the strain rate covariance is:

$$S_{ikjl} = \frac{S^2}{10}\left[\delta_{ij}\delta_{kl} + \delta_{il}\delta_{jk} - \frac{2}{3}\delta_{ik}\delta_{jl}\right] \tag{3.18}$$

where $\delta_{ij}$ is the identity tensor. The rotation rate covariance is obtained using a similar analysis to yield:

$$R_{ikjl} = \frac{R^2}{6}\left[\delta_{ij}\delta_{kl} - \delta_{il}\delta_{jk}\right] \tag{3.19}$$

where the anti-symmetry property for $R_{ikjl}$ is $R_{ikjl} = -R_{kijl}$.

The assumption of finite correlation times means that the integrals in Equation 3.17 converge. After substituting Equations 3.18 and 3.19 into Equation 3.17, an analytical expression results for the pair diffusivity:

$$D_{ij}^f = \frac{r^2}{30}\left[4S^2\tau_s\frac{r_i r_j}{r^2} + (3S^2\tau_s + 5R^2\tau_r)\left(\delta_{ij} - \frac{r_i r_j}{r^2}\right)\right] \tag{3.20}$$

where r is the magnitude of the relative position vector, $r_i$.

Hydrodynamic interactions can be incorporated into the derivation of the turbulent diffusivity presented above by writing the particle velocity as a superposition of the imposed velocity field and the velocity change created by particle-particle hydrodynamic interactions. Assuming that the particle Reynolds number, $Re = \Gamma a_1^2/\nu$, is small, the relative particle velocity can be written in the form:

$$\dot{r}_i = L_{il}(r(t))r_l = \Gamma_{il}r_l - \left[A(r)\frac{r_i r_k}{r^2} + B(r)\left(\delta_{ik} - \frac{r_i r_k}{r^2}\right)\right]S_{kl}r_l \tag{3.21}$$

where A(r) and B(r) are monotonic functions of radial position that decay over distances comparable to the particle radius (Batchelor & Green, 1972a; Kim & Karrila, 1991). The above expression is substituted into Equation 3.13, and after simplification gives:

$$D_{ij}^f = \frac{r^2}{30}\left[4S^2\tau_s[A-1]^2\frac{r_i r_j}{r^2} + \left[3S^2\tau_s(B-1)^2 + 5R^2\tau_r\right]\left(\delta_{ij} - \frac{r_i r_j}{r^2}\right)\right] \quad (3.22)$$

which is the pair diffusivity of particles experiencing hydrodynamic interactions.

To summarize, the expression given for $D_{ij}^f$ is the pair diffusion coefficient of particles immersed in a statistically stationary isotropic random velocity field with small total strain. Further, the flow field must be linear on length scales comparable to the particle radius and have independent and finite strain and rotation rate correlation times.

### 3.2.2 Drift velocity

The drift velocity given by Equation 3.12 can be simplified using the properties of the assumed isotropic random velocity field. First consider the case without hydrodynamic interactions. In the absence of interactions, the particles will follow the fluid motion so the relative velocity, $\dot{r}_i$, can be replaced with the relative velocity of the fluid, $u_i$. Then, by continuity, $du_i/dr_i = 0$ and consequently $V_i^f = 0$.

When hydrodynamic interactions are included, particles no longer follow the fluid motion. Instead the relative particle velocity is given by Equation 3.21. The drift velocity depends on the divergence of the relative particle velocity gradient which has been reported as (Batchelor, 1977):

$$\frac{\partial \dot{r}_i}{\partial r_i} = w \frac{r_i S_{ij} r_j}{r^2}$$ (3.23)

where,

$$w(r) = -3(A-B) - r\frac{dA}{dr}$$ (3.24)

and, it has been shown that w(r) is always positive (Batchelor, 1977).

Equations 3.21 and 3.23 are substituted into Equation 3.12 and the resulting expression is simplified using the tensor relation for the strain rate autocorrelation function (Equation 3.18) to yield:

$$V_i^f = \frac{2\tau_S S^2}{15} w(A-1) r_i$$ (3.25)

Since w is positive and (A-1) is always negative, the drift velocity given by Equation 3.25 is negative causing the particle pairs to move inward. At large separations $(A-1) \rightarrow 1$ and w is proportional to $r^{-6}$ (Batchelor & Green, 1972b) so the drift decays rapidly to zero as the particle separation increases. In the lubrication regime, where the gap between the particles is small compared to their radius, A approaches 1 and W monotonically reaches a constant value of 6.372 (Batchelor, 1977). Therefore, as the particles approach contact, the drift velocity also goes to zero. The magnitude of the drift velocity for identical spherical particles is shown in Figure 3.1 as a function of the radial separation scaled on the particle
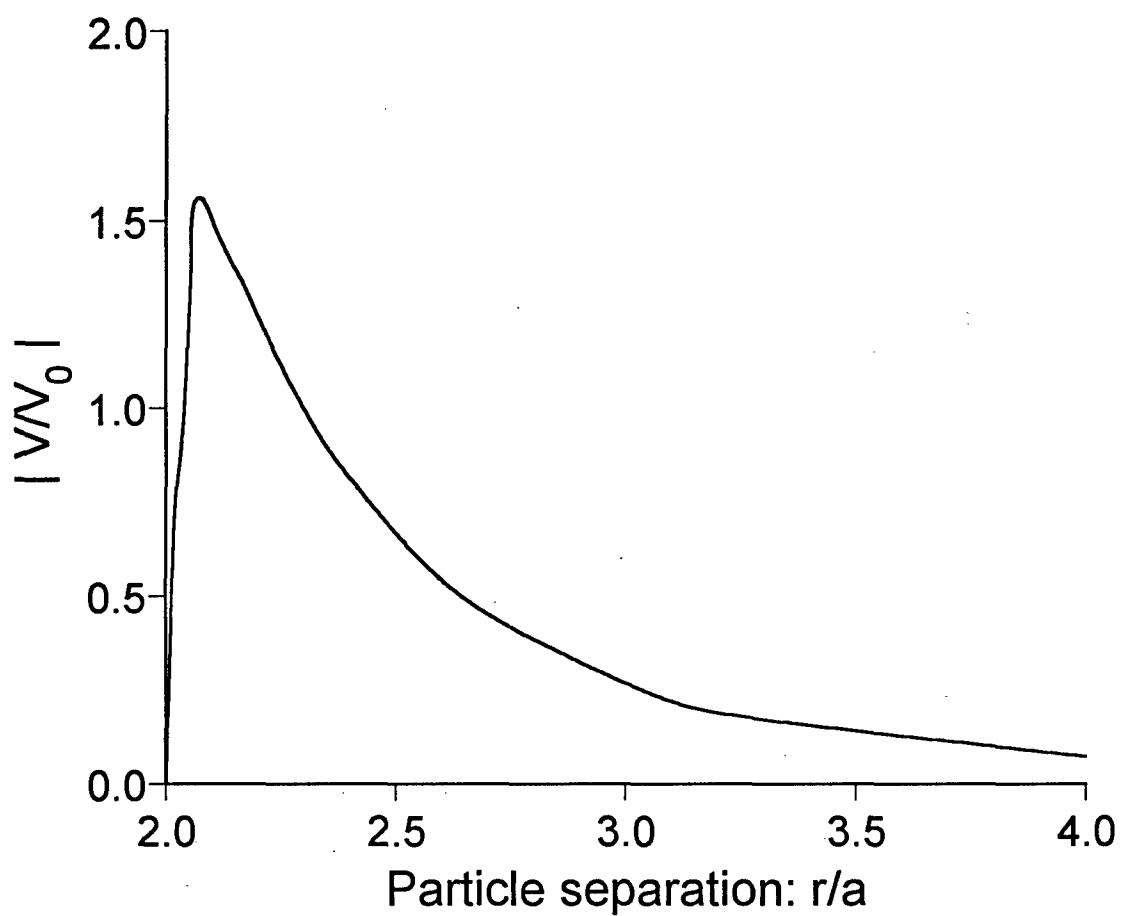
**Figure 3.1**: Radial component of the hydrodynamic drift velocity as a function of the relative separation between two equal size particles scaled by the particle radius.

radius. In Figure 3.1 the drift velocity is scaled with $V_0 = 2\tau_S S^2 a/15$ where a is the particle radius. At $r/a \approx 2.08$ the magnitude of the drift velocity goes through a maximum value of about $1.5V_0$, and by a separation of about 4a the magnitude of the drift velocity has decayed to 5% of its maximum value.

The derivation of the evolution equation for P (Equation 3.11) assumes that there is a separation of time scales between P and $\Omega$. This assumption may now be examined. Denoting $\tau_Q$ as the characteristic evolution time for P, the separation of time scales implies that $\tau_Q/\tau_S \gg 1$. The evolution time for P scales with the characteristic time for two particles to diffuse over a distance comparable to the particle radius: $\tau_Q = a^2/D_r^f$, where $D_r^f$ is the radial component of the hydrodynamic pair diffusivity. We can estimate the order of magnitude of the diffusivity by inspection of Equation (3.20). Without considering the details of the hydrodynamic interactions $D_r^r = O(S^2 a^2 \tau_S)$. This yields $\tau_Q/\tau_S \sim (\tau_S S)^{-2}$. Since the total strain is given to be small, the constraint that $\tau_Q/\tau_S \gg 1$ is automatically satisfied.

### 3.2.3 *Steady-state pair probability distribution*

The presence of the drift velocity means that particles influenced by hydrodynamic interactions will preferentially drift towards small particle separations at steady state. A schematic illustrating the coordinate system and boundary conditions is shown in Figure 3.2. A spherical coordinate system is placed in a frame of reference that moves with a particle of radius $a_1$ and a relative position vector connects the centers of size 1- and size 2-particles. The particles are immersed in a randomly varying linear
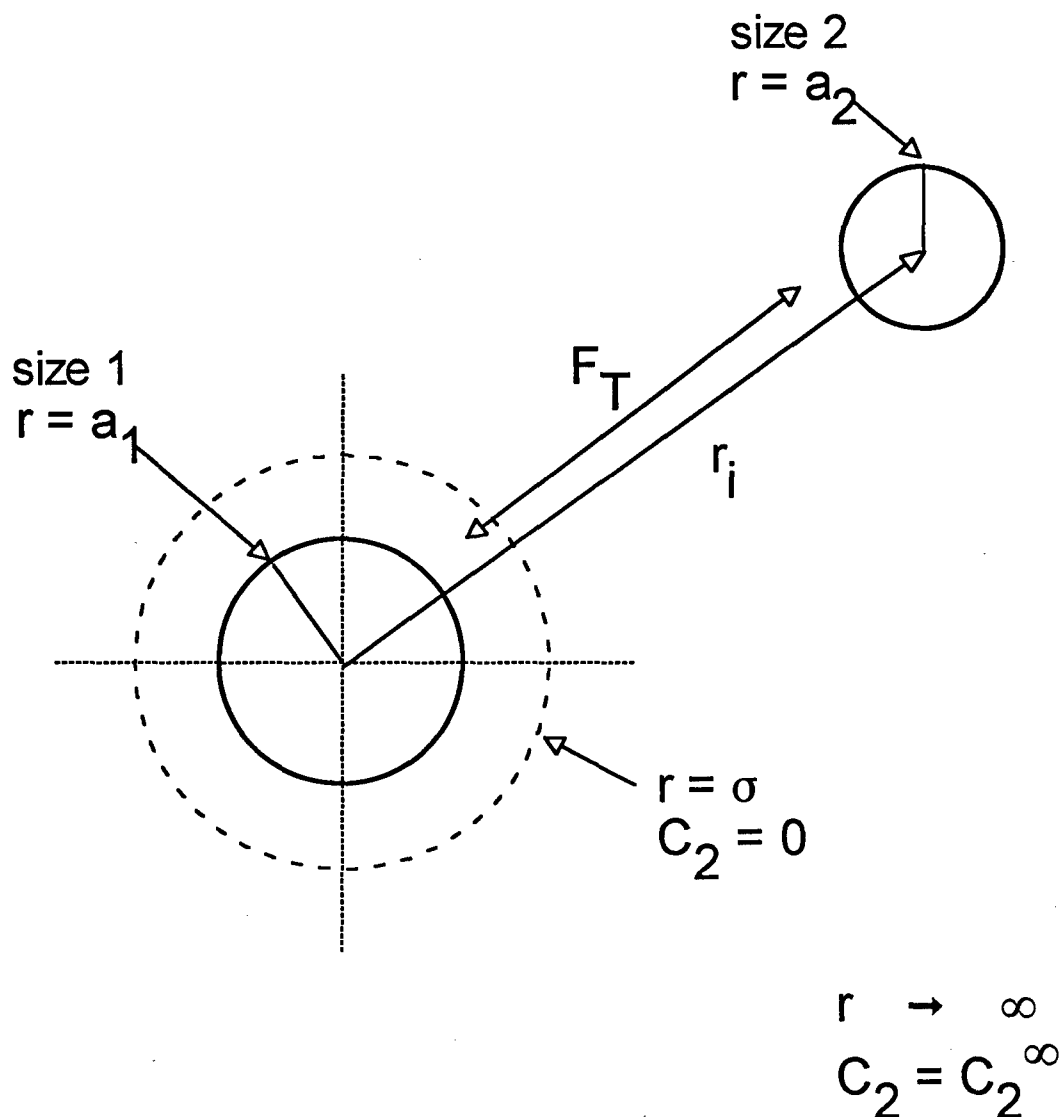
**Figure 3.2**: Schematic illustrating the coordinate system and boundary conditions for computing the steady state pair probability distribution with and without particle coagulation. Two particles of radius $a_1$ and $a_2$ are separated by a distance r. Radially symmetric interparticle forces, $F_T$, act upon the centers of the two particles. At large separations, the particle concentrations reach their bulk value, while there is an absorbing boundary condition at the surface of the excluded volume when coagulation is considered.

flow field that can be characterized by the pair probability equation derived above. For the steady state pair probability distribution calculations, the particles are assumed to have the same radius and the system is dilute enough so that only binary interactions occur. At large relative separations the pair probability attains its bulk value $P \rightarrow C_1^\infty C_2^\infty$. The flux of pair probability is zero at the collision radius. The hydrodynamically induced particle flux comes from Equation 3.11 and is given by:

$$j_i = V_i^f P - D_{ij}^f \frac{\partial P}{\partial r_j} \tag{3.26}$$

where $j_i$ is the flux of pair probability. As discussed above, in the absence of hydrodynamic interactions the drift velocity is zero. At steady state, $j_i = 0$ and Equation 3.26 can be integrated to obtain $P = C_1^\infty C_2^\infty$ everywhere in the absence of hydrodynamic interactions.

As already noted, the presence of hydrodynamic interactions causes a drift in the pair probability that leads to a non-uniform distribution. Because the flow is isotropic, the circumferential components of the flux will be zero. Substituting Equations 3.22 and 3.25 into Equation 3.26 and considering only the radial component gives:

$$j_r = V_0 C_1^\infty C_2^\infty (A-1) \left[ wrP - (A-1)r^2 \frac{dP}{dr} \right] \tag{3.27}$$

where P is normalized with its value at infinity and r is normalized with the particle radius for the remaining part of this section. Setting $j_r = 0$ and rearranging leads to an ODE for P:

$$\frac{dP}{dr} = -\left(\frac{w}{A-1}\right)\frac{P}{r} \qquad (3.28)$$

An analytical solution to Equation 3.28 cannot be found; however, the functional form of Equation 3.28 can be obtained in the lubrication regime. First, Equation 3.28 is recast in terms of the non-dimensional gap width $\xi = r - 2$. For small particle separations $w = 6.372 + 20.385\xi - 2.34/\ln(1/\xi)$, $A = 1 - 4.077\xi$ and $r = 2$. Making these substitutions and integrating gives:

$$P = \frac{B_1 \xi^{-0.78} e^{-2.39\xi}}{\ln(1/\xi)^{0.29}} , \qquad \xi \ll 1 \qquad (3.29)$$

where the constant of integration, $B_1$ can be found by matching P in the lubrication region to the full solution of P. This expression for P valid in the lubrication region is identical to one derived previously by Batchelor & Green (1972b). [Note, Batchelor and Green (1972b) omit the exponential term in Equation 3.29 because it is negligible in the lubrication region; however, it is included in Equation 3.29 for completeness.] Batchelor and Green derive an equation for the pair probability in a linear velocity field that is valid assuming all particle trajectories come from or go to infinity. The result is a pair probability that is only a function of the radial separation and indepenendent of the applied velocity gradient. In other words, they show that a change in the velocity field (provided all relative trajectories are open) yields the same steady state pair probability. The universality of this expression for P has been verified by our derivation where we consider the pair probability in a fluctuating linear flow. The

restriction against closed streamlines would seem to preclude the applicability of Batchelor and Green's analysis to the arbitrary random linear flow being studied here since it is conceivable that a realization of the random linear flow will contain closed trajectories. The assumption of small total strain; however, mitigates the presence of closed stream lines. At small total strain closed stream lines are not persistent thus particles trapped in closed trajectories will be released on times that scale with the flow correlation times.

The full solution to Equation 3.28 was obtained by numerical quadrature using a 5th order Runge-Kutta routine. The integration was started at $r = 10$ where hydrodynamic interactions were unimportant and P = 1. Near and far field forms for A were taken from Kim & Karrila (1991). A plot of A versus relative separation was used to choose $r = 2.05$ as the transition between the near and far field approximations. For $r < 4$, w was obtained from spline interpolation of values tabulated by Batchelor (1977). Beyond $r = 4$, the definition of w (Equation 3.23) was used to find w from far field expressions for A and B (Kim & Karrila, 1991). Figure 3.3 shows the distribution of P as a function of radial separation. Non-linear regression of Equation 3.29 in the lubrication region yields $B_1 = 0.21$. For comparison Batchelor and Green (1972b) estimate $B_1$ to be 0.234 by fitting Equation 3.23 to two points in the lubrication region. The two estimates for $B_1$ are quite close; however, the estimate obtained here is considered more accurate since it matches numerical data over a range of gap widths.

The pair probability distribution shown in Figure 3.3 reveals a significant accumulation of particles at small separations. When $r = 2.01$,
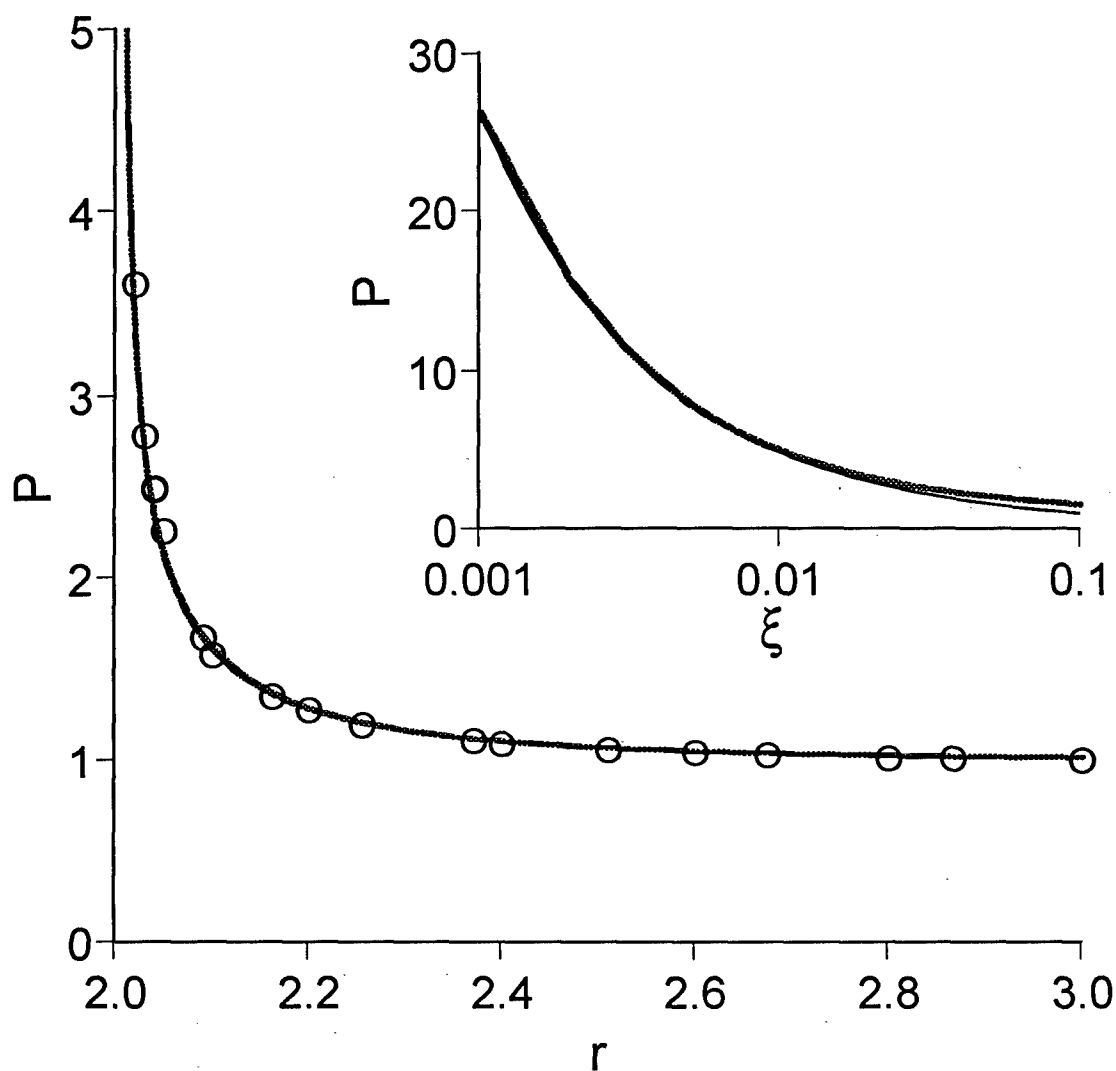
**Figure 3.3**: The steady state pair probability distribution in the absence of particle aggregation as a function of the radial separation scaled with the particle radius. For comparison symbols representing the pair probability calculations by Batchelor & Green (1972b) are included. The inset shows the behavior of the pair probability in the lubrication regime by plotting P against the gap width scaled by the particle radius. The thin line in the inset shows the analytical approximation to the pair probability valid in the lubrication region, Equation 3.29.

P is 5.07 times higher than the value at infinite separation. By $r = 2.65$, P is within 5% of the bulk concentration. Finally at $r = 10$, P is indistinguishable from 1 which demonstrates that the outer integration boundary did not influence the numerical results.

### 3.3 A diffusion approximation to coagulation

In the limit of small total strain where the product of the characteristic velocity gradient with its correlation time is small, the transport of coagulating particles in an isotropic random linear flow can be treated as diffusive. In this section an expression is derived for the coagulation rate constant (or kernel) that includes the effects of interparticle forces and hydrodynamic interactions.

#### 3.3.1 *Problem statement*

With the exception of the inner boundary condition, the system set up for the coagulation problem is identical to that used in determining the steady state pair probability distribution. Figure 3.2 shows a schematic of the coagulation problem. The particles are influenced by Brownian motion, hydrodynamic interactions and a radially acting force, $F_T$, that includes, but is not limited to, van der Waals attraction and double layer repulsion. The coagulation rate is determined by including interparticle forces and Brownian motion into the pair probability conservation equation and calculating the collision rate of size 2-particles with the size 1-particle test sphere. Particles stick on contact so that the probability of finding type 1- and 2-particle singlets separated by a distance $\sigma = a_1 + a_2$ is $P = 0$.

As r → ∞, the particle concentrations reach their bulk values and the pair probability is normalized such that $P \rightarrow C_1^\infty C_2^\infty$.

In general, the rate of doublet formation can be written as:

$$\frac{dC_{1,2}^\infty}{dt} = kC_1^\infty C_2^\infty \qquad (3.30)$$

where k is the coagulation kernel or rate constant, $C_{1,2}^\infty$ is the bulk concentration of aggregates formed from a type-1 and -2 particle and $C_1^\infty$ and $C_2^\infty$ are the bulk concentrations of type-1 and -2 particles, respectively. The coagulation kernel incorporates the transport mechanisms leading to coagulation (e.g., Brownian motion, fluid shear, gravitational settling) and the effect of interparticle interactions (e.g., hydrodynamic interactions and interparticle forces). The effects of transport and particle-particle interactions can be separated by relating the coagulation rate constant to the stability factor: $k = k^0/W$, where $k^0$ is the coagulation rate in the absence of interparticle interactions and W is the stability factor. A large W indicates a stable suspension; conversely, small W means that the colloidal suspension aggregates readily.

To simplify the investigation of coagulation, consideration is restricted to a low particle Reynolds number dilute system where the volume fraction of particles is much less than one. The fact that the system is dilute suggests that the local mixing time is short compared with the coagulation time and hence the pair probability is at a quasi-steady state. The assumption of low particle Reynolds number limits the analysis to particles less than about 100 μm in radius for aqueous systems. The

analysis is restricted to binary interactions and focuses on the role of fluid shear by assuming particle settling and inertial effects are negligible. The pair diffusion formulation readily allows inclusion of the effects of Brownian motion; thus, the ensuing analysis is valid for arbitrary Peclet number.

### 3.3.2 *Coagulation rate*

To derive the steady state pair probability equation for the relative motion of two particles affected by a random flow field, Brownian motion and potential forces, the principle of linear superposition is used. This yields:

$$0 = \frac{1}{r^2}\frac{\partial}{\partial r}r^2\left[(V_r^f + V_r^i)P - \left(D_r^f + D_r^b\right)\frac{dP}{dr}\right] \qquad (3.31)$$

where $D_r^b$ is the Brownian pair diffusivity and $Vr^i$ is the relative velocity induced by the interparticle potential. The linearity of Stokes equations of motion implies that the effects of hydrodynamic interactions on $D_r^f$, $D_r^b$, $V_r^f$ and $V_r^i$ can be superimposed. Since, the diffusion coefficient and drift velocity for the random linear flow were derived assuming that the relative motion of the particles was small over the flow time scale ($\tau_s$), it is important that the relative motion imparted by $D_r^b$ and $V_r^i$ do not affect the relative motion of the particle pair on a time scale $\tau_s$. This constraint will be satisfied as long as $D_r^f$ is at least comparable to $D_r^b$ and $V_r^i$ and the total strain, $\Gamma\tau_s \ll 1$. If these conditions are not satisfied, then the error in $D_r^f$ is unimportant because the motion is driven solely by Brownian motion and colloidal forces.

The system geometry and boundary conditions are illustrated in Figure 3.2. Only the radial component of the conservation equation needs be considered because of spherical symmetry. Batchelor provides the following expression for $V_r^i$ in terms of the interparticle potential (1976):

$$V_r^i = -\frac{1}{6\pi\mu}\left(\frac{1}{a_1}+\frac{1}{a_2}\right) G(r)\frac{d\phi(r)}{dr} \qquad (3.32)$$

where $\mu$ is the viscosity, $\phi(r)$ is the interparticle potential, and $G(r)$ is a non-dimensional function of radial position that accounts for particle-particle hydrodynamic interactions. Values of $G(r)$ range from 1 when the particles are infinitely separated to zero at contact (Kim & Karrila, 1991; Batchelor, 1976).

Integrating Equation 3.31 once results in an expression for the collision rate of size 1- and 2- particles:

$$K = 4\pi r^2\left[(V_r^f+V_r^i)P - (D_r^f+D_r^b)\frac{dP}{dr}\right] \qquad (3.33)$$

where $K = k\, C_1^\infty C_2^\infty$ is a constant independent of radial position because the flux across spherical shells around the test particle is fixed at steady state.

At this point several simplifications can be made in order to obtain an analytical solution. Since the primary interest is in the behavior of colloidal particles in a random velocity field, non-interacting particles that are not influenced by Brownian motion are selected here as the base state. Neglecting hydrodynamic interactions (A=1 in Equations 3.22 and 3.25,

G=1 in Equation 3.32 and w = 0 in Equation 3.25), interparticle potentials ($V_r^i$ = 0), and Brownian diffusion ($D_r^b$ = 0) , Equation 3.33 becomes:

$$K = D_0 r^4 \frac{dP}{dr} \qquad (3.34)$$

where $D_0 = 8\pi S^2 \tau_S/15$. Equation 3.34 can be solved by separating and integrating from P = 0 at r = $\sigma$ to P = $C_1^\infty C_2^\infty$ at r $\rightarrow \infty$ to obtain the force-free coagulation kernel:

$$k^0 = \frac{8\pi}{5} S^2 \tau_s \sigma^3 \qquad (3.35)$$

where $\sigma = a_1 + a_2$ as defined above and the superscript 0 indicates that this the coagulation rate constant in the absence of particle interactions. The coagulation rate constant is a function of strain rate (S) as well as the total strain ($S\tau_S$) in the system. For comparison Equation 3.35 is plotted in Figure 3.4 against the total strain along with coagulation rate constants obtained for non-interacting particles in steady simple shear and uniaxial extension (Zeichner & Schowalter, 1977). In Figure 3.4 the rate constants have been normalized by $S\sigma^3$ to highlight differences between the three flows. The coagulation rate constant in a random linear flow with small total strain is significantly lower than that in simple shear and uniaxial extension.

Other possible simplifications of Equation 3.33 that result in analytical solutions include non-interacting Brownian particles with no
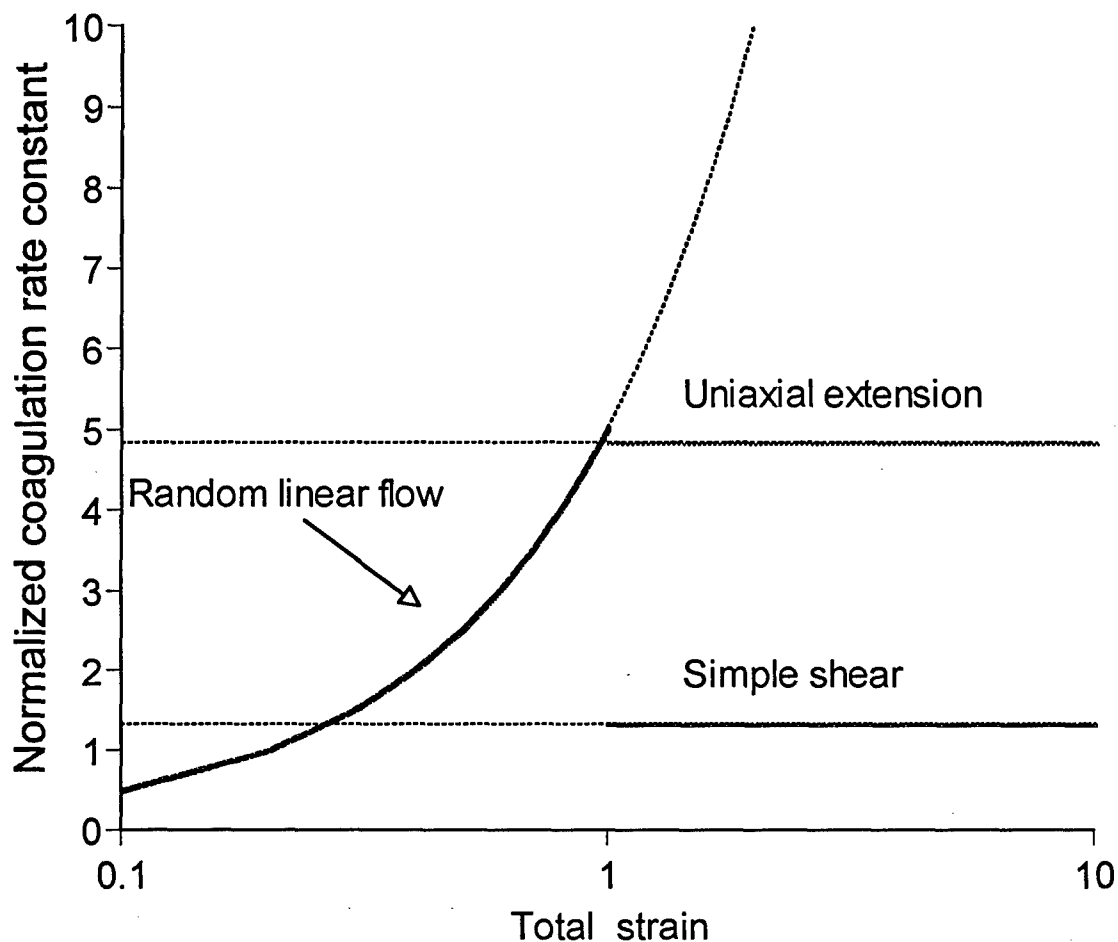
**Figure 3.4**: Comparison of the coagulation rate constant normalized by $S\sigma^3$ for non-interacting particles as a function of total strain. Shown are curves for steady uniaxial extension and steady simple shear (Zeichner & Schowalter, 1977) that are valid in the limit of large strain. The curve labeled random linear flow represents Equation 3.35 and it is valid in the limit of small strain.

fluid motion (Smoluchowski, 1917) and non-interacting particles in the presence of fluid motion and Brownian diffusion. The latter expression can be obtained by neglecting hydrodynamic interactions (A = 1, G = 1, w = 0) and interparticle forces ($V_r^i$ = 0) in Equation 3.33 to obtain:

$$k^{0\prime} = \frac{2\pi S^2 \tau_s \sigma^3}{15 Pe} \left[ \frac{1}{1 + 2Pe^{1/2}\left[\tan^{-1}(2Pe^{1/2}) - \pi/2\right]} \right] \qquad (3.36)$$

where,

$$Pe = \frac{8\pi\mu\tau_s S^2}{5k_b T(1+\beta)^2}\left(\frac{\sigma}{2}\right)^3,$$

$k_b$ is the Boltzmann constant, and T is the absolute temperature. Expanding the $\tan^{-1}$ term in the limits of zero and infinite Peclet number recovers the Brownian coagulation (Smolochowski, 1917) and $k^0$ (Equation 3.35) limits, respectively.

In the sections that follow, analytical and numerical methods are used to derive the ratio of coagulation rate including interparticle forces, hydrodynamic interactions and Brownian diffusion to the base state coagulation rate defined in Equation 3.35.

### 3.3.3 Determining the stability factor

In this section an integral solution for the coagulation rate that depends on the relations used for the interparticle potential is derived. In the limit of large particles and weak van der Waals forces an analytic approximation can be obtained to the integral solution. The analysis given below is confined to the effects of van der Waals attraction and electrical

double layer repulsion although it may be generalized to include other spherically symmetric interparticle potentials.

3.3.3.1 Constitutive relations for interparticle forces

The effects of van der Waals attractions and double layer repulsion on the coagulation rate are considered here. Hamaker was the first to calculate the van der Waals force between two dissimilar spherical particles. In the limit of small particle separations when the gap width between particles is much smaller than the average particle radius, Hamaker's form of the van der Waals attractive potential reduces to (Israelachvili, 1992):

$$\phi_{vdw} = \frac{-A_H \beta}{3(1+\beta)^2 \xi} \tag{3.37}$$

where $\phi_{vdw}$ is the potential due to van der Waals attraction, $\beta$ is the radius ratio ($a_2/a_1$), and $A_H$ is the Hamaker constant. Davis (1984) gives Hamaker's equation for the van der Waals potential at arbitrary gap width.

Phase shifts caused by the finite propagation speed of the electromagnetic dipole field lead to retardation of the dispersion forces at distances several multiples of the London wavelength, $\lambda$; therefore, Hamaker's result overestimates the actual van der Waals attraction. Schenkel & Kitchner (1960) provide an analytical approximation for the retarded van der Waals potential that has been modified by Davis (1984) so that they apply to different size spheres:

$$\phi_{vdw} = -\left(\frac{\beta}{3(1+\beta)^2}\right)\left(\frac{A_H}{\xi + 0.885 N_L \xi^2}\right) \quad \text{for } \xi < 4/N_L \text{ and,} \tag{3.38}$$

$$\phi_{vdw} = -\left(\frac{\beta}{(1+\beta)^2}\right)\left(\frac{A_H}{\xi^2}\right)\left[\frac{4.9}{15N_L} - \frac{8.68}{45N_L\xi} + \frac{4.72}{105N_L\xi^2}\right] \qquad (3.39)$$

for $\xi > 4/N_L$ and $\xi \ll 1$. In Equations 3.38 and 3.39, $N_L$ is the radius of the two particles scaled by the London retardation wavelength, $\lambda$, ($N_L = 2\pi\sigma/\lambda$). The London wavelength is taken to be 100 nm (van de Ven & Mason, 1977; Davis, 1984). These best-fits to the retarded van der Waals potential are valid in the lubrication regime only (i.e., where $\lambda \ll \sigma/2$). Constraining $\lambda \ll \sigma/2$, so van der Waals attraction decays in the lubrication regime leads to the restriction that $N_L \gg 4\pi$ which is satisfied for all the particle sizes examined in this paper.

Electrostatic repulsion caused by the interpenetration of the ion double layers surrounding charged particles may be incorporated using the Gouy-Chapman model for the electrical double layer. Russel et al. (1989) summarize the various approximations available for calculating the potential due to electrostatic repulsion along with their limits of applicability. For small gaps [$\xi\kappa' < 2$, where $\kappa' = \kappa\sigma/2$ is the inverse Debye length ($\kappa$) scaled by the average particle radius] and thin double layers ($\kappa' > 2$) the constant surface potential version of the linearized Derjaguin approximation is used (Russel et al., 1989):

$$\phi_{DL} = \left(\frac{a_1\beta}{1+\beta}\right)4\pi\epsilon_D\epsilon_0\psi^2\ln\left(1 + e^{-\kappa'\xi}\right) \qquad (3.40)$$

where $\phi_{DL}$ is the potential due to double layer repulsion, $\epsilon_D$ is the dielectric constant of the surrounding fluid, $\epsilon_0$ is the permittivity of the

vacuum, and $\psi$ is the surface potential. In the limit of large gaps ($\gamma\kappa' > 2$), a constant surface potential may be assumed:

$$\phi_{DL} = \left(\frac{a_1\beta}{1+\beta}\right) 4\pi\epsilon_D\epsilon_0\psi^2 e^{-\kappa'\xi} \qquad (3.41)$$

Following DLVO theory (Israelachvili, 1992), the total interparticle potential may be expressed as a superposition of the van der Waals attraction and double layer repulsion:

$$\frac{\phi}{k_bT} = N_A\left(\hat{\phi}_{vdw} + N_R\hat{\phi}_{DL}\right) \qquad (3.42)$$

where the hat($^\wedge$) indicates that the potentials have been scaled such that $N_A$ expresses the magnitude of the van der Waals attraction relative to thermal energy and $N_R$ is a ratio of electrostatic repulsion to van der Waals attraction. $N_A$ and $N_R$ are defined respectively as:

$$N_A = \frac{A_H}{k_bT}\left(\frac{\beta}{(1+\beta)^2}\right) \quad \text{and} \quad N_R = \frac{4\pi\epsilon_D\epsilon_0\psi^2\sigma}{A} \qquad (3.43)$$

The force due to the interparticle potential is $-d\phi/dr$ and its typical functional form is shown in Figure 3.5 for a pair of 4 $\mu$m radius particles. The van der Waals force (thin dashed line) begins to become significant when the gap width, h, is proportional to $\lambda/2\pi$, which corresponds to a gap width on the order of the London retardation wavelength. The solid thin line shows the total force acting on the particles as a sum of the van der Waals attraction and double layer repulsion. For this system
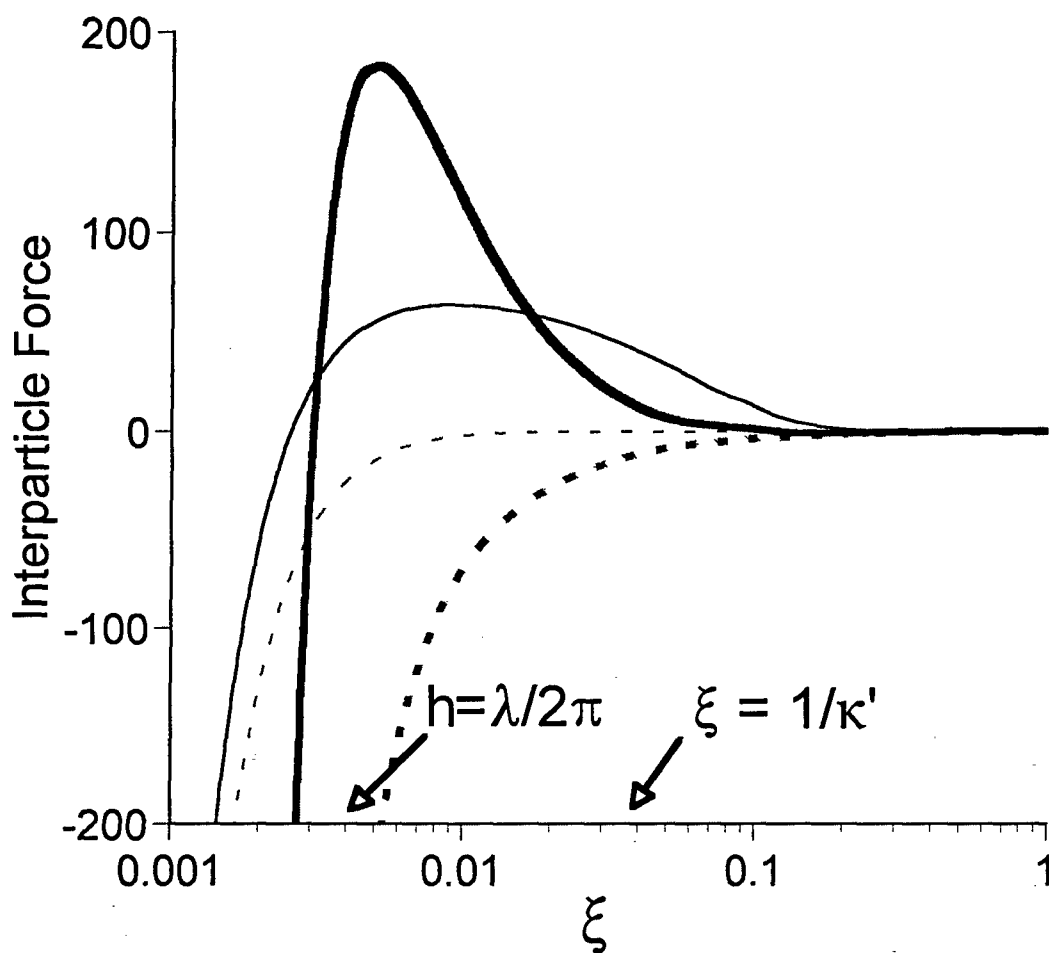
**Figure 3.5**: Example of the interparticle force as a function of distance. Shown are the force due to van der Waals attraction (thin dashed line) and total force composed of van der Waals attraction and double layer repulsion (thin solid line). The effective interparticle force defined by Equation 3.45 is shown with (thick solid line) and without (thick dashed line) double layer repulsion. Example results are for 4 μm radius particles with a surface potential of -9.4 mV in a $10^{-3}$ M ionic strength solution ($N_L$ = 500, $N_F$ = 500, $N_R$ = 1500 and $\kappa'$ = 25).

$N_R = 1500$ and $\kappa' = 25$ corresponding to polystyrene particles with a surface potential of -9.4 mV in a $10^{-3}$ M ionic strength solution. A repulsive energy barrier is seen beginning at $\xi \sim 1/\kappa'$ and it extends to gap widths comparable to the London retardation wavelength before van der Waals forces dominate the total force again.

### 3.3.3.2 Scaling analysis

Hydrodynamic interactions, van der Waals attraction and electrostatic repulsion all influence particle aggregation. Table 3.1 lists these interparticle interactions as well as their length scales and magnitudes. These characteristic forces and length scales along with the Brownian diffusion coefficient and the particle radius ratio can be used to form six non-dimensional groups that define the parameter space for the stability factor. Table 3.2 lists the six dimensionless parameters chosen and provides an estimate of their typical magnitudes. These characteristic ranges were calculated by considering an aqueous dispersion of colloidal particles with $\sigma = 1.0$ to $100$ μm, $A_H = 10^{-19}$ to $10^{-21}$ J, $\Gamma = 0.1$ to $1000$ s$^{-1}$ and $\psi = 0$ to $100$ mV.

### 3.3.3.3 Derivation of the stability factor

The full solution to the radial pair probability conservation equation (Equation 3.31) can be found in terms of two embedded integrals. Equations 3.22, 3.25, and 3.32 are substituted into Equation 3.33, the relative position vector is scaled with the average particle radius and the pair probability is scaled with its value at infinite particle separation. By defining a non-dimensional coagulation kernel of the form, $\hat{k} = A/3\mu$, a scaled radial flux equation is obtained:

**Table 3.1**: Relevant scaling factors

| Force | Length scale | Magnitude |
|-------|-------------|-----------|
| hydrodynamic | $a_1$ | $\pi\mu\Gamma a_1^2$ |
| van der Waals | $\lambda$ | $A_H/\lambda$ |
| electrical double layer | $1/\kappa$ | $\epsilon\epsilon_0\psi^2 a_1$ |

**Table 3.2**: Non-dimensional parameters and their typical magnitudes.

| Parameter | Typical value | Description |
| --- | --- | --- |
| $\beta = a_2/a_1$ | 0.125 to 1.0 | Radius ratio |
| $N_F = \dfrac{8\pi\mu S^2 \tau_s}{5A_H}\left(\dfrac{\sigma}{2}\right)^3$ | $\sigma = 100\ \mu m$: $10^3$ to $10^9$ <br> $\sigma = 1\ \mu m$: $10^{-3}$ to $10^3$ | Ratio of hydrodynamic drag to van der Waals attraction |
| $Pe = \dfrac{8\pi\mu\tau_s S^2}{5k_b T(1+\beta)^2}\left(\dfrac{\sigma}{2}\right)^3$ <br> $Pe = N_F\left(\dfrac{A_H}{k_b T}\right)\left(\dfrac{\beta}{(1+\beta)^2}\right)$ | $\sigma = 100\ \mu m$: $10^4$ to $10^8$ <br> $\sigma = 1\ \mu m$: $10^{-2}$ to $10^2$ | Ratio of diffusivity caused by the fluctuating velocity gradient to the Brownian diffusivity |
| $N_R = \dfrac{4\pi\sigma\epsilon_D\epsilon_0\psi^2}{A_H}$ | $\sigma = 100\ \mu m$: 0 to $10^7$ <br> $\sigma = 1\ \mu m$: 0 to $10^5$ | Ratio of double layer repulsion to van der Waals attraction |
| $N_L = \dfrac{2\pi\sigma}{\lambda}$ | $10^2$ to $10^4$ | Ratio of average particle radius to London wavelength |
| $\kappa' = \kappa\,\sigma/2$ | $\sigma = 100\ \mu m$: 0 to $10^5$ <br> $\sigma = 1\ \mu m$: 0 to $10^3$ | Ratio of London wavelength to Debye length |

$$k = \hat{k}(\xi + 2)^2 \cdot$$

$$\left[ \left\{ G\frac{d\phi}{d\xi} + N_F w(A-1)(\xi+2) \right\} P - N_F \left\{ (\xi+2)^2 (A-1)^2 + Pe^{-1}G \right\} \frac{dP}{d\xi} \right] \quad (3.44)$$

with the non-dimensional parameters defined in Table 3.2. Solution of Equation 3.44 can be obtained using an integrating factor. Multiplying both sides of Equation 3.44 by:

$$I = \exp\left( \int_\xi^\infty F d\xi' \right) = \exp\left( \int_\xi^\infty \frac{-G\dfrac{d\phi}{d\xi'} + N_F w(A-1)(\xi'+2)}{N_F\left[(\xi'+2)^2(1-A)^2 + Pe^{-1}G\right]} d\xi' \right) \quad (3.45)$$

and rearranging, yields:

$$\frac{d}{d\xi}[PI(\xi)] = \frac{k}{\hat{k}N_F(\xi+2)^2\left[(\xi+2)^2(1-A)^2 + Pe^{-1}G\right]} I(\xi) \quad (3.46)$$

The argument F in Equation 3.45 can be thought of as the effective interparticle force after hydrodynamic interactions have been included. Figure 3.5 illustrates the functional form of this argument with (thick solid line) and without (thick dashed line) the presence of double layer repulsion when equal size 4 μm radius particles are assumed with $N_R = 1500$, $\kappa' = 25$, $Pe^{-1} = 0$, and $N_F = 500$. (As noted previously, this set of parameters corresponds to polystyrene particles with a surface potential of -9.4mV in a $10^{-3}$ M ionic strength solution.) For the system without double layer repulsion (thick dashed line), the interparticle force goes to zero far from the particle which indicates that the system is behaving like two non-

interacting spheres. For distances roughly equal to the London wavelength ($h = \lambda/2\pi$), van der Waals attractions becomes significant and F becomes negative. The same qualitative behavior is seen at large and small particle separations for the curve that includes double layer repulsion (heavy solid line). In this case, however, F has a positive valued maximum at $\xi$ corresponding to $1/10\kappa'$ indicating an energy barrier that impedes flocculation. For this situation, primary minimum flocculation into the deep van der Waals potential energy well may not occur because the colliding particles cannot overcome the repulsive energy barrier. A shallow secondary minimum may exist beyond the energy barrier and weak secondary minimum flocculation could occur under some conditions. The effect of the viscous forces on the effective interparticle potential between the particles can be seen by comparing the lines without hydrodynamic interactions (thin lines) with those that include hydrodynamic interactions (thick lines). Hydrodynamic interactions amplify the force acting between the particles. With hydrodynamic interactions a purely attractive potential (dashed lines) has a van der Waals attractive force that becomes significant at larger gap widths. When double layer repulsion is present (solid lines) the hydrodynamic interactions amplify the repulsive force leading to a higher effective barrier to primary minimum coagulation.

Two factors contribute to these observations, namely: the presence of hydrodynamic drift and the ratio of hydrodynamic interactions found in F. Drift in the pair probability leads to the accumulation of particle pairs at small separations; thus, the drift velocity acts as an additional attractive force. The presence of drift is expected to decrease colloidal stability

because the migration of particles to smaller separations increases the chance that the particles will successfully collide. The importance of the drift depends on its magnitude compared to the interparticle potential. Using lubrication approximations for w and A (i.e., w ~ 6.372, A-1 ~ -4.077$\xi$) gives a characteristic drift velocity of $50N_F\xi$. The velocity due to the van der Waals force scales with $1/\xi$ where $G = 2\xi$ when $\xi \ll 1$. Equating the two velocities shows that the van der Waals attraction and drift velocity have equal magnitudes when $\xi^2 \sim 1/100N_F$. At the location of maximum drift ($\xi = 0.08$ from Figure 3.1) the drift velocity is significant for $N_F > 2$ which is within the expected range for $N_F$ given in Table 3.2. Enhancement of particle aggregation due to the drift velocity contributes to the instability of colloidal suspensions. Situations can be envisioned where the inward flux of particles caused by drift can overcome a repulsive energy barrier caused by a diffuse double layer. An analogous scaling comparing the flux due to double layer repulsion to the flux due to drift suggests that when $N_F > N_r\kappa'$ double layer repulsion will be mitigated by the drift velocity.

The other important effect of hydrodynamic interactions is to amplify the drift velocity and interparticle potential. This behavior is illustrated by examining the functional form of the hydrodynamic interactions in the lubrication region, i.e., where $\xi \ll 1$. Referring to Equation 3.45 it is seen that the effective interparticle force depends on $G/N_F(1-A)^2$. In the lubrication regime $G/(1-A)^2 \sim 1/\xi$ and for $N_F\xi < 1$ the hydrodynamic forces can be expected to increase the impact of the interparticle forces. In contrast, when $N_F\xi > 1$ viscous forces diminish the

effect of interparticle forces. For the case presented in Figure 3.5, $N_F\xi \sim 1$ when $\xi = 1/\kappa' = 0.02$. For gap widths greater than $\xi = 0.02$ the interparticle force is reduced while at smaller gap widths the interparticle force is augmented. Indeed, the effective repulsive force shown by the thick solid line in Figure 3.5 is augmented when $\xi < 0.02$. A similar amplification effect is expected for the drift velocity term where Equation 3.45 shows that the effective drift depends on $w/(1-A) \sim 1/\xi$ in the lubrication region.

The solution to Equation 3.46 is obtained by integrating $\xi$ from particle contact to infinity, noting that as $\xi \to \infty$, $P \to 1$ and $I \to 1$ and when $\xi \to 0$, $P \to 0$ and $I \to 0$. After dividing the result into the force-free flocculation kernel (Equation 3.35) an integral expression for the stability factor is obtained:

$$W = 24 \int_0^\infty \left[ \frac{I(\xi)}{(\xi+2)^2 (A-1)^2 + Pe^{-1}G} \right] \frac{d\xi}{(\xi+2)^2} \qquad (3.47)$$

Since these results are predicated on a pair diffusion methodology, one might wish to compare Equation 3.47 to the stability coefficient integral for particles coagulating in response to Brownian diffusion. Due to a judicious cancellation in the Brownian coagulation stability factor, hydrodynamic interactions are only present in the pre-exponential factor of the stability integral, and hence the effects of viscous interactions are subordinate to interparticle forces (Spielman, 1970). In contrast, when using pair diffusion to describe particle motion due to a fluctuating velocity field, hydrodynamic interactions are in the exponent of the stability factor

integrand (Equation 3.45). This is because it is a different hydrodynamic function that controls relative motion in shear flow (i.e., 1-A) from that which controls relative motion due to potential forces and Brownian motion (i.e., G). In other words viscous interactions are significantly more important in this problem.

The development of the coagulation rate and the stability factor ignores the coupling between hydrodynamic and electrical forces (termed electroviscous effects) (Russel et al., 1989). This effect arises for charged particles that are surrounded by a diffuse electrical double layer. When a charged particle moves, the fluid immediately surrounding the particle appears more viscous because of the extra work required to move both the particle and its surrounding diffuse double layer (Russel et al., 1989; Kim & Karrila, 1991). The increased viscosity manifests itself as an additional retardation on the relative particle mobility.

The ion Peclet number, $Pe^i$, and the Hartmann number, Ha, characterize the importance of electroviscous effects. The ion Peclet number compares the relative magnitude of particle convection to ion diffusion. When $Pe^i$ is large the double layer cloud is not fast enough to react to the particle movement. This disequilibrium between the particle and its ion cloud leads to the formation of a retardation force that slows particle movement. $Pe^i = S/D^i\kappa^2$ where $D^i \sim 10^{-9}$ m$^2$/s is the ion diffusivity; thus, deformation of the double layer is expected to be most important for diffuse double layers and small particles. The Hartmann number, Ha = $\epsilon_D\psi^2/4\pi\mu D^i$, compares the relative strength of the electrical force to the viscous force. Electroviscous forces would be anticipated to be most

important for large surface potentials; however, since this effect only arises in the double layer it will have little effect for thin double layers. If the total strain is assumed to be 0.01 then the conditions presented in Fig. 5 ($\kappa'$ = 25, $N_R$ = 1500, $N_F$ = 500 and 4 μm particles) give $Pe^i$ = 0.004 and Ha = 0.01 which suggests that electroviscous effects are unimportant. Beyond noting here that electroviscous effects could be important in some cases in the calculation of colloidal stability (i.e., for low ionic strengths and small colloids), its effect has been neglected in the subsequent analysis of coagulation.

3.3.3.4 Asymptotic approximation for weak van der Waals attraction and non-Brownian particles

An analytical approximation to Equation 3.47 is possible for equal size particles if there is no double layer repulsion or electrostatic retardation and Brownian motion is ignored. If it is also assumed that the van der Waals attraction and hydrodynamic interactions are only important in the lubrication regime, then analytic lubrication approximations to the hydrodynamic interactions and van der Waals forces can be substituted into the integrals for $I(\gamma)$ and W. The assumption that the drift velocity is only important in the lubrication region cannot be made. As noted above, the effective drift velocity is proportional to $1/\xi$ in the lubrication region which would lead to a divergence of the integral $I(\xi)$ if the lubrication approximation is applied to all gap widths.

In the derivation presented below, the problem of drift being important outside the lubrication regime is circumvented by the splitting the integral for $I(\xi)$ into an inner and outer piece. Lubrication approximations

for drift and van der Waals attraction are used in the inner integral to obtain an analytical solution. The outer integration includes only drift and is computed numerically. As shown below, Equation 3.47, the integral for W, is dominated by the lubrication region. While not mathematically exact, the approximation does allow an analytical determination of the power law dependence of $N_F$ on the stability factor.

Let $Q = Q_V + Q_D$ equal to the integral in Equation 3.44 where the integral has been broken into a part containing the interparticle potential, $Q_V$, and a part containing the drift velocity, $Q_D$. For instance,

$$Q_V = \int_\xi^\infty \frac{-G\dfrac{d\phi}{d\xi'}}{N_F\left[(\xi'+2)^2(1-A)^2 + Pe^{-1}G\right]}\, d\xi' \qquad (3.48)$$

where $Q_V$ is assumed to decay within the lubrication region. To obtain the asymptotic approximation for $Q_V$, the lubrication approximations to the hydrodynamic interaction functions, $A(\xi)$ and $G(\xi)$, and Eq 3.37 are substituted into Equation 3.48. The resulting expressions are further simplified by noting that, since $\xi \ll 1$ in the lubrication regime, $(\xi + 2) \sim 2$. Solution to the simplified relation for $Q_V$ yields:

$$Q_V = -Q_{VI}/\xi^2 \qquad (3.49)$$

where $Q_{VI} = 1/(199.5N_F)$.

Making the lubrication assumptions on $Q_D$ shows that it does not decay in the lubrication regime. Instead $Q_D$ is broken into an inner and outer integral yielding,

$$Q_D = \int_{\xi_L}^{\infty} \frac{w}{(\xi'+2)(A-1)} d\xi' + \int_{\xi}^{\xi_L} \frac{w}{(\xi'+2)(A-1)} d\xi' \qquad (3.50)$$

where $\xi_L$ is the boundary between the inner and outer regions and it was chosen to be 0.01. The first integral in Equation 3.50 was found from numerical quadrature to be -1.625. The second integral is calculated analytically by substituting the lubrication approximations for A and w (In this case w is taken to be 6.732.). The final expression for $I(\xi)$ is given by:

$$I(\xi) = 0.197 \left( \frac{\xi}{\xi_L} \right)^{-0.781} \exp\left[ -\frac{Q_{VI}}{\xi^2} \right] \qquad (3.51)$$

The approximation for W is obtained by applying the lubrication assumptions to Equation 3.47 and substituting Equation 3.51 in for $I(\xi)$. Solution to the simplified relation for W gives:

$$W_0 = B_2 N_F^{0.11} \qquad (3.52)$$

where the theoretical estimate for the constant $B_2$ is 5.01.

In the limit of negligible Brownian motion and retardation, $W_0$ is related to the ratio of the viscous forces to the van der Waals attractive force at lengths comparable to the particle radius. Over the typical $N_F$ parameter space (defined in Table 3.2), the stability factor varies one order of magnitude. When the particle radius increases from 0.5 to 50 μm, $W_0$ has a 5-fold increase indicating a more stable suspension. Increasing the

shear rate by a factor of 100 increases $W_0$ by a factor of 1.7. Higher $N_F$ corresponds to weak van der Waals attraction, meaning hydrodynamic lubrication forces between the particles are effective at hindering particle aggregation. The trend with increasing particle radius is expected; as the particle size increases, the hydrodynamic resistance to collision begins acting at larger distances compared with the London wavelength. Therefore, van der Waals attraction is not sufficient to bring the particles together.

Figure 3.6 illustrates the constraints to the validity of the asymptotic approximation on the $N_F$ / $N_L$ plane where $N_F$ is the ratio of viscous forces to van der Waals forces and $N_L$ is the ratio of particle radius to London retardation wavelength. The shaded region shows the expected region of $N_F/N_L$ parameter space that can be physically realized given typical shear rates and particle radii (see Table 3.2). Shown as solid lines are demarcations for van der Waals attraction decaying in the lubrication regime ($\lambda \ll \sigma/2$), negligible Brownian diffusion ($Pe \rightarrow \infty$) and negligible retardation.

For retardation effects to be unimportant, the effective interparticle potential acting on the particles must be insignificant at distances comparable to the London retardation wavelength, $\lambda$. The effective interparticle potential scales in proportion to $F\xi$, where F is defined in Equation 3.45. Requiring $F\xi$ to be much less than one at $h = \lambda/2\pi$ leads to the result that $N_L \gg (1000N_F)^{1/2}$.

Figure 3.6 shows that the asymptotic approximation is valid for large particles (large $N_L$) and strong flows (large $N_F$). Retardation is the primary
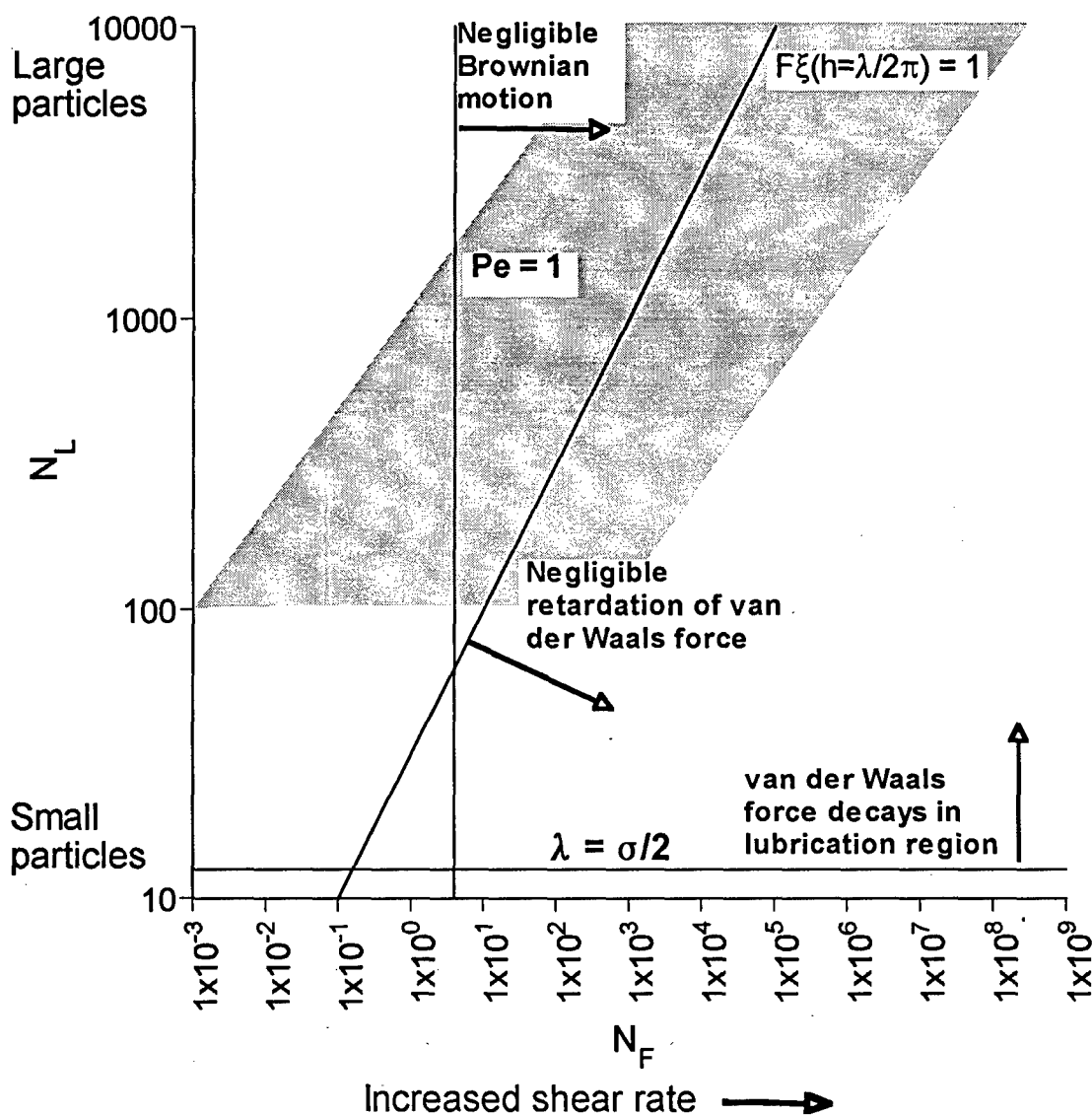
**Figure 3.6**: Map showing the constraints on the asymptotic approximation. Solid lines indicate the boundaries where lubrication approximations are valid ($\lambda = \sigma/2$), Brownian motion is negligible (Pe = 1) and electrostatic retardation is negligible ($\xi F = 1$ at $h = \lambda/2\pi$). The shaded area indicates the values of $N_F$ and $N_L$ expected for typical coagulating systems.

constraint on the region of applicability while the lubrication approximation appears to be valid for all practical particle sizes ($N_L = 10^2$ to $10^4$).

Operationally, the asymptotic approximation has been found to be within 5% of the full numerical solution (presented below) for $N_F > 10^9$ which is outside the range of typical values shown in Table 3.2. Further comparison of the numerical and asymptotic results is provided in Section 3.4.

The asymptotic analysis provides a good method for computing the dependence of the stability factor on $N_F$ because the $N_F$ dependence comes from the lubrication regime where van der Waals forces are important. The stability factor integral does not converge in the lubrication region so there is an error associated with using the lubrication approximation for $w/(A-1)$ in the w integrand. Since the integrals containing the drift term are independent of $N_F$ this error only affects the numerical pre-exponential factor. Numerical integration of the actual stability factor equation for $N_L = 10,000$ and $N_F > 10^{11}$ gives a pre-exponential factor of $B_2 = 5.53$ (see details in the next Section). The asymptotic prediction of $B_2 = 5.01$ compares well with the prediction based upon non-linear regression of the exact numerical solution. The approximation works so well because the lubrication form for $w/(A-1)$ is, surprisingly, an excellent approximation for $w/(A-1)$ out to large separation distances.

In summary the influence of shear rate and particle size on the coagulation rate is found to be curtailed by the presence of interparticle interactions. For the non-interacting system (Equation 35), the coagulation rate constant was proportional to $\tau_s S^2 \sigma^3$; however, in the asymptotic limit

of no retardation or Brownian motion, the coagulation rate increases in proportion to $(\tau_s S^2 \sigma^3)^{0.89} (A_H/\mu)^{0.11}$.

## 3.4 Colloidal stability in chaotic flows

### 3.4.1 *Numerical Method*

Using the diffusion approximation permits investigation of the effects of van der Waals attraction, electrostatic repulsion and hydrodynamic interactions on colloid stability. Estimates for the stability factor, W, at arbitrary $N_F$, $N_L$ and Pe are obtained by reexpressing Equations 3.45 and 3.47 as a set of coupled ordinary differential equations and solving them using a 5th order Runge-Kutta algorithm (Press et al., 1992). The local integration error is constrained to $10^{-5}$ and the error is regulated during integration by using adaptive step control. At the start of the integration, particles are separated by 20 average particle radii — a separation distance where interparticle and hydrodynamic interactions are negligible. The governing equations are then integrated backwards until the separation distance scaled by the average particle radius is less than $0.0002/N_L$ and the integrals converge.

Near and far field forms of the hydrodynamic interactions were taken from Kim & Karrila (1991). Plots of the hydrodynamic interaction functions as a function of gap width were used to decide when to switch from the near field to the far field form. To achieve a relatively smooth transition in the hydrodynamic interactions, log-linear interpolation of the near and far field solutions was used in the neighborhood of particle separations scaled with the average radius of 2.05.

Appendix D contains a description of the computer program used in these calculations.

### 3.4.2 Results and Discussion

As discussed in 3.3, the stability factor for turbulent coagulation in the diffusion limit depends on six non-dimensional parameters (Table 3.2). Illustrating the behavior of the stability factor for all possible parameter combinations would be infeasible; however, salient features of the effect of these parameters on the magnitude of the stability factor are summarized below. First, the asymptotic approximation valid in the limit of small gap widths, negligible Brownian motion, double layer repulsion and electrostatic retardation is compared to numerical solutions of W. Next, the influence of double layer repulsion is examined by varying the surface potential of the particles and the size of the double layer to investigate the transition from stable to destabilized suspensions. To illustrate the significance of the results, a comparison is given of the effect of particle-particle interactions on colloidal stability for the random linear flow examined in this chapter to the calculations made by Greene et al. (1994) and van de Ven & Mason (1977) for steady linear flow fields.

Figure 3.7 shows the combined effects of shear rate ($N_F = 10^{-2}$ to $10^9$) and particle radius ($N_L = 100$ to $10000$, $\beta = 1$) on the normalized stability factor for fully destabilized (e.g., $N_R = 0$), equal size colloidal particles. The stability factor in Figure 3.7 is normalized with the non-retarded asymptotic limit: $W_0 \cong 5.53 N_F^{0.11}$ (Equation 3.52). Results are shown for $N_L = 100$, $N_L = 1000$, and $N_L = 10000$. The dashed lines are obtained in the absence of Brownian diffusion and the solid lines show the
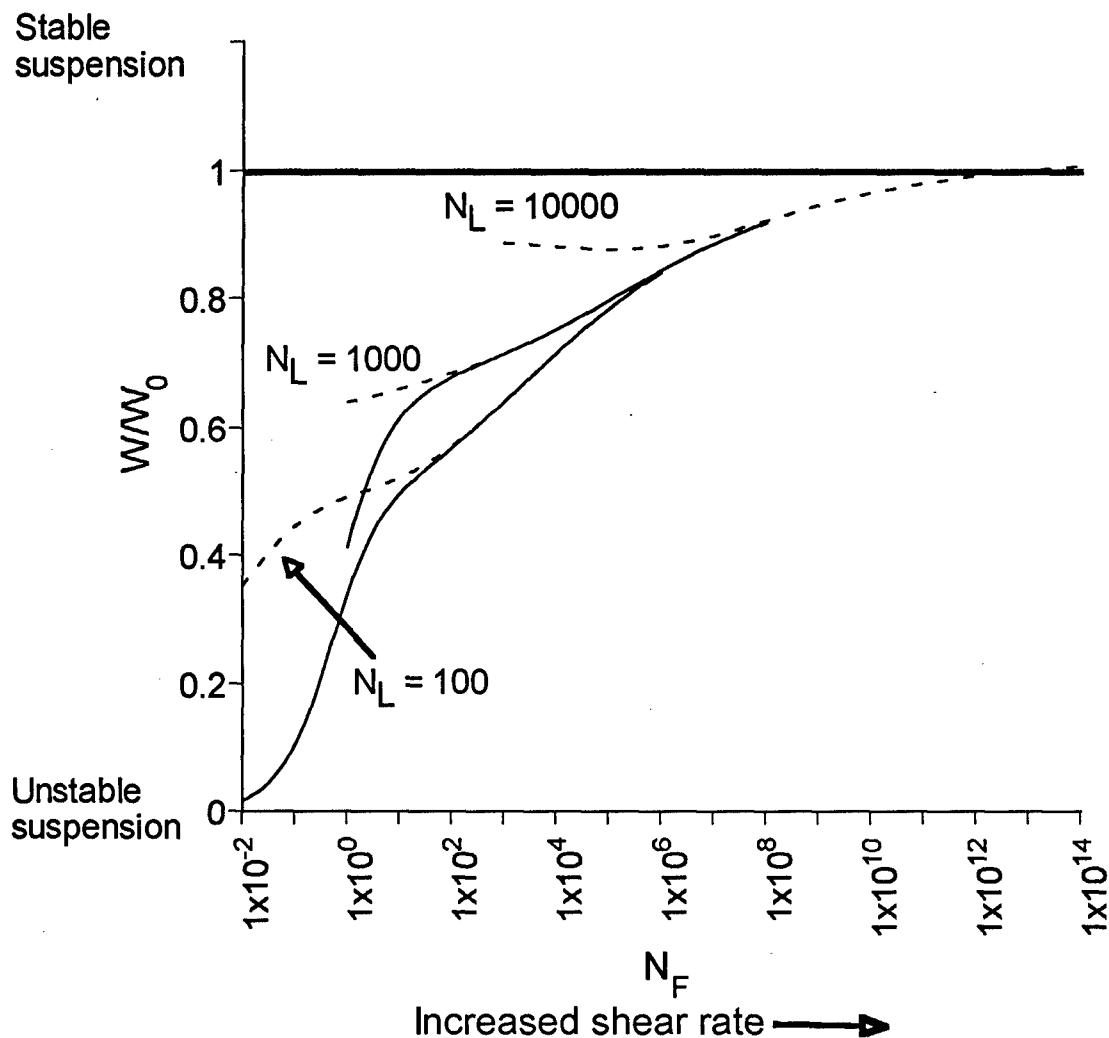
**Figure 3.7**: The stability factor normalized by the asymptotic limit (Equation 3.52) versus $N_F$ and $N_L$ for particles with equal radii in the absence of double layer interactions. The dashed and solid lines represent solutions in the absence and presence of Brownian motion, respectively.

predicted colloidal stability when Brownian diffusion is included. The Peclet number controls the relative strength of Brownian diffusion compared with diffusion due to fluid motion and is a function of $A_H/k_bT$, $N_F$, and $\beta$ (see Table 3.2). Unless otherwise indicated $A_H/k_bT$ was fixed at 1.0; thus, specifying $N_F$, and $\beta$ makes the Peclet number a dependent parameter. For the current example with equal size particles, $Pe = \frac{1}{4}N_F$. The value of $A_H/k_bT = 1$ corresponds roughly to the Hamaker constant of polystyrene spheres in water at room temperature, $T = 298K$ (Russel et al., 1989). As shown in Figure 3.8, W is insensitive to the value of $A_H/k_bT$ except for very weak flows.

Figure 3.7 shows that as the flow strength increases (increasing $N_F$) the stability factors approach the asymptotic solution ($W/W_0 = 1.0$). The asymptotic solution is approached slowly and is valid for only unreasonably high values of $N_F$. Calculations that include Brownian diffusion lead to lower normalized stability factors for small values of $N_F$. As $N_F$ increases for each curve there is a transition from a stability factor dominated by van der Waals attraction to one where the drift velocity is important. The change in the dominating mechanism for collision is seen by the inflection point in the curves. The location of the transition is found by balancing the particle fluxes due to drift and van der Waals attractions at $h = \lambda/2\pi$ ($\xi = 2/N_L$) to give: $N_F = N_L^2/400$.

The importance of Brownian motion is illustrated in Figure 3.8 where the normalized stability factor ($W/W_0$) is plotted against $N_F$ for several values of $A_H/k_bT$ and $N_L = 100$, $\beta = 1.0$. For $A_H/k_bT = 1$, the effect of the Brownian motion is discernable for $N_F < 1$ which corresponds
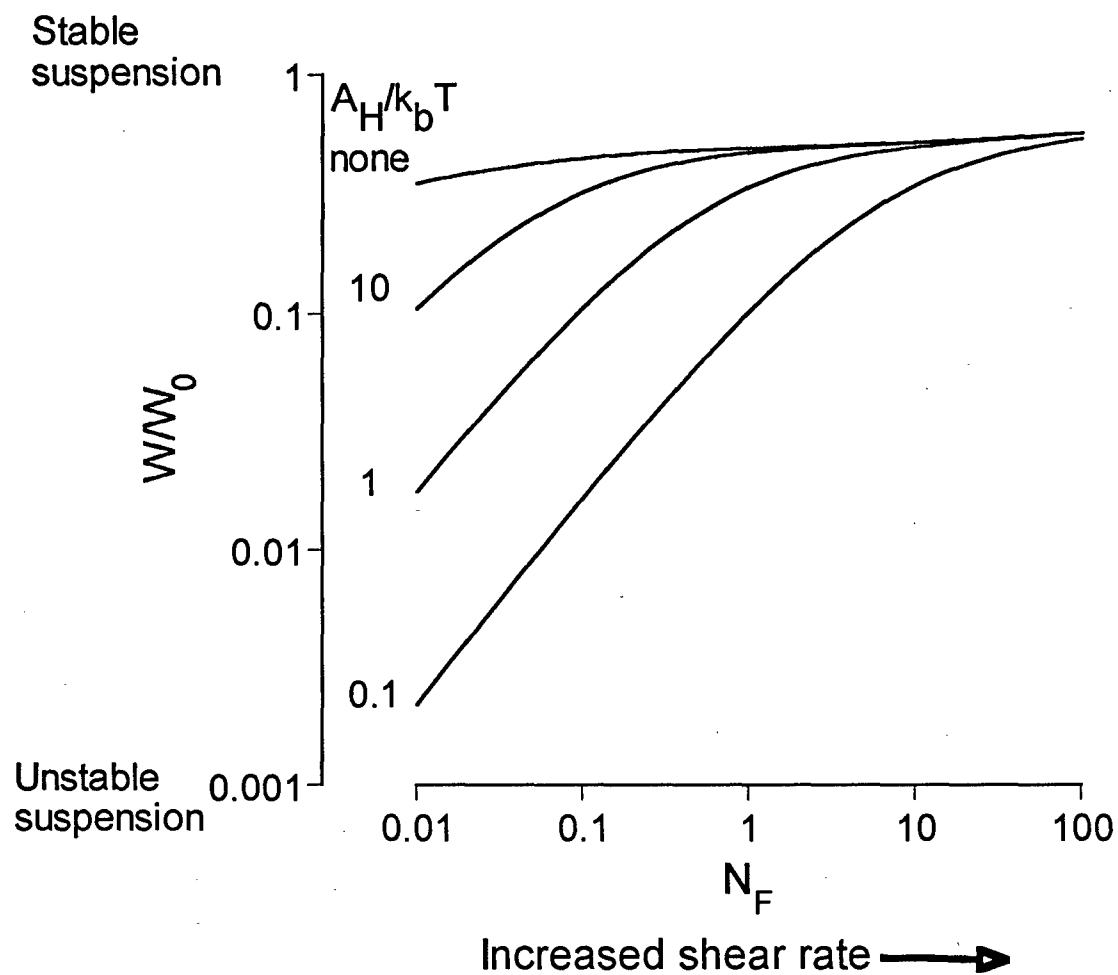
**Figure 3.8**: Sensitivity of the stability factor results to the strength of Brownian diffusion. The normalized stability factor is plotted against the flow strength parameter, $N_F$, for destabilized particles with $N_L = 100$.

to a Peclet number of order 1 or smaller. As $N_F$ increases Brownian motion becomes insignificant and the numerically computed stability factor approaches the asymptotic limit given by Equation 3.52. When $N_F$ is large, the diffusivity due to the fluctuating velocity field transports the particles until they are close enough for van der Waals forces to cause them to collide. While at small $N_F$ the flow field transports the particles to an intermediate length scale where Brownian motion becomes important. In this case, transport to separations where van der Waals forces are important is accomplished by Brownian motion. Equating the particle flux due to the random velocity field with the flux due to the Brownian motion at $\xi = 2/N_L$ leads to an estimate for the minimum $N_F$ at which flow field transports the particles close enough for van der Waals attraction to cause a collision. This balance leads to the criterion that $N_F > (N_L/10)(k_bT/A_H)$ for the hydrodynamic flux to dominate particle transport. This scaling estimate for the transition from shear to Brownian dominated coagulation is in agreement with the numerical results.

The influence of Brownian motion on coagulation in the randomly varying flow is considerably weaker than that determined for steady linear flows (Feke & Schowalter, 1983 and 1985). Feke and Schowalter (1983) used a perturbation technique to determine the effect of Brownian motion in steady simple shear and uniaxial extensional flow. They found that for $A_H/k_bT \sim 1$, the influence of Brownian motion extended to Pe of about 100 and that it could act to either increase or decrease the overall coagulation rate (Feke & Schowalter, 1985). The addition of even small amounts of Brownian motion (compared to the shear rate) allowed particles to diffuse

across regions of closed trajectories, thus measurably affecting the calculated coagulation rate (Feke & Schowalter, 1983). In a system with a randomly fluctuating linear velocity field, large concentration gradients do not develop since the diffusive motions imparted by the fluid shear keep the particles well-mixed. Therefore, the role of Brownian motion in randomly varying linear flows is suppressed except when the fluid shear is too weak to bring the particles close enough for van der Waals attraction to dominate.

Situations where double layer repulsion is present are now considered. As illustrated in Figure 3.5, significant double layer repulsion can lead to a repulsive force barrier. The energy barrier can prevent particles from reaching the primary minimum dominated by attractive van der Waals forces, hence $W \rightarrow \infty$.

Figures 3.9 and 3.10 illustrate the effect of double layer thickness for calculations obtained by setting $N_L = 2000$ and $N_R = 6000$ and assuming equal sized particles, while $N_F$ and the normalized inverse Debye length, $\kappa'$, are allowed to vary. The constant $N_F$ lines in Figure 3.9 exhibit an abrupt transition from stable to unstable suspensions as the double layer thickness is decreased ($\kappa'$ getting larger) beyond $\kappa'$ about 10,000. For more diffuse double layers, the stability factor increases with decreasing double layer thickness until a value near $\kappa' = 5000$ is reached. Above $\kappa' = 5000$ the stability factor decreases sharply signaling the transition from significant double layer repulsion to a destabilized system in which the double layer thickness no longer extends beyond the deep van der Waals potential energy well.
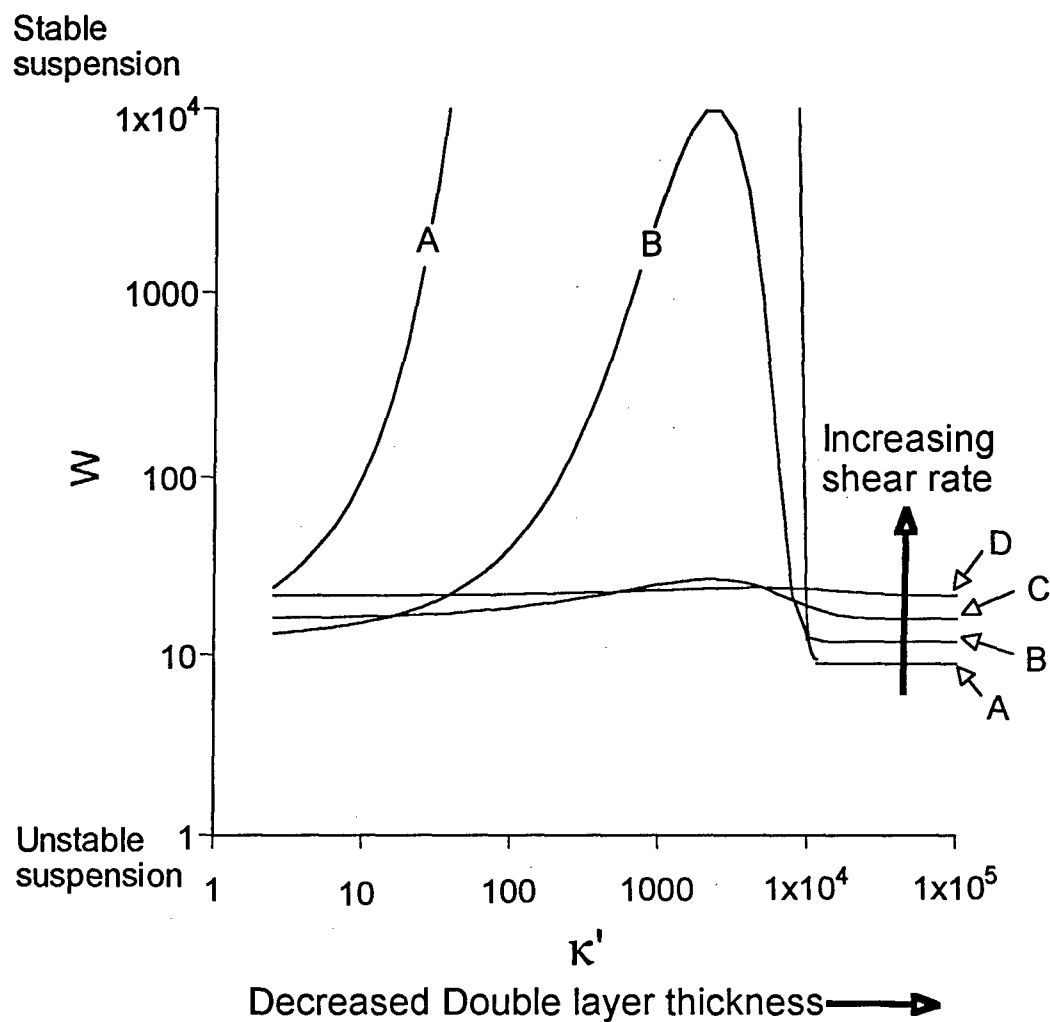
**Figure 3.9**: Influence of double layer thickness (proportional to $1/\kappa'$) on the stability factor, W, for several values of $N_F$. For this analysis $N_L = 2000$, $\beta = 1$, and $N_R = 6000$. Labeled curves represent A) $N_F = 10^3$, B) $N_F = 10^4$, C) $N_F = 10^5$ and, D) $N_F = 10^6$.
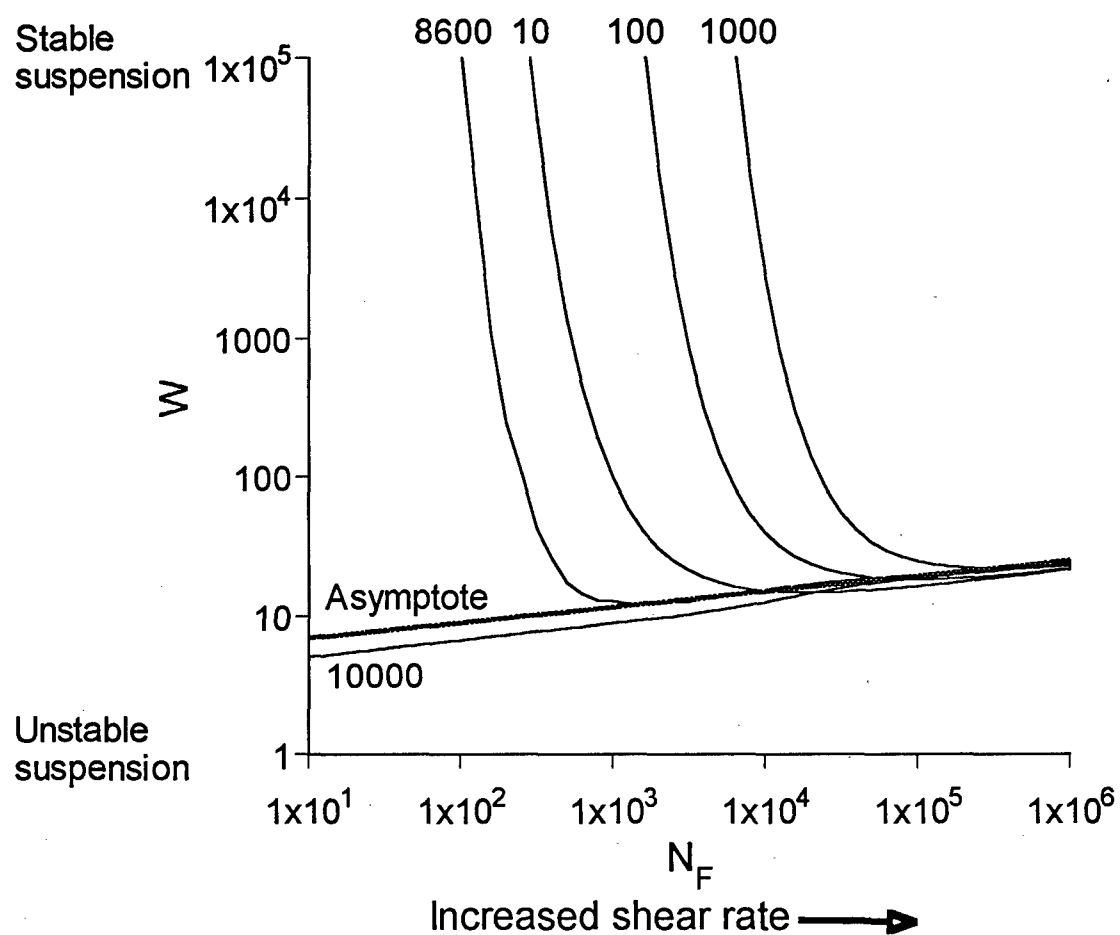
**Figure 3.10**: The stability factor, W, as a function of the shear rate parameter($N_F$). Labeled curves correspond to simulations run with $\kappa'$ varied between 10 and 10000. $N_L = 2000$, $\beta = 1$, $N_R = 6000$.

The behavior of W seen in Figure 3.9 is consistent with the current physical understanding of the repulsive force. The repulsive force generated by the double layer scales with $N_r\kappa'$ where $N_R$ characterizes the surface potential of the particles and $\kappa'$ is the inverse Debye length. For low values of $\kappa'$, the double layer is very diffuse so that the repulsive force barrier to primary flocculation is broad and weak. As $\kappa'$ continues to increase, the double layer thins and the barrier becomes higher. At still larger $\kappa'$ the double layer thickness approaches the London retardation wavelength ( $\kappa' \sim 1000$) and van der Waals attraction begins to overwhelm the electrical double layer repulsion. Because W depends on the exponential of the interparticle force, the narrow but high energy barriers lead to larger W; thus an increase in W is seen as the energy barrier sharpens until van der Waals attraction causes the magnitude of the energy barrier to decrease.

The effect of shear rate is shown in Figure 3.10 for $\kappa' = 10$, 100, 1000, 8600 and 10000. Also shown on the graph as a thick solid line is the asymptotic approximation given by Equation 3.52 that is valid for uncharged particles with large $N_F$. Figure 3.10 illustrates that increasing shear rate (increasing $N_F$) destabilizes the colloidal system and hence at high shear, W decreases to the value without double layer repulsion. The increased shear overcomes the repulsive energy barrier, allowing the particles to reach the primary particle minimum. Consider the curve labeled $\kappa' = 100$ which depicts the coagulation of 16 $\mu$m radius particles with a surface potential of -9.4 mV in a 0.03 M ionic strength solution. If the total strain is assumed to be 0.01 and the velocity gradient is equally

partitioned between the strain and rotation components of the flow (e.g., $S^2$ = $R^2$) then for shear rates above about 400 s$^{-1}$ ($N_F = 10^4$) double layer repulsion has been mitigated due to the high levels of shear.

Order of magnitude analysis is useful for estimating the critical $N_F$ at which the shear overcomes the repulsive barrier. Balancing the hydrodynamic flux with the flux due to the double layer repulsion at $\xi = 1/\kappa'$ yields: $N_F = N_R \kappa'/10$. This estimates the critical $N_F$ for the $\kappa' \leq 1000$ curves where colloidal stability increases to larger flow strengths as $\kappa'$ increases because the energy barrier becomes steeper. Beyond a $\kappa'$ of about 5000 the curves begin to shift left (see the $\kappa' = 8600$ curve in Figure 3.10) and approach the destabilized curve given by $\kappa' = 10000$. The system shown by the curve labeled $\kappa' = 8600$ acts like a destabilized system down to low $N_F$ compared to the $\kappa' = 1000$ result and as $N_F$ continues to decrease the suspension becomes highly stabilized. When $\kappa' = 8600$ the interparticle potential is on the margin between a stabilized and destabilized system and the addition of hydrodynamic interactions causes a transition from stable to unstable suspension depending on the value of $N_F$. This behavior can be understood by reconsidering the role of hydrodynamic interactions in determining the effective force, F. In Section 3.3 it was noted in conjunction with Figure 3.5 that hydrodynamic interactions can either augment or reduce the interparticle forces depending on the value of $N_f \xi$. If $N_f \xi < 1$ then viscous forces amplify the interparticle force and if $N_f \xi > 1$ the converse is true. The length scale at which double layer repulsion is significant, denoted as $\xi^{DL}$, is given by the Debye length ($1/\kappa'$), that is $\xi^{DL} \sim 10^{-4}$. For $N_F$ greater than about $10^4$ the effect of double

layer repulsion will be reduced. In Figure 3.10 it may be seen that for $N_F$ greater than about $10^3$ the $\kappa' = 8600$ curve is destabilized. Below this $N_F$ value the double layer repulsion is amplified by the hydrodynamic interactions and the stability factor increases.

The effects of colloid surface potential and shear rate are shown in Figures 3.11 and 3.12. In Figure 3.11 values of W are plotted against $N_R^{1/2}$ (which is proportional to the surface potential, $\psi$), while $\kappa' = 1000$, $\beta = 1$, and $N_L = 2000$. For low values of $N_R^{1/2}$ the stability factor is not influenced by electrostatic repulsion as evidenced by the horizontal lines; however, at a critical value of $N_R$ dependent on the value of $N_F$, double layer repulsion becomes significant and W increases rapidly. In Figure 3.12 the stability factor is shown as a function of $N_F$. In this figure a sharp transition is observed between stable and destabilized suspensions. Values of $N_F$ to the right of the transition have lower stability factors because the elevated shear rates at these higher $N_F$'s act to propel colliding particles over the repulsive energy barrier. The transition from unstable to stable suspensions shifts towards larger shear rates as the strength of the double layer repulsion increases. (Note that the possibility of floc break up at high shear has not been considered.) The minimum in W corresponds to the transition from a double layer repulsion dominated system to one dominated by viscous forces. The simple balance of viscous to double layer forces used to interpret Figure 3.9 and 3.10 describes the transition to a destabilized suspension as a function of $N_F$ and $N_R$.
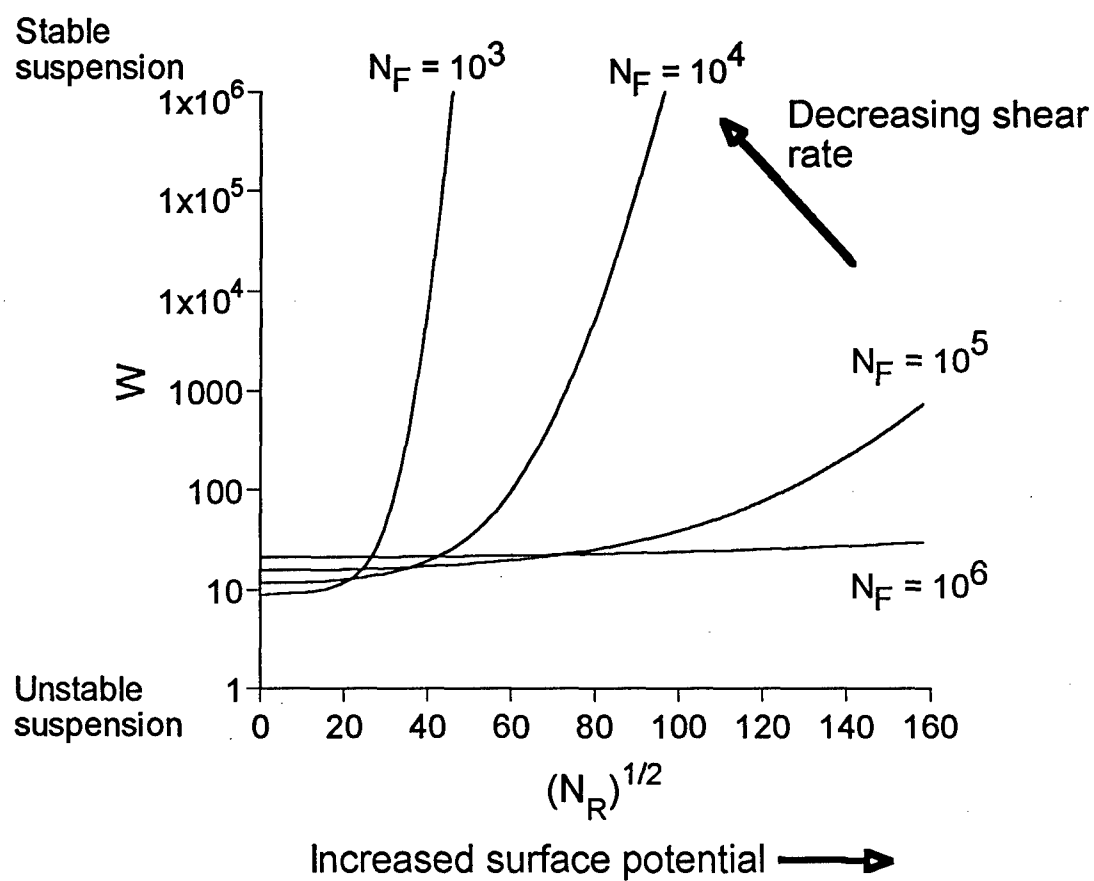
**Figure 3.11**: The effect of $N_R$ on W for various $N_F$ and $\beta = 1$, $N_L = 2000$ and $\kappa' = 1000$. The square root of $N_R$ is proportional to the surface potential of the coagulating particles. The numbers labeling the curves indicate different values of $N_F$.
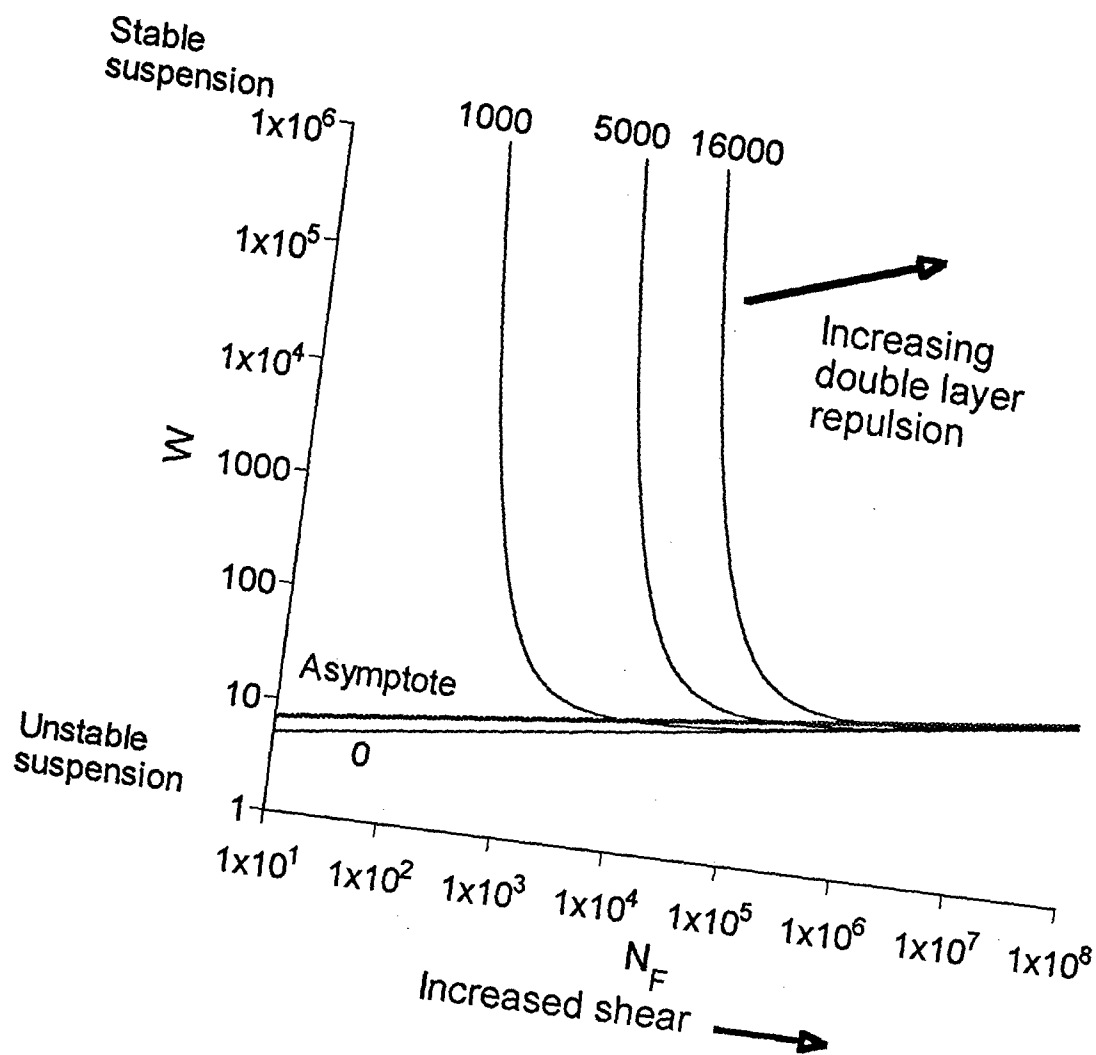
**Figure 3.12**: The consequence of varying shear rate, $N_F$, on the stability factor, $W$. The curves are labeled with the appropriate values of $N_R$. Integrations were done with $\beta = 1$, $N_L = 2000$ and $\kappa' = 1000$.
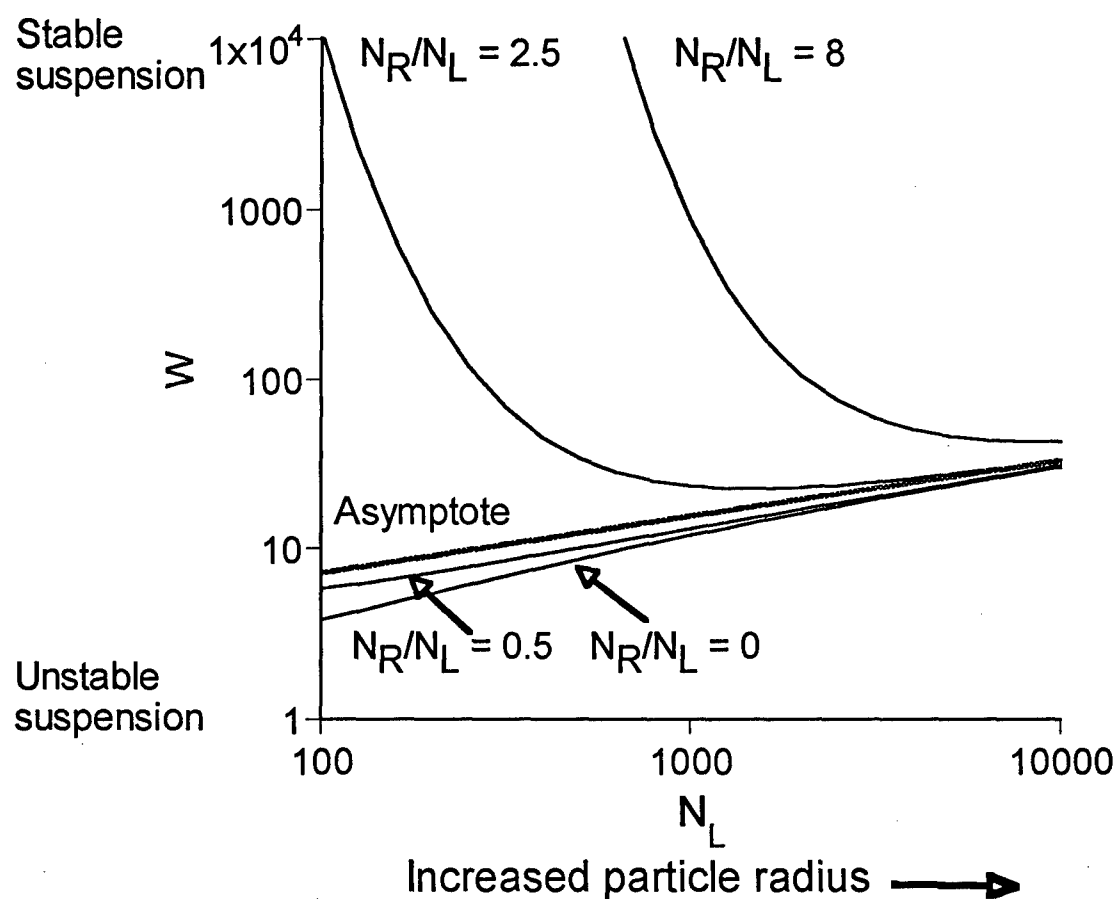
**Figure 3.13**: The effect of particle size, $N_L$, on colloidal stability, W, is shown for various values of the ratio of double layer repulsion to van der Waals attraction, $N_R$. The plot is for equal size particles when $N_F/N_L^3 = 1.25 \times 10^{-5}$ and $\kappa'/N_L = 0.5$. Labels on the curves designate the values of $N_R/N_L$ used.

The effect of particle size is illustrated in Figure 3.13 for various ratios of double layer repulsion to van der Waals attraction. In this figure $\kappa'/N_L = 0.5$, $N_F/N_L^3 = 1.25 \times 10^{-5}$, and $\beta = 1$ and the stability factor is plotted against $N_L$. $N_F$, $N_R$ and $\kappa'$ have been rescaled with the London retardation wavelength to remove the effect of particle radius from these parameters. Shown are curves depicting various values of $N_R/N_L$, the parameter that compares the importance of double layer repulsion to van der Waals attraction. Without electrostatic interactions and for large $N_L$, the suspension approaches the asymptotic limit described by Equation 3.52. The addition of double layer repulsion causes W to increase relative to the asymptotic limit reflecting the fact that larger $N_R$ means a higher energy barrier to coagulation. However, with increasing particle size the stability factor approaches the asymptote again. Particles with small diameters are strongly stabilized owing to the existence of a double layer whose thickness is comparable to the particle radius. With $\kappa'$ fixed and the particle radius increasing, double layer repulsion becomes unimportant compared to viscous stress imparted by increased lubrication forces.

The results in Figures 3.9 to 3.13 give the stability factor for flocculation into the primary minimum of the interparticle potential, corresponding to direct particle-particle contacts. However, a weak secondary minimum may sometimes arise at separations larger than that corresponding to the repulsive barrier. Without resorting to trajectory analysis, the determination of stable secondary flocculation is difficult to ascertain. The steady-state diffusion equation cannot account for the fact

that particles entering the secondary minimum may not remain because the minimum is too weak relative to the disrupting influence of fluid shear.

### 3.4.3 Comparison to coagulation in steady flows

It is interesting to compare the relative coagulation rates of colloidal particles in steady linear flows to coagulation rates in stochastic linear flows. As shown above (Section 3.3 and Figure 3.4) non-interacting particles aggregate more slowly in random linear flows in the diffusive limit than they do in steady linear flows with a comparable strain rate. In addition, the stability factor calculations presented here serve as a prototype for determination of colloidal stability in random flows and thus permit a contrast of the influence of interparticle interactions on colloid stability in random versus steady flows.

Computations of the stability factor in steady linear flows are prevalent (Greene et al., 1994; van de Ven & Mason, 1977; Zeichner & Schowater, 1977; Adler, 1977). Recently, Greene et al. (1994) calculated the stability factor for particles in a number of steady linear flows under the influence of hydrodynamic interactions and van der Waals attraction. Using trajectory analysis Greene et al. (1994) examined linear flows that contained more strain than vorticity and showed that the stability factor is nearly insensitive to flow type, *except* for flows near simple shear. Since the fluctuating velocity field considered in this manuscript could be viewed as an ensemble average over all possible linear flows, a simplistic hypothesis is to expect the stability factors obtained here to correspond to an ensemble average of the stability factors calculated in Greene et al.'s (1994) analysis. Yet, the above analysis has shown that when the flow field

can be treated using a diffusion formulation, hydrodynamic forces are more significant and there is a significant drift velocity that acts like an attractive force bringing the particles together; therefore, stability factors obtained when the diffusion approximation is valid are likely to be smaller than for steady flows with comparable shear rates.

For consistency in the comparison with Greene et al., calculations with the diffusion approximation are determined for the case of non-Brownian particles, negligible electrostatic double layer interactions, and using the non-retarded analytical expression for dispersion forces originally derived by Hamaker (see Davis, 1984 for the expression). Figure 3.14 compares the stability factor for the random flow and the stability coefficients obtained by Greene et al. (1994) for simple shear and hyperbolic extension (two dimensional extensional flow) as a function of $N_F$ for $N_L = 395$ (approximately 3 μm radius particles). Calculations of the stability factor for these two flows encompass the gamut of stability factor magnitudes expected for steady linear flows (Greene et al., 1994). The stability factor is shown plotted against $N_F/(S\tau_S)$ for two values of the total strain. The analysis in this manuscript is only valid for small total strain and the $S\tau_S = 1$ result shown in Figure 3.14 is mean to illustrate the limiting behavior as the total strain increases. Numerical simulations (given in Chapter 4) suggest that the pair probability formulation used in this chapter is valid for $S\tau_S < 0.1$. The stability factor for coagulation using the diffusion approximation, shown as the curves is comparable to both the simple shear and hyperbolic extension stability factors. The computed stability factors for the random linear flow increase with total strain and, as
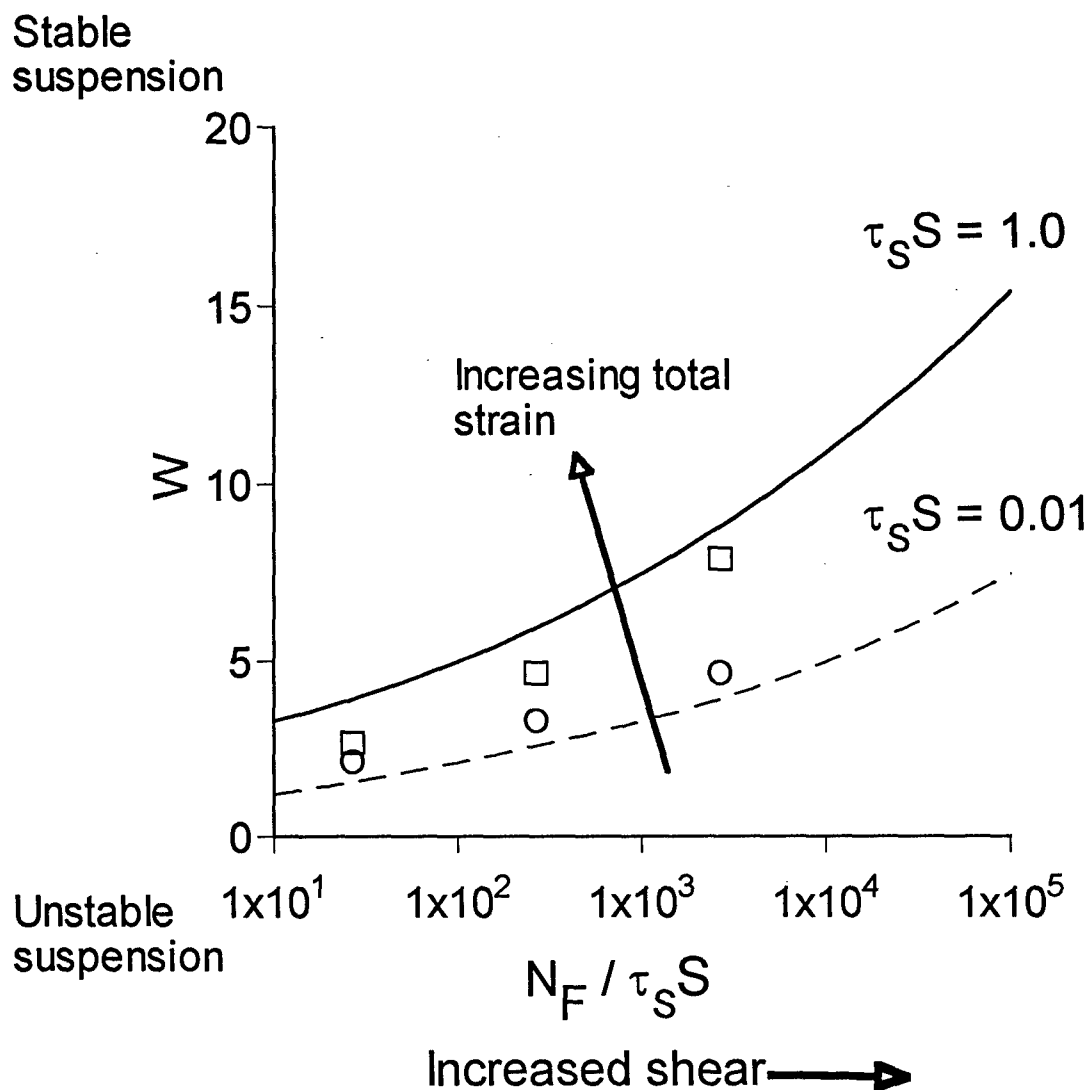
**Figure 3.14**: Comparison of the stability factor, W, obtained from the pair diffusion approximation (curves) with stability factors obtained for stationary simple shear and hyperbolic extension as a function of $N_F/S\tau_s$ (shear rate). Values are shown assuming equal-sized, non-Brownian colloids and a non-retarded van der Waals attraction without double layer repulsion. Trajectory analysis for simple shear (□) and uniaxial (two-dimensional) extension (O) are from Greene et al. (1994).

the flow becomes more diffusive, colloidal stability decreases. This behavior can be understood by comparing the interaction of two particles in a steady and unsteady linear flow. In the steady flow, the particle pair have one opportunity for collision before the steady flow separates the particles. In the diffusive limit, two approaching particles will experience multiple encounters before separating. The probability that one of these encounters will lead to a successful collision is large; thus, the stability of the flow decreases in the diffusion limit. This should not be interpreted to mean that the rate of coagulation will be faster in the limit of small total strain. Recall that the coagulation rate in the random linear flow is proportional to the total strain; thus, while the collisions are more efficient (i.e, a lower W), the overall rate decreases with decreases total strain.

Trajectory calculations by Zeichner and Schowalter (1977) show that W is proportional to $S^{0.23}$ in simple shear and $S^{0.11}$ in uniaxial extensional flow. Both the random flow considered in this thesis and the uniaxial extension have the same dependence on the shear rate. In the diffusion limit rotation of the fluid is unimportant, so the flow can be visualized simply as a fluctuating strain field. In both the random linear flow and the uniaxial extension all trajectories are open; therefore, Batchelor and Green's (1972b) analysis of the pair probability distribution in linear flows applies. Given that the pair probability does not depend on the flow time scales or flow type, W in the uniaxial extensional flow should have the same dependence on the shear rate as the random linear flow examined here. In simple shear, on the other hand, closed trajectories exist (Batchelor & Green, 1972b)[30]; thus, their work does not apply and power

law relation between shear rate and the stability factor would be expected to be different.

For the case when double layer forces are included, the calculations for the random linear flow are compared to work done by van de Ven & Mason for spherical particles with equal radii (van de Ven & Mason, 1977). Results of van de Ven & Mason(1977; their Figure 3.6) were converted to the non-dimensional scaling parameters used in this work. In Figure 3.15 the stability factor is plotted against $(N_R)^{1/2}$ for $N_F/(S\tau_S) = 508$, $N_L = 250$ and $\kappa' = 200$. Discontinuities in the results taken from van de Ven & Mason were present in the original figure. The light lines correspond to this author's calculations for total strains of 0.01 and 1. There is a strong dependence on the total strain with the small total strain results showing a transition to a stabilized suspension. As the total strain decreases the hydrodynamic flux decreases and double layer forces become more important (see the discussion for Figure 3.11). The comparison suggests that the transition from unstable to stable suspensions may occur at a lower surface potential in the randomly varying flow.

Stability factors computed for the random linear flow are comparable to calculations that have been previously obtained for steady linear flows (Greene et al., 1994; van de Ven & Mason, 1977; Zeichner & Schowalter, 1977; Adler, 1977). As the flow time scales decrease, the suspension stability decreases because two approaching particles have more opportunity for collision before the flow field separates the particles. At the same time, as the total strain decreases the strength of the flow decreases so the effects of double layer repulsion can be more significant
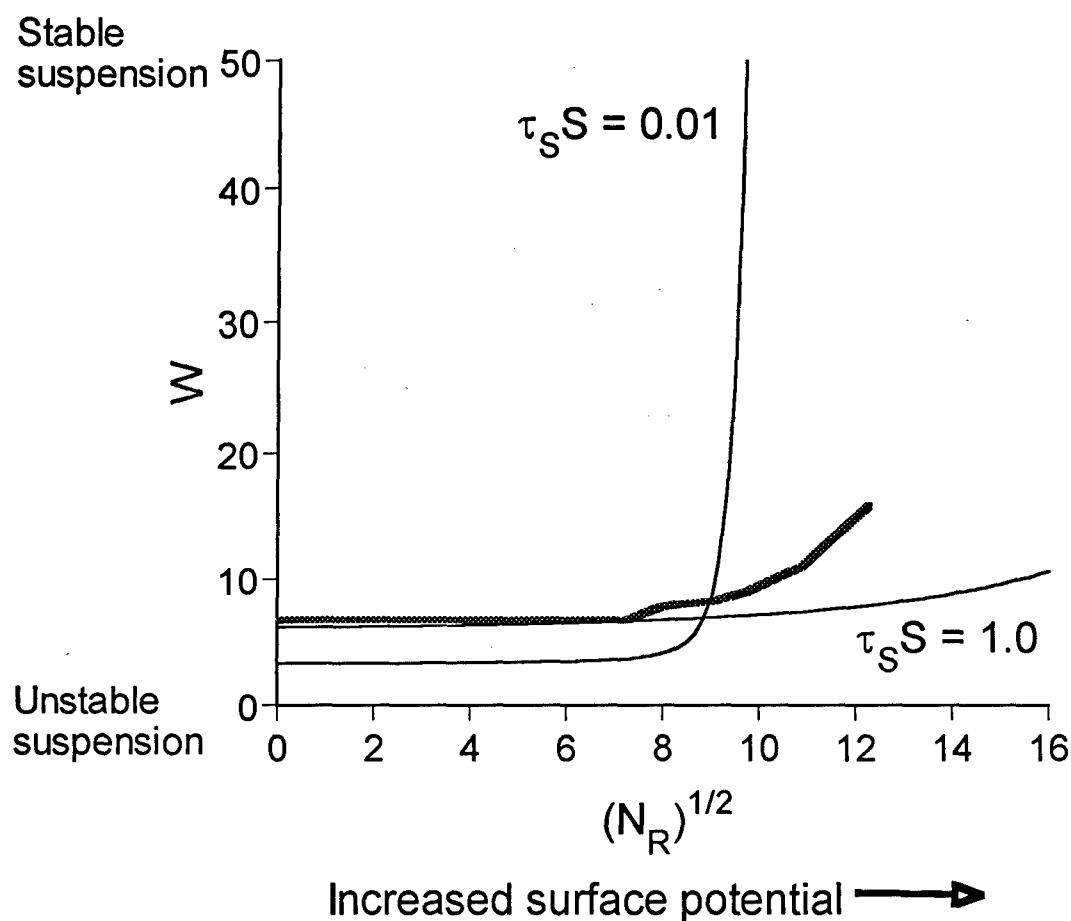
**Figure 3.15**: Comparison of the stability factor obtained from the pair diffusion approximation with stability factors obtained for stationary simple shear as a function of $N_R$ (strength of the double layer repulsion). Thin lines correspond to W values in the diffusive limit and the heavy line is taken from van de Ven & Mason (1977). Curves are labeled with values of the total strain. For this example $N_L = 250$, $\kappa' = 200$, $N_F/S\tau_S = 508$, and $\beta = 1$.

in the random linear flow. The transition from unstable to stable suspension occurs for a much lower surface potential in the diffusion limit.

## 3.5 Application to turbulent coagulation

The results obtained for coagulation in an isotropic, randomly varying linear flow field can be used to estimate the turbulent coagulation rate of particles that are small compared with the length scales of turbulence, i.e., smaller than the Kolmogorov scale. In this section results from direct numerical simulations of turbulence are used to calculate the diffusivity for a pair of particles with diameters smaller than the Kolmogorov scale. The analytical and numerical calculations of coagulation in the previous sections can then be used to assess colloidal stability in turbulent flows.

Before applying the results to the question of turbulent coagulation, a brief review is provided of the implications of Kolmogorov's similarity hypotheses (see Tennekes and Lumley, 1972). The tenets of the similarity hypotheses allow estimation of the velocity and length scales of the smallest turbulent eddies. By balancing the turbulent dissipation rate with the viscous dissipation rate the Kolmogorov scales are obtained: $\eta = (\nu^3/\epsilon)^{1/4}$, $V_\eta = (\epsilon\nu)^{1/4}$ and, $\Gamma_\eta = (\epsilon/\nu)^{1/2}$, where $\eta$, $V_\eta$ and $\Gamma_\eta$ are the Kolmogorov length, velocity and velocity gradient scales, respectively, while $\nu$ is the kinematic viscosity and $\epsilon$ is the turbulent dissipation rate. For particles smaller than $\eta$ only the Kolmogorov scale eddies are dynamically important for determining the rate of particle collision because they have the highest shear rates. Since turbulence at the Kolmogorov

scale is approximately isotropic, the results obtained in Sections 3.2-3.4 can be applied by choosing the characteristic velocity gradient, $\Gamma = \Gamma_\eta$ and setting the strain and rotation correlation times and magnitudes equal to values typical for homogeneous isotropic turbulence (e.g., $S^2 = R^2 = 1/2\Gamma_\eta^2$).

As a first step, estimates for the strain and rotation rate correlation time are obtained and used to assess the suitability of the diffusion approximation to turbulent coagulation. Pope and coworkers conducted direct numerical simulations (DNS) of homogeneous isotropic turbulence (Yeung & Pope, 1989; Girimaji & Pope, 1990; Pope, 1990) and calculated the Lagrangian strain and rotation rate correlation functions. Artificial forcing was used in their calculations to keep the turbulence simulation statistically stationary. The computer simulations provided statistics on the two-time Lagrangian velocity gradient autocorrelation function over Taylor-scale Reynolds numbers, $R_\lambda$, ranging from 38 to 93 where $R_\lambda = u\lambda/v$, $\lambda = \left(u^2/(\partial u_1/\partial x_1)^2\right)^{1/2}$ is the Taylor scale, u is the integral velocity, $u_1$ is the velocity in the $x_1$, direction and v is the kinematic viscosity. At all Reynolds numbers Pope (1990) found that, while the correlation time of the strain amplitude scales with the integral time scale, the directional component of the strain rate is correlated over times that scale with the Kolmogorov time. He noted that this rapid loss of directional correlation disproves the persistence of strain hypothesis that has been used as a modeling framework for conceptualizing relative particle diffusion and mixing at the small scales of turbulence. According to the persistence of strain hypothesis, originally proposed by Townsend

(1951), the local Lagrangian strain rate changes little over the Kolmogorov time scale (Pope, 1990). In the context of particle aggregation, the persistent strain hypothesis is tantamount to assuming the turbulent velocity field is static during a collision event.

Non-linear regression of Girimaji & Pope's data leads to the conclusion that, in turbulence, the strain and rotation rate correlation functions decay exponentially, like:

$$<S_{ik}(0)\, S_{jl}(t)> \ = \ S_{ikjl}\exp\left(-\frac{t}{\tau_s}\right) \tag{3.53}$$

where an analogous expression can be written for the rotation rate correlation time by replacing all S's with R's. The exponential form fit the strain rate data with an $r^2 = 99.6\%$ and by numerically integrating the autocorrelation data of Girimaji and Pope (1990) an estimate of $\tau_s \approx 2.3/\Gamma_\eta$ is obtained. Similarly, an $r^2 = 95\%$ is obtained when fitting the rotation rate autocorrelation data to the exponential form shown in Equation 3.34 and a value of $\tau_R \approx 7.2/\Gamma_\eta$ is estimated for the rotation rate correlation time.

### 3.5.1 Turbulent pair diffusivity and coagulation rate

It is important to remember that the total strain in turbulence is order one compared with the time scale of the fluid motion. Yet, most previous attempts at modeling the turbulent coagulation rate (Delichatsio & Probstein, 1973; Camp & Stein, 1943; Saffman & Turner, 1956) have been based upon the persistence of strain limit so they are asymptotically valid when the product of the Kolmogorov shear rate and its correlation time are large.

In contrast, the pair diffusion model for coagulation outlined in Section 3.3 is valid in the small strain limit. From the definition of the turbulent dissipation rate (e.g., $\Gamma^2 = 2S^2 = 2R^2$) and the estimated values for the strain and rotation rate correlation times taken from Girimaji & Pope's DNS results, an expression for the turbulent pair diffusion coefficient can be obtained using Equation 3.19. For comparison, Lundgren derived an equation for the turbulent pair diffusivity in the absence of hydrodynamic interactions by expressing the pair diffusivity as an integral over the two-point Lagrangian velocity autocorrelation function (Lundgren, 1981). He then rewrote the turbulent diffusivity in terms of the two-point single-time Eulerian velocity correlation function using approximations that he argued were valid in the limit of short and long time differences. For statistically stationary homogeneous isotropic turbulence, Lundgren arrived at the following form for the pair diffusivity at the Kolmogorov scale:

$$D_{ij}^t = \frac{r^2 \Gamma_\eta}{3\sqrt{5}} \left[ \frac{r_i r_j}{r^2} + 2\left( \delta_{ij} - \frac{r_i r_j}{r^2} \right) \right] \qquad (3.54)$$

Note that the diffusivity in Equation 3.54 is twice that shown in Lundgren's original paper because of a difference in the definitions of the pair diffusivity. Using Equation 3.17 and the estimates from DNS a value of 0.153 is found for the radial component of the turbulent diffusivity. By contrast Lundgren estimates the value to be 0.149, about 3% smaller than the result obtained here and well within the error of the numerical integration of Girimaji and Pope's (1990) DNS data. The analysis of the

pair diffusivity in turbulence presented in this chapter shows that the circumferential diffusivity depends on both the rotation and strain rate correlation time scales. Lundgren's prediction for the circumferential component underestimates the angular component of the pair diffusion coefficient by a factor of 20 which suggests that the prior analysis did not correctly consider the effect of rotation on the diffusion coefficient.

The rate of turbulent coagulation is obtained by substituting the values for the strain and rotation rate correlation times into Equations 3.35 and 3.47. For non-interacting particles:

$$\frac{dC_{12}^{\infty}}{dt} = \frac{9.2\,\pi}{5}\,\sigma^3 \Gamma_{\eta} C_1^{\infty} C_2^{\infty} \qquad (3.55)$$

The derivation of the turbulent coagulation rate constant using the diffusion approximation was first carried out by Levich (1962). In his analysis, Kolmogorov's similarity hypothesis was used to deduce that the turbulent pair diffusivity was proportional to $r^2$. The estimated turbulent diffusivity was then used in a steady-state radial diffusion equation to obtain a form similar to Equation 3.55, but Levich did not provide an estimate for the numerical coefficient or examine the limits of applicability of the model.

Saffman and Turner (1956) represented the turbulent velocity field as a stationary, locally linear flow taken to be extensional. By considering the turbulence to be steady over a coagulation event, Saffman & Turner

restrict their analysis to the large total strain limit — the opposite limit to that considered in this manuscript. Assuming homogeneous, isotropic turbulence and Gaussian statistics for the fluctuating velocity gradient, Saffman and Turner (1956) derived the aggregation rate between two particles with radii of $a_1$ and $a_2$:

$$\frac{dC_{1,2}}{dt} = \left(\frac{8\pi}{15}\right)^{1/2} \Gamma_\eta \sigma^3 C_1^\infty C_2^\infty \qquad (3.56)$$

This prediction for the coagulation rate in the absence of interparticle forces is similar in form to that obtained in the small strain limit (Equation 3.55) except that the numerical coefficient is about 4.5 times smaller.

To the author's knowledge, no attempt has been made to determine the effects of hydrodynamic interactions and interparticle forces on turbulent coagulation. Typically, researchers assume that the stability factors obtained from trajectory analyses under laminar conditions of simple shear adequately represent the effects of interparticle interactions in turbulent aggregation (see for example, Valioulis et al., 1984). As shown above while colloidal stability in a fluctuating velocity field is similar to that obtained in simple shear, W increases with $N_F$ at a slower rate in the random flow. Rates of aggregation can also be significantly smaller in random flows because of the dependence on the total strain. Thus, the use of simple shear as a surrogate for the turbulent flow field in the dissipation subrange could lead to significant errors.

3.6 <u>Summary and conclusions</u>

In this chapter an analysis is presented of hydrodynamic pair diffusion and coagulation in a randomly varying isotropic flow field. The velocity field is specified to be statistically stationary in time and a linear function of position at separations comparable to the particle radius. The strain and rotation rate components of the velocity gradient field are allowed to fluctuate with different correlation times and the analysis is restricted to flows with small strain amplitude where a pair diffusion formulation can be used. The radial diffusivity is shown to depend exclusively upon the rate of strain while the circumferential pair diffusivity is a function of both the strain and rotation rates. Using a radial pair probability conservation equation an analytical expression is derived for the coagulation rate in the absence of interparticle interactions and Brownian motion. Interparticle forces, hydrodynamic interactions and Brownian motion are included by calculating a stability factor, $W$, that is the ratio of coagulation rate for non-interacting particles to that with interparticle forces, hydrodynamic interactions and Brownian motion. The stability factor can be calculated numerically from a two-dimensional quadrature. An asymptotic solution valid in the lubrication regime is presented for non-Brownian particles that are influenced by hydrodynamic interactions and non-retarded van der Waals forces.

The effect of retarded van der Waals attraction, double layer repulsion and hydrodynamic interactions was examined by varying the six non-dimensional parameters that fully characterize the aggregating system. In general, increasing particle size and shear rate in the absence of double

layer interactions leads to increased colloidal stability. Increasing the solution ionic strength (decreasing the double layer thickness) leads to an abrupt decrease in the stability factor beyond which double layer repulsion becomes negligible. Increasing shear causes a decrease in the stability factor for the systems with significant double layer repulsion because the higher shear rates allow the colliding particles to surmount the repulsive energy barrier. The effect of surface potential at constant Debye length was also examined. Again, increases in shear rate caused a commensurate decrease in W. Finally, particles that are small compared to the double layer thickness are shown to be very stable.

Numerical studies of coagulation between non-interacting particles in strongly mixed chaotic laminar flows indicate that coagulation rates in chaotic flows are a monotonically increasing function of total strain. In the small strain limit, when the fluctuating velocity field can be represented by a pair diffusivity, the coagulation rates for non-interacting particles are shown here to be proportional to the total strain. Compared to steady linear flows with comparable shear rate, coagulation in the diffusive limit for a random linear flow field is considerably slower. The stability factor calculations obtained for coagulation in a randomly varying linear velocity field are compared with those obtained for stationary linear flows (Green et al., 1994; van de Ven & Mason, 1977; Zeichner & Schowalter, 1977; Adler, 1984) and the stability coefficients in both simple shear and hyperbolic extensional flow are found to be similar to those for the random flow.

The coagulation rate expression was applied to aggregation in turbulent flows. The diffusion approximation to turbulent coagulation is valid in the limit where the characteristic time for two particles to collide is large compared with the flow evolution time (small total strain limit). In contrast, the turbulent coagulation theory developed by Saffman and Turner (1956) applies to the opposite limit when the particle collision time is short compared with the velocity field correlation time. DNS of turbulence computed by Pope and coworkers show that the time scale of the turbulent velocity gradient is between these two limits (Yeung & Pope, 1989; Girimaji & Pope, 1990; Pope, 1990), suggesting that the actual coagulation rate may be intermediate between the predictions given in this chapter and that of Saffman and Turner (1956).

# REFERENCES

ADLER, P. M.  1981 Heterocoagulation in shear flow. *J. Coll. Int. Sci.* **83**, 106-115.

APPIAH, A. & O'MELIA, C. R.  1990 Coagulation processes: destabilization, mixing and flocculation. In *Water Quality and Treatment*, 4th ed. (ed. F.W. Pontius). McGraw-Hill.

O'MELIA, C. R.  1980 Aquasols: the behavior of small particles in aquatic systems. *Env. Sci. Tech.* **14**, 1052-1060.

BATCHELOR, G. K. & GREEN, J. T.  1972a The hydrodynamic interaction of two small freely-moving spheres in a linear flow field. *J. Fluid Mech.* **56**, 375-400.

BATCHELOR, G. K. & GREEN, J. T.  1972b The determination of the bulk stress in a suspension of spherical particles to order $c^2$. *J. Fluid Mech.* **56**, 401-427.

BATCHELOR, G. K.  1976 Brownian diffusion of particles with hydrodynamic interaction. *J. Fluid Mech.* **74**, 1-29.

BATCHELOR, G. K.  1977 The effect of Brownian motion on the bulk stress in a suspension of spherical particles. *J. Fluid Mech.* **83**, 97-117.

BIDKAR, U. R. & KHAKHAR, D. V.  1990 Collision rates in chaotic flows: dilute suspensions. *Phys. Rev. A* **42**, 5964-5969.

CAMP, T. R. & STEIN, P. C.  1943 Velocity gradients and internal work in fluid motion. *J. Bost. Soc. Civil. Eng.* **30**, 219-237.

DANIELSON, T. J., MUZZIO, F. J. & OTTINO, J. M.  1991 Aggregation and structure formation in chaotic and regular flows. *Phys. Rev. Let.* **66**, 3128-3131.

DAVIS, R. H.  1984 The rate of coagulation of a dilute polydisperse system of sedimenting spheres. *J. Fluid Mech.* **145**, 179-199.

DELICHATSIOS, M. A. & PROBSTEIN, R. F.  1973 Coagulation in turbulent flow: theory and experiment. *J. Coll. Int. Sci.* **51**, 394-405.

FEKE, D. L. & SCHOWALTER, W. R.  1985 The influence of Brownian diffusion on binary flow-induced collision rates in colloidal dispersions. *J. Coll. Int. Sci.* **106**, 203-214.

FEKE, D. L. & SCHOWALTER, W. R.  1983 The effect of Brownian diffusion on shear-induced coagulation of colloidal dispersions. *J. Fluid Mech.* **133**, 17-35.

GIRIMAJI, S. S. & POPE, S. B.  1990 A diffusion model for velocity gradients in turbulence. *Phys. Fluids A* **2**, 242-256.

GREENE, M. R., HAMMER, D. A. & OLBRICHT, W. L.  1994 The effect of hydrodynamic flow field on colloidal stability. *J. Coll. Int. Sci.* **167**, 232-246.

ISRAELACHVILI, J.  1992 *Intermolecular and surface forces*, 2nd Ed. Academic Press.

JHON, M. S., SEKHON, G. & ARMSTRONG, R.  1987 The response of polymer molecules in a flow. In *Advances in Chemical Physics* (ed. I. Prigogine & S.A. Rice).  Wiley.

KIM, S. & KARRILA, S. J.  1991 *Microhydrodynamics: principles and selected applications*.  Butterworth-Heinemann.

KOCH, D. L. & SHAQFEH, E. S. G.  1991  Screening in sedimenting suspensions. *J. Fluid Mech.* **224**, 275-303.

LEVICH, V. G.  1962 *Physicochemical Hydrodynamics*.  Prentice-Hall.

LUNDGREN, T. S. 1981 Turbulent pair dispersion and scalar diffusion. *J. Fluid Mech.* **111**, 27-57.

MUZZIO, F. J. & OTTINO, J. M. 1988 Coagulation in chaotic flows. *Phys. Rev. A* **38**, 2516-2524.

OTTINO, J. M., MUZZIO, F. J., TJAHJADI, M., FRANJIONE, J. G., JANA, S. C. AND KUSCH, H. A. 1992 Chaos, symmetry and self-similarity: exploiting order and disorder in mixing processes. *Science* **257**, 754-760.

OTTINO, J. M. 1991 Unity and diversity in mixing: stretching, diffusion, breakup, and aggregation in chaotic flows. *Phys. Fluids A* **3**, 1417-1430.

POPE, S. B. 1985 PDF methods for turbulent reactive flows. *Prog. Energy Combust. Sci.* **11**, 119-192.

POPE, S. B. 1990 Lagrangian microscales in turbulence. *Phil. Trans. R. Soc. Lond. A* **333**, 309-319.

PRESS, W. H., TEUKOLSKY, S.A., VETTERLING, W.T. & FLANNERY, B.P. 1992 *Numerical Recipes in C.* Cambridge Univ. Press.

RUSSEL,W. B., SAVILLE, D.A. & SCHOWALTER, W.R. 1989 *Colloidal Dispersions.* Cambridge U. P.

SAFFMAN, P. G. & TURNER, J.S. 1956 On the collision of drops in turbulent clouds. *J. Fluid Mech.* **1**, 16-30.

SCHENKEL, J. H. & KITCHENER, J.A. 1960 A test of Derjaguin-Verwey-Overbeek theory with a colloidal suspension. *Trans. Faraday Soc.* **56**, 161-173.

SHAQFEH, E. S. G. & KOCH, D. L. 1988 The effect of hydrodynamic interactions on the orientation of axisymmetric particles flowing through a fixed bed of spheres or fibers. *Phys. Fluids* **31**, 728-743.

SHAQFEH, E. S. G. & KOCH, D.L. 1992 Polymer stretch in dilute fixed beds of fibers or spheres. *J. Fluid Mech.* **244**, 17-54.

SMOLUCHOWSKI, M. 1917 Versuch Einer Mathematischen Theorie der Koagulations - Kinetik Kolloider Losungen. *Z. Physik. Chem.* **92**, 129.

SPIELMAN, L. A. 1970 Viscous interactions in Brownian coagulation. *J. Coll. Int. Sci.* **33**, 562-571.

TENNEKES, H. & LUMLEY, J. L. 1972 *A first course in turbulence.* MIT Press.

TOWNSEND, A. A. 1951 The diffusion of heat spots in isotropic turbulence. *Proc. R. Soc. Lond. A* **209**, 418-430.

VALIOULIS, I. A., LIST, E. J. & PEARSON, H. J. 1984 Monte Carlo simulation of coagulation in discrete particle-size distributions. Part 2. Interparticle forces and the quasi-stationary equilibrium hypothesis. *J. Fluid Mech.* **143**, 387-411.

VALIOULIS, I. A. & LIST, E. J. 1984 Collision efficiencies of diffusing spherical particles: hydrodynamic, van der Waals and electrostatic forces. *Adv. Coll. Int. Sci.* **20**, 1-20.

VAN DE VEN, T. G. M. & MASON, S. G. 1977 The microrheology of colloidal dispersions VII. Orthokinetic doublet formation of spheres. *Coll. Poly. Sci.* **255**, 468-479.

YEUNG, P. K. & POPE, S. B. 1989 Lagrangian statistics from direct numerical simulations of isotropic turbulence. *J. Fluid Mech.* **207**, 531-586.

ZEICHNER, G. R. & SCHOWALTER, W. R. 1977 Use of trajectory analysis to study stability of colloidal dispersions in flow fields. *AIChE J.* **23**, 243-254.

# CHAPTER 4:

# TURBULENT COAGULATION OF COLLOIDAL PARTICLES[*]

## 4.1 Introduction

Turbulent-shear-induced coagulation is an important process leading to the aggregation of colloidal particles in both engineered and natural environmental processes. Turbulent mixing is heavily employed in water treatment and the chemical industries to enhance the aggregation and removal of fine particles. In natural aquatic systems many pollutants associate strongly with particles and therefore considerable effort has been focused on understanding the dynamics of particles in natural environments (O'Melia, 1980).

Estuaries serve as an excellent example of natural systems in which particle aggregation due to turbulence controls contaminant transport. Polluted suspended sediment in river water mixes with sea water in the estuary resulting in destablization and the subsequent aggregation of colloidal particles. Large contaminated agglomerates form that can readily settle through the water column and deposit onto the estuarine sediments (Stumm & Morgan, 1981).

Given typical estuarine conditions, with turbulent dissipation rates ranging from 0.002 to 0.7 $cm^2/s^3$ (Krone, 1970) and colloidal particles with

---

radii between 0.5 and 10 μm and a density of 2.0 g/cm³ (McCave, 1984), scaling analysis incorporating coagulation rate constants summarized by Pearson el al. (1984) can be used to ascertain the relative importance of the various coagulation mechanisms. For 5 μm particles, coagulation rates resulting from Brownian motion are estimated to be 14 to 2000 times slower than turbulent shear coagulation for turbulent energy dissipation rates between 0.002 to 0.7 cm²/s³ , respectively.

Turbulent coagulation also dominates over differential-settling-induced coagulation when 5 μm particles with a density of 2.0 g/cm³ aggregate with particles ranging from 4.4 to 5.7 μm at low turbulence levels and 2.5 to 8.4 μm particles at high turbulence levels. Furthermore, the importance of differential settling decreases with decreasing density difference between the fluid and the particles.

Turbulent acceleration can increase the coagulation rate of particles due to differences in particle inertia. From the work of Saffman & Turner (1956), the ratio of coagulation due to shear and particle inertia in a turbulent flow can be calculated as a function of the particle relaxation time (i.e., the time it takes an initially stationary particle to accelerate to the fluid velocity), the relative density difference between the bulk fluid and the particle and the turbulent dissipation rate. Again, when the parameter estimates typical for estuarine conditions are used, turbulent shear coagulation is calculated to dominate for similarly sized particles. At low turbulence levels, the transition from turbulent shear to inertia dominated collisions occurs for 5 μm particles interacting with particles less than 3.8 μm and greater than 6.2 μm. Since the importance of particle inertia

decreases with the density difference between the particle and the fluid, inertia driven coagulation is expected to be less important for more neutrally buoyant, organic-based colloidal particles.

In general, scaling analysis suggests that coagulation caused by turbulent shear is likely to control the aggregation process in estuaries for like-sized colloids, neutrally bouyant particles with radii greater than one micron.

Despite the importance of turbulent coagulation, only a limited number of theoretical analyses have been attempted and very little experimental work has been done to assess the applicability of existing turbulent coagulation models. In this chapter the issue of analytical model validity is addressed by performing computer simulations of turbulent shear coagulation. The relative trajectory of particle pairs in isotropic turbulence is analyzed using velocity gradient statistics taken from direct numerical simulations of turbulence (DNS; Girimaji & Pope, 1990). Results from the simulations are compared with models for turbulent coagulation that are found in the literature (i.e., Saffman & Turner, 1956; Chapter 3; Brunk et al., 1997a).

Although several heuristic models for turbulent coagulation have been proposed (Delichatsios & Probstein, 1975; Camp & Stein, 1943; Casson & Lawler, 1990), the discussion presented here will focus on models that attempt to represent the physics of turbulent coagulation. The model developed by Saffman & Turner (1956) yields an expression for the turbulent aggregation rate that is valid in the limit of persistent strain where the product of the characteristic strain rate and its correlation time (i.e., the

total strain) is large. The author has recently investigated the opposite limit where turbulent transport of coagulating particles can be likened to a pair diffusion process (Chapter 3; Brunk et al., 1997a). Evidence from DNS (Pope, 1990; Girimaji & Pope, 1990) suggests that the strain rate field for isotropic turbulence is intermediate between these two limits. In the intermediate regime, analytical expressions for the turbulent coagulation rate are unattainable; thus, a computer algorithm is used to simulate the coagulation of particles that are smaller than the length scales of turbulence.

Figure 4.1 shows the standard coagulation problem where calculation of the collision rate between monodisperse particles is of interest. The coordinate system is placed in a Lagrangian reference frame that moves with a test particle and relative position vectors connect the centers of the test sphere and nearby particles. In this description, the system is assumed to be sufficiently dilute such that only binary (1:1) interactions occur. The coagulation rate is obtained by calculating the number of two-particle collisions that occur between the representative test particle at the origin of the coordinate system and other colloids. Doublet formation is assumed to be irreversible so that the probability density for pairs of free particles (P) approaches zero at the excluded volume surface: $r = \sigma = 2a$. At large distances from the test sphere ($r \to \infty$), the pair probability of monodisperse particles attains its bulk value, $P = C_1^2$, where $C_1$ is the bulk concentration of singlet particles in the system.

Given the assumption of negligible doublet breakup, the initial rate of doublet formation in a dilute suspension is:
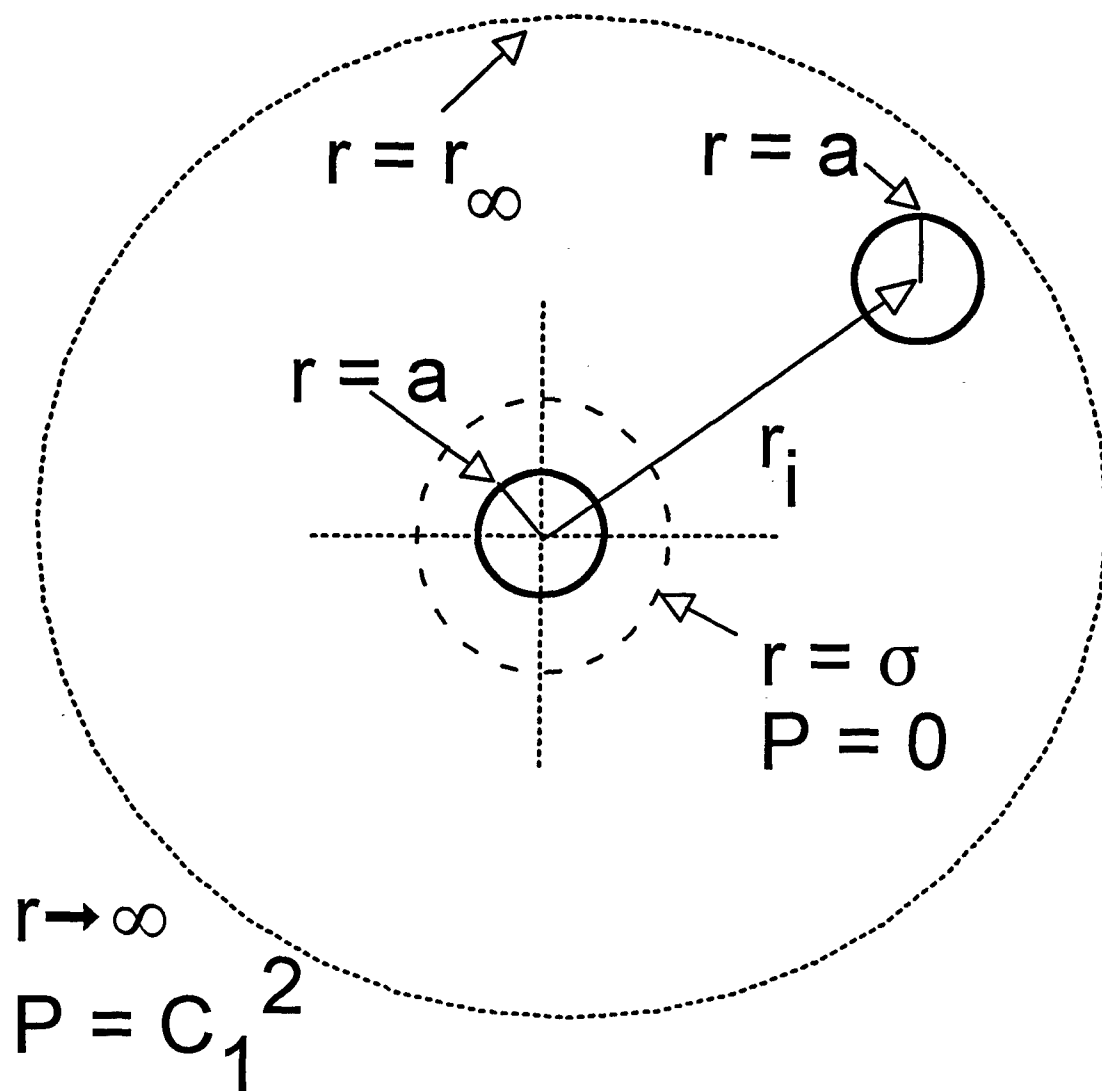
**Figure 4.1**: Schematic illustrating the coordinate system and boundary conditions for turbulent coagulation. Two particles with radii a are separated by a distance r. Far from the test sphere, $r \to r_\infty$ the pair probability for the particles reaches its bulk value, $C_1^2$ and upon reaching the collision radius, $r = \sigma = 2a$ the pair probability of singlet particles is zero.

$$\frac{dC_2}{dt} = kC_1^2 \tag{4.1}$$

where k is the coagulation kernel or coagulation rate constant and $C_2$ is the bulk concentration of doublet particles. The rate expression given by Equation 4.1 assumes there are no particle sources in the system. A consequence of the assumption that the suspension is dilute is that $C_2$ and $C_1$ are independent of position on length scales greater than the particle radius. That is, the time between collisions is much longer than the local mixing time so that local fluctuations in the bulk particle concentration can be neglected.

For the model simulations that follow, particle diameters are assumed to be smaller than the Kolmogorov length scale (i.e., the length scales of the smallest turbulent eddies), but large enough so the Peclet number is large and Brownian motion can be ignored. Since the smallest scales of turbulence have the highest shear rates (Tennekes & Lumley, 1972), they will dominate the coagulation process. The size and shear rate of the smallest turbulent eddies is estimated by balancing the turbulent energy flux from large to small eddies with viscous dissipation. Characterizing the energy flux with the turbulent dissipation rate, $\epsilon$, and the viscous dissipation with the kinematic viscosity, $v$, leads to the Kolmogorov estimates for eddy length and velocity gradient:

$$\eta = \left(\frac{v^3}{\epsilon}\right)^{1/4} \tag{4.2}$$

$$\Gamma_\eta = \left(\frac{\epsilon}{\nu}\right)^{1/2} \qquad (4.3)$$

where $\eta$ is the Kolmogorov length scale and $\Gamma_\eta$ is the Kolmogorov velocity gradient.

In natural aquatic environments, such as an estuary, typical Kolmogorov length scales vary from 1.5 mm to 350 μm (Krone, 1970), while turbulence produced in flocculation tanks used for wastewater treatment might have Kolmogorov lengths as small as 30 μm (O'Melia, 1980). The stipulation that the particles be smaller than the length scales of turbulence is, therefore, applicable to all but the most intense turbulent flows and the largest colloidal particles.

Recently Sundaram & Collins (1996) investigated coagulation of finite-volume particles using DNS. Their calculations were restricted to non-interacting particles with appreciable inertia (e.g., heavy particles suspended in a gas phase). DNS revealed that inertia causes particles whose density is greater than that of the fluid to accumulate in regions of high local strain and low vorticity (Squires & Eaton, 1991; Wang & Maxey, 1993). The extent of preferential accumulation depends on the value of the Stokes number (St), which is a ratio of the particle response time, ($2\rho a^2/9\mu$, where $\rho$ is the particle density and $\mu$ is the fluid viscosity) to the fluid time scale (L/u' where L and u' are the integral length and velocity scale of turbulence, respectively) (Squires & Eaton, 1991). Inertia is important at intermediate values of St, while at large Stokes numbers the

particles are so heavy they are unresponsive to the turbulent flow field.
When St $\rightarrow$ 0 the particles have no inertia and they follow the fluid motion
(Squires & Eaton, 1991). The calculations of Squires & Eaton (1991) and
Sundaram & Collins (1996) are primarily concerned with particles
suspended in air where Stokes numbers are large. In contrast, this research
focuses on computing the coagulation rate for aqueous colloidal
suspensions with no appreciable buoyancy. To the author's knowledge,
the limit of low particle inertia has not been investigated by DNS;
therefore, it remains impossible to determine the range of St over which the
well mixed assumption used in this thesis applies. For particles smaller
than the Kolmogorov length scale, the Stokes number based on the
Kolmogorov time scale ($St_\eta$) would control particle segregation. Assuming
neutrally buoyant particles, $St_\eta \approx \Gamma_\eta a^2/\nu$, which is the Reynolds number
based on the particle size and the Kolmogorov shear rate. For particle
sizes less than 10% of $\eta$, $St_\eta < 0.01$ suggesting that particle inertia can be
neglected and the particles can be assumed to be distributed
homogeneously throughout the turbulent flow.

The coagulation kernel, k, given in Equation 4.1, accounts for the
various transport mechanisms leading to particle collision (e.g., turbulent
shear, Brownian motion and differential settling), and the influence of
interparticle interactions such as van der Waals attraction, hydrodynamic
interactions and electrostatic double layer repulsion. Transport
mechanisms and interparticle interactions are usually separated by writing
the coagulation kernel as the quotient of an ideal rate constant, $k^0$, that
ignores interparticle forces and hydrodynamic interactions and a stability

factor, W, that incorporates the effects of these interactions (Russel et al., 1989):

$$k = \frac{k^0}{W} \tag{4.4}$$

Equivalently, the rate constant can be described in terms of a collision efficiency, $\alpha = W^{-1}$, expressing the fraction of ideal collisions that actually would occur when interparticle interactions are included.

Asymptotic expressions for $k^0$ in turbulence have been obtained in the large and small total strain limits. Assuming the product of the characteristic strain rate and its correlation time are large, Saffman & Turner (1956) derive the coagulation rate constant of non-interacting particles in stationary, homogeneous, isotropic turbulence. In the neighborhood of a test particle, they propose that the local turbulent velocity field can be represented as a pseudo-steady linear extensional flow. The particle collision rate is then written as a flux integral over the excluded volume surface area and is simplified by assuming isotropic and Gaussian velocity gradient statistics. The resulting average coagulation rate constant in the large strain limit is:

$$k^0 = \left( \frac{8\pi}{15} \right)^{1/2} \Gamma_\eta \sigma^3 \tag{4.5}$$

In Chapter 3 of this thesis, the author extended the analysis of Levich (1962) and calculated the coagulation rate in the limit of small strain with and without particle interactions (Chapter 3; Brunk et al.,

1997a). At small total strain, net particle movement is the result of many uncorrelated velocity field fluctuations; therefore, relative particle movement can be characterized with a pair diffusivity. This analysis is restricted to small gap widths where the flow field is a randomly varying isotropic linear flow with Gaussian statistics and separate rotational and extensional correlation times. The turbulent coagulation rate constant is found by solving a steady-state pair probability equation for the flux of particles diffusing toward a test sphere (Chapter 3; Brunk et al., 1997a). In the absence of particle interactions:

$$k^0 = \frac{4\pi}{5}(\Gamma_\eta \tau_S)\Gamma_\eta \sigma^3 \qquad (4.6)$$

This prediction has a functional form similar to the large strain limit determined by Saffman & Turner, Equation 4.5, except for the additional dependence on the total strain, $\Gamma_\eta \tau_S$. It can be further shown that the effects of finite Peclet number, hydrodynamic interactions, and interparticle forces may be easily included at the small strain limit (Chapter 3; Brunk et al., 1997a).

Evidence from DNS suggests that the total strain in isotropic turbulence is order one. Using DNS, Pope and coworkers (Pope, 1990; Girimaji & Pope, 1990; Yeung & Pope, 1989) investigated one-point, two-time Lagrangian autocorrelation functions of the strain and rotation rates in homogeneous, isotropic turbulence over Taylor-scale Reynolds numbers from 38 to 93. [N.B. the one-point, two-time Lagrangian strain rate autocorrelation function means the covariance of the strain rate at two

different times for the same fluid element. The Taylor-scale Reynolds number is defined as $R_\lambda = u'\lambda_T/\nu$ where $\lambda_T = \left((u')^2/\left\langle(\partial u_1/\partial x_1)^2\right\rangle\right)^{1/2}$ is the Taylor scale and $u_1$ is the velocity in the $x_1$ direction.] At all Reynolds numbers, Pope (1990) found that, while the correlation time for the amplitude of the Lagrangian strain rate scales with the integral time scale, the strain rate loses directional information in approximately a Kolmogorov time. This result contradicts the long standing hypothesis of persistent strain in turbulence. According to the persistent strain hypothesis (Townsend, 1951; Pope, 1990), the local Lagrangian strain rate scales with the integral time scale. In the context of particle aggregation, this hypothesis forms the basis of Saffman & Turner's (1956) analysis and is equivalent to assuming the flow field remains static over a collision event.

Based on the DNS results, it is reasonable to expect that neither the large nor small total strain asymptotic limits will adequately represent coagulation in isotropic turbulence. Estimates of the turbulent coagulation rate at arbitrary strain must be determined by simulations before the regions of validity for the asymptotes can be established. Below, in Section 4.2, a simulation technique is developed to compute the coagulation rate for arbitrary total strain and total rotation. In Section 4.3 results are presented for simulations conducted without the presence of particle interactions for arbitrary total strain, and compared with results for strain rates of practical interest with the commonly used asymptotic limits. Finally, in Section 4.4 the influence of hydrodynamic interactions and van der Waals attractions is considered in the coagulation simulations. The collision efficiency is computed and the effect of varying the total strain

and the relative magnitude of the van der Waals attraction relative to viscous interactions is examined.

## 4.2 Computer simulation: development and method

To evaluate the utility of the large and small strain limiting cases, a computer simulation is developed here for coagulation in a randomly varying flow field with statistics selected to reproduce those for Gaussian isotropic turbulence. The evolution equation for the relative motion of a pair of particles in isotropic turbulence is derived here and the constitutive relations for the fluctuating velocity gradient and interparticle potential are presented. In the forthcoming analysis, the particle-separation-based Reynolds number, $Re = Ur/v$ (where $U$ is the relative particle velocity and $v$ is the kinematic viscosity), is assumed small so that Stokes equations apply to the relative particle motion. Coagulation is controlled by relative particle motions at small separations where the velocity field is linear in the separation distance. In the following discussion the fluctuating velocity gradient will be described in terms of a Fourier series with coefficients and frequencies chosen randomly to satisfy the constraints of Gaussian isotropic turbulence. The effects of retarded van der Waals attraction and hydrodynamic interactions are also considered in the algorithm. Generalization to other spherically symmetric interparticle potentials can be made in a similar manner.

Assuming inertia is negligible, the evolution of the relative particle separation can be described as a superposition of the motion driven by the

linear flow field and the velocity caused by a radially acting interparticle potential:

$$\frac{dr_i}{dt} = \Gamma_{ik}(t)r_k - C_{ij}S_{jk}r_k - \left(\frac{M_{ij}}{6\pi\mu a}\right)\frac{\partial\phi(r)}{\partial r_j} \qquad (4.7)$$

where $\Gamma_{ik}(t)$ is a randomly fluctuating velocity gradient tensor, $C_{ij}(r)$ is the hydrodynamic mobility function for two particles in a linear flow field (Batchelor & Green, 1972), $S_{jk} = \frac{1}{2}(\Gamma_{jk} + \Gamma_{kj})$ is the strain rate, $M_{ij}(r)/6\pi\mu a$ is the relevant hydrodynamic mobility function for two particles experiencing equal and opposite forces (Batchelor, 1976) and $\phi(r)$ is the radially acting interparticle potential. The magnitude of the fluctuating velocity gradient is assumed to be large compared with mean shear so only the fluctuating motions are dynamically important in determining particle movement and coagulation.

Batchelor and Green (1972) provide an explicit tensor expression for $C_{ij}$ in terms of the particle separation vector and two scalar functions of the relative position and particle radius ratio, namely:

$$C_{ij} = A(r)\frac{r_i r_j}{r^2} + B(r)\left(\delta_{ij} - \frac{r_i r_j}{r^2}\right) \qquad (4.8)$$

where $A(r)$ and $B(r)$ are non-dimensional functions of radial position and radius ratio that are tabulated by Batchelor & Green (1972) and Kim & Karilla (1991). The hydrodynamic relative mobility tensor scaled with the Stokes drag has the following form (Batchelor, 1976):

$$M_{ij} = \frac{r_i r_j}{r^2} G(r) + \left( \delta_{ij} - \frac{r_i r_j}{r^2} \right) H(r) \qquad (4.9)$$

where G(r) and H(r) are non-dimensional functions of relative position and particle radius ratio that are tabulated in Batchelor (1976) and Kim & Karilla (1991).

### 4.2.1 Characterization of $\Gamma_{ij}(t)$

The fluctuating velocity gradient tensor, $\Gamma_{ij}(t)$, is a small scale quantity of turbulence with an energy spectrum that peaks in the dissipation subrange of turbulence. Since directional biases imposed at the large scales are lost during the turbulent energy cascade process, Kolmogorov's similarity hypothesis applies and $\Gamma_{ik}(t)$ may be assumed to be isotropic. For the following analysis, the probability distribution function (pdf) of $\Gamma_{ik}(t)$ is approximated as Gaussian. It has been established that rare events attributed to internal intermittency lead to the formation of exponential tails on the velocity derivative pdf (Pope, 1996). Since exponential decay is much slower than the tailing of the standard Gaussian distribution, this leads to higher order moments, such as the superskewness (the 6th moment of the velocity gradient), that are orders of magnitude larger than values predicted from a normal distribution (Pope, 1996). However, experimental evidence shows that the exponential tails of the velocity gradient distribution contribute negligibly to lower order statistics such as second moments. The analysis of turbulent shear coagulation in the large and small total strain limits (Saffman & Turner, 1956; Chapter 3; Brunk et al.,

1997a) depends only on the second moment. Because intermittency has a negligible effect in the two asymptotic limits, the effects of intermittency are also anticipated to not strongly influence turbulent coagulation at intermediate total strains.

Since a joint-normal distribution is assumed for $\Gamma_{ik}(t)$, only the mean and covariance tensor must be specified to fully define the pdf of $\Gamma_{ik}(t)$. Following the work of Kraichnan (1970), $\Gamma_{ij}(t)$ is written as a temporal Fourier series with random Fourier coefficients and frequencies selected from specified pdfs (see below) to reproduce the two-time Lagrangian statistics of the fluctuating turbulent velocity gradient. As the number of terms in the Fourier series increases, the velocity gradient field automatically becomes Gaussian by the Central Limit Theorem.

The fluctuating velocity gradient is written as a random Fourier series for the rate of strain tensor, $S_{ik}(t)$, and the rotation rate tensor, $R_{ik}(t)$ = ½($\Gamma_{ik}$ - $\Gamma_{ki}$). The dependence of $\Gamma_{ik}(t)$ on the strain and rotation rates is made explicit since they evolve according to different time scales (Girimaji & Pope, 1990). The Fourier series representation of $\Gamma_{ik}(t)$ is:

$$\Gamma_{ik}(t) = \sum_{n=1}^{N} \left[ \hat{S}_{ik}^{n} \exp(i\pi\, \omega_S^n t) + \hat{R}_{ik}^{n} \exp(i\pi\, \omega_R^n t) \right] \qquad (4.10)$$

where N is the number of terms in the Fourier series, $i = (-1)^{1/2}$, $\hat{S}_{ik}^{n}$ and $\hat{R}_{ik}^{n}$ are independent Gaussian random variables with zero mean that represent the strain and rotation components of the turbulent velocity gradient, and $\omega_S^n$ and $\omega_R^n$ are random frequencies chosen from pdfs that reproduce the desired strain and rotation rate autocorrelation functions.

Expressions for the covariance of the Fourier coefficients and the pdfs of the frequencies are developed below. An explicit derivation is provided of the relations for the strain rate. The comparable equations involving the rotation rate can be found analogously. Taking the symmetric part of Equation 4.10 yields:

$$S_{ik}(t) = \sum_{n=1}^{N} \hat{S}_{ik}^n \exp(-i\pi\omega_S^n t) \tag{4.11}$$

Multiplying Equation 4.11 by $S_{jl}(t + \tau)$ and taking the ensemble average leads to an expression for the strain rate autocorrelation function:

$$<S_{ik}(0)S_{jl}(\tau)> = \left\langle \sum_{n,m=1}^{N} \hat{S}_{ik}^n \hat{S}_{jl}^{m*} \exp(i\pi\omega_S^m \tau) \right\rangle \tag{4.12}$$

where stationarity has been assumed (i.e., the statistics of the fluctuating velocity field are independent of the time origin) and the * denotes the complex conjugate. Next, the tensors, $\hat{S}_{ik}^n$ and $\hat{S}_{ik}^m$, are assumed to be independent for $n \neq m$ and the Fourier coefficients and $\omega_S^m$ are assumed to be independent random variables:

$$<S_{ik}(0)S_{jl}(\tau)> = \sum_{n=1}^{N} <\hat{S}_{ik}^n \hat{S}_{jl}^*> \int_{-\infty}^{\infty} \exp(i\pi\omega_S^n \tau) P(\omega_S^n) d\omega_S^n \tag{4.13}$$

where $P(\omega^n)$ is the pdf of $\omega^n$. The Fourier transform of Equation 4.13 is:

$$\mathscr{F}(<S_{ik}(0)S_{jl}(\tau)>) =$$
$$\sum_{n=1}^{N} <\hat{S}_{ik}^n \hat{S}_{jl}^*> \int_{-\infty}^{\infty}\int_{-\infty}^{\infty} \exp(i\pi\omega_S^n \tau) \exp(-i\pi\omega_S \tau) P(\omega_S^n) d\omega_S^n d\tau \tag{4.14}$$

Orthogonality of the complex exponentials greatly simplifies Equation 4.14 to:

$$\mathscr{F}(<S_{ik}(0)S_{jl}(\tau)>) = N<\hat{S}_{ik}\hat{S}_{jl}^*>P(\omega_S) \tag{4.15}$$

The autocorrelation function for the strain rate in isotropic turbulence derived in the Appendix D is:

$$<S_{ik}(0)S_{jl}(t)> = S_{ikjl}\exp\left(\frac{-t}{\tau_s}\right) \tag{4.16}$$

where $S_{ikjl} = <S_{ik}(0)S_{jl}(0)>$ is the covariance of the strain rate given by Equation D.4. The exponential decay law given in Equation 4.16 was found to represent the DNS data for the strain rate autocorrelation function accurately (Girimaji & Pope, 1990). Non-linear regression of Girimaji & Pope's (1990) data based on Equation 4.16 resulted in a strain rate correlation time, $\tau_S$, of $2.3/\Gamma_\eta$ with an $r^2$ of 99.5%. Similarly, the exponential decay fit the rotation rate autocorrelation function to yield a rotation rate correlation time, $\tau_R$, of $7.2/\Gamma_\eta$ with an $r^2$ of 95%. The Fourier transform of Equation 4.16 gives:

$$\mathscr{F}(<S_{ik}(0)S_{jl}(\tau)>) = \frac{2\tau_S S_{ikjl}}{1 + (\pi\omega_S\tau_S)^2} \tag{4.17}$$

Comparing Equations 4.15 and 4.17, the pdf of $\omega_s$ is chosen to be:

$$P(\omega_S) = \frac{\tau_S}{1 + (\pi\omega_S\tau_S)^2} \tag{4.18}$$

such that it satisfies the normalization condition, namely:

$$\int_{-\infty}^{\infty} P(\omega_s)\, d\omega_s = 1 \qquad (4.19)$$

The remaining terms in Equations 4.15 and 4.17 specify the covariance of the random Fourier coefficients for the extensional flow component as:

$$\langle \hat{S}_{ik}\hat{S}_{jl}^* \rangle = \frac{2 S_{ikjl}}{N} \qquad (4.20)$$

The strain rate autocorrelation function, Equation 4.16, is a real, even function of time leading to the constraint that the real and imaginary parts of $\hat{S}_{ik}$ are independent. For simplicity the variances of the real and imaginary parts are assumed to be equal. These restrictions on the statistics of $\hat{S}_{ik}$ and the assumption of equal variances for the real and imaginary particles imply that if:

$$\hat{S}_{ik} = A_{ik} + i B_{ik} \qquad (4.21)$$

then,

$$\langle A_{ik} B_{jl} \rangle = \langle B_{ik} A_{jl} \rangle = 0$$
$$\langle A_{ik} A_{jl} \rangle = \langle B_{ik} B_{jl} \rangle = \frac{S_{ikjl}}{N} \qquad (4.22)$$

Similarly, the pdf of $\omega_R$ and the variance of $<R_{ik} R_{ji}>$ can be found. Final results for the rotational component of the Fourier series may be obtained by replacing the S's in Equations 4.11 to 4.22 with R's.

For each realization of the random flow, the Fourier coefficients defined by Equations 4.10 were randomly picked from a joint normal distribution with zero mean and a variance satisfying Equations 4.20 to 4.22. Similarly, the random frequencies for the specified strain and rotation rate correlation times were determined from the pdfs defined in Equation 4.18. Uniform and normally distributed random numbers used in describing a realization of $\Gamma_{ik}(t)$ were chosen using algorithms supplied in the *ranlib library* from NETLIB (Brown & Lovato, 1996).

The Fourier series included enough terms so that in the limit of many realizations, the specified second-order statistics of $\Gamma_{ij}(t)$ were obtained. Figure 4.2 shows three components of the velocity gradient autocorrelation coefficient calculated by averaging 2,000 realizations of $\Gamma_{ij}(t)$ when N in Equation 4.10 was 200. The solid lines are calculations derived from DNS for homogeneous isotropic turbulence (see Appendix E; Girimaji & Pope, 1990) and the symbols represent results obtained using the Fourier series representation. The simulated fluctuating velocity gradient had autocorrelation functions that quantitatively agree with the velocity gradient autocorrelation coefficients obtained from DNS.
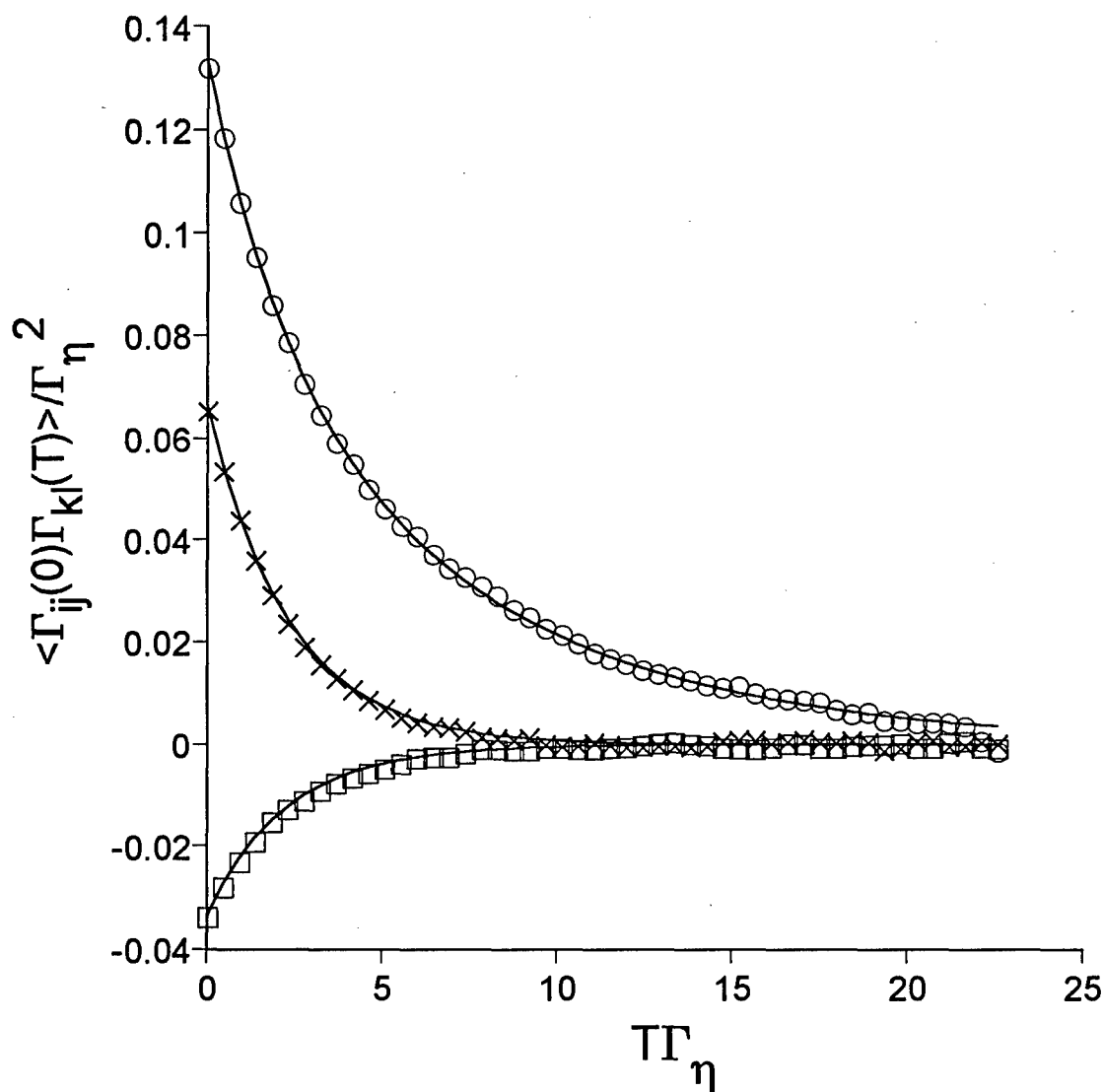
**Figure 4.2**: Three components of the fluctuating velocity gradient autocorrelation function as obtained by averaging 2000 realizations of the velocity gradient Fourier series representation. The random velocity gradient was represented by 200 Fourier modes. Components shown are $<\Gamma_{11}\Gamma_{11}>/\Gamma_{\eta}^2$ (O), $<\Gamma_{11}\Gamma_{22}>/\Gamma_{\eta}^2$ (X), and $<\Gamma_{12}\Gamma_{12}>/\Gamma_{\eta}^2$ (□). The simulation results show close agreement to the calculations based on DNS (solid lines).

### 4.2.2 *Constitutive relation for the interparticle potential*

A van der Waals attractive potential corrected for retardation was used for the interparticle potential included in the equation of motion (Equation 4.7). Van der Waals attractions result from induced-dipole/induced-dipole interactions between neighboring atoms. The pairwise sum of these attractions over a macroscopic body leads to a significant attractive potential that decays rapidly over distances comparable to the particle radius (Russel et al., 1989). Due to the finite propagation speed of electromagnetic waves, dipole/dipole correlations between interacting atoms become out of phase at distances greater than the London retardation wavelength, $\lambda$, which further reduces the dispersion forces. In this work $\lambda$ is set equal to 100 nm (van de Ven & Mason, 1977; Davis, 1984) in qualitative agreement with measurements (Suresh and Walz, 1996). Schenkel & Kitchner (1960) provide an analytical approximation for the retarded van der Waals potential given by:

$$\phi_{vdw} = -\frac{A_H}{12(\xi + 0.885 N_L \xi^2)} \quad \text{for } \xi < 4/N_L \text{ and,} \tag{4.23}$$

$$\phi_{vdw} = -\left(\frac{A_H}{4\xi}\right)\left[\frac{4.9}{15 N_L \xi} - \frac{8.68}{45 N_L^2 \xi^2} + \frac{4.72}{105 N_L^3 \xi^3}\right] \tag{4.24}$$

for $\xi > 4/N_L$ and $\xi \ll 1$. In Equations 4.23 and 4.24, $\xi = (r-2a)/a$ is the gap width scaled by the particle radius, $A_H$ is the Hamaker constant, and $N_L$ is the diameter of the two particles scaled by the London retardation

wavelength: $N_L=2\pi\sigma/\lambda$. These approximate expressions for the retarded van der Waals potential are valid in the limit of small separations (i.e., the lubrication regime). Constraining $\lambda \ll \sigma/2$, so that van der Waals attraction decays in the lubrication regime, leads to the restriction that $N_L \gg 4\pi$, which is satisfied for all the particle sizes examined in this chapter.

### 4.2.3 *Scaling*

Scaling of Equation 4.7 is accomplished by normalizing the particle separation, $r_i$, with the particle radius, the time with the Kolmogorov time, and the velocity gradient with the Kolmogorov velocity gradient. Since the van der Waals attraction becomes significant for gap widths comparable to the London wavelength, the gradient of the potential scales with $A_H/4\lambda$. The final form of the equation of motion is:

$$\frac{dr_i}{dt} = \Gamma_{ik}(t)r_k - C_{ij}S_{jk}r_k - \frac{N_L}{8\pi N_S}M_{ij}\frac{\partial\phi(r)}{\partial r_j} \qquad (4.25)$$

where $N_S$ is defined in Table 4.1 as the ratio of viscous to van der Waals forces. For the remainder of this chapter scaled variables are utilized. Table 4.1 lists the expected magnitudes of the scaled parameters assuming an aqueous dispersion of 1 to 100 $\mu$m diameter colloidal particles with $\Gamma_\eta=0.1$ to 1000 s$^{-1}$ and $A_H = 10^{-19}$ to $10^{-21}$ J.

### 4.3 Turbulent coagulation for non-interacting particles

### 4.3.1 *Simulation procedure*

Simulations at arbitrary total strain and rotation were conducted in the absence of particle interactions to compare with the asymptotic limits

**Table 4.1**: Non-dimensional parameters and their typical magnitudes

| Parameter | Interpretation | Magnitude |
|---|---|---|
| $\tau_S\Gamma_\eta$, $\tau_S\Gamma_\eta$ | Total strain (rotation) | 0 to $\infty$ |
| $N_L = 4\pi a/\lambda$ | Particle radius to London retardation wavelength | $10^2$ to $10^4$ |
| $N_S = 12\pi\mu a^3\Gamma_\eta/A_H$ | Viscous to van der Waals forces | $\sigma=1\mu m$: $10^{-3}$ to $10^3$ $\sigma=100\mu m$: $10^3$ to $10^9$ |

provided by Saffman & Turner (1956) and Brunk et al. (1997a; Chapter 3). The general simulation approach began by generating a realization of the random linear flow using the Fourier series method described in Section 4.2. The most obvious way to proceed would then be to create particles at the outer simulation boundary such that the constant bulk concentration was maintained. Numerical integration could then be used to track the position of the particles so that their rate of collision with the test sphere (as illustrated in Figure 4.1) could be determined. However, since most particles in the bulk fluid (at $r = \infty$) do not collide with the test sphere in this approach, the efficiency of the numerical calculations would be low.

The efficiency of the computer simulations can be greatly improved by running the simulation backward in time. Instead of creating particles at $r = r_\infty$ and calculating the collision rate with the test particle, the particles are created at $r = \sigma$ and the simulation calculated the particle flow rate through the outer simulation boundary. Since the conservation equation for non-interacting particles is linear and time reversible, the flux calculated in the time reversed simulation is equal in magnitude to that obtained using the conventional boundary conditions shown in Figure 4.1.

In the absence of particle interactions, the equation of motion, Equation 4.25, for the particles reduces to:

$$\frac{dr_i}{dt} = \Gamma_{ij}(t) r_j \qquad (4.26)$$

indicating that the particles follow the fluid motion. The only physical parameters that influence the coagulation dynamics in this case are the total

strain and total rotation. In turbulence, the ratio of the strain rate to rotation rate is fixed because the turbulent dissipation rate is partitioned equally between the strain and rotational flow components; consequently, the effect of varying this ratio was not considered in the numerical analysis.

For each turbulent coagulation simulation, a unique realization of the spatially linear flow was generated using the Fourier series method outlined in Section 4.2.1. During each time step the simulation checked to see if a particle should be created at the excluded volume surface. In the absence of interactions, particles follow the fluid motion; therefore, the flux of pair probability at the particle surface is proportional to $C_1^2(\mathbf{u}\cdot\mathbf{n})$ when $(\mathbf{u}\cdot\mathbf{n}) > 0$ and the flux is zero otherwise. (Here, $\mathbf{n}$ is the outward pointing unit vector normal at the randomly chosen location, and $\mathbf{u}$ is the local velocity.) At locations of high local flux, the probability that a particle enters the near field around the test particle is high, while the probability that a particle is swept into the simulation domain is low in regions of low volumetric flux. The probability of creating a particle is therefore proportional to the volumetric flux at the randomly chosen location:

$$P_{creation} = -\frac{\mathbf{u}\cdot\mathbf{n}}{(\mathbf{u}\cdot\mathbf{n})_{MAX}} \qquad (4.27)$$

where $P_{creation}$ is the probability of creating a particle, and $(\mathbf{u}\cdot\mathbf{n})_{MAX}$ is the maximum volumetric flux that occurs at any position on the surface, $r = \sigma$, and at any time throughout the simulation. In the simulations, the maximum volumetric flux was estimated as $(\mathbf{u}\cdot\mathbf{n})_{MAX} \approx \sigma<\Gamma_{11}^2>^{1/2}$ and then refined by trial and error. The final estimate for $(\mathbf{u}\cdot\mathbf{n})_{MAX}$ was large enough

so that high shear fluctuations in the velocity gradient field would not lead to particle creation probabilities greater than 1. To evaluate Equation 4.27, the simulation selected a random position on $r = \sigma$ using the acceptance-rejection technique developed by von Neumann (1951) and computed the volumetric flux at the random location. If the calculated $P_{creation}$ was negative, a particle was not created since the volumetric flux was inward. For positive probabilities, the simulation created a particle if a uniform random number less than $P_{creation}$ was generated.

Although many particles existed within the control volume at any time, only encounters between a particle and the test sphere were considered. That is, the particles that were in relative motion around the test sphere passed through one another. In the actual physical application with dilute particle suspensions, the volume fraction of coagulating particles is very small so the likelihood for three-particle encounters is negligible. Simulating coagulation with higher volume fractions that considered only two particle interactions enhanced numerical efficiency while still reflecting the correct physics for a dilute suspension.

For each particle within the simulation domain, the equation of motion, Equation 4.26, was integrated numerically using a fifth-order Runge-Kutta algorithm with adaptive time step control. The maximum time step allowed was set at the period of the fastest Fourier mode, so the Runge-Kutta scheme resolved this mode with a minimum of five intermediate time steps. The permissible integration error was established by balancing the penalty for evaluating Equation 4.10 at many time steps with the requirement that non-interacting particles follow the stream lines

of the flow. Descriptions of the programs are given in Appendix E. To set the maximum integration error, calculations performed in a steady strain field were used. Ideally in the steady flow all of the particles should reach $r = r_\infty$ since they are created in regions of outward going flux. When the integration error was too large, some particles crossed the stream lines of the flow and returned to the test sphere. A maximum local integration error equal to 1% of the relative particle separation distance was found to eliminate streamline crossing.

Particles that reached $r = r_\infty$ or returned to $r = \sigma$ were removed from the simulation. The average particle flow rate through the system, Q, was calculated as the total number of particles that reached the outer simulation boundary divided by the total simulation time. Statistics on Q and the radial pair probability density profile were obtained at intervals of $\tau_\infty$, the characteristic time for a particle to travel from $r_\infty$ to $\sigma$. In the large total strain limit, $\tau_\infty$ scales with the Kolmogorov time; however, in the diffusion limit it can take much longer for particles to reach the test sphere. When diffusion dominates the system, $\tau_\infty$ is estimated by relating the radial components of the turbulent diffusivity given by Equation 3.20 to one-half of the time derivative of the mean square displacement to obtain (Russel et al., 1989):

$$\frac{1}{2}\frac{d<r^2>}{dt} = \frac{\tau_s \Gamma_\eta}{15}<r^2> \tag{4.28}$$

This ODE for the mean square displacement was integrated to estimate the characteristic time for particles to diffuse from $r = \sigma$ to $r = r_\infty$ as:

$$\tau_\infty = \left(\frac{1}{\tau_s \Gamma_\eta}\right) \ln\left(\frac{<r_\infty^2>}{<\sigma^2>}\right) \quad (4.29)$$

In the computer simulations, characteristic times were estimated for both the small and large total strain limit, and the longer of the two was used as $\tau_\infty$ for the simulation.

Each realization of the flow field was simulated until the particle flux at the excluded volume surface and the outer simulation boundary differed by less than 2% from its value at the previous $\tau_\infty$. A simulation typical achieved steady state in less than 20 characteristic times.

At steady state, the net flux of particles entering at the surface of the excluded volume ($r = \sigma$) is constant and can be written as:

$$C_1 <u \cdot n> = \frac{1}{\pi \sigma^2}\left(\frac{<u \cdot n>}{(u \cdot n)_{MAX}}\right) \quad (4.30)$$

The right-hand side of Equation 4.30 can be interpreted as the product of the maximum particle flux at the excluded volume surface for the test particle (i.e., the maximum particle flux is one particle created over the surface of the excluded volume per time step or $1/\pi\sigma^2$) and the average probability of creating a particle during a time step. Solving for $C_1$ yields:

$$C_1 = \frac{1}{\pi \sigma^2 (u \cdot n)_{MAX}} \quad (4.31)$$

The coagulation kernel for each realization was calculated as $k^0 = Q/C_1$.

For each set of system parameters the coagulation rate constant was obtained by ensemble averaging over sufficient independent realizations to achieve the desired level of accuracy. For the simulations with non-interacting particles, ensemble averaging continued until the standard deviation of $k^0$ was less than 2% of its mean value. The number of realizations required to achieve good statistics varied strongly with total strain. For total strains less than 1, as few as 10 realizations were needed, while at total strains greater than 10, nearly 1000 realizations were required to achieve low statistical errors. At small total strain, particles experience a rapidly fluctuating flow so that net particle movement is the result of many uncorrelated normally distributed velocity gradient fields. In effect, coagulation results are time and also ensemble averaged in this limit. In contrast, at the large strain limit, the flow field varies slowly and particles experience a nearly stationary flow; thus, obtaining good statistics depended solely on ensemble averaging over many realizations.

Along with the parameters summarized in Table 4.1, the outer simulation boundary, $r_\infty$, the maximum volumetric flux at $r_\infty$ and the number of Fourier modes, N, were specified at the beginning of a simulation. Initial computations were conducted to investigate the effect of the simulation parameters on the reported results. For most coagulation simulations, the Fourier series used to represent the fluctuating velocity gradient field was truncated at 300 Fourier modes. The effect of N was evaluated by simulating isotropic turbulence ($\tau_S\Gamma_\eta = 2.3$ and $\tau_R\Gamma_\eta = 7.2$) while varying the number of components in the Fourier series from N = 25 to N = 400. For this simulation series, the maximum particle flux was held

constant and each data point represented the average of 100 realizations. To facilitate comparison, statistical fluctuations were reduced by starting each member of the simulation set with the same random number generator seeds. In this way, velocity gradient field Fourier modes present in all the simulations were the same and the random numbers sampled when introducing new particles were identical.

Figure 4.3 summarizes the results by plotting normalized coagulation rate against the number of elements in the Fourier series. The error bars denote +/- one standard deviation. The normalized rate constant, k, monotonically increased towards an asymptotic value as N was increased. The normalized coagulation rate rose 3.7% when increasing N from 25 to 400 while k grew only 0.4% when N doubled from 200 to 400. Statistical error decreased with increasing N, from a coefficient of variation (i.e., the standard deviation divided by the mean) of 1.4% at N = 25 to 1.2% at N = 200, and to 0.9% at N = 400. The decrease in statistical uncertainty was presumed to occur because the pdf of each flow realization was better approximated by a Gaussian distribution at large N. Given the magnitude of the coefficient of variation for $k_0$, the marginal improvement gained from increasing N = 200 to N= 400 was not deemed to be significant. Consequently, N's between 200 and 400 were used in the simulations reported below.

The outer simulation limit was chosen to minimize boundary effects. In the limit of large total strain, curved stream lines that exit and reenter the simulation control volume may exist. Since particles that exit the simulation boundary cannot reenter, this would lead to a higher than
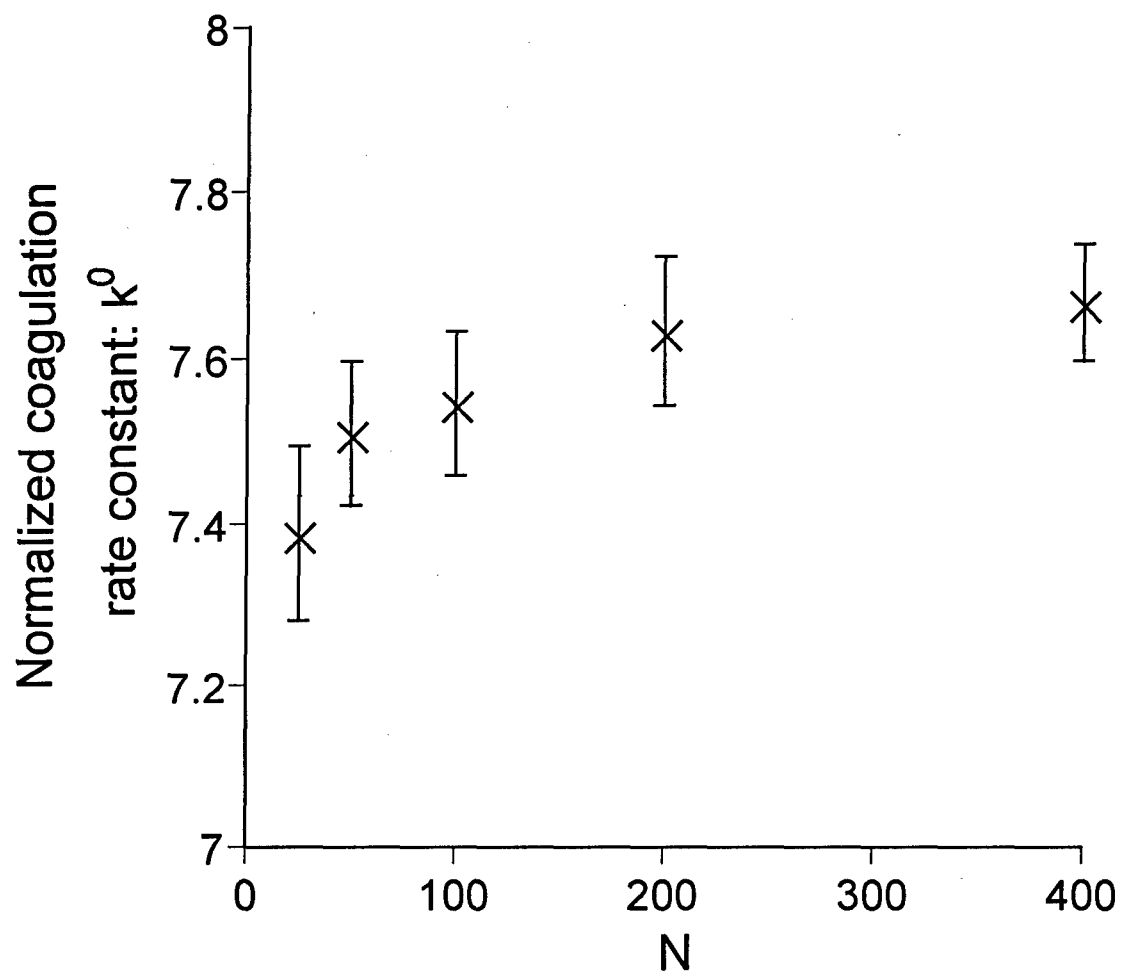
**Figure 4.3**: The effect of N (number of Fourier modes) on the ensemble average of the turbulent coagulation kernel for 100 realizations of the system. Error bars denote +/- one standard deviation.

expected net flux through the outer simulation boundary. Simulations conducted in the persistent strain limit for $r_\infty$ ranging from 5 to 30 resulted in computed coagulation rates that were not statistically different. Therefore, recirculating stream lines broken by the finite simulation boundary were not consequential when estimating the collision rate for $r_\infty$ > 5.

The effect of the finite simulation volume is anticipated to be largest in the limit of small total strain where the turbulent coagulation process is diffusive. To compute the boundary effect in the small total strain limit, the radial component of the pair probability equation is solved with absorbing boundary conditions at the inner and outer simulation boundary (see Chapter 3 or Brunk et al., 1997a). The resulting steady state coagulation rate constant normalized by the particle radius and Kolmogorov shear rate is:

$$k^0 = \frac{32\pi}{5} \tau_s \Gamma_\eta \left[ \frac{r_\infty^3}{r_\infty^3 - \sigma^3} \right] \qquad (4.32)$$

The term in brackets is the contribution of the finite outer boundary to the calculated coagulation rate constant. For most simulations discussed below, $r_\infty = 10$. With $r_\infty = 10$, the coagulation kernel in the diffusive limit increases about 0.8% above that for an infinite domain. An error of 0.8% is negligible compared to the statistical error in the calculations and has been ignored in the ensuing analysis.

At intermediate strain the effect of the outer simulation boundary was surmised to lie between the large and small strain extremes; therefore, the magnitude of boundary effects at the small strain limit was used to set an appropriate outer simulation boundary so that the outer boundary had a negligible influence on the numerical calculations.

### 4.3.2 *Simulation results*

In this section the effect of varying the total strain and rotation on the coagulation rate is discussed and the simulation results are contrasted with the analytical solutions for large and small total strain limits that are summarized in Section 4.1. Additional simulations are provided that investigate the affect of the total rotation on the rate of particle coagulation.

Sample particle trajectories at large, intermediate and small total strain are illustrated in Figures 4.4 to 4.6 for non-interacting particles in the pseudo-steady limit ($\tau_S\Gamma_\eta \rightarrow \infty$, $\tau_R\Gamma_\eta \rightarrow \infty$; Figure 4.4), for isotropic turbulence ($\tau_S\Gamma_\eta = 2.3$, $\tau_R\Gamma_\eta = 7.2$; Figure 4.5) and in the diffusion limit ($\tau_S\Gamma_\eta \rightarrow 0$, $\tau_R\Gamma_\eta \rightarrow 0$; Figure 4.6). At large values of the correlation time the flow is persistent and the particle motion appears steady (Figure 4.4). Comparing Figures 4.4 through 4.6 shows that, as the correlation time decreases, the flow field becomes more random as evidenced by the increasingly tortuous motion of the particles. For the examples shown, the time between collision increased from $6.2/\Gamma_\eta$ to $32/\Gamma_\eta$ as the flow correlation times decreased from $\infty$ toward 0. The trajectory at the small correlation time (Figure 4.6) is shown every $1/(2\Gamma_\eta)$ time step. The particle motion in Figure 4.6 has an obvious random component indicating that the motion is
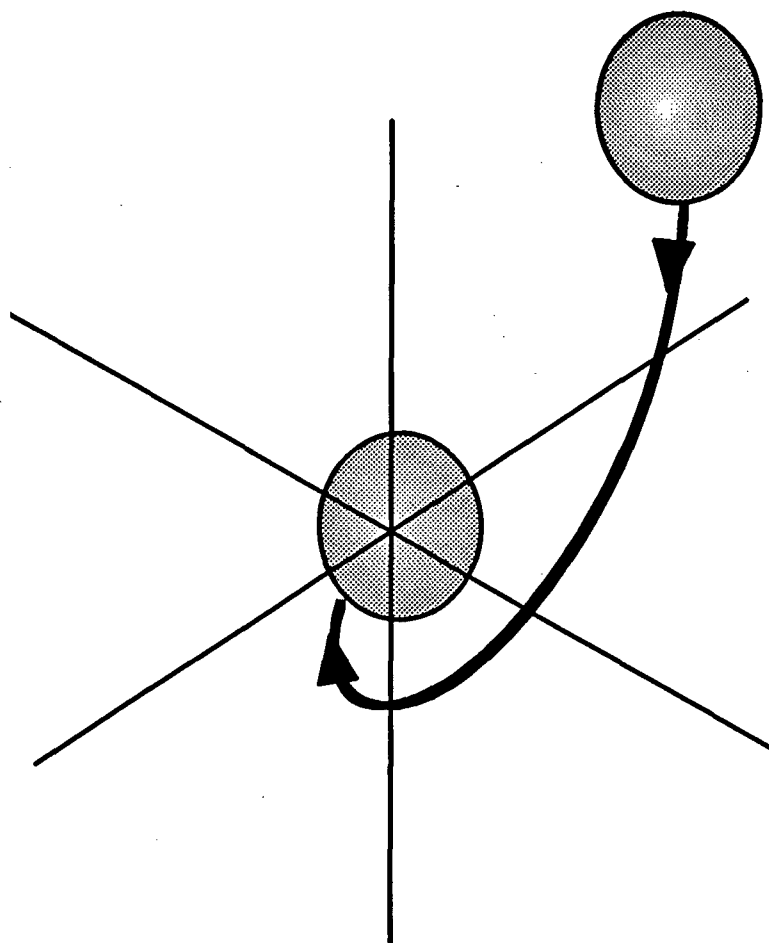
**Figure 4.4**: Sample trajectory for the relative motion of two particles in a pseudo-steady linear flow (i.e., $\tau_S \Gamma_\eta \to \infty$, $\tau_R \Gamma_\eta \to \infty$).
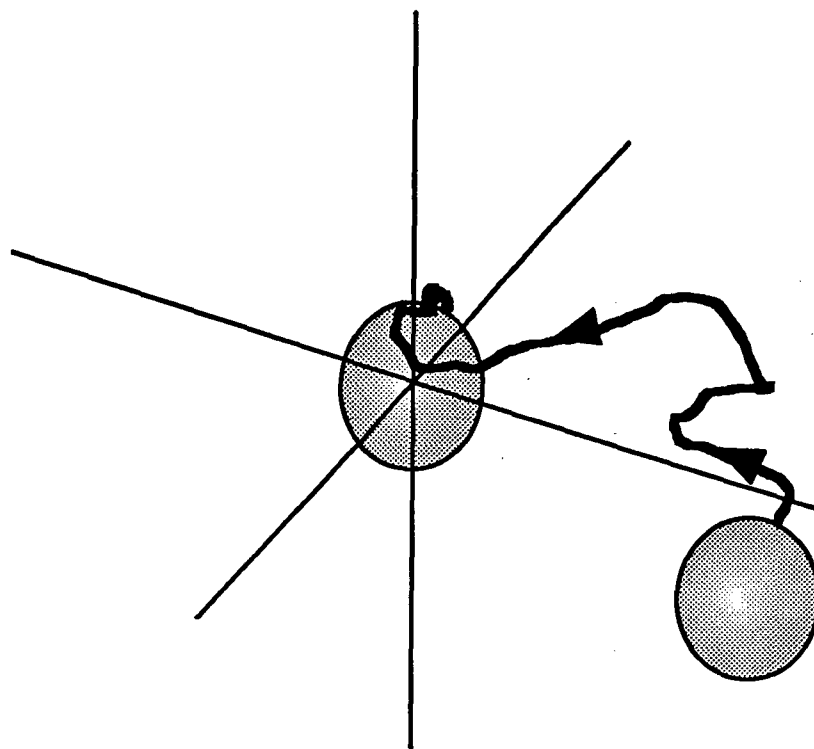
**Figure 4.5**: Sample trajectory for the relative motion of two particles in isotropic turbulence (i.e., $\tau_S \Gamma_\eta = 2.3$, $\tau_R \Gamma_\eta = 7.2$).
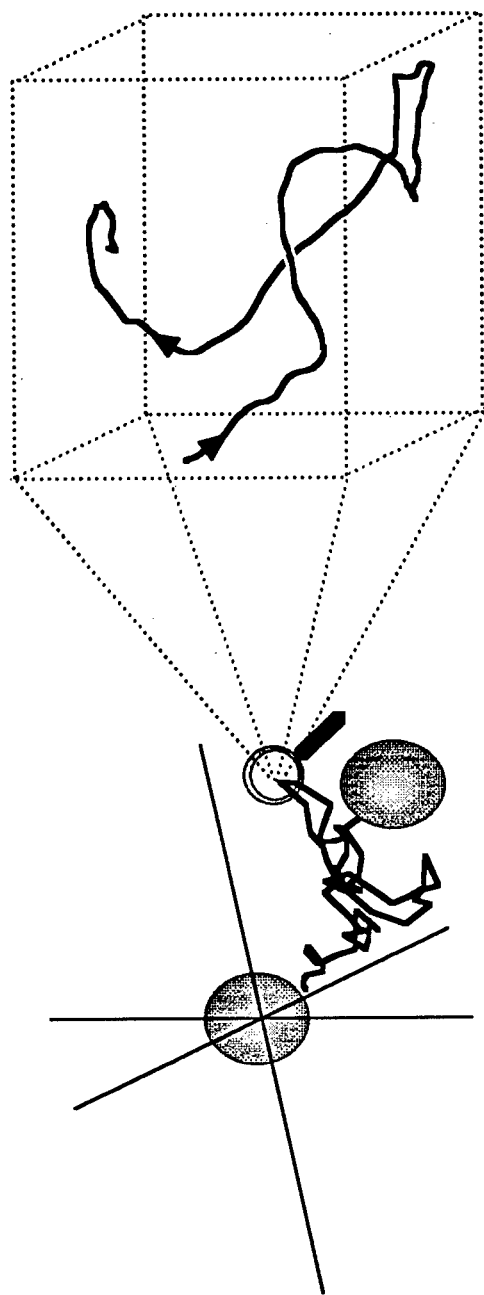
**Figure 4.6**: Three dimensional example trajectory of relative particle motion when the total strain and rotation are small and the flow is diffusive. The trajectory is shown every $1/2\Gamma_\eta$ time step. The expanded view illustrates the motion that occurs during a $1/2\Gamma_\eta$ time step.

diffusive. Isotropic turbulence, illustrated in Figure 4.5, has characteristics between the pseudo-steady and diffusive limits; therefore, it shows behavior between these two extremes.

Figure 4.7 illustrates how the coagulation kernel normalized with the Kolmogorov shear rate and particle radius changes when $\tau_S\Gamma_\eta$ and $\tau_R\Gamma_\eta$ are varied while maintaining $\tau_S\Gamma_\eta/\tau_R\Gamma_\eta = 0.32$, corresponding to isotropic turbulence. The square symbols represent the simulation data, and unless otherwise shown, the standard deviations of the data points are smaller than the symbols. The symbol denoted by the solid square represents the expected physical state for isotropic turbulence as estimated from DNS data ($\tau_S\Gamma_\eta = 2.3$ and $\tau_R\Gamma_\eta = 7.2$). Also shown are the asymptotic limits of large (thick solid line) and small (thin solid line) total strain. At small total strain the pair diffusion formulation (Chapter 3; Brunk et al., 1997a), given by Equation 4.6, is valid and $k^0 = 32\pi\tau_S\Gamma_\eta/5$ in normalized form. The simulations reach 95% of the pair diffusion limit by $\tau_s\Gamma_\eta = 0.115$ (see Figure 4.7). With increasing total strain, the simulation results increase until, at a total strain of about 10, the calculated $k^0$ levels off and becomes independent of the applied total strain. The large total strain asymptotic limit was estimated by running simulations with an infinite total strain and rotation (i.e., the flow is stationary). At large total strain (thickhorizontal line on Figure 4.7) $k^0 = 9.896$ +/- 0.0805. By $\tau_s\Gamma_\eta = 23$ and $\tau_r\Gamma_\eta = 72$ the simulations are within 98% of the large total strain asymptote.

The Saffman & Turner model's prediction in the large strain limit, Equation 4.5, is $k^0 = 10.36$ in non-dimensional form and is shown as the dashed line on Figure 4.7. It is evident that this model overestimates the

**Figure 4.7**: The effect of simultaneously varying $\tau_S\Gamma_\eta$ and $\tau_R\Gamma_\eta$ on the normalized turbulent coagulation rate constant. In these simulations the ratio of total rotation to total strain was fixed at 3.13 as obtained from an analysis of the DNS data. The square symbols represent simulation data with the filled square being the prediction for isotropic turbulence ($\tau_S\Gamma_\eta$ = 2.3, $\tau_R\Gamma_\eta$ = 7.2). Unless shown, the +/- one standard deviation error bars on the simulation results are smaller than the symbols. Asymptotic limits for small total strain (thin line), large total strain (thick line), and the Saffman & Turner (1956) prediction (dashed line) are also shown. Simulations performed at infinite total strain and rotation are shown with (thick solid line) and without (▲) the effects of rotation. An interpolation of the asymptotes shown as the dotted line closely approximates the simulation data.

Total Strain: $\tau_S \Gamma_\eta$

Normalized coagulation rate constant: $k^0$

actual coagulation rate in the large strain limit by about 5%. A z-test shows that the difference between the infinite total strain simulation results and the Saffman & Turner model's predictions is statistically significant (p value = $10^{-8}$). In Saffman & Turner's theoretical analysis the local turbulent velocity field is represented as a linear irrotational flow, while the simulations described here include both strain and rotational components of the velocity field. Considering the effects of strain and rotation separately, one expects the rate of coagulation to be independent of rotation because a solid body rotation, by itself, does not cause a net flux of particles towards the test sphere. The simulation results, however, indicate that the effects of rotation and extension are not superimposable in coagulation. To confirm this possibility, computer simulations were run at infinite total strain in a purely extensional flow. The ensemble averaged coagulation rate, shown by the triangle on Figure 4.7, falls on the Saffman & Turner prediction and a z-test reveals that the simulation prediction for $k^0$ is not statistically different from the Saffman & Turner prediction of 10.36 (p value = 0.46). When simulating an irrotational flow, the computed turbulent coagulation agrees with the Saffman & Turner large total strain asymptote; therefore, the addition of rotation must decrease the turbulent shear coagulation rate.

The reason that strain and rotation are not superimposable is that the combination can lead to particle trajectories that leave and later return to the excluded volume surface and thus contribute no particle flux. Although one can superimpose strain and rotation when calculating the flow into $r = \sigma$, adding rotation to the pure straining flow field leads to recirculating trajectories that have no net contribution to the coagulation rate. It follows

that the coagulation rate is overstated in an analysis that neglects rotation. This effect is explored in more detail below.

For isotropic turbulence ($\tau_S \Gamma_\eta = 2.3$ and $\tau_R \Gamma_\eta = 7.2$), $k^0 = 8.62$ +/- 0.02 for the normalized coagulation kernel. The Saffman & Turner model prediction of $k^0 = 10.35$ overestimates the true coagulation rate by 20%. Similarly, the diffusion approximation, Equation 4.6, evaluated at $\tau_S \Gamma_\eta = 2.3$, estimates the normalized coagulation rate to be 46.24, approximately 5 times larger than the actual value. Although both asymptotic limits fail to predict the turbulent coagulation rate for isotropic turbulence, they can be used to construct an interpolation of the simulation data. A hyperbolic approximation of the following form can be used to interpolate between the asymptotic solutions:

$$k^0 = \frac{P_1 \tau_s \Gamma_\eta}{1 + Q_1 \tau_s \Gamma_\eta} \tag{4.33}$$

Applying the small and large total strain asymptotic limits to Equation 4.33 leads to $P_1 = 32\pi/5$ and $Q_1 = 0.65\pi$. This interpolation, shown as the dotted line in Figure 4.7, closely approximates the simulation data with an error of $\leq 5\%$.

Perhaps one of the most interesting aspects of these results is that the addition of rotation can cause a decrease in the coagulation rate. The effect of rotation has been previously identified in stationary linear flows (Greene et al., 1994; Zeichner & Schowalter, 1977). Zeichner & Schowalter (1977) derive the coagulation rate in a uniaxial extensional flow (a pure strain field) and compare the results with coagulation in

simple shear (a flow that contains rotation) with and without interparticle interactions. For the same rate of strain, they find that the $k^0$ for simple shear is about 3.5 times smaller than the $k^0$ calculated for uniaxial extension. In the same vein, Greene et al. (1994) note that linear flows with high vorticity have closed streamlines and that these closed streamlines can be expected to substantially decrease the kinematics of particle aggregation. Since the turbulent flow field in the neighborhood of a test particle can be conceptualized as an ensemble average over all possible linear flows, one would expect the coagulation rate to be lower than is predicted in the absence of rotation.

The correlation time for the rotation rate can also be anticipated to influence the coagulation rate. When the rotation is persistent (i.e., the total rotation is large) recirculating streamlines present in the flow can be expected to endure and thus the coagulation rate would be lower. Conversely, when the rotation rate correlation time is small, the location of streamlines that return to the excluded volume fluctuates and the effect of the curved streamlines is expected to be mitigated. Numerical simulations run at $\tau_S \Gamma_\eta = 1.15$ and various $\tau_R \Gamma_\eta$ illustrate the effects of persistent rotation. Shown in Figure 4.8 are the normalized coagulation rate constants for values of $\tau_R$ ranging from 0 to 720. Each simulation set started with the same random seeds to facilitate comparison and enough realizations were computed to achieve a coefficient of variation less than 2%. The normalized coagulation rate constant, $k^0$, ranged from 9.26 +/- 0.16 at $\tau_R = 0$ to 8.50 +/- 0.09 at $\tau_R = 720$. Increasing the rotation rate
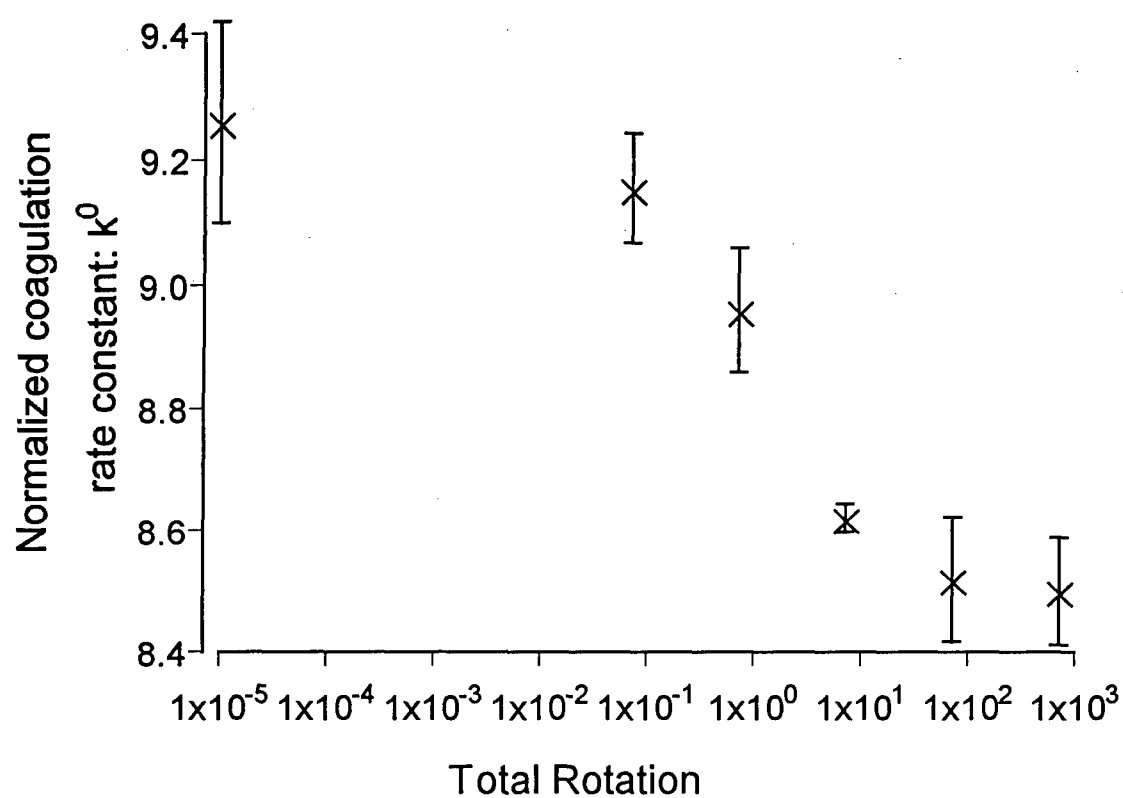
**Figure 4.8**: The normalized coagulation rate constant as a function of the rotation rate correlation time while keeping $\tau_s\Gamma_\eta = 1.15$. Error bars are +/- one standard deviation from the mean.

correlation time decreased the calculated $k^0$ to about 92% of its maximum value, in agreement with expectations.

Pair probability distributions for three simulation conditions and analytical results for the small total strain limit (diffusion limit) are compared in Figure 4.9. Computed pair probability profiles are shown for $(\tau_S \Gamma_\eta, \tau_R \Gamma_\eta) = (0.23, 0.72)$(circles), $(2.3, 7.2)$(triangles) and $(\infty, \infty)$(squares). For pure convection (large total strain), where the relative velocity is proportional to the separation distance, $P(r)$ is expected to decay in proportion to $1/r^3$. Similarly in the small total strain limit a $1/r^3$ decay is expected since the turbulent diffusion coefficient is proportional to the separation distance squared. Hence, it is not surprising that each simulation condition shown in Figure 4.9 has the $1/r^3$ dependence in the pair probability. The concentration distributions obtained at larger correlation times have discontinuous drops to zero concentration at the boundaries of the simulation domain. As the correlation times decrease and the relative particle motion becomes more diffusive, the concentration profile at the domain boundaries begins to decrease faster than $1/r^3$. The profile in the diffusion limit can be found as a solution to a pair probability equation using the diffusivity given by Equation 3.19 to represent transport due to turbulence. The pair probability in the small total strain limit has the following form in the presence of the outer boundary:

$$\frac{P}{C_1^2} = \frac{8}{r^3}\left(\frac{r_\infty^3 - r^3}{r_\infty^3 - 8}\right) \tag{4.34}$$
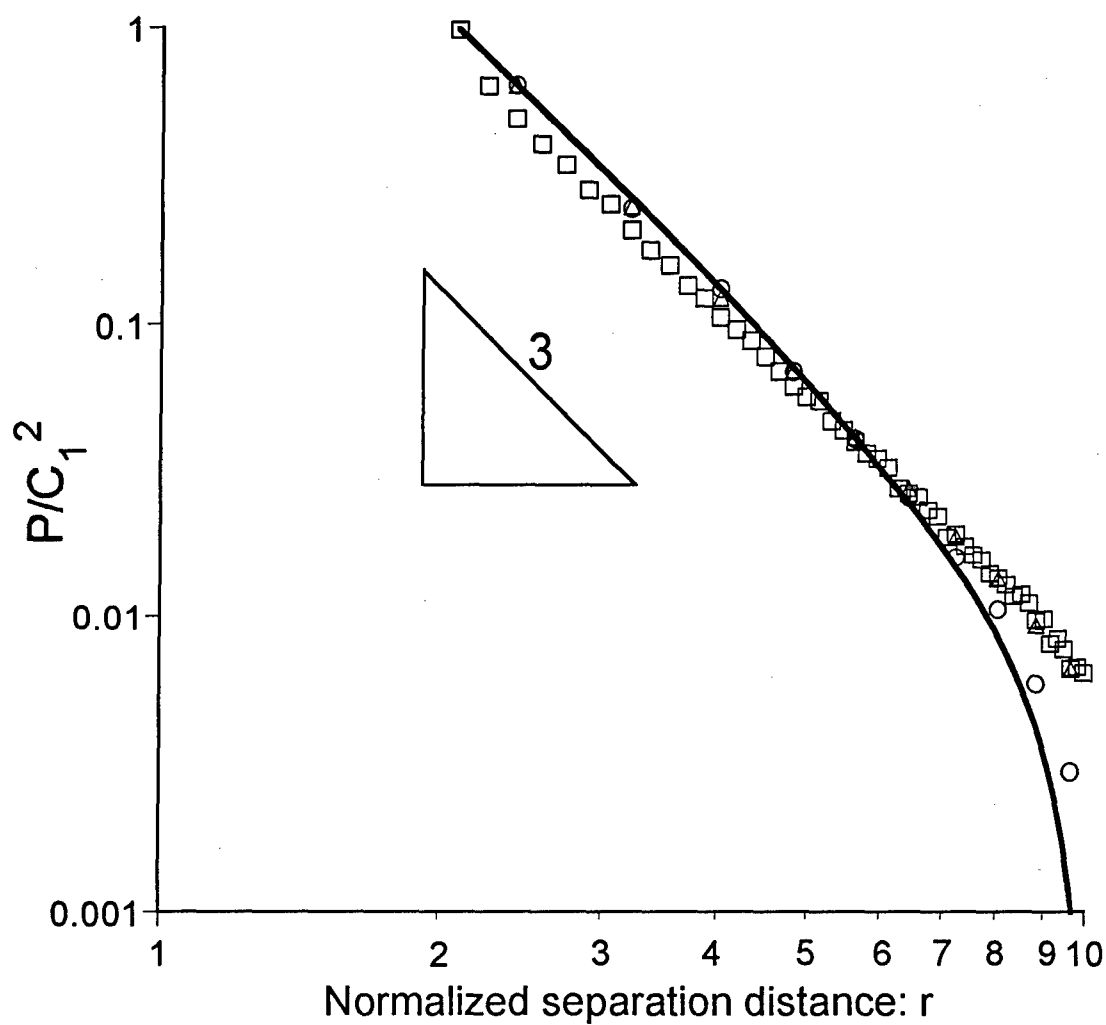
**Figure 4.9**: Radial concentration profiles calculated for $(\tau_s\Gamma_\eta, \tau_r\Gamma_\eta) =$ (0.23, 0.72) (O), (2.3, 7.2) ($\triangle$) and ($\infty$, $\infty$) ($\square$). The solid line represents the analytical prediction valid in the limit of small total strain.

where the term in the parentheses corrects for the finite size of the computational domain. Results for $\tau_S\Gamma_\eta \to 0$, $\tau_R\Gamma_\eta \to 0$ are shown as the solid line in Figure 4.9. Effects of the finite outer boundary became important at about r = 7 in the small total strain limit and are characterized by a more rapid decrease in the concentration relative to the $1/r^3$ decay. This behavior is closely matched by the $(\tau_S\Gamma_\eta, \tau_R\Gamma_\eta) = (0.23, 0.72)$ simulations shown with the circles.

## 4.4 Turbulent coagulation for interacting particles

It is reasonable to expect that particle interactions such as hydrodynamic interactions and van der Waals forces will affect the turbulent coagulation rate. Hydrodynamic interactions are the result of viscous drag on the colloidal particles and the lubrication forces that amass in the gap between two colliding particles. Without a compensating attractive interparticle force, hydrodynamic interactions prevent particle collision. At small particle separations, attraction due to dispersion (i.e., van der Waals) forces can overcome the viscous resistance to collision and lead to particle contact. The inclusion of these two forces into the coagulation kernel provides the minimum requirements to predict experimental results. In this section, alterations to the simulation procedure are described — most notably, the simulations must be performed by a less efficient forward integration in time. Then the effects of varying the particle size, relative strength of van der Waals to hydrodynamic forces and the total strain (rotation) are examined.

### 4.4.1 *Simulation method*

In contrast to the situation without particle interactions, the particle conservation equation is neither linear nor time reversible when interactions are included. This means the efficient time-reversed simulation method used in the non-interacting case (see Section 4.3.1) can no longer be employed. Instead, the coagulation rate constant was calculated from the trajectories of particles released at $r = r_\infty$ that reached the excluded volume surface of the test sphere. For large values of $r_\infty$ this methodology became very inefficient as most particles created at the outer simulation boundary left the simulation domain without interacting with the test particle. The efficiency of the calculation was improved by decreasing $r_\infty$; however, this came at the expense of some degree of computational accuracy as described in Section 4.3.1

In these simulations $r_\infty = 5$ was selected as a compromise between the error resulting from using a small simulation domain and the inefficiency of the forward time numerical computations for large simulation domains. As discussed in Section 4.3.1, the finite value of $r_\infty$ can affect the calculated value of $k^0$ in the diffusion limit. Using Equation 4.32, $k^0$ is expected to be overestimated by as much as 6% as the total strain is decreased. Simulations of non-interacting particles conducted at several values of $\tau_S \Gamma_\eta$ and $\tau_R \Gamma_\eta$ were used to develop corrections for the finite box size. Using simulations for non-interacting particles to assess the effect of $r_\infty$ was deemed to be reasonable because interactions were weak at $5 < r_\infty < 10$. For each total strain examined, several realizations at $r_\infty = 5$ and $r_\infty = 10$ were computed using the same random number seeds to

minimize statistical fluctuations. Using $r_\infty = 5$ had less than a 2% effect, with the impact decreasing with increasing total strain. This result suggests that the smallest total strain examined in the simulations presented below was larger than that required for the pair diffusion formulation to become valid. Corrections on the order of 2% were not considered to be statistically significant, so the simulation results obtained with $r_\infty = 5$ are presented here without correction.

For the case of interacting particles, the computer program generated a unique realization of the flow field and computed the relative trajectories of the particles using the full equation of particle motion given by Equation 4.25. At each time step, a modified form of Equation 4.27 was used to determine if a particle should be created at $r = r_\infty$. Instead of evaluating Equation 4.27 using the hydrodynamic conditions at $r = \sigma$, the local flux was evaluated at $r = r_\infty$ and $(\mathbf{u} \cdot \mathbf{n})_{MAX} \approx r_\infty \langle \Gamma_{11}^2 \rangle^{1/2}$. This methodology for particle creation assumed that at large separations the particles follow the fluid motion, so the flux at the outer simulation boundary was accurately represented by $(\mathbf{u} \cdot \mathbf{n})C_1$. Indeed, at $r = 5$ the hydrodynamic interactions due to a linear flow have only a 3.5% effect on the particle radial velocity while van der Waals forces between a newly created particle and the test sphere are negligible.

The simulation tracked the particles until they either collided with the test sphere or left the simulation boundary. Statistics on the average influx of particles through the excluded volume surface, Q, were collected periodically until steady state was reached. The program then computed the average coagulation rate for each flow field realization as before using

the relation $k = Q/C_1$. The particle concentration at $r = r_\infty$, $C_1$, was given by Equation 4.31 evaluated at $r_\infty$ rather than $\sigma$.

Traversing the lubrication regime, where the gap thickness is small compared to the particle radius and hydrodynamic forces are significant, was expected to be the rate limiting step for coagulation; therefore, it was essential that the simulations accurately resolved the motion at small particle separations. The maximum local integration error of 1% set previously also kept the simulation sufficiently accurate in the lubrication region. When two particles were separated by small gap widths, the time step was automatically refined by the error control algorithm to reflect the large van-der-Waals- and hydrodynamic-induced particle fluxes.

Adding interparticle interactions led to another difficulty, namely: at particle contact both the hydrodynamic interaction and the van der Waals forces diverge. The singularities in the van der Waals and hydrodynamic interactions were avoided by choosing a collision radius slightly larger than the particle diameter, $r = \sigma + 0.01\lambda$. At this particle separation, the relative particle velocity induced by the van der Waals attraction overwhelmed effects of the flow resistence and the particles were assumed to colloid in the next time step.

### 4.4.2 *Simulation results*

Along with the total strain and rotation, two additional parameters govern the coagulation dynamics in systems with particle interactions, namely: the shear number, $N_S$, describing the relative importance of viscous and van der Waals forces, and $N_L$, the ratio of the particle radius to the London retardation wavelength (i.e., the length scale over which van

der Waals attraction decays) (see Table 4.1). In this section the effects of varying the shear number and particle size are considered for coagulation in isotropic turbulence. The effect of varying the total strain and rotation on the coagulation rate constant and the collision efficiency for a single particle size and shear number are also evaluated.

Simulations in isotropic turbulence ($\tau_S \Gamma_\eta = 2.3$ and $\tau_R \Gamma_\eta = 7.2$) were run for $N_L = 237, 474$ and $4740$ corresponding to 3.9, 7.6 and 76 μm diameter particles in a flow characterized by $N_S$ ranging from $10^{-1}$ to $10^9$. Results from these simulations, plotted as the collision efficiency, $\alpha$, versus $N_S$, are shown in Figure 4.10 along with error bars denoting +/- one standard deviation. The results indicate that the effect of particle interactions is significant. For the parameter range investigated, the collision efficiency is smaller than about 50%, indicating that fewer than 1 out of 2 collisions that occur in the non-interacting case actually transpire when particle interactions are included in the analysis. Increasing the particle size adversely affects the collision efficiency because lubrication forces are more significant for larger particles. For each particle size the collision efficiency goes through a maximum at a critical $N_S = N_S^*$ that depends on the particle size. Within the error, the data for all three particle sizes collapses onto a single curve to the right of the maxima.

The maximum in the collision efficiency indicates that there is an optimal combination of shear rate and particle size that results in the most efficient coagulation. The interplay of mechanisms that leads to the maximum in the collision efficiency for each particle size can be understood by considering the relative velocity due to turbulent shear and

**Figure 4.10:** The collision efficiency, $\alpha$, as a function of the shear number, $N_S$, for various particle sizes ($N_L$). The symbols represent a = 1.9 $\mu$m ($\square$), 3.8 $\mu$m (O) and 38 $\mu$m ($\triangle$) and the error bars are +/- one standard deviation. The power law fit was obtained by non-linear regression of the data to the right of the maximums.

$$\alpha = \frac{0.6 N_S^{-0.11}}{\ln(N_S)^{0.29}}$$

Collision efficiency

$N_S$: Increased shear rate

$N_S$: Increased particle size
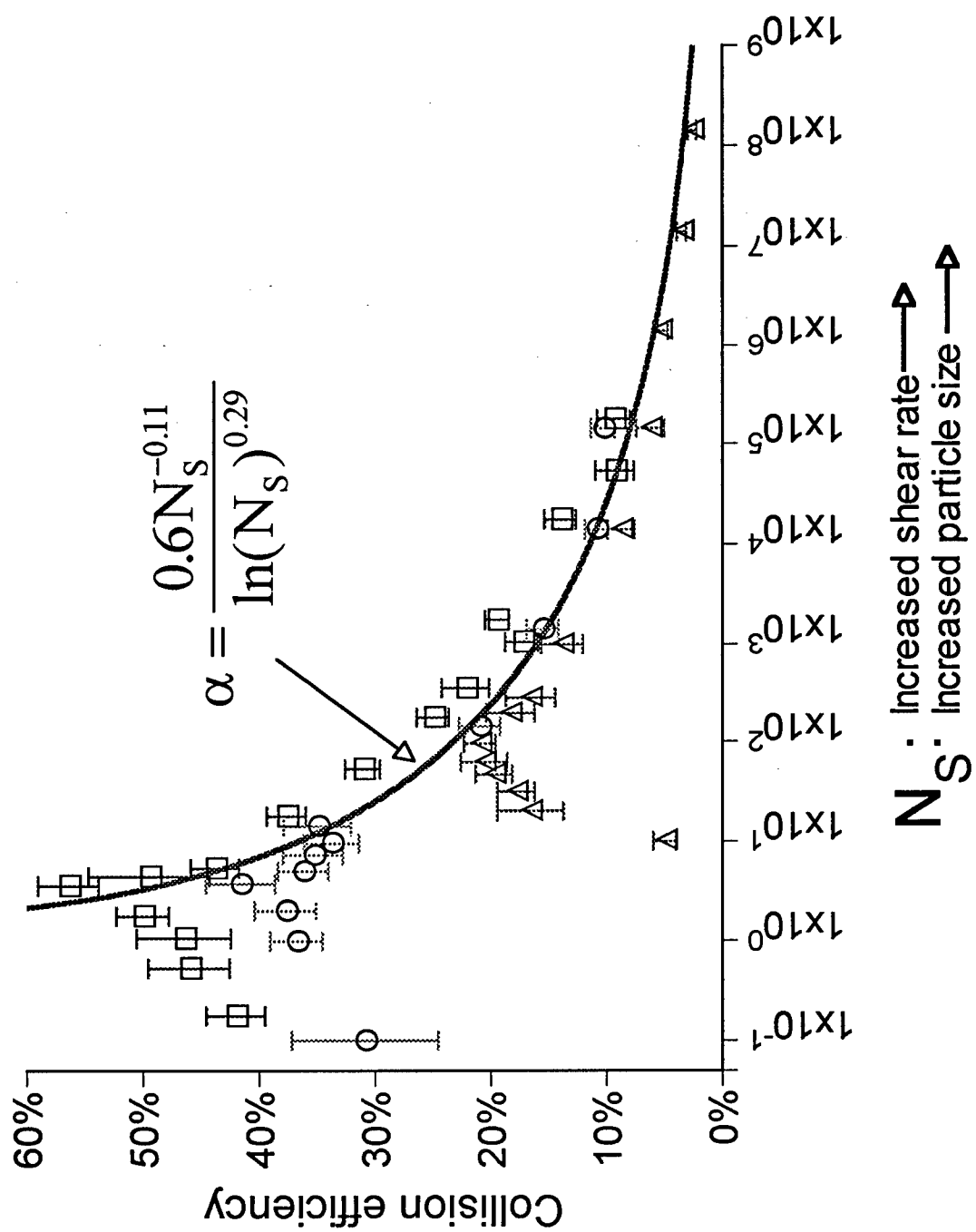
the van der Waals force at separations where the van der Waals force becomes significant. At this gap width van der Waals attractions have sufficient magnitude to draw the particles together. Depending on the particle size, the critical gap width scales with either the London retardation length, or, if the particles are small enough, the length scale at which lubrication forces break down. In the lubrication regime (i.e., $\xi \ll 1$), the velocity due to the fluid shear, $V_S$ is proportional to $\Gamma_\eta \sigma(1-A(r))$ where the lubrication resistance to motion, $1-A(r)$, is $4.077\xi$ (Russel et al., 1989). Furthermore, the relative particle velocity due to the van der Waals force scales in proportion to $V_{VDW} \sim A_H G(r)/12\pi\mu\xi^2$, where the lubrication resistance to motion $G(r) = 2\xi$ (Russel et al., 1989). Balancing these two velocities yields:

$$\frac{V_S}{V_{VDW}} \sim C^2 \xi^{*2} N_S* \qquad (4.35)$$

where $\xi^*$ is the critical gap width at which van der Waals forces become important and it is defined as the minimum of $4\pi/N_L$ and 0.1. $\xi^* = 4\pi/N_L$ corresponds to a gap width of $\lambda$ and $\xi^* = 0.1$ is meant to characterize the gap width at which lubrication forces break down. $N_S*$ in Equation 4.35 is the critical shear number that gives the maximum collision efficiency, and C is a constant found to be about 10 when balancing the turbulent shear and van der Waals attraction. When $C^2 \xi^{*2} N_S = 1$, the turbulent shear is just strong enough to bring the particles to the gap widths where van der Waals forces dominate and collision is assured. For $C^2 \xi^{*2} N_S > 1$, particle motion due to turbulence dominates van der Waals forces so particles are

pushed toward smaller gap widths before van der Waals forces take over and allow the particles to collide. Since lubrication resistence is higher for relative movement due to shear, the collision efficiency decreases when the shear dominates to smaller gap widths. When $N_S > N_S^*$ Figure 4.10 shows that the collision efficiency is nearly independent of the particle size (i.e., independent of $N_L$). This is because the point at which van der Waals forces take over from the lubrication force and draws the particles together is much smaller than the retardation length, so $\lambda$ and hence $N_L$ become irrelevant. At the opposite extreme, when $C^2 \xi^{*2} N_S < 1$ turbulent shear is too weak to transport the particle to gap widths comparable to $\xi^*$. As a result, van der Waals forces are unable to cause particle collision and the collision efficiency declines.

The prediction for $N_S^*$ obtained from the force balance (Equation 4.35) is compared in Figure 4.11 with the simulation data. Here the critical $N_S = N_S^*$ is plotted against $N_L$, where $N_L$ is the ratio of the particle size to the London wavelength (see Table 4.1). The critical shear number dependence on $N_L$ is shown for the three particle sizes given in Figure 4.10 as well as for particle diameters of 12.5, 25, 40 and 159 $\mu$m. The solid line with C = 40 is the prediction for $N_S^*$ valid when $\lambda$ characterizes the distance at which van der Waals forces becomes important. As $N_L$ decreases the particle radius rather than the London retardation length is the appropriate scaling for the van der Waals force. Letting $\xi^* = 0.1$ and C = 20 gives the dashed line. The critical shear number prediction given by the solid line works well for the large particles (i.e., $N_L \geq 2000$), but it
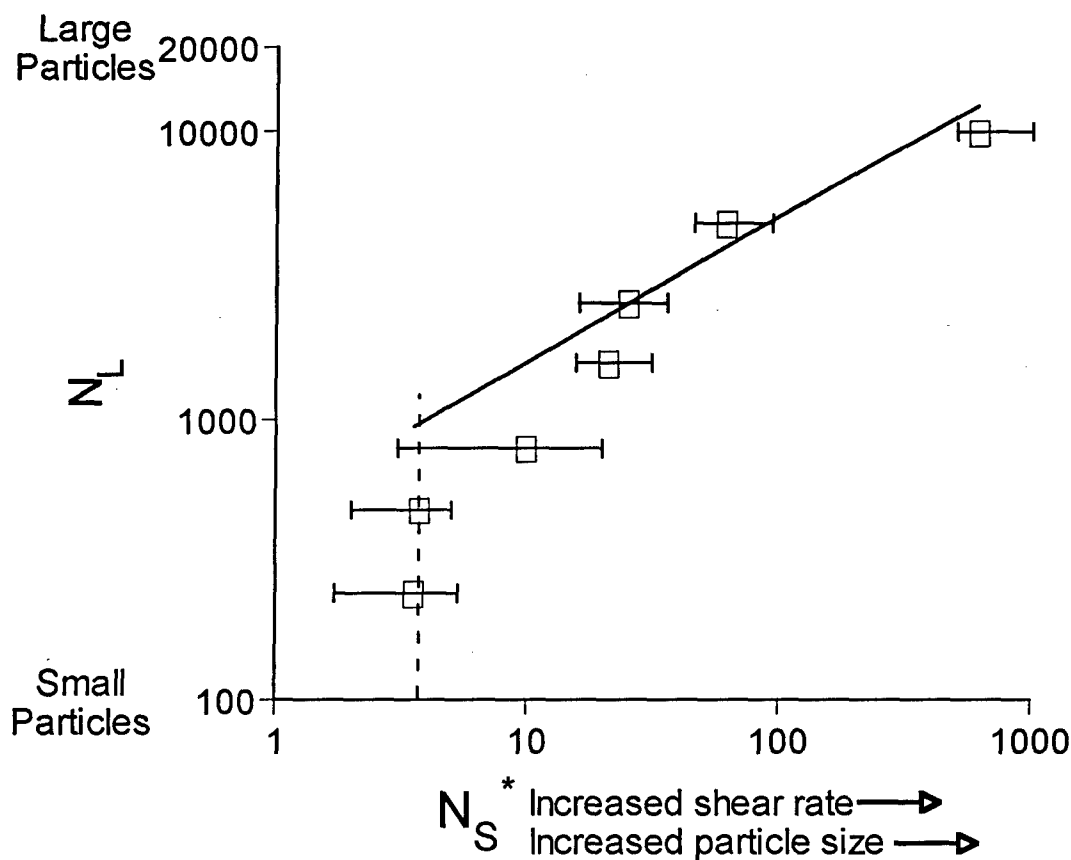
**Figure 4.11**: The dependence of the particle size ($N_L$) on the critical shear number, $N_S$*, at which the collision efficiency goes through a maximum. The line are scaling predictions assuming that flux due to the velocity gradient field and that due to the van der Waals attraction are balanced at the maximum collision efficiency. The solid line applies to large particles where the characteristic length scale for the van der Waals attraction scales with the London retardation length. The dashed line applies for small particles where the particle radius provides the correct length scale for the van der Waals attraction.

underestimates $N_S^*$ for $N_L \lesssim 2000$. For the two smallest particles ($\sigma = 3.9$ and 7.8 $\mu m$) simulated, $N_S^*$ seems to be independent of $N_L$, in agreement with the scaling that uses the particle radius as the characteristic length scale for the van der Waals forces.

The scaling relation developed above to explain the maximum in the collision efficiency curves is based upon the concept that the van der Waals attraction force acts to draw particles together once the turbulence has transported them to a critical separation distance. For shear numbers above the critical value, the turbulence has sufficient strength to bring the particle pair to separations smaller than $\lambda$, beyond which point van der Waals attractions inevitably cause a particle collision. It follows that the collision efficiency could be estimated by calculating the particle flux through the critical separation distance ($\xi = \xi^*$) by using an estimate for the pair probability based upon hydrodynamically interacting particles (without van der Waals attraction). This analysis assumes that the pair probability is unperturbed by the van der Waals attraction for gap widths larger than the critical separation, so the effect of van der Waals attractions can be ignored when estimating the pair probability. For $N_S > N_S^*$, the gap width at which the shear and van der Waals forces balance is less than the London wavelength; therefore, consideration can be restricted to the non-retarded van der Waals potential and the lubrication region. Batchelor & Green (1972) derived the pair probability for particles influenced by hydrodynamic interactions in a linear flow. In the lubrication regime ($\xi \ll 1$) they obtained:

$$P(\xi) \approx \frac{0.234 C_1^2}{\xi^{0.781}[\ln(1/\xi)]^{0.29}} \qquad (4.36)$$

as before, $C_1^2$ is the pair probability of singlet particles at large particle separations. Although this result is applicable to linear flow fields with open streamlines, it is used here to interpret the simulation results for the unsteady turbulent flow.

An estimate for $\alpha$ may be obtained by taking the ratio of the particle flux at $\xi^*$ with hydrodynamic interactions to the particle flux in the absence of particle interactions. The critical gap width, $\xi^*$, is given by the flux balance used to calculate Equation 4.35. The result is $\xi_c \sim N_S^{1/2}$ and, after some manipulation, the following prediction for the collision efficiency results:

$$\alpha = \alpha^0 \frac{N_S^{-0.11}}{[\ln(N_S)]^{0.29}} \qquad (4.37)$$

where $\alpha^0$ is an order one constant. The solid line in Figure 4.10 is the collision efficiency predicted using Equation 4.37 where $\alpha^0 = 0.6$. For the simulation data to the right of the maximum, $N_S > N_L^2/C^2$, Equation 4.37 fits the data with an $r^2$ of 94%. By assuming the primary contribution to the collision efficiency comes from the difference in the pair probability with and without hydrodynamic interactions, Equation 4.37 is able to predict the variation of $\alpha$ with the shear number.

For subsequent comparison with other calculations, it is useful to note that for $N_S > 10$ and $N_S > N_S^*$, Equation 4.37 behaves like a power law of the form:

$$\alpha = 0.52 N_S^{-0.16} \qquad (4.38)$$

Since the normalized coagulation kernel is $k = \alpha k^0$, this implies that the coagulation rate constant increases with $\Gamma_\eta^{0.84}$ for isotropic turbulence.

Comparing this estimate with values predicted for the asymptotic limits of small and large total strain is worthwhile. Predictions derived for non-Brownian particles in the small strain limit indicate that $k \sim \Gamma_\eta^{0.89}$ (Chapter 3; Brunk et al., 1997a). Compared with the moderate total strain result, coagulation is slightly less retarded by particle interactions in the diffusion limit. As previously noted, the presence of hydrodynamic drift that brings the particles close together increases the collision efficiencies in the small strain limit (Chapter 3; Brunk et al., 1997a). To the authors' knowledge the effects of particle-particle interactions have not been computed for turbulent flows in the limit of large total strain.

Computations of collision efficiencies in steady linear flows, however, are prevalent (Greene et al., 1994; van de Ven & Mason, 1977; Zeichner and Schowalter, 1977; Adler, 1981). Recent trajectory calculations computed for a number of steady linear flows have shown that the stability factor for flows with more strain than vorticity is nearly insensitive to flow type, except for flows similar to simple shear (Greene et al., 1994). In the large total strain limit, the pseudo-stationary linear flow field around a test particle can be conceptualized as an ensemble average

over all possible linear flows; therefore, the collision efficiency in the large strain limit is expected to correspond to the average collision efficiency for all possible steady linear flows. Based upon Greene et al.'s conclusion that collision efficiency is insensitive to flow type $\alpha$'s calculated for simple shear and uniaxial extension are considered.

Zeichner & Schowalter (1977) calculate the stability factors for uniaxial extension and simple shear for particles influenced by retarded van der Waals attraction and hydrodynamic interactions. An examination of their computations (Zeichner & Schowalter, 1977) reveals that k is proportional to $\Gamma_\eta^{0.77}$ for simple shear (using the correction published in Feke & Schowalter, 1983) and $\Gamma_\eta^{0.89}$ for uniaxial extension. In isotropic turbulence ($\tau_S\Gamma_\eta = 2.3$ and $\tau_R\Gamma_\eta = 7.2$), the dependence of k on the shear rate is intermediate between the steady linear flow cases.

Based on the above analysis, variations of the coagulation rate constant can be predicted as a function of the total strain when the shear number and particle size are held constant. In the small total strain limit the asymptotic approximation valid when the interparticle forces decay in the lubrication regime gives the normalized coagulation rate constant, k $\approx$ $0.25(\tau_S\Gamma_\eta)^{0.89}N_S^{-0.11}$ (Chapter 3; Brunk et al., 1997a). The estimate for isotropic turbulence comes from combining $k^0 = 8.62$ and Equation 4.38 to yield k $\approx 5N_S^{-0.16}$. At large total strain, $k^0 = 9.96$ and k $\approx 5.6N_S^{-0.23 \text{ to } -0.11}$, where the collision efficiency preexponential factor given in Equation 4.38 was used to estimate the collision efficiency coefficient in the large total strain limit. These power laws suggest that the simulated coagulation rate should remain relatively constant or decrease slightly from moderate to

large total strains. For small total strain the coagulation rate should decrease because the coagulation rate constant depends on a positive power of the total strain.

The effect of simultaneously varying $\tau_S\Gamma_\eta$ and $\tau_R\Gamma_\eta$ is shown in Figure 4.12. The results are for 3.8 μm diameter polystyrene particles ($N_L = 237$) in turbulent flows with shear rates of 28 $s^{-1}$ ($N_S = 1761$) and 280 $s^{-1}$ ($N_S = 17610$). The symbols represent the simulation data for $\Gamma_\eta = 28$ $s^{-1}$ (squares), and $\Gamma_\eta = 280$ $s^{-1}$ (circles). Comparing Figures 4.12 and 4.7 shows that at small total strain k has the same trend as $k^0$; an increase in the normalized coagulation rate constant is seen with increasing total strain up to $\tau_S\Gamma_\eta \sim 1$. Beyond $\tau_S\Gamma_\eta \sim 1$ the normalized coagulation rate constant goes through a minimum at $\tau_S\Gamma_\eta \sim 5$. Differences in coagulation rate constant calculations at total strains of 1 and 5 are statistically significant (z-test, $p = 0.026$ when $N_S = 1761$ and $p = 0.003$ when $N_S = 17610$). Within the statistical uncertainty of the data, the normalized rate constant remains unchanged as the total strain increases above $\tau_S\Gamma_\eta \sim 5$; however, the fact that both data sets show the normalized rate constant increasing again for total strains above 5 does lend some credence to the trend.

The relative drop in the coagulation rate constant when going from $\tau_S\Gamma_\eta$ of 1 to 5 can be used to estimate the Kolmogorov shear rate power law expected in the large total strain limit. In the absence of interparticle interactions, the normalized rate constants differ slightly (compare $k^0 = 8.62$ for isotropic turbulence and $k^0 = 9.96$ in the large total strain and large total rotation limit). Assuming the pre-exponential factors for interacting
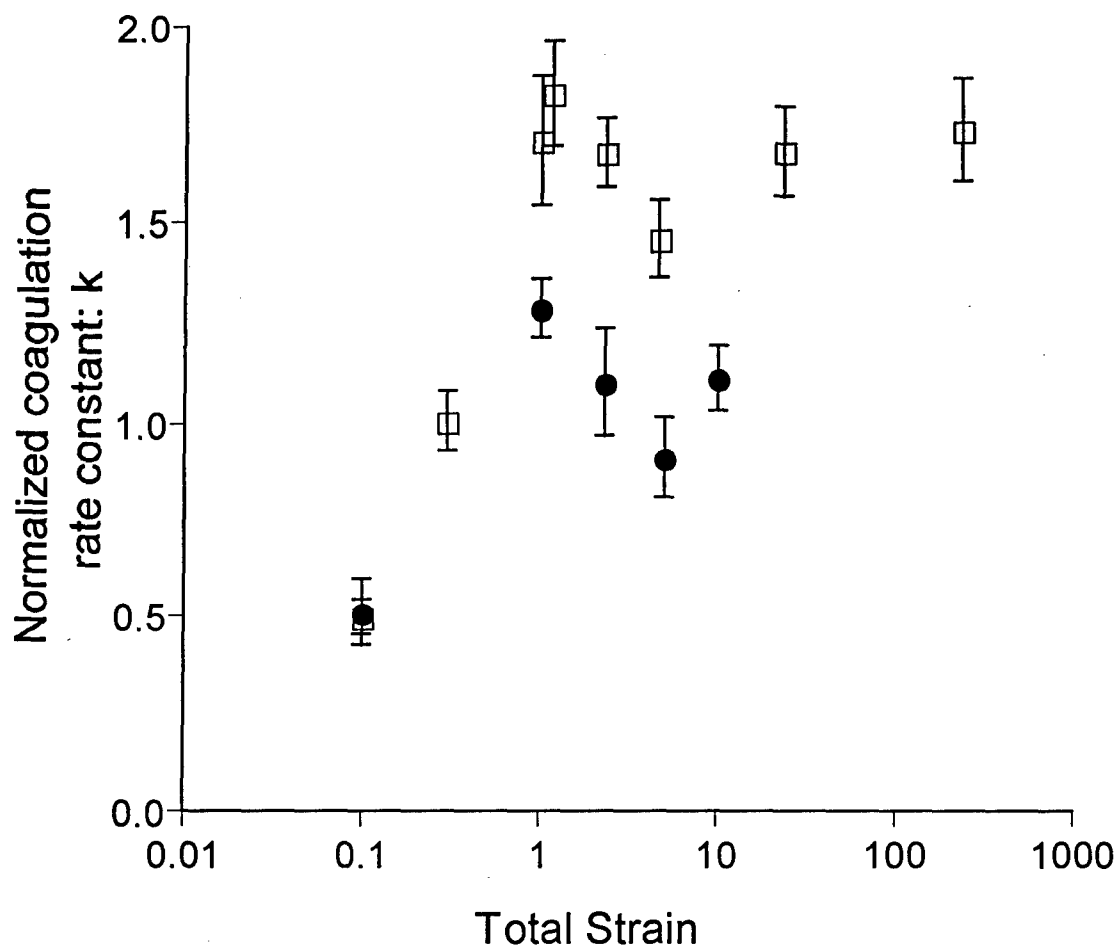
**Figure 4.12**: The coagulation rate constant against the total strain for 1.9 μm radius particles and $N_S = 1761$ (□) and $N_S = 17610$ (●). Symbols represent the simulation data and the error bars are +/- one standard deviation from the mean. Results are for a fixed ratio of total rotation to total strain equal to 3.13.

particles at moderate and large total strain are similar, the two data sets in Figure 4.12 suggest that $k \sim \Gamma_\eta^{0.78}$ at large total strain. This dependence on the shear rate is more closely aligned to the prediction for simple shear (Feke & Schowalter, 1983) than with uniaxial extension (Feke & Schowalter, 1983).

The apparent correspondence between the large total strain limit and the simple shear rates might have been expected. In both simple shear and turbulence, the shear rate partitions equally between rotational and extension components. The importance of rotation has been demonstrated to decrease the coagulation rate in both the random flow discussed in this chapter and steady linear flows (Greene et al., 1994).

The collision efficiency, $\alpha = k/k^0$, calculated from the data presented in Figure 4.12 is shown in Figure 4.13. $\alpha$ varies between 16 and 30% for the $\Gamma_\eta = 28$ s$^{-1}$ computations (squares) and between 10 and 30% for the $\Gamma_\eta = 280$ s$^{-1}$ simulations. In both cases, the small total strain calculations show the largest collision efficiencies. In the small total strain limit the collision efficiency varies as $\alpha \approx (\tau_s \Gamma_\eta)^{-0.11} N_s^{-0.11}$, which increases as the total strain decreases. The reason coagulation at small total strain is more efficient may be explained by considering the relative motion of two particles in the large and small total strain limits. Neglecting the influence of closed stream lines, at large total strain interacting particles have essentially one opportunity to interact and collide before the persistent flow field sweeps them away from each other. In the diffusive limit, particle trajectories are random and a pair of particles will have multiple encounters before they separate. Thus each particle pair is given several chances to
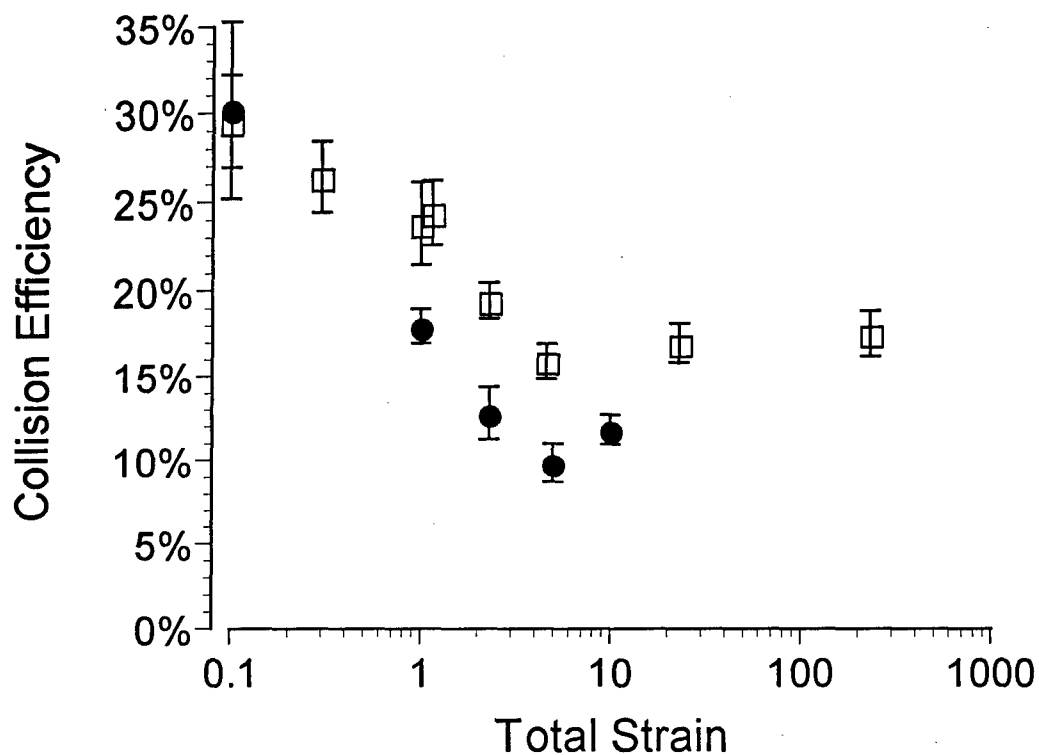
**Figure 4.13**: The effect of simultaneously varying $\tau_S\Gamma_\eta$ and $\tau_R\Gamma_\eta$ on the collision efficiency for 1.9 $\mu$m radius particles when $N_S = 1761$ ($\square$) and $N_S = 17610$ ($\bullet$). The error bars are +/- one standard deviation from the mean and the ratio of total rotation to total strain is held fixed at 3.13.

collide in the small strain limit and that increases the probability that the two particles will have a successful collision.

## 4.5 Conclusion

The objectives of this study were threefold: 1) to develop a simulation method, valid at arbitrary total strain and rotation, that could be used to compute the trajectories of coagulating particles with radii smaller than the Kolmogorov length of turbulence; 2) to compare the coagulation rate constant for non-interacting particles at arbitrary total strain to the asymptotic limits of large and small strain derived previously (Saffman & Turner, 1956; Chapter 3; Brunk et al., 1997a); and 3) to compute the effect of particle interactions on coagulation in isotropic turbulence.

The relative motion of a particle pair was simulated by solving an equation of motion valid for particles with diameters smaller than the Kolmogorov length scale. The velocity field was assumed to be a randomly varying, locally linear flow field. The velocity gradient was expanded as a temporal Fourier series with components constrained to reproduce the two-time Lagrangian statistics of the fluctuating turbulent velocity gradient tensor. Resulting simulations for the non-interacting particles indicate that both large and small total strain asymptotes overestimate the actual coagulation rate. A hyperbolic interpolation of the asymptotic limits reproduces the numerical calculation to within 5% of the actual values; thus, by knowing the asymptotic forms in the diffusion (Chapter 3; Brunk et al., 1997a) and pseudo-stationary limits, the behavior in the intermediate regime can be estimated over the range of strain rate

correlation times. Saffman & Turner (1956) provide an estimate for the coagulation rate valid for irrotational flows in the large total strain limit; however, their result over predicts the turbulent coagulation simulations in this limit by about 5%. Rotation is shown here to decrease the observed coagulation rate at large total strain and the absence of rotation in the Saffman & Turner model explains the discrepancy with these computer simulations.

The presence of rotation is thought to lead to recirculating streamlines in the flow. Since coagulation is limited to open streamlines that can bring particles from the bulk, the presence of curved stream lines that leave and return to the excluded volume surface decreases the coagulation rate. Additional investigations into the separate effects of the strain and rotation rate correlation times show that the coagulation rate decreases as the rotation rate correlation time increases. This decrease results from persistent recirculating streamlines that form in the system at large total rotation. At small $\Gamma_\eta \tau_R$, rotation does not effect the coagulation rate because there is some probability that as the velocity field evolves, a particle on a stream line that returns to the excluded volume surface of the test sphere can escape its trajectory before returning to $r = \sigma$.

The consideration of hydrodynamic interactions and retarded van der Waals attractions leads to significant decreases in the computed coagulation rate constant. For instance, a 4 μm diameter particle experiencing $\Gamma_\eta = 10 \text{ s}^{-1}$ has a collision efficiency, $\alpha$, of about 20%. In other words, only one collision between interacting particles occurs for every five that occur in the absence of interparticle interactions. For a

given particle size an optimal shear rate that leads to a maximum coagulation efficiency exists. At the maximum collision efficiency, the turbulent shear is just strong enough to bring the particle pair to gap widths at which van der Waals forces can take over and cause a collision. For larger shear rates, the turbulence drives the particles to small gap widths before the van der Waals attraction is sufficient to cause a collision. Since lubrication forces increase with decreasing gap width, the large shear rates experience a larger resistence to collision and the transport efficiency of the turbulence declines. For weak turbulence, the shear is not strong enough to transport particles to gap widths where van der Waals forces are significant and therefore the collision efficiency is lower. A simple balance based on the turbulent particle flux and the flux due to the van der Waals attractive forces predicts the location of the maximum collision efficiency.

Simulations performed at a constant shear number (i.e., ratio of viscous to van der Waals forces) and various values of the total strain show that order one total strains have the highest coagulation rate. Two competing effects lead to this result: the transport rate of the flow field and the probability that two interacting particles will collide before the flow field transports them away from each other. The rate of transport toward the test sphere increases with total strain as the transport mechanism changes from diffusive transport at small total strain to transport in a pseudo-steady flow field at large total strain. The higher rates of transport found at large total strains increase the coagulation rate constant because more particles are available for coagulation. Working against this process is the efficiency of the particle encounters. In simplest terms, at large total

strain, approaching particles have essentially one opportunity for successful collision before the persistent flow field carries them away from each other. In contrast, in the diffusive limit of small total strain, particle positions fluctuate randomly so that approaching particles will undergo many close encounters before they either collide or are transported away from each other. The many opportunities for collision available in the diffusion limit increases the probability that the particles will actually collide, so the efficiency of the process is higher than at large total strain. The synergistic combination of relatively efficient particle transport and multiple particle encounters that occurs for total strains of order one explains why flows with moderate total strain have the highest coagulation rate.

The simulations conducted in this research are an important step in improving the understanding of colloidal aggregation in turbulence. Coagulation rates have been computed for experimentally realizable particle sizes, shear rates and Hamaker constants. What remains is to obtain accurate experimental measurements of turbulent coagulation to verify the model predictions. In Chapter 6, turbulent coagulation rates are measured for monodisperse particles under conditions of isotropic turbulence created by an oscillating grid reactor and the results are compared to the simulations (Chapter 6; Brunk et al., 1997b). The apparatus used for these experiments is described and characterized in Chapter 5.

# REFERENCES

ADLER, P. M. 1981 Heterocoagulation in shear flow. *J. Coll. Int. Sci.* **83**(1), 106-115.

BATCHELOR, G. K. & GREEN, J. T. 1972 The hydrodynamic interaction of two small freely-moving spheres in a linear flow field. *J. Fluid Mech.* **56**(2), 375-400.

BATCHELOR, G. K. & GREEN, J. T. 1972 The determination of the bulk stress in a suspension of spherical particles to order $c^2$. *J. Fluid Mech.* **56**(3), 401-427.

BATCHELOR, G. K. 1976 Brownian diffusion of particles with hydrodynamic interaction. *J. Fluid Mech.* **74**(1), 1-29.

BROWN, B. W. & LOVATO, J. April 1996 *RANLIB.C: Library of C Routines for Random Number Generation*, NETLIB, NETLIB.ATT.COM.

BRUNK, B. K., KOCH, D. L. & LION, L. W. 1997a Hydrodynamic pair diffusion in isotropic random velocity fields with application to turbulent coagulation. *Accepted by Phys. Fluids*.

BRUNK, B. K., KOCH, D. L., & LION, L. W. 1997b Observations of coagulation in isotropic turbulence. *Submitted J. Fluid Mech.*

CAMP, T. R. & STEIN, P.C. 1943 Velocity gradients and internal work in fluid motion. *J. Bost. Soc. Civil Eng.* **30**(4), 219-237.

CASSON, L. W. & LAWLER, D. F. 1990 Flocculation in turbulent flow: measurement and modeling of particle size distributions. *AWWA J.* **8**, 54-68.

DAVIS, R. H. 1984 The rate of coagulation of a dilute polydisperse system of sedimenting spheres. *J. Fluid Mech.* **145**, 179-199.

DELICHATSIOS, M. A. & PROBSTEIN, R. F. 1975 Coagulation in turbulent flow: theory and experiment. *J. Coll. & Int. Sci.* **51**(3), 394-405.

FEKE, D. L. & SHOWALTER, W.R. 1983 The effect of Brownian diffusion on shear-induced coagulation of colloidal dispersions. *J. Fluid Mech.* **133**, 17-35.

GIRIMAJI, S. S. & POPE, S.B. 1990 A diffusion model for velocity gradients in turbulence. *Phys. Fluids A* **2**(2), 242-256.

GREENE, M. R., HAMMER, D. A. & OLBRICHT, W. L. 1994 The effect of hydrodynamic flow field on colloidal stability. *J. Coll. Int. Sci.* **167**, 232-246.

KIM, S. & KARRILA, S. J. 1991 *Microhydrodynamics: Principles and Selected Applications*, Chs. 7,11. Butterworth-Heinemann.

KRAICHNAN, R. H. 1970 Diffusion by a random velocity field. *Phys. Fluids* **13**(1), 22-31.

KRONE, R. B. 1978 *Estuarine Transport Processes*, (ed. B. Kferfve). University of South Carolina Press.

LEVICH, V. G. 1962 *Physicochemical Hydrodynamics*. pp. 139-231. Prentice-Hall.

MCCAVE, I. N. 1984 Size spectra and aggregation of suspended particles in the deep ocean. *Deep-Sea Research* **31**(4), 329-352.

O'MELIA, C. R. 1980 Aquasols: the behavior of small particles in aquatic systems. *Env. Sci. & Tech.* **14**(9), 1052-1060.

PEARSON, H. J., VALIOULIS, I.A. & LIST, E.J. 1984 Monte Carlo simulation of coagulation in discrete particle-size distributions. Part 1. Brownian motion and fluid shearing *J. Fluid Mech.* **143**, 367-385.

POPE, S. B. 1990 Lagrangian microscales of turbulence. *Phil. Trans. R. Soc. Lond. A.* **333**, 309-319.

POPE, S. B. 1996 *Turbulent flows (draft of chapters 1-7)*, Section 6.7.2.

RUSSEL, W. B., SAVILLE, D. A. & SCHOWALTER, W. R. 1989 *Colloidal Dispersions*. Cambridge University Press.

SAFFMAN, P. G. & TURNER, J. S. 1956 On the collision of drops in turbulent clouds. *J. Fluid Mech.* **1**, 16-30.

SCHENKEL, J. H. & KITCHENER, J. A. 1960 A test of the Derjaguin-Verwey-Overbeek theory with a colloidal suspension. *Trans. Faraday Soc.* **56**, 161-173.

SQUIRES, K. D. & EATON, J. K. 1991 Particle response and turbulence modification in isotropic turbulence. *Phys. Fluids A* **2**(7), 1191-1203.

STUMM, W. & MORGAN, J. J. 1981 *Aquatic Chemistry: An Introduction Emphasizing Chemical Equilibrium in Natural Waters*, Section 10.7. Wiley.

SURESH, L. & WALZ, J. Y. 1996 Effect of surface roughness on the interaction energy between a colloidal sphere and a flat plate. *J. Coll. Int. Sci.* **183**, 199-213.

SUNDARAM, S. & COLLINS, L. R. 1996 Numerical considerations in simulating a turbulent suspension of finite-volume particles. *J. Comp. Phys.* **124**, 337-350.

TENNEKES, H. & LUMLEY, J. L. 1972 *A First Course in Turbulence*. MIT Press.

TOWNSEND, A. A. 1951 The diffusion of heat spots in isotropic turbulence. *Proc. R. Soc. Lond. A* **209**, 418-430.

VAN DE VEN, T. G. M. & MASON, S. G. 1977 The microrheology of colloidal dispersions VII. Orthokinetic double formation of spheres. *Coll. Poly. Sci.* **255**, 468-479.

VON NEUMANN, J. 1951 Various techniques used in connection with random digits. *U.S. Nat. Bur. Stands. Appl. Math Ser.*, **12**, 36.

WANG, L. & MAXEY, M. R. 1993 Settling velocity and concentration distribution of heavy particles in homogeneous isotropic turbulence. *J. Fluid Mech.* **256**, 27-68.

YEUNG, P. K. & POPE, S. B. 1989 Lagrangian statistics from direct numerical simulations of isotropic turbulence. *J. Fluid Mech.* **207**, 531-586.

ZEICHNER, G. R. & SCHOWALTER, W. R. 1977 Use of trajectory analysis to study stability of colloidal dispersions in flow fields. *AIChE J.*, **23**(3), 243-254.

# CHAPTER 5:

# MODELING NATURAL HYDRODYNAMIC SYSTEMS WITH A DIFFERENTIAL-TURBULENCE COLUMN*

## 5.1 Introduction

Pollutant fate and transport in aquatic environments depend on complex physical, biological, and chemical mechanisms. Water quality management activities, including assessment of the impact of spills, remediation of contaminated sediment areas and location of sensitive facilities require understanding of not only the overall hydrodynamic circulation and transport patterns, but also the local details of turbulence/sediment/pollutant interactions within the water column. Current understanding of these systems is limited, and the development of environmentally sound practices and processes would benefit from a more precise understanding of the fate of pollutants discharged into water environments (NRC, 1989). For complete understanding of the interactions between hydrodynamic and physical/chemical processes within aquatic environments, careful study in a laboratory setting is a necessity. To this end, a new apparatus, termed a differential turbulence column

(DTC), has been built to provide a controlled laboratory environment for the study of natural hydrodynamic systems. Oscillating grids are used in the DTC to replicate turbulence levels typical of aquatic systems. An acoustic Doppler velocimeter (ADV, Sontek Inc.) coupled with a computer-driven positioning system provides characterization of the spatial distribution of turbulence and, *in situ* sampling and vertically spaced sample ports provide mechanisms for introducing chemical species and monitoring chemical dynamics.

The recently developed apparatus has several advantages over conventional flume-type hydrodynamic simulators for studying simultaneous chemical and hydrodynamic interactions. The DTC's self-contained structure allows detailed accounting of any chemical species introduced into the system. More importantly, the apparatus is ideal for studies of chemical processes over long time spans that are difficult to carry out in flume-type systems where time relates to distance. For instance, consider the case of particle trapping in a stratified estuary where the particle may undergo several processes including turbulent diffusion, transport across the density interface, coagulation and settling. Through dimensional analysis and scaling arguments, relative time scales can be assigned to each mechanism. Order of magnitude analysis suggests that particle flocculation and transport through the stratified layer will be rate limiting processes and will occur on time scales of several minutes. On the other hand, turbulent transport of momentum and mass are expected to occur on the order of seconds. Therefore, laboratory studies of physical/chemical reactions and transport processes under stratified

estuarine conditions may require resolution of time scales ranging from seconds to hours so that competing reactions can be observed. Simulating such a system in a conventional open channel flume would require an unacceptably long channel.

This chapter highlights the design of the DTC as well as the results of initial turbulence and sediment loading tests that characterize the hydrodynamics of the reactor. Turbulence in the DTC is quantified by comparing it to established grid-stirred turbulence scaling laws. Open channel flow turbulence and sediment loading are simulated in the DTC and compared with established behavior.

The particle transport time scaling described above (see also Chapter 1) suggests that turbulent transport of mass and momentum will appear steady on time scales appropriate for analyzing rate limiting processes like coagulation and transport across the salinity interface. Verification that the DTC can reproduce steady state turbulence intensity and sediment loading profiles is, therefore, an important first step in simulating the chemical and hydrodynamic behavior of more complex environmental systems.

## 5.2 The Differential Turbulence Column

The DTC (see Figure 5.1) is a 20 cm x 40 cm x 100 cm reactor designed to simulate a vertical section of a natural water column by reproducing hydrodynamic and chemical conditions typical of estuarine and riverine environments. The apparatus was designed to meet several criteria, including: 1) generation of vertical profiles in salinity and

Two axis
positioning
system

Sample
collector

One of two
water reservoirs

Five
individually
controlled
turbulence
generating
grids

Inline
filter

Baffled fill/drain
port
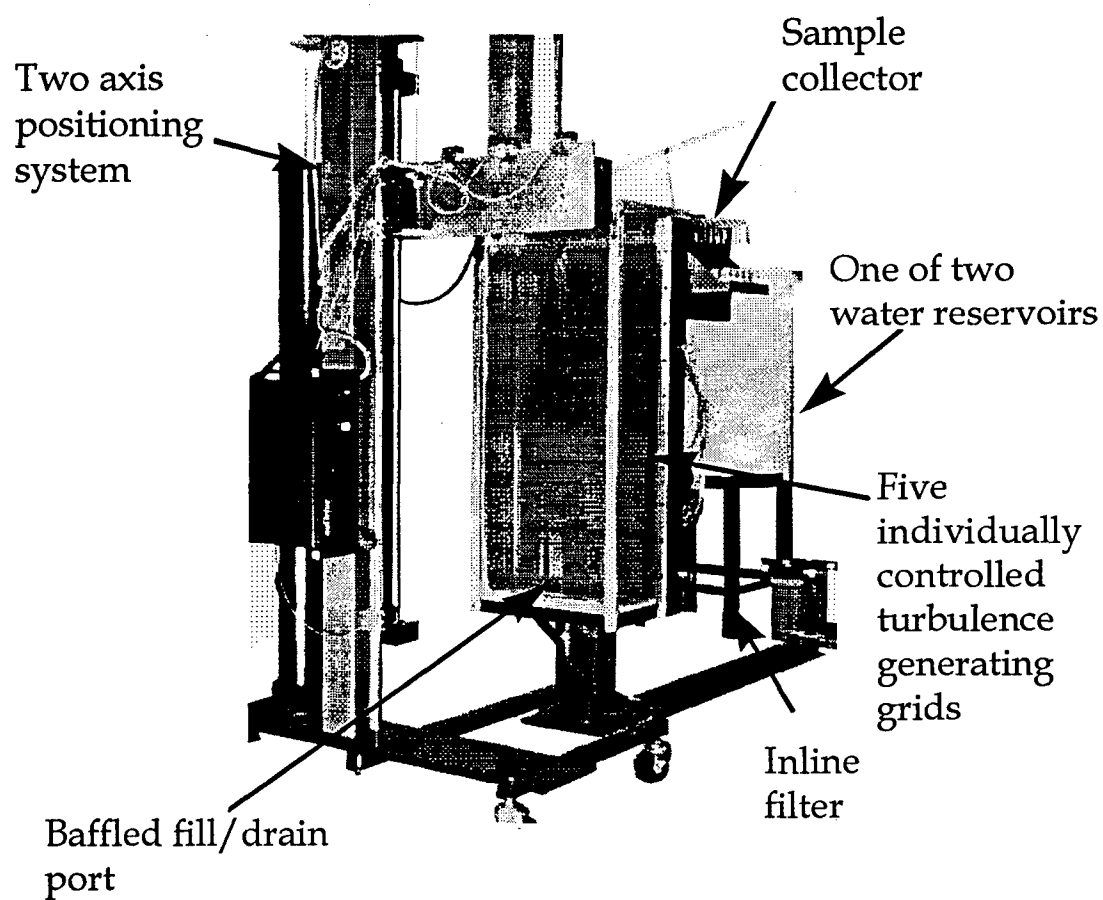
**Figure 5.1**: Differential Turbulence Column (DTC) with two-axis
positioning system.

turbulence, 2) provision for high resolution *in situ* sampling so that the details of pollutant and particle transport could be observed, 3) a closed system to simplify mass balances on chemical and physical species, and 4) automation for studies of long duration.

The schematic diagram shown in Figure 5.2 emphasizes the salient features of the DTC. Stainless steel comprises the back and base of the apparatus, while glass is used for the front, left and right sides to permit viewing of the system. The grid design used in the apparatus was modeled after the recommendations of other investigators who have used grid-stirred devices (Hopfinger & Toly, 1976; Thompson & Turner, 1975; De Silva & Fernando, 1992). Five horizontally oscillating grids, 40 cm wide by 20 cm high with a solidity of 37.6%, were equally spaced vertically along the back of the column. Each stainless steel grid is constructed of 2.67 mm rod woven into a square mesh with 1.27 cm center-to-center spacing. Linear bearings connected between the drive shafts and the grids allow movement in the horizontal direction only. The grid connecting rods are attached to drive wheels through ball joints. The radial location of the ball joint on the drive wheel can be adjusted to obtain grid strokes ranging from 10 to 40 mm in 5 mm increments. Each drive wheel is connected to an individually controlled electric gear motor capable of operating over a range from 1 to 8.5 Hz.

A baffled inlet/outlet allows the system to be filled with any combination of fresh and salt water to mimic the salinity profiles common to estuarine systems. Twenty sampling tubes at 5 cm intervals enter the DTC from the vertical centerline of the rear stainless steel panel. The

3-D View



Five independently
controlled turbulence
generating grids.

100 cm

Sample ports every

5cm down vertical
axis.

z

y

x

40 cm
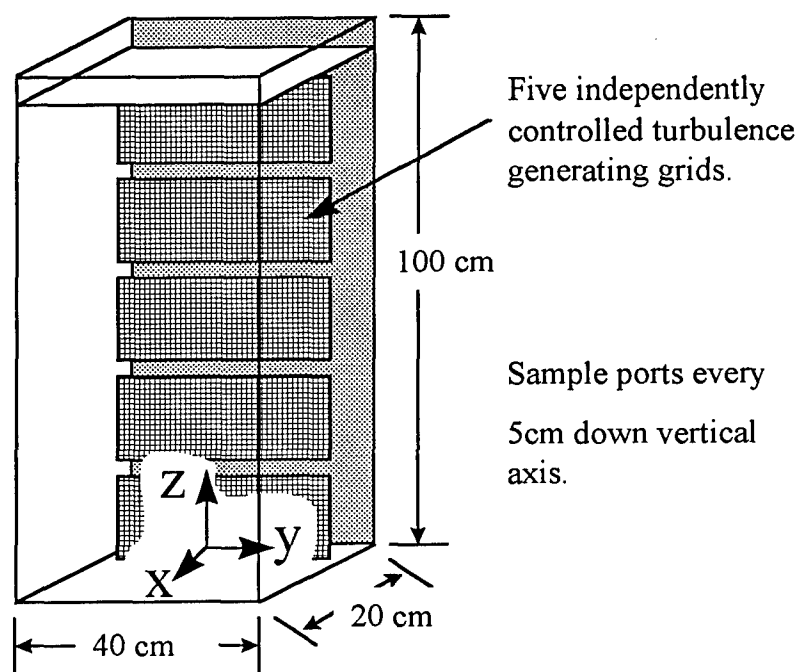
20 cm

**Figure 5.2**: Schematic of the DTC

219

**Figure 5.2** (Continued)



Side View
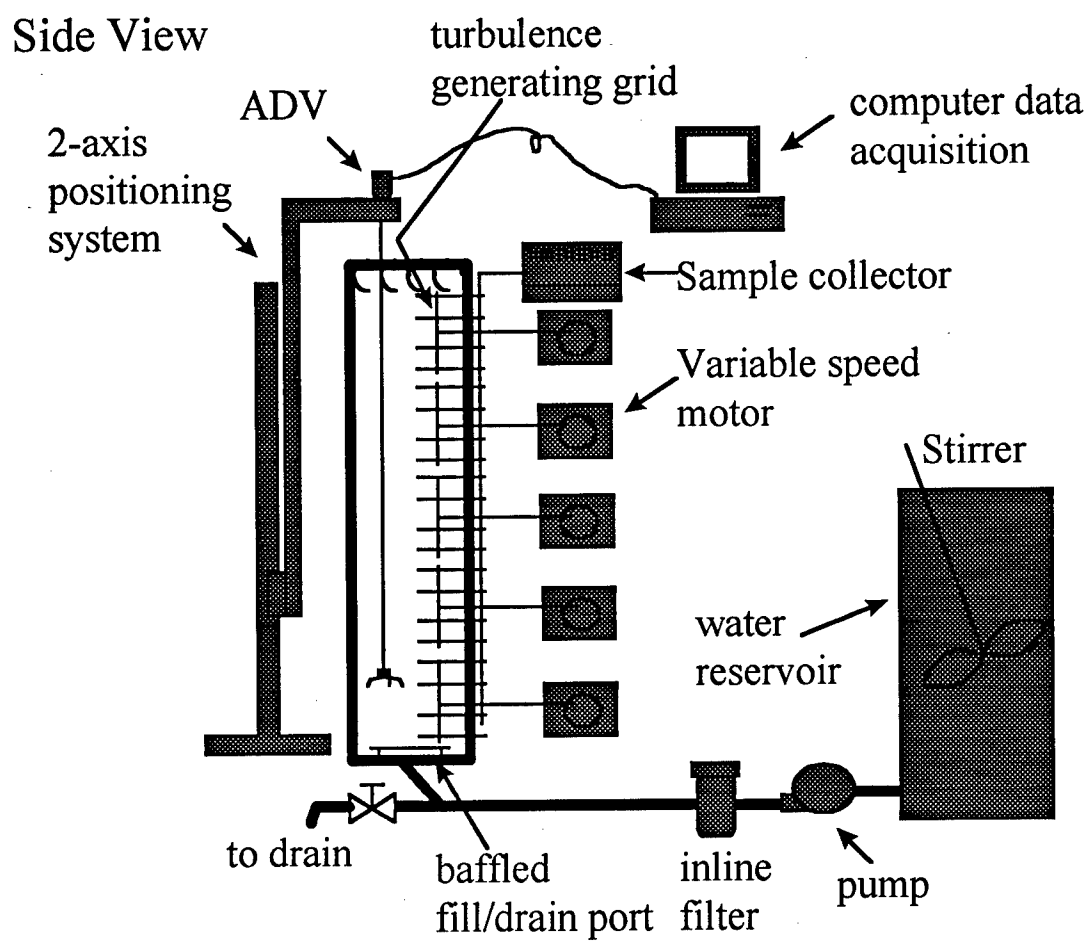
sampling locations can be manually adjusted from front to back of the DTC (x = 0 to x = 20 cm; see Figure 5.2 for the coordinate system used in this analysis.). The sample tubes are connected to a manual sampling device that uses gravity flow to sample from all ports simultaneously. Material collected from the vertically spaced sample ports is stored in particle free vials for subsequent analysis by a particle counter (Coulter Multisizer II, Coulter Corp.).

A computer controlled 2-axis positioning system allows *in situ* measurement within the water column and can accommodate multiple local sensing and sampling devices. Currently, a miniature acoustic Doppler velocimeter (ADV, Sontek, Inc.) and a micro-conductivity probe are mounted to measure velocity and salinity fluctuations, respectively. A sample tube attached to the positioning system also permits withdrawal of water samples at the location of the ADV and conductivity probes. The positioning system and sampling probes are interfaced to a computer. Data acquisition and analysis software allows the computer to collect and analyze data from the DTC experiments.

## 5.3 ADV Theory and Limitations

The ADV uses pulse-to-pulse coherent Doppler technology to provide 3-component velocity information at a rate of 25 Hz (Lohrman et al., 1994). The ADV emits 10 MHz sonic pulses that reflect off ambient particles within the liquid. By comparing phase shifts between subsequent pulses the instrument can provide velocity information for a cylindrical control volume 3 mm in radius by 3 to 9 mm high. The control volume is

located about 5 cm below the transmit/receive transducers to minimize the effect of the probe on the velocity measurements (Lohrman et al., 1994).

Because the ADV analyzes the echoes returning from sonic bursts, interference due to echo from the apparatus walls, termed pulse-to-pulse interference, can result in inaccurate results (Lohrman, 1994). Pulse-to-pulse interference is characterized by a sharp increase in signal noise levels. Such interference was observed at only one location in the reactor and data collected at the interference position were not considered in subsequent analysis.

## 5.4 One Point Turbulence Statistics

One point statistics were obtained for homogeneous conditions with all grids operating at 4, 6, and 8 Hz. After several minutes of equilibration, the ADV sampled at several locations in the DTC for 10 minutes each. Both the Eulerian time spectra of the turbulent kinetic energy (TKE) and the integral time scale were computed at each sample location.

The Eulerian time spectra of the TKE when all grids operated at 6 Hz is shown in Figure 5.3. The spectra was smoothed by passing the raw velocity fluctuation data through a 5-point running average filter and averaging over all sampling locations within the DTC. The graph shows the expected 5/3 slope (Tennekes & Lumley, 1976) for the inertial range of turbulence. In addition, Figure 5.3 shows an energy spike at 6 Hz corresponding to the grid frequency. Limitations on ADV sampling rate prevented resolution of the spectra down to Kolmogorov scales.
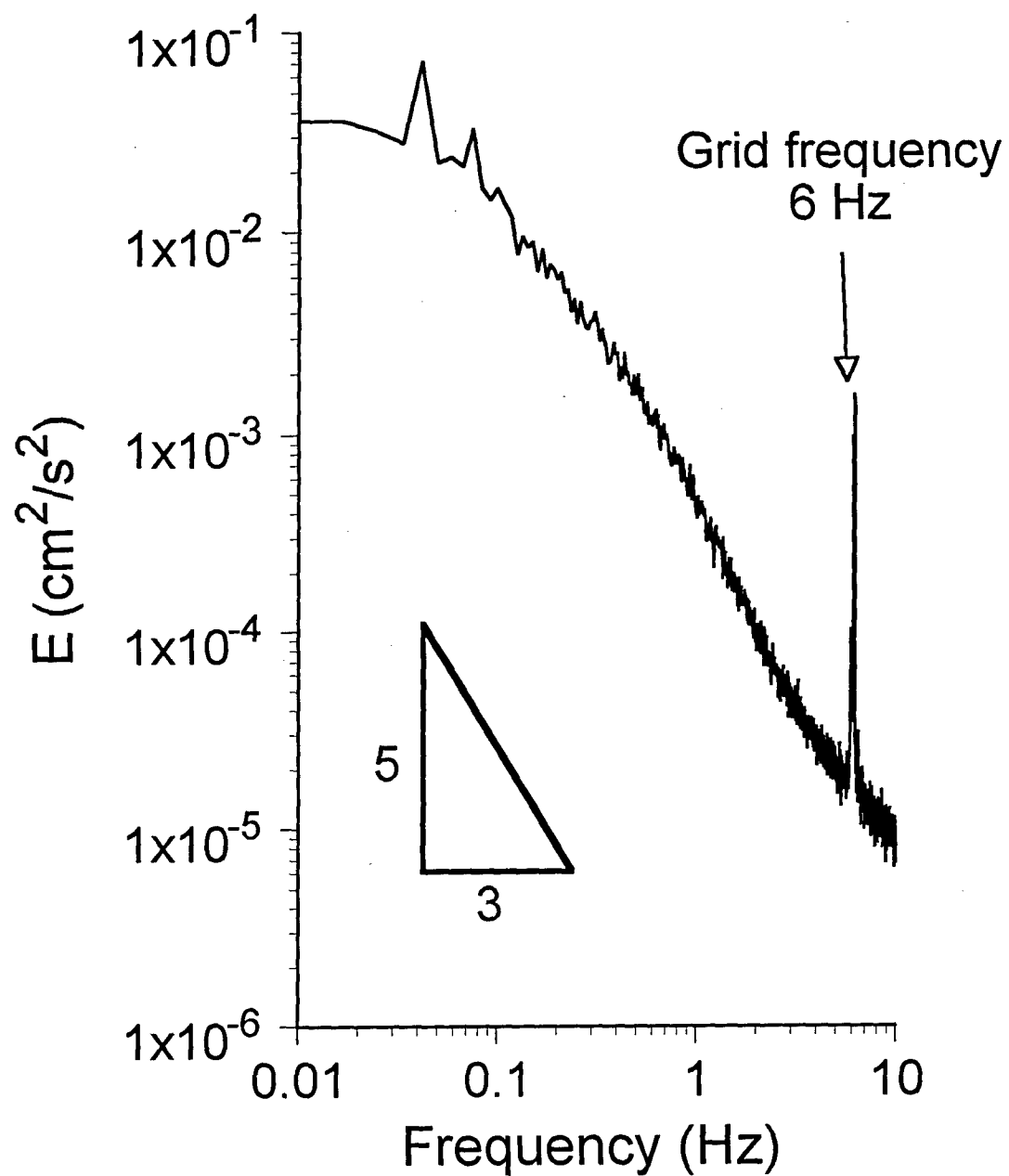
**Figure 5.3**: Eulerian time spectra of TKE for homogeneous conditions (grid frequency of 6 Hz; stroke of 4 cm).

Both the autocorrelation function of the instantaneous velocity signals as well as a running average with variable averaging window were calculated on the velocity data stream to deduce the appropriate sampling time as a function of turbulence intensity. To obtain good turbulence statistics, sampling time must exceed the integral time scale by several multiples.

The velocity autocorrelation coefficient was determined by sampling with the ADV probe at a single location for 10 minutes while all the grids were operated at 4, 6, or 8 Hz. The integral of the velocity autocorrelation coefficient yields the integral time scale for the turbulence.

The running average calculation with variable averaging window size, also termed the detrended root mean square (rms) velocity average, was found by computing the rms velocity using different time intervals of instantaneous velocity data. The detrended rms velocity average showed an asymptotic approach to a steady value as the averaging window became large enough to sample all the time scales of the turbulence field.

Figure 5.4 shows an example of a velocity autocorrelation coefficient and detrended rms velocity signal when all grids were operated at 6 Hz with a stroke of 4 cm. The autocorrelation coefficient suggests an integral time scale of less than 6 seconds (Figure 5.4a), while the running average calculation with variable window size indicates that the rms velocity reaches an asymptote when velocity records of 20 seconds or longer are averaged. In all cases, the running average calculation produced larger estimates for the integral time scale. As a conservative estimate, all

**Figure 5.4**: Two methods to determine the integral time scale for turbulence: (a) velocity autocorrelation coefficient; (b) effect of averaging time on the observed rms velocity.

A.
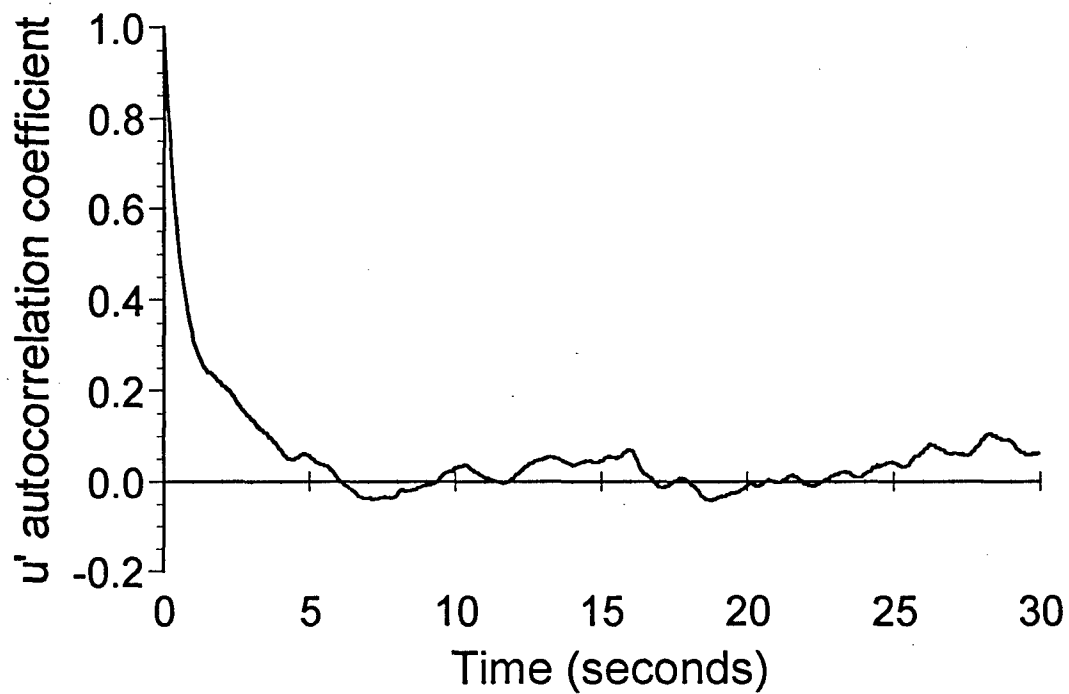


B.
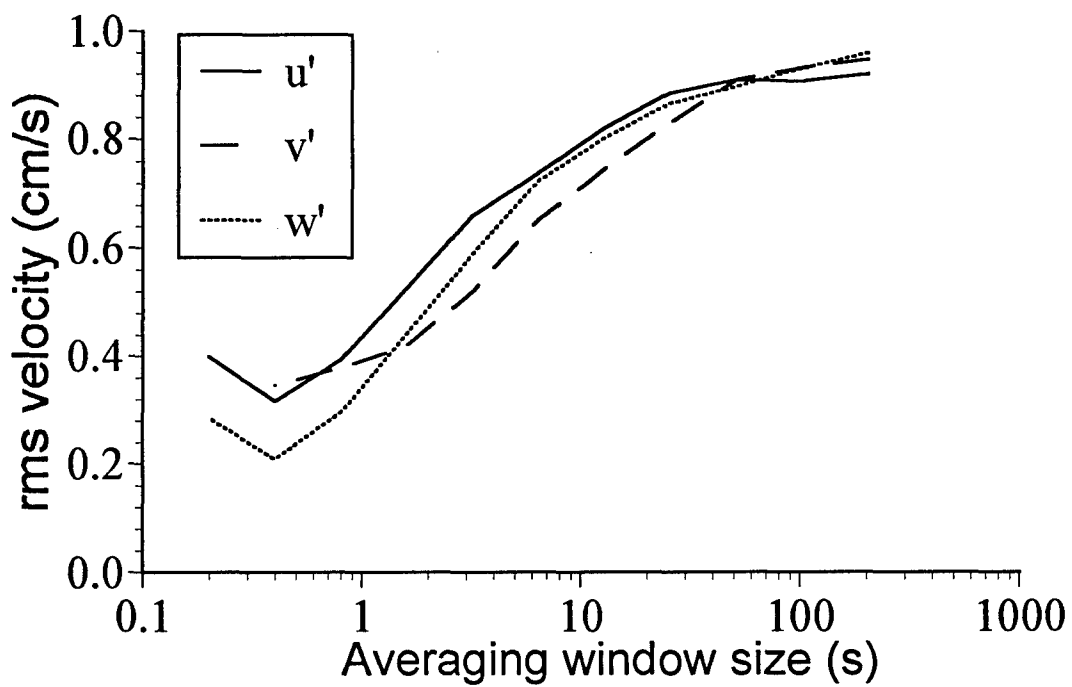
subsequent experiments used the correlation times predicted by the detrended rms velocity calculation (Figure 5.4b) as a lower limit on the sampling time of the ADV. Similar analyses were performed in the reactor for grid frequencies of 2 and 4 Hz. These experiments indicated that appropriate sampling times were 40 and 20 seconds for 2 and 4 Hz, respectively.

## 5.5 Characterizing Grid Turbulence

Grid-stirred turbulence has often been used in situations where a well-defined homogeneous, isotropic turbulent field is required (e.g., Thompson & Turner, 1975; Hopfinger & Toly, 1976). Hopfinger & Toly (1976) were some of the first researchers to investigate the behavior of grid-stirred turbulence and provide scaling laws predicting the turbulent velocity and length scales associated with this turbulence generating mechanism. For the rms velocity parallel to grid motion, they proposed:

$$\frac{u'}{fS} = C_{ht}\frac{S^{1/2}M^{1/2}}{x} \tag{5.1}$$

where u' is the rms velocity in the direction parallel to grid motion, f is the grid frequency, S is the stroke, M is the mesh size, x is the perpendicular distance from the grid and $C_{ht}$ is an order one constant estimated to be about 0.25. The scaling suggested by this relation has subsequently been verified in many grid systems (e.g., Brumley & Jirka, 1987; De Silva & Fernando, 1992). Equation 5.1 implies that grid stirred turbulence will be

homogeneous in planes perpendicular to the grid motion, but that it decays with distance from the grid.

Experiments were performed in the DTC under homogeneous conditions, with all grids operating identically, to verify the Hopfinger & Toly scaling relation as well as to assess the degree of isotropy of the system. End effects and other gross heterogeneities in a plane parallel to the middle grid were checked through detailed mapping of the turbulent kinetic energy (TKE). In this experiment the DTC operated with all grids oscillating at 6 Hz and 4 cm stroke. The ADV was configured to sample with multiple sweeps across the middle grid at a distance of 11 cm from the grid stroke center. Each horizontal sweep from y = -15 to 15 cm lasted 1,000 seconds and was 1 cm below the previous sweep. Figure 5.5 shows a contour plot of the TKE variation across the middle grid. Dark areas indicate regions of low TKE while lighter regions contained high TKE. Measured TKE varied from 0.72 to 2.97 $cm^2/s^2$ with an average TKE of 1.67 $cm^2/s^2$ and a standard deviation of 0.38 $cm^2/s^2$. Both the absence of long term structure and the relatively narrow variance relative to the average TKE suggest that the apparatus produces homogeneous turbulence.

Experiments performed over the f, S, and x parameter space, summarized in Table 5.1, were run to verify that the rms velocities measured by the ADV were consistent with the scaling proposed in Equation 5.1. All grids in the reactor operated with identical strokes and frequencies and the ADV measured the velocity at several locations within the reactor. The spatial homogeneity in the system as demonstrated by the
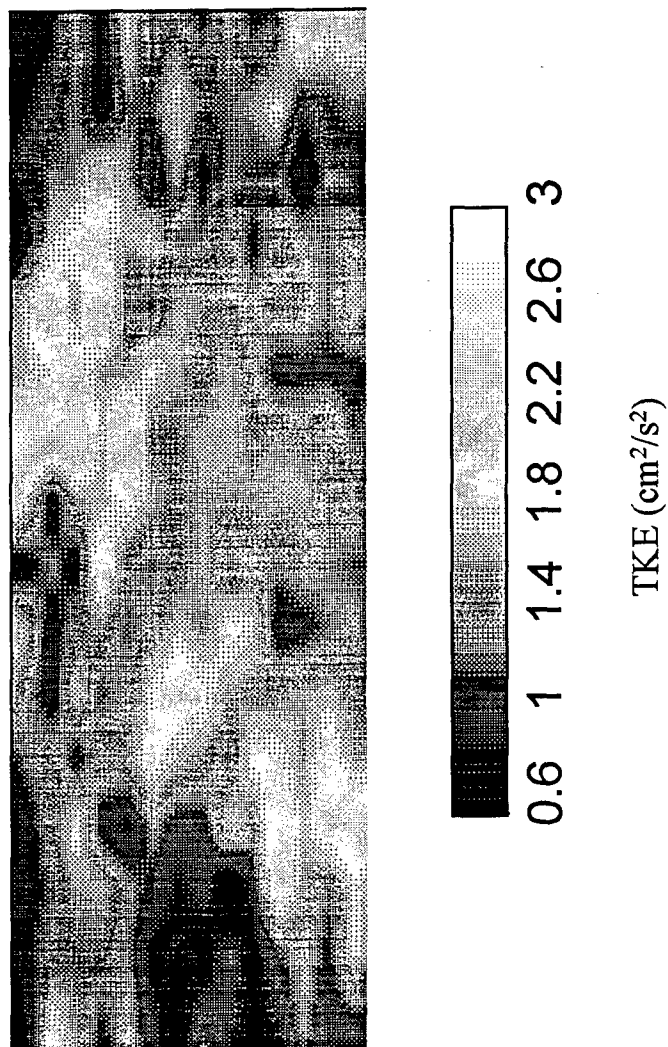
**Figure 5.5**: TKE map in front of middle grid (DTC operating at frequency of 6 Hz and stroke of 4 cm)

**Table 5.1**: DTC experimental parameters used in grid turbulence scaling relation verification.

| Distance from grid (cm) | Grid stroke (cm) | Grid frequency (Hz) |
|---|---|---|
| 11 | 2 | 2, 4, 6, 8 |
| 11 | 4 | 2, 3, 4, 6, 8 |
| 16 | 4 | 2, 4, 5, 6 |

TKE map permitted the rms velocity data collected throughout the DTC water column to be averaged together.

To simplify the analysis the Hopfinger & Toly relation, Equation 5.1, was converted to a scaling relation for the TKE. Assuming isotropy, so that u' = v' = w', where v' and w' are the y and z velocity components respectively, the TKE can be expressed as:

$$TKE = \frac{3}{2}u'^2 = \frac{3}{2}C_{ht}^2\frac{f^2S^3M}{x^2}$$

(5.2)

Although this facilitates data analysis by combining the 3-dimensional velocity data, error analysis indicates that the TKE will have twice the coefficient of variation as the rms data.

The measured TKE plotted against the right-hand side of Equation 5.2 is summarized in Figure 5.6. Each data point was obtained by sampling the reactor at several locations for times longer than the correlation time and then spatially averaging the velocity traces. The error bars in Figure 5.6 denote two standard deviations. The absolute error increases with increasing measured TKE; however, the coefficient of variation (the TKE standard deviation divided by the mean value) varied between 16 and 34% except for one point at 56% and it did not show a trend with increasing measured TKE. This suggests that the larger standard deviation at higher measured TKE values results from the presence of larger TKE fluctuations which naturally occur in the more turbulent conditions. A line with zero intercept fit the data with an $r^2$ of 92%. The slope of the linear regression predicted that $C_{ht} = 0.26$ with 95%
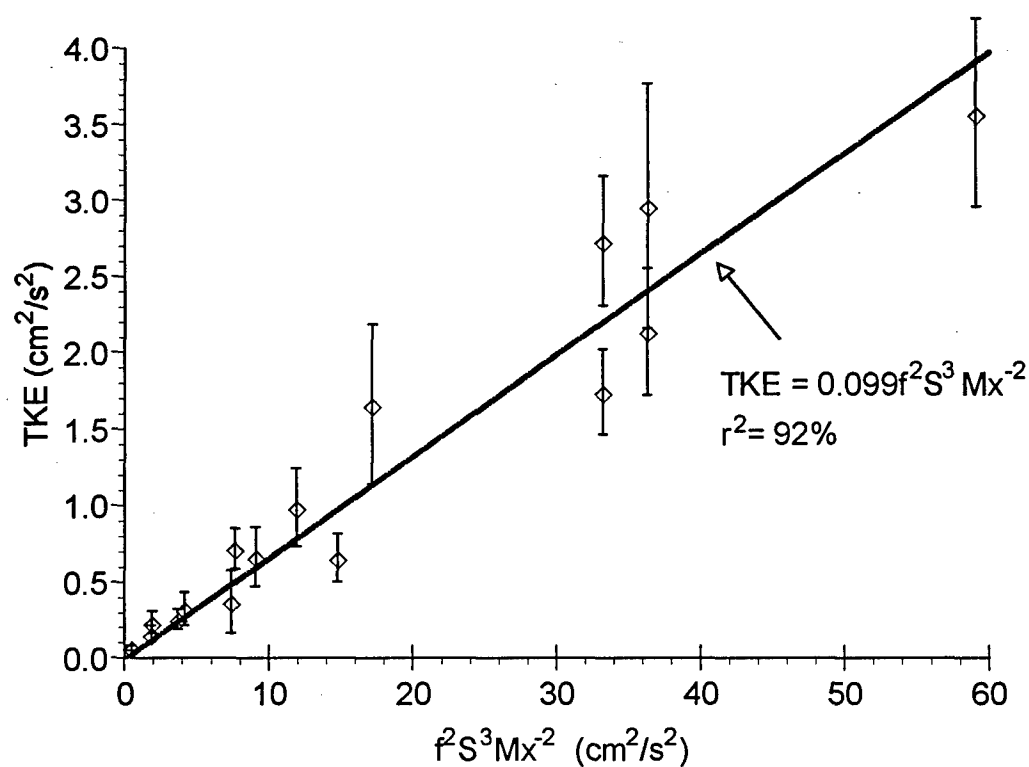
**Figure 5.6**: Summary of experiments verifying Hopfinger and Toly (1976) scaling relations for grid-stirred turbulence.

confidence intervals of ±0.01; therefore, the turbulence fields generated within the DTC agree very well with the scaling behavior predicted by Hopfinger & Toly (1976).

## 5.6 Simulation of Open Channel Flow Turbulence

Simulation of open channel flow rms velocity in the DTC illustrates the capability of the apparatus to replicate the hydrodynamics of natural aquatic environments. In open channel flow, turbulence generated by shear instabilities created at the channel bottom propagate up through the water column. After examining a large body of experimental measurements, Nezu & Nakagawa (1993) showed that an empirical exponential decay law represents the distribution of turbulent intensity as a function of height. They suggest that u' can be represented by:

$$\frac{u'}{U^*} = C_{ocf}\exp\left(-\frac{z}{h}\right)$$

(5.3)

where $U^*$ is the bottom friction velocity, h is the height of the water column and $C_{ocf}$ is an order one constant determined to be about 2.3. Analogous expressions can be written for v' and w' as a function of height. Again, to simplify the analysis, isotropy was assumed and Nezu & Nakagawa's expressions (1993) for the rms velocities were converted to a relation for the vertical TKE distribution:

$$\frac{TKE}{TKE^*} = C_{ocf}^2\exp\left(-2\frac{z}{h}\right)$$

(5.4)

where TKE* is the turbulent kinetic energy associated with the bottom friction velocity:

$$TKE^* = \frac{3}{2}U^{*2} \tag{5.5}$$

Combining Equation 5.3 with the Hopfinger & Toly scaling relation, Equation 5.1, yielded an expression that was used to set up the oscillating grids so that the apparatus mimicked open channel flow turbulence:

$$fS^{3/2} = \frac{C_{ocf}}{C_{ht}}\frac{U^*x}{M^{1/2}}\exp(-z/h) \tag{5.6}$$

The height, z, used for each grid was chosen to be at the grid center. Once the grid stroke and frequency of the bottom grid were selected, the frequencies and strokes of the other grids could be calculated by taking the ratio of Equation 5.6 for any grid with Equation 5.6 for the bottom grid:

$$\frac{(fS^{3/2})}{(fS^{3/2})_{bottom\ grid}} = \exp\left(\frac{10-z}{h}\right) \tag{5.7}$$

If the grid stroke is kept constant for all grids, then Equation 5.7 states that the grid frequencies for the four higher grids from bottom to top are 82, 67, 55 and 45%, respectively, of the bottom grid frequency.

Open channel flow TKE was simulated in the DTC with the grids operating at a stroke of 4 cm and bottom grid frequency varying from 2.5 to 8.0 Hz. Velocity data were collected at several vertical positions by sampling with the ADV along horizontal transects. Assuming horizontal

homogeneity, the data obtained during each horizontal sweep were combined to obtain a horizontally averaged TKE. The experimental TKE normalized by the TKE at the bottom of the DTC water column is plotted in Figure 5.7 as a function of distance from the bottom. The empirical prediction of Equation 5.4 based on Nezu & Nakagawa's (1993) observations is plotted as the solid line on the graph. Although there is experimental scatter, the data follow the expected exponential trend. Much of the variance in the experimental data can be explained by the data reduction method. Error analysis indicates that converting rms velocity data to TKE effectively doubles the experimental error. In any regard, non-linear regression of the data with Equation 5.5 results in an $r^2$ of 67% and supports the conclusion that the experimental data follows the predicted exponential decay.

## 5.7 Simulating Sediment Loading in Homogeneous Turbulence

At steady state in a system with horizontal homogeneity, suspended sediment transport can be characterized by a balance between upward sediment transport due to turbulent diffusion and downward sediment transport due to settling:

$$C\omega + \epsilon_s \frac{dC}{dz} = 0 \qquad (5.8)$$

where C is the mean particle concentration, $\omega$ is the terminal settling velocity of the individual sediment particles and $\epsilon_s$ is the turbulent diffusion coefficient. Equation 5.8 assumes that the system can be characterized by a single length scale so that the mixing length model for turbulent diffusion
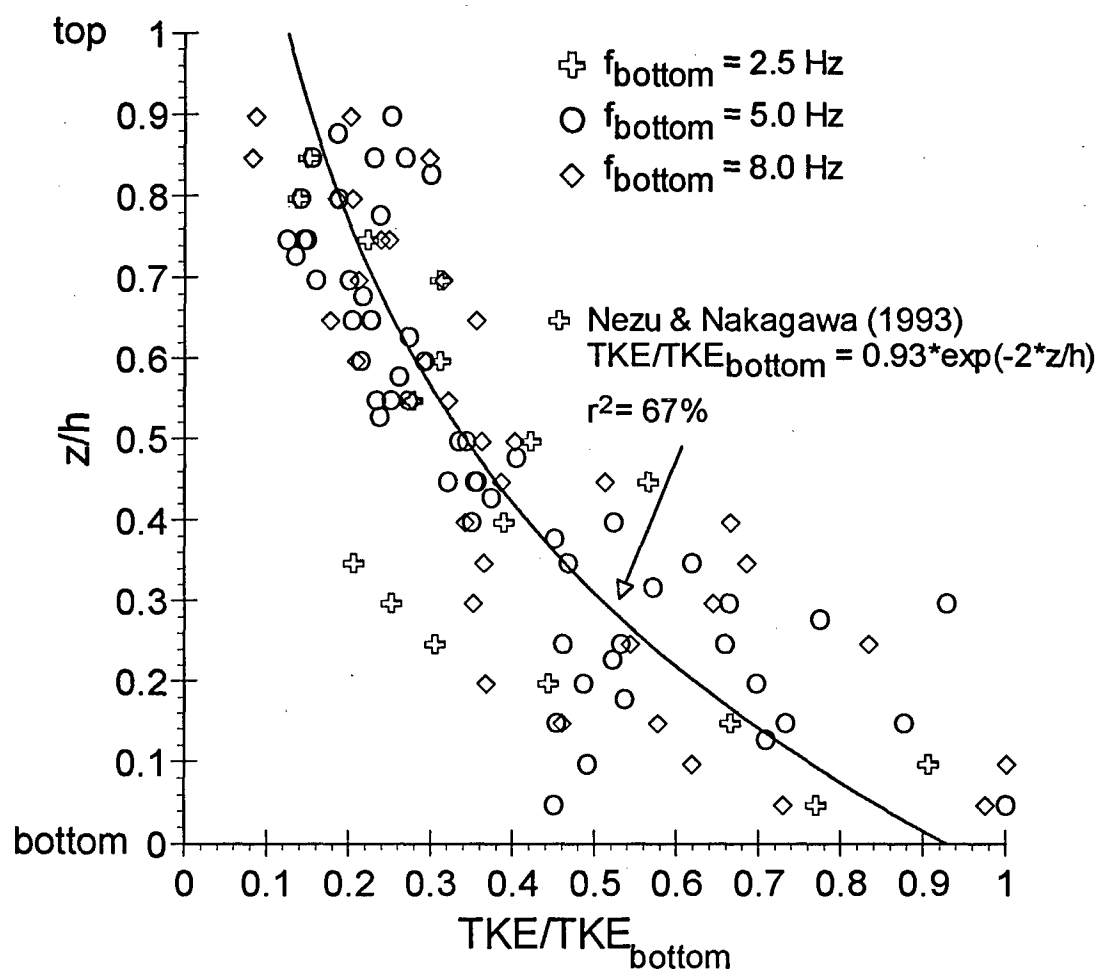
**Figure 5.7**: Vertical TKE profile normalized with bottom TKE when simulating open-channel flow turbulence in DTC.

can be employed (Tennekes & Lumley, 1972). For two-dimensional uniform turbulent flow $\epsilon_s$ is constant and Equation 5.8 integrates to yield (Vanoni, 1975):

$$\frac{C}{C_a} = \exp[-\frac{\omega}{\epsilon_s}(z-a)] \qquad (5.9)$$

where $C_a$ is the concentration at the reference height, a.

The DTC does not seem to uphold the assumption of horizontal homogeneity because it produces grid-generated homogeneous turbulence in vertical YZ planes, but not in horizontal planes. The scaling deduced by Hopfinger & Toly indicates that the turbulence intensity decays with the distance from the oscillating grid while the integral turbulent length scale increases in proportion to distance from the grid (Hopfinger & Toly, 1976). Assuming a simple mixing length model, turbulent diffusion (the product of the integral velocity and length scale) is invariant with distance from the grid. This cancellation of distance dependence means the apparatus should produce horizontally homogeneous turbulent diffusion.

Several homogeneous experiments were run using a mixture of glass microbeads (Cataphote, Inc.), with diameters ranging from 13 to 60 $\mu$m and a density of 2.45 g/cm$^3$. To facilitate sediment resuspension off the column floor, the bottom grid was replaced with an L-shaped grid. The L-shaped grid increased the sediment loading of the column by increasing fluid shear at the bottom of the DTC. Velocity profile measurements indicated that the L-shaped grid affected the lower 20 cm of the DTC. In this region, sediment concentration was highly variable and therefore was

not considered in the reported experimental results. Sediment concentration as a function of height was obtained by pumping the fluid through a tube that was connected to the positioning system. Before each sample was collected, the tubing was purged to remove fluid held over from previous samples. The positioning system was set to move horizontally from y = -15 to +15 cm and sediment sampling occurred during this horizontal sweep to obtain an average sediment concentration for each depth. The particle size distribution of each sediment sample was measured four times over a particle diameter range of 10 to 64 µm using the Coulter Multisizer II. After combining the replicates into a single data set, the concentrations of particles within ±1 µm of 15, 20, 25, 30, 40 and 45 µm diameter were extracted from the size distribution data. The physical properties for each size range were determined by assuming that all the particles had a diameter in the middle of the size range. Typical experimental results are shown in Figure 5.8 where the particle concentration of 40 µm glass beads normalized by the bottom concentration ($C_a$) is graphed as a function of height when all grids operated at 6 Hz and 4 cm stroke. The model line was obtained by a non-linear regression fit of the data to Equation 5.9. Multivariate regression was used to compute the experimental diffusion coefficient and the reference concentration. The settling velocity was calculated from the Stokes settling velocity equation. According to the mixing length model (Tennekes & Lumley, 1972),

$$\epsilon_s = \frac{1}{Sc_{turb}} u'l \qquad (5.10)$$
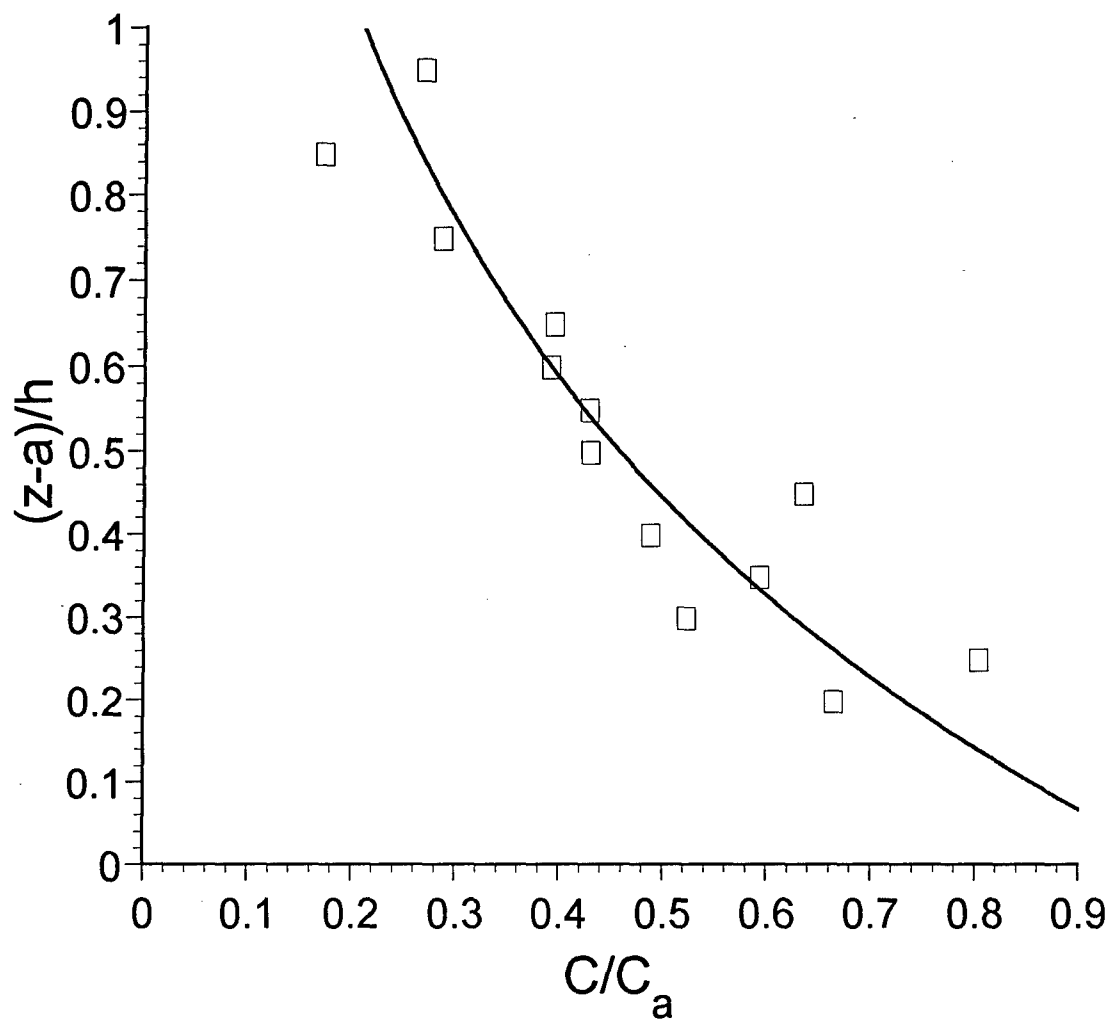
**Figure 5.8**: Typical concentration profile obtained from simulation of sediment loading in homogeneous turbulence (grids at 6 Hz and 4 cm stroke).

where $Sc_{turb}$ is the turbulent Schmidt number, u' is the root mean square (rms) velocity, and $l$ is a characteristic mixing length in the DTC. The turbulent Schmidt number compares turbulent momentum and mass transport. The Reynolds analogy suggests that turbulence should transport momentum and mass similarly; yet it has been demonstrated that mass transport of suspended sediments under turbulent conditions can be considerably different from turbulent momentum transport (Jobson & Sayer, 1970; Vanoni, 1975). The success of the Reynolds analogy would depend on whether the particles follow the fluid motion. Deviations from the Reynolds analogy would be anticipated when $\omega \gg u'$ and the particle relaxation time exceeds the time scale of the turbulence (i.e., $d^2\rho/18\mu$, where d is the particle diameter, $\rho$ is the particle density and $\mu$ is the fluid viscosity). Discrepancies tend to increase with sediment concentration and size. For the glass microspheres used in this research $u'/\omega > 3$ and the ratio of turbulent time scale to particle relaxation time exceeded $10^4$ indicating that the particles should follow the fluid motion. Experimentally Jobson & Sayer (1970) determined $Sc_{turb}$ to be 0.98 for 123 $\mu$m glass beads, indicating that the Reynolds analogy holds relatively well. The glass microspheres used in the current work are less than 123 $\mu$m in diameter and thus deviations from the Reynolds analogy can be expected to be even smaller. Given the errors associated with measurement, it seems acceptable to assume an $Sc_{turb}$ of unity.

In Figure 5.9 the regressed turbulent mass diffusion coefficient was plotted against u' as obtained from Equation 5.1. If the mixing length model applies, $\epsilon_s$ should increase linearly with u' and the resulting slope
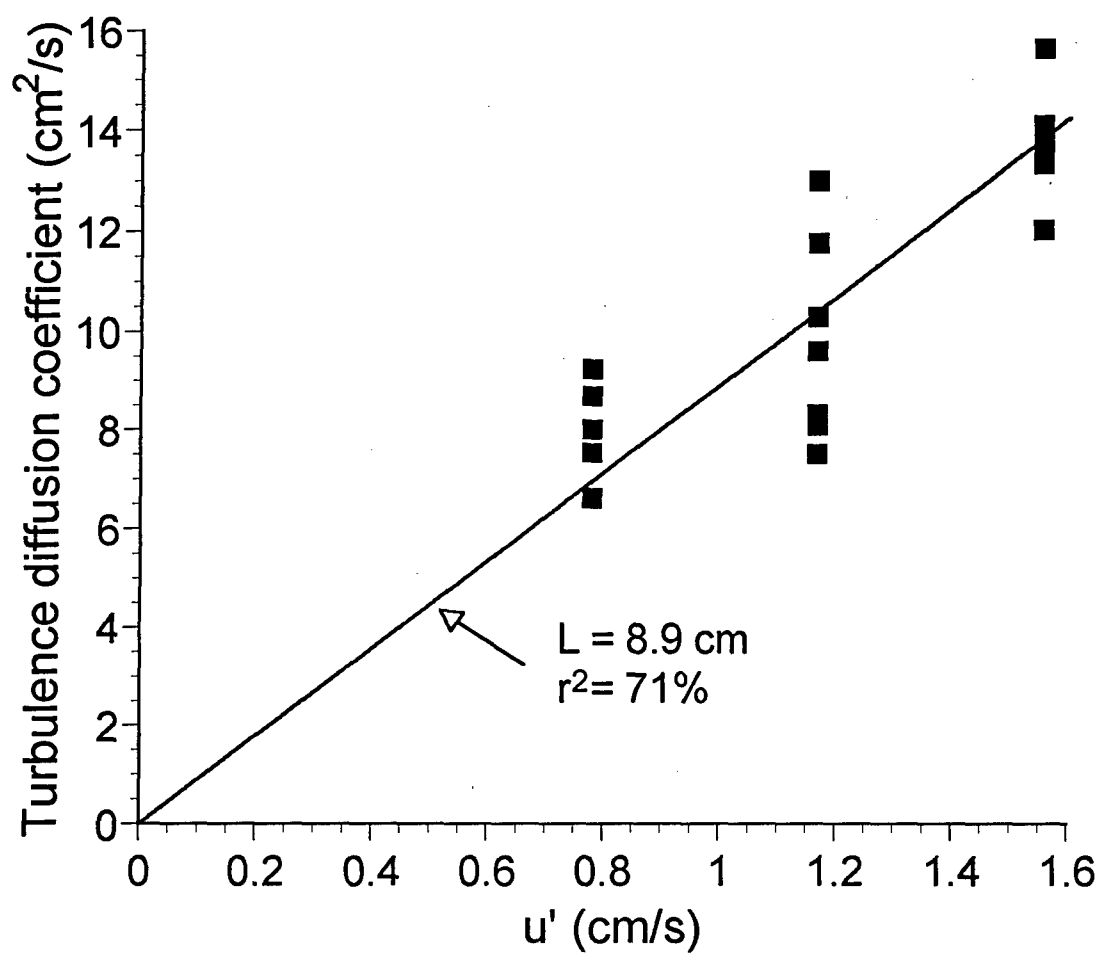
**Figure 5.9**: Turbulent diffusion coefficient obtained from regression of homogeneous turbulence sediment loading data as a function of RMS turbulent velocity.

will be the mixing length of the DTC. The best fit line shown in Figure 5.9 had a slope of 8.9 cm with an $r^2$ of 71%.

The integral length scale obtained from the mixing length model can be compared to other integral length scale approximations. The product of the integral velocity (Equation 5.1) and time scales yields an estimate for the integral length scale of about 10 cm. Additionally, based on scaling arguments, the integral length scale for turbulence is usually estimated to be on the order of the smallest dimension of the flow reactor which is 20 cm for the DTC. The regressed large scale eddy size of 8.9 cm compares remarkably well with these other order of magnitude estimates.

## 5.8 Simulating Sediment Loading in Open Channel Flow

In open channel flow, turbulence intensity decays with distance from the bottom of the channel; therefore, turbulent mass transport depends on vertical position and the sediment loading as a function of depth is no longer a simple exponential function as was found in Equation 5.9. To obtain an expression for the turbulent mass diffusivity in open channel flow, the Reynolds analogy was again invoked:

$$\epsilon_s = \frac{1}{Sc_{turb}} \epsilon_m \tag{5.11}$$

where $\epsilon_m$ is the turbulent diffusion coefficient for momentum exchange. Assuming that the Prandtl-von Kármán velocity defect law applies to the open channel flow system, Rouse (1937) showed that the turbulent momentum diffusivity, $\epsilon_m$, is governed by:

$$\epsilon_m = \kappa U^* z\left(\frac{h-z}{h}\right) \qquad (5.12)$$

where $\kappa$ is the von Kármán universal constant. By substituting Equation 5.12 into the sediment flux balance, Equation 5.8, Rouse (1937) derived an expression for the sediment loading in open channel flow:

$$\frac{C}{C_a} = \left(\frac{h-z}{z}\frac{a}{h-a}\right)^R \qquad (5.13)$$

where R is the Rouse parameter. The Rouse number is a non-dimensional parameter describing the ratio of particle transport by settling to particle transport by turbulence:

$$R = \frac{\omega}{\dfrac{1}{Sc_{turb}}\kappa U^*} \qquad (5.14)$$

The DTC was set up to simulate sediment loading under open channel flow turbulence conditions. Experiments were run with the bottom grid frequency at 4, 6 and 8 Hz, a mixture of glass microspheres ranging in diameter from 13 to 60 μm were added to the system, and the suspended sediment concentration was allowed to reach steady state. Samples were removed from the water column as a function of depth using the sampling technique described earlier. Each sample was analyzed with the Coulter Multisizer II and particle concentrations for several particle size ranges were obtained. Typical experimental concentration profiles for

Rouse numbers of 0.34 and 0.10, along with theoretical predictions, are shown in Figure 5.10. In this analysis, $\omega$ was obtained from the Stokes settling velocity equation. Again, recognizing that the concentrations and sediment sizes used in this experiment were small, the effect of sediment on turbulent transport was neglected (Vanoni, 1975; Jobson & Sayre, 1970) and the clear water value of 0.4 was chosen for $\kappa$. The bottom shear velocity, $U^*$, was found from the grid scaling relation (Equation 5.1) using the stroke, frequency and mesh size of the bottom grid and assuming a measurement distance 10 cm from the center of the grid oscillations.

Additional experiments were completed at theoretical Rouse numbers ranging from 0.02 to 0.7. The experimental concentration profiles were fit to Equation 5.13 using non-linear regression with the Rouse number as the fitting parameter. Figure 5.11 compares the theoretical prediction for the Rouse number with that obtained via experiment. In general, the data fall along the 45° line supporting the conclusion that the DTC is capable of mimicking sediment loading in open channel flow systems.

## 5.9 Summary and Conclusions

Dimensional analysis indicates that there is a range of time scales associated with pollutant and particle transport in natural hydrological systems. For instance, turbulent transport is expected to occur in seconds while coagulation and particle settling require many minutes. Ultimately, to understand how pollutants and particles are transported in natural environments, the evolution of rate limiting processes must be examined in
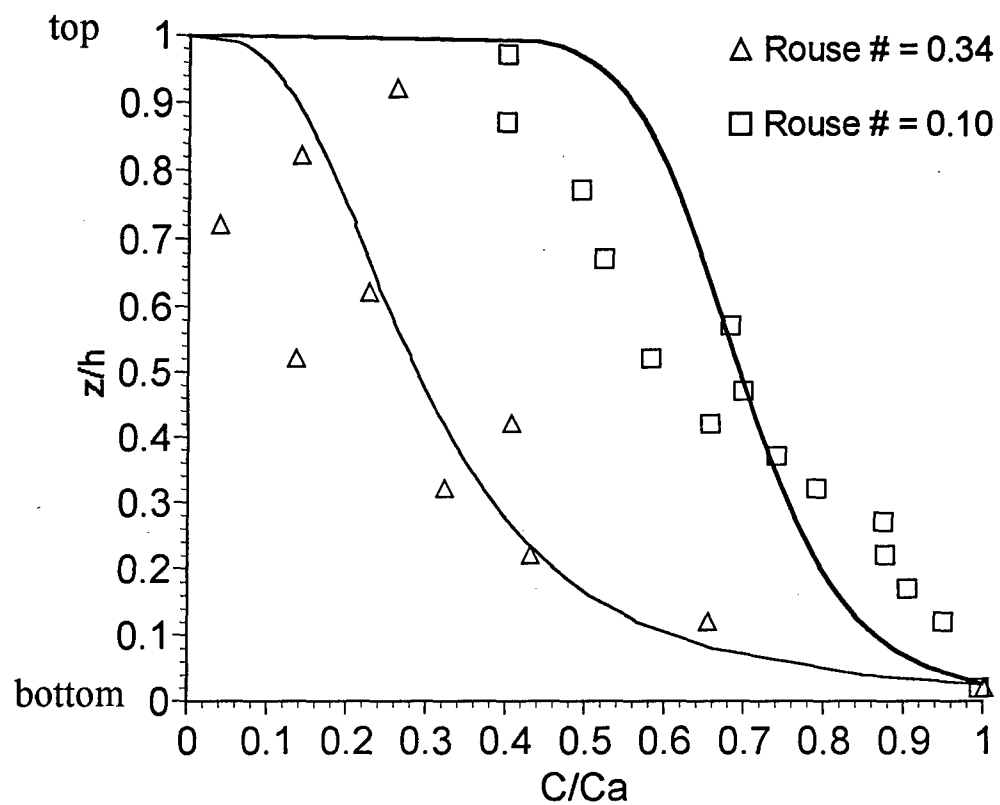
**Figure 5.10**: Concentration profiles obtained from DTC experiments that simulated sediment loading in open-channel flow turbulence.
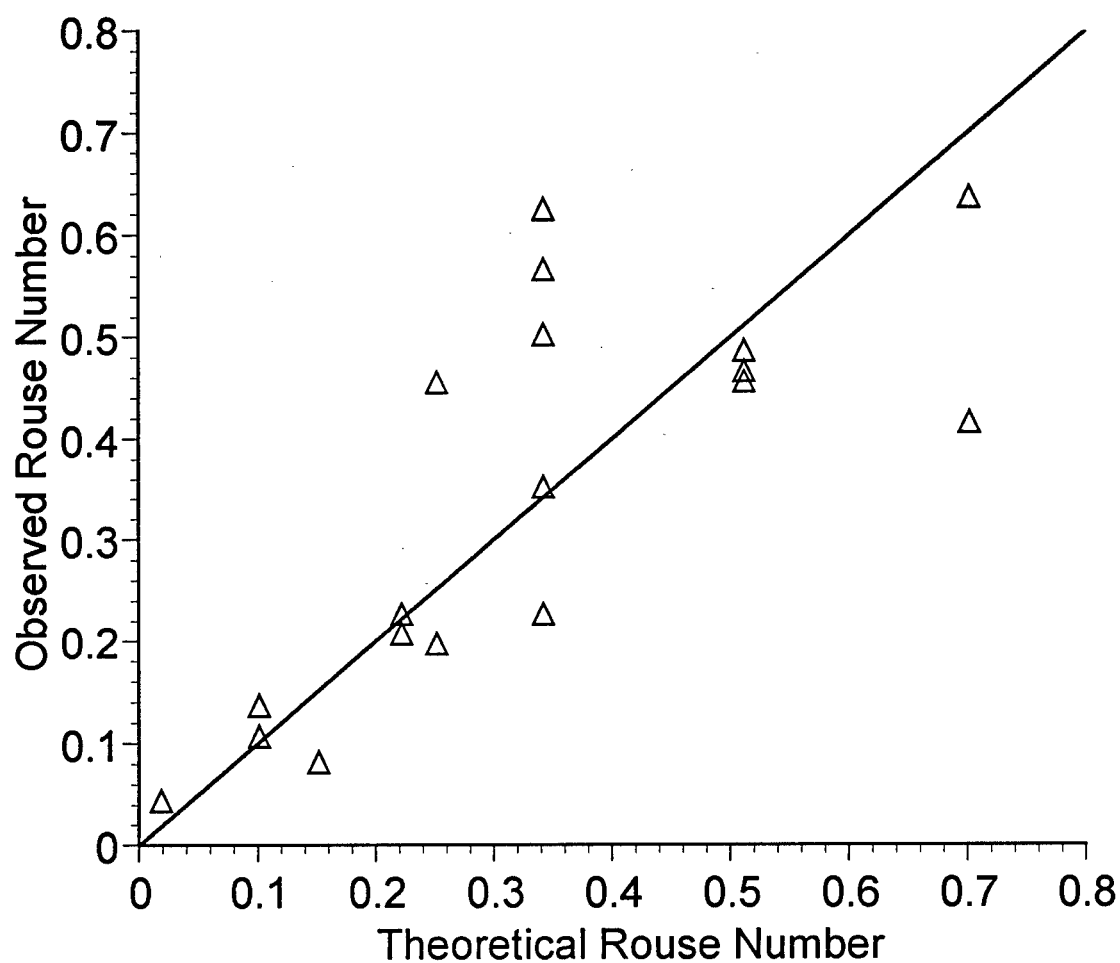
**Figure 5.11**: Comparison of theoretical prediction of Rouse number for various open-channel flow sediment loading experiments to values obtained from nonlinear regression of experimental concentration data.

carefully designed laboratory simulations. In this context, short time scale processes such as turbulent transport can be considered to be at steady state and it is important to characterize this steady state behavior. The tests described in this chapter are an important step in the laboratory simulation of pollutant and particle transport because they indicate that the DTC apparatus can replicate the desired steady state concentration and turbulent distributions.

The DTC offers excellent capabilities for simultaneous control of solution chemistry, mass transport and turbulence. It includes a 20 cm x 40 cm x 100 cm deep water column, five vertically spaced grids that generate variable turbulence as a function of depth and 20 vertically spaced sample ports spaced at 5 cm intervals. A computer controlled 2-axis positioning system currently is mounted with a miniature ADV capable of providing 3-component velocity fluctuations at 25 Hz. Experiments were run to probe the DTC's ability to simulate homogeneous and open channel flow type turbulence and to replicate sediment loading typical for these flow conditions.

Grid generated turbulence has been previously used in laboratory situations where a well-defined turbulence field is required. Experiments undertaken to examine the DTC's ability to produce well-defined turbulence showed that the apparatus exhibits a good degree of isotropy and it obeys the scaling relation first proposed by Hopfinger & Toly (1976).

As a next step, the turbulence profiles associated with open channel flow were simulated in the DTC. Experiments performed with the bottom

grid frequency varying from 2.5 to 8.0 Hz indicate that the DTC can replicate the exponential decay associated with turbulence in open channel flow. Sediment loading profiles for homogeneous and open channel flow turbulence were simulated using glass microbeads of various sizes. Concentration profiles measured for various particle sizes indicate that the expected exponential profile for sediment loading under homogeneous turbulence can be accurately replicated in the DTC. Additionally, the analysis suggested that the turbulent momentum diffusivity observed in the apparatus is of the same order as that predicted from the mixing length model.

Sediment loading, when the DTC mimicked open channel flow turbulence, was observed to follow the power law proposed by Rouse (1937). The experimentally determined Rouse parameter that compares the importance of particle settling to turbulent sediment transport was found to agree well with the value obtained from theoretical prediction.

The experiments reported herein demonstrate the DTC's success in simulating turbulence and sedimentation as they occur in fluvial hydraulic systems.

# REFERENCES

BRUMLEY, B. H. & JIRKA, G. H. 1987 Near-surface turbulence in a grid-stirred tank. *J. Fluid Mech.* **183**, 235-263.

DE SILVA, I. P. D. & FERNANDO, H. J. S.. 1992 Some aspects of mixing in a stratified turbulent patch. *J. Fluid Mech.* **240**, 601-625.

HOPFINGER, E. J. & TOLY, J. A. 1976 Spatially decaying turbulence and its relation to mixing across density interfaces. *J. Fluid Mech.* **78**, 155-175.

JOBSON, H. E. & SAYRE, W. W. 1970 Vertical transfer in open channel flow. *Journal of the Hydraulics Division* **96**, 703-724.

KRONE, R. B. 1978 Aggregation of sediment particles in estuaries. In *Estuarine Transport Processes* (ed. B. Kferfve). University South Carolina Press, Columbia, South Carolina, pp 177-190.

LOHRMAN, A., November 1994, Personal communication.

LOHRMAN, A., CABRERA, R. AND KRAUS, N. C. 1994 Acoustic Doppler Velocimeter (ADV) for laboratory use. In *Symp. on Fundamentals and Advancements in Hydraulic Measurements and Experimentation* (ed. Clifford A. Pugh ). ASCE, pp. 351-365.

NRC. 1989 *Contaminated Marine Sediments -- Assessment and Remediation*, National Academy Press, pp. 1-19.

NEZU, I. & NAKAGAWA, H. 1993 *Turbulence in Open-Channel Flows*. A.A. Balkema, pp. 12-25, 48-81.

ROUSE, H. 1937 Modern conceptions of the mechanics of fluid turbulence. *Transactions ASCE* **102**, 463-543.

TENNEKES, H. AND LUMLEY, J. L.. 1972 *A First Course in Turbulence*. MIT Press, pp. 43-50.

THOMPSON, S. M. AND TURNER, J. S.. 1975 Mixing across an interface due to turbulence generated by an oscillating grid. *J. Fluid Mech.* **67**, 349-368.

VANONI, V. A. 1975 *Sedimentation Engineering.* ASCE, pp. 69-77.

# CHAPTER 6:

## OBSERVATIONS OF COAGULATION IN ISOTROPIC TURBULENCE*

6.1 <u>Introduction</u>

Turbulence-induced coagulation is an important process leading to the aggregation of colloidal particles in both industrial and environmental processes (McCave, 1984). Turbulent mixing is heavily employed in the water treatment and chemical industries to enhance the aggregation and removal of fine particles (Appiah & O'Melia, 1990). In natural aquatic systems, pollutants tend to associate strongly with particles and hence considerable effort has been focused on understanding the dynamics of particles in natural environments (O'Melia, 1980). In estuaries, for instance, contaminated suspended particles in river water mix with sea water resulting in colloidal destabilization, aggregation, particle settling, and the accumulation of contaminated sediments onto the estuarine benthos (Stumm & Morgan, 1981).

Despite the importance of turbulent coagulation, the fundamental understanding of the processes leading to coagulation in turbulence is limited. Over the past 40 years a variety of turbulent coagulation models have been proposed (Saffman & Turner, 1956; Chapter 3 and 4; Brunk et

---

al., 1997a&b; Delichatsios & Probstein, 1975; Camp & Stein, 1943; Casson & Lawler, 1990); yet, without well-controlled experiments that satisfy the assumptions of the various models, choosing between the theoretical paradigms is problematic. Surprisingly, only a few experimental studies have been undertaken that attempt to meet the hypotheses made in the model calculations. For experimental coagulation rate measurements to be compared reliably with theoretical predictions, the experimental system must generate well defined, nearly isotropic turbulence; the initial particles (singlets) must be monodisperse; only the initial rate of flocculation should be considered so that particle breakup and the formation of higher order aggregates are negligible; and the system should be dilute so binary collisions dominate the coagulation process (Chapter 3; Brunk et al., 1997a). As indicated below few, if any, of the existing experimental studies meet these assumptions.

In the environmental engineering literature, jar tests are often used to obtain a qualitative understanding of how the coagulation rate is affected by stirring rate or turbulence intensity (Stumm & Morgan, 1981). Delichatsios and Probstein (1975) have correctly noted that the experimental conditions for jar tests are far from ideal because the highly inhomogeneous turbulence created in these systems violates key assumptions of existing turbulence models. As an alternative, Delichatsios and Probstein studied turbulent coagulation in pipe flow (1975). Because turbulence in pipe flow is well understood, it was hoped that these experiments could be used to distinguish between alternate model formulations for the coagulation rate constant. Pipe flow experiments have

two main disadvantages: 1) measurement time is limited by the length of pipe used and 2) large velocity gradients caused by mean flows can significantly affect the reported coagulation rate (Clark, 1985).

Results from the experiments of Delichatsios and Probstein (1975) agreed with their empirical coagulation model. The model, however, was derived by analogy with the kinetic theory of gas, it did not consider the effects of particle-particle interactions such as van der Waals attraction, and it ignored spatial and temporal distributions of the turbulence intensity. Instead, the work used an empirical estimate for the Kolmogorov shear rate in the turbulent core of the pipe. As is demonstrated in this chapter (see Section 6.5), both the spatial distribution of turbulence and interparticle interactions can have a considerable influence on the interpretation of the experimental data. Hydrodynamic interactions between particles decrease the coagulation rate significantly because of viscous resistance to particle collision. Moreover, in the presence of particle interactions, the coagulation rate is a nonlinear function of the turbulent shear rate (Chapter 4; Brunk et al., 1997b) and so it is inappropriate to use an average shear rate to characterize the turbulent coagulation rate. Rather, it is important to know the detailed spatial distribution of the turbulent shear rate to compute the observed rate of coagulation.

Use of an oscillating grid is another option for generating well-characterized turbulence (Hopfinger & Toly, 1976; Brumley & Jirka, 1987). Casson & Lawler (1991) reported on coagulation experiments conducted in a grid-stirred apparatus; however, they did not account for turbulence intensity decay with distance from the operating grids. In

addition, these investigators used colloidal particles that had a broad particle size distribution, and they reported flocculation rates over long times during which aggregates larger than doublets formed. At long times and for broad particle size distributions, coagulation between multi-particle aggregates can be significant, and the measured coagulation rate does not pertain to the singlet aggregation reaction. Moreover, most coagulation models treat particle aggregates as if they were spherical particles with a volume equal to the total volume of the singlet particles in the floc. These models cannot be expected to be quantitative at large times since the coalescence formulation inaccurately represents the shape of the aggregates (Elimelech et al., 1995).

In this work, the turbulent shear coagulation rate was measured for monodisperse polystyrene latex particles in turbulence generated by a grid-stirred apparatus. In Section 6.2 below the kinetic theory of coagulation is briefly summarized and dimensional analysis is used to derive the form of the coagulation rate constant. Pertinent results from the computer simulation of turbulent coagulation presented in Chapter 4 (Brunk et al., 1997b) are also reviewed briefly in Section 6.2. Section 6.3 describes the general experimental procedures and data analysis techniques used in the coagulation experiments reported in this chapter. Measurements were made of the initial coagulation rate of monodisperse polystyrene latex particles by monitoring the disappearance of singlet particles and correcting the data for particle break up. A necessary input for the computer simulation is the Hamaker constant which characterizes the magnitude of the van der Waals attractive potential between the

coagulating particles. Brownian coagulation experiments described in Section 6.4 were used to estimate the Hamaker constant. The turbulent coagulation experiments were conducted in the locally homogeneous, isotropic turbulence created by an oscillating grid. Turbulence intensities in grid-generated turbulence decay with distance from the grid. Because bulk mixing is fast compared with coagulation, the coagulating particles will experience a spatially varying turbulence field over the course of an experiment. For quantitative comparison between the computer simulations and the experiments, knowledge of the spatial distribution of turbulence within the reactor is necessary. Determination of the turbulence intensity distribution within the grid-stirred reactor is described in Section 6.5.2 and related through scaling arguments to the spatial distribution of the Kolmogorov shear rate. Coagulation rates of destabilized particles are presented in Section 6.5.3 as a function of the average Kolmogorov shear rate in the reactor. The measured coagulation rates are compared with results obtained from the dynamical simulations of coagulating particles that are smaller than the scales of turbulence (Section 6.5.4).

## 6.2 Review of turbulent coagulation theory
### 6.2.1 Kinetic rate expression for turbulence

This investigation is restricted to the initial rate of doublet formation in a dilute suspension of monodisperse singlet particles. Consequently, the loss of singlets in the system is due only to the formation of doublets and the kinetic rate expression is second order in the singlet concentration:

$$\frac{1}{2}\frac{dS}{dt} = -kS^2 \qquad\qquad (6.1)$$

where S is the number concentration of singlet particles and k is the coagulation rate constant. The rate constant incorporates both the transport mechanisms leading to coagulation (e.g., turbulent shear, Brownian motion and differential settling) and the effect of interparticle interactions (e.g., van der Waals attraction and hydrodynamics). Generally, the coagulation rate constant is decomposed into the product of an ideal rate constant, $k^0$, that includes the effect of non-interacting particle transport, and a collision efficiency, $\alpha$, that incorporates hydrodynamic interactions (i.e., viscous drag and lubrication forces) and chemical interactions (i.e., van der Waals attraction and electrostatic double layer repulsion). The collision efficiency is defined as the ratio of the coagulation rate obtained when particle interactions are considered to the ideal coagulation rate without particle interactions. Generally, the collision efficiency is less than 1 indicating that only a fraction of the collisions occurring for non-interacting particles actually transpire when particle interactions are included in the analysis. Theoretical and empirical expressions for $k^0$ are available (see Pearson et al., 1984 for a table of ideal rate constants for a variety of particle transport mechanisms); however the collision efficiency must usually be obtained through numerical integration or dynamic simulations of coagulation.

In turbulence, colloidal particles are typically orders of magnitude smaller than the length scales of turbulence. Since the rate of strain increases with decreasing turbulence length scale (Tennekes & Lumley,

1972), the small scales of turbulence (the Kolmogorov scales) dominate the relative motion of neighboring particles and thus the rate of aggregation. The magnitude of the Kolmogorov scales can be estimated from scaling arguments that balance the turbulent energy flux with the characteristic viscous dissipation. The results are the Kolmogorov scales of length, $\eta$, and velocity gradient, $\Gamma$:

$$\eta = \left( \frac{\nu^3}{\epsilon} \right)^{1/4} \tag{6.2}$$

$$\Gamma = \left( \frac{\epsilon}{\nu} \right)^{1/2} \tag{6.3}$$

where $\epsilon$ is the turbulent dissipation rate and $\nu$ is the kinematic viscosity used to parameterize the effects of viscosity. Direct numerical simulations (DNS) indicate that the turbulent velocity gradient experienced by a fluid particle is controlled by two correlation time scales: $\tau_S$ and $\tau_R$ for the strain and rotational components of the flow, respectively (Girimaji & Pope, 1990). Non-linear regression of strain and rotation rate correlation functions taken from DNS (Girimaji & Pope, 1990) indicates that $\tau_S \Gamma \approx$ 2.3 and $\tau_R \Gamma \approx 7.2$ (Chapter 4; Brunk et al., 1997b).

Dimensional analysis can be used to ascertain the functional form of the turbulent shear coagulation rate constant. Since any directional information imposed at large scales of turbulence will be lost during the energy cascade process, isotropy and homogeneity are assumed at the small scales of turbulence and therefore the only length scale affecting the

coagulation rate constant of monodisperse particles will be their radius, a. For sufficiently large separation of the colloidal and turbulence length scales, a « η, the flow field in the neighborhood of two coagulating particles may be assumed to be approximately linear and can be characterized by the velocity gradient. If particle inertia can be safely neglected then the flow field provides the only time scales in the scaling analysis. Representing the fluctuating velocity gradient with its magnitude and correlation time yields the expectation that $k_T = f(\Gamma, \tau_S, \tau_R, a)$ or, after combining into non-dimensional groups:

$$k_T = \alpha_T \beta(\tau_S \Gamma, \tau_R \Gamma) \Gamma a^3 \tag{6.4}$$

where the subscript T denotes that this is the turbulent shear coagulation rate constant, a is the radius of a singlet particle, $\alpha_T$ is the collision efficiency that accounts for the effect of interparticle interactions. The function $\beta(\tau_S \Gamma, \tau_R \Gamma)$ accounts for the kinematics of the flow field and it is made explicit in several turbulent coagulation models (Saffman & Turner, 1956, Chapters 3 and 4; Brunk et al., 1997a&b, Delichatsios & Probstein, 1975, Camp & Stein, 1943). For large total strain and rotation, particle coagulation occurs in a pseudo-steady flow field and β becomes independent of the flow time scales. In the limit of small total strain, particle transport is diffusive leading to a β that is proportional to the total strain (see Chapter 3; Brunk et al., 1997a).

### 6.2.2 *Review of turbulent coagulation dynamical simulations*

In Chapter 4 (Brunk et al., 1997b), computer simulations of interacting particles in Gaussian isotropic turbulence are used to estimate

the turbulent coagulation rate constant in the presence and absence of hydrodynamic interactions and van der Waals attractions. Below, salient results are summarized for comparison with experimental measurements of turbulent coagulation.

Analytical predictions for turbulent-shear-induced coagulation have been derived for the large and small total strain limits. The total strain can be conceptualized as a measure of the total amplitude of the temporally varying flow and it is defined as the product of the characteristic strain rate and its correlation time (i.e., $\Gamma\tau_s$). The well-known turbulent coagulation model derived by Saffman & Turner (1956) applies in the large total strain limit where the velocity field is persistent, while the author has investigated coagulation in the small strain limit (Chapter 3; Brunk et al., 1997a), where the rapidly fluctuating velocity field causes diffusive transport. DNS investigations of Lagrangian statistics in isotropic turbulence have indicated that the total strain is order one (Pope, 1990; Girimaji & Pope, 1990) bringing into question the applicability of both previously derived asymptotic limits to turbulent coagulation.

In the numerical simulations, trajectory calculations of turbulent coagulation at arbitrary total strain were used to predict the actual coagulation rate and to compare with the large and small total strain asymptotic limits (Chapter 3; Brunk et al., 1997b). For particles smaller than the length scales of turbulence, the relative motion of particles was represented as a temporally varying linear flow field. The fluctuating velocity gradient was assumed to be isotropic and Gaussian with two-time Lagrangian statistics taken from DNS (Girimaji & Pope, 1990).

Coagulation rates were obtained in the presence and absence of hydrodynamic interactions and van der Waals attractions. The reader is referred to Chapter 4 (see also Brunk et al., 1997b) for complete details on the simulation procedure and an interpretation of the results.

In the absence of particle-particle interactions the turbulent coagulation rate constant depends on the total strain and total rotation in the system. A best-fit to the simulation data suggests that:

$$\beta = \frac{32\pi}{5}\left(\frac{\tau_s\Gamma}{1+0.65\pi(\tau_S\Gamma)}\right) \qquad (6.5)$$

Simulations based on the correlation times $\tau_S\Gamma_\eta = 2.3$ and $\tau_R\Gamma_\eta = 7.2$, obtained from DNS calculations in isotropic turbulence (see Chapter 4; Brunk et al., 1997b), indicate that $\beta = 8.62$ +/- 0.02, so that:

$$k_T = 8.62\,\alpha_T\Gamma a^3 \qquad (6.6)$$

The collision efficiency, $\alpha_T$, has been calculated for non-Brownian particles experiencing hydrodynamic interactions and retarded van der Waals attraction. When van der Waals attractions and hydrodynamic interactions are included, two additional non-dimensional parameters govern the behavior of the system. $N_L = 4\pi a/\lambda_L$ is the ratio of the particle size to the London retardation wavelength, $\lambda_L$. The retardation wavelength characterizes the distance at which van der Waals attractions are reduced because of the finite propagation speed of electromagnetic radiation between atoms on neighboring particles (Russel et al., 1989). The shear number, $N_S = 12\pi\mu a^3\Gamma/A_H$, describes the relative importance of the viscous

and van der Waals forces. Here, $\mu$ is the fluid viscosity and $A_H$ is the Hamaker constant.

Coagulation rates in isotropic turbulence were computed in Chapter 4 for several values of $N_L$ and $N_S$. When $N_L > 10$, the collision efficiencies simulated for the 3.9 $\mu$m diameter particles used in the experiments described in this Chapter, could be represented ($r^2 = 97\%$) with the following power law:

$$\alpha_T = 0.56 N_S^{-0.16} \qquad (6.7)$$

This result implies that, in the presence of particle interactions, the coagulation rate constant increases in proportion to $\Gamma^{0.84}$.

### 6.3 Coagulation experiments

Below, experimental protocols used to measure the singlet concentration evolution in a coagulating suspension are described. Subsequently, the data analysis technique used to extract the coagulation rate constant from the rate of singlet particle depletion is presented.

### 6.3.1 *Experimental procedure*

Monodisperse sulfate polystyrene latex particles (Interfacial Dynamics Corp., OR) having a density of 1.055 g/cm$^3$ were used as the coagulating particles for the experiments. Using a Coulter Multisizer II (Coulter Corp., FL), the number averaged particle diameter was measured to be 3.9 +/- 0.3 $\mu$m indicating that the microspheres were nearly monodisperse. The particles were stored at 4°C in distilled water before use. During coagulation experiments, a density-matched saline solution,

created by adding 75.6 g/L NaCl to distilled water, was used to suspend the latex particles and to eliminate the effects of settling, particle inertia, and double layer repulsion between particles.

Coagulated samples were stored for analysis in a density-matched, glucose-based storage solution made by adding 6.5 g/L NaCl, 2.5g/L NaN$_3$ and 137 g/L glucose to distilled water. The glucose was added to increase the solution density to within 1% of the bead density, NaCl was used as a background electrolyte and NaN$_3$ was used to inhibit bacterial growth in the storage solution. All storage solutions were pre-filtered through 0.4 μm membrane filters to remove background particulates.

Density matching was important because it prevented particles from settling out of suspension during and after an experiment and it reduced gravity- and turbulent-acceleration-induced coagulation of different size particles. The density difference between the particles and the solution was always less than 0.01 g/cm$^3$. For this maximum density difference the calculated particle settling velocity was insignificant compared to the turbulent integral scale velocities measured in the experiments. Similarly, using estimates from Saffman & Turner (1956), coagulation due to turbulent acceleration was predicted to be unimportant compared to turbulent shear for the experimental conditions reported in this manuscript (see Section 6.5). The coagulation rate constant for differential settling of a singlet and a doublet particle was at least 5 times smaller than the turbulent shear and Brownian coagulation rate constants when coagulation kernels summarized by Pearson et. al. (1984) were used. Since the rate of differential settling coagulation depends on the concentration of doublets in

the system, it was inconsequential as long as the experiments contained few doublets. Therefore, using density-matched solutions and analyzing only data for which there were excess singlets assured that turbulent shear controlled the observed particle motion and coagulation.

During an experiment, aliquots of coagulating suspension were periodically withdrawn and diluted in particle-free plastic vials containing the density matched glucose-based storage solution. The particle size distributions of the diluted samples were measured within 1 hour. Preliminary experiments showed that coagulated particles could be stored longer than 6 hours without significant alteration of the observed particle size distribution and concentration. Samples were measured using the Coulter Multisizer with a 100 $\mu$m aperture. The instrument measures changes in conductivity that occur as particles are transported through the aperture. The magnitude and duration of the conductivity spikes are related to the volume of the particle passing through the aperture. Particle volumes are converted into particle diameters assuming spherical particles.

There are three significant analytical concerns associated with the Coulter Multisizer. First, the concentration of particles in the suspension must be low enough so that the probability of measuring two particles simultaneously, termed the coincidence, is small. By diluting samples to contain about 10,000 particles/ml, coincidence was kept to less than 2% of the sample population. Second, the statistical uncertainty in the concentration caused by counting a finite number of particles was reduced by measuring at least of 20,000 particles for each sample. Finally, since the maximum shear rates at the aperture are large (The shear rate at the

wall is greater than $10^5$ s$^{-1}$ for the apertures used in this analysis.) control experiments were required to ensure doublet breakup near the aperture opening did not skew the measurements (Gibbs, 1982). To test for the effects of doublet breakage, coagulation experiments were analyzed using 30, 100 and 140 μm diameter apertures. The particle concentrations measured with the three apertures agreed to within 10% indicating that each aperture was sampling the particle suspension similarly despite the 10-fold variation in the wall shear rate over the 30 to 140 μm aperture size range. It is possible that doublets actually broke up near the aperture, but did not separate sufficiently to be counted as separate particles by the device. This experimental evaluation indicates that aggregate breakup in the Coulter Multisizer II did not influence the measured doublet concentration.

Figure 6.1 shows an example of the raw output from the Coulter Multisizer at the beginning (dashed line) and end (solid line) of a coagulation experiment. The emergence of a distinct doublet peak indicates that flocculation was occurring and could be accurately measured with the instrument.

Calculation of the initial coagulation rate constant from the experimental particle size distribution data depends on knowing the ratio of the singlet concentration to its initial value rather than the absolute singlet concentration (see discussion below). The number concentration in the diameter interval from 3.0 to 3.9 μm (designated with the vertical dotted lines on Figure 6.1) was used as a measure of the singlet concentration. By choosing this size interval, the error caused by counting unusually small
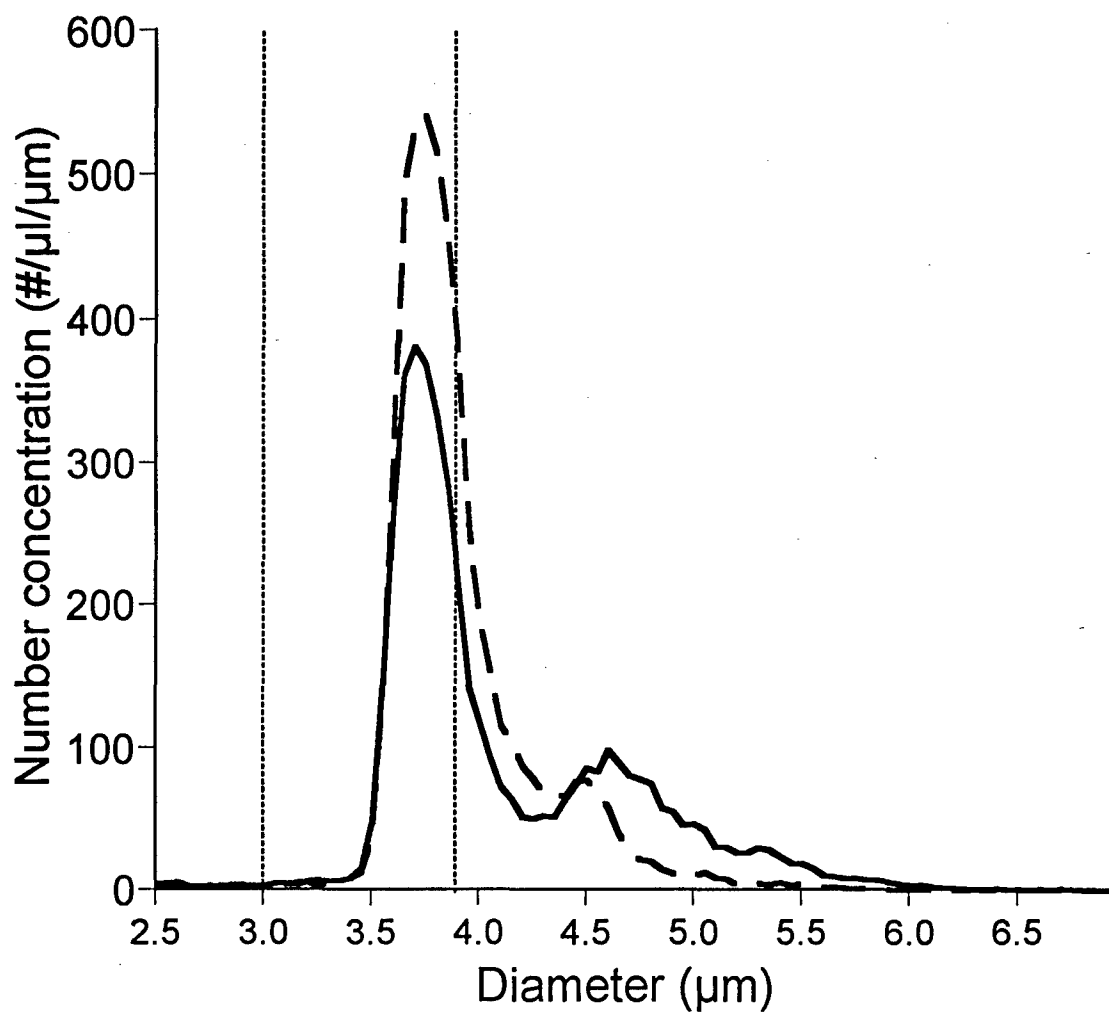
**Figure 6.1**: Typical particle size distributions obtained at the beginning (dashed line) and end (solid line) of a coagulation experiment. The final results show the formation of a significant doublet peak compared to the initial particle size distribution, indicating coagulation of the singlet particles. Dotted lines bracket the region of particle size distribution used as a measure of the singlet concentration.

doublet particles (created by the aggregation of two smaller than average singlet particles) as singlets was significantly reduced. Since some singlets were outside the selected size range the number concentration in the 3.0 to 3.9 μm interval was normalized by its value at the beginning of a coagulation experiment. The error introduced by truncating the size interval used to determine singlet concentration canceled out in calculations of the relative concentration; therefore, relative concentration was deemed to be more accurate than the singlet concentration.

### 6.3.2 *Coagulation rate constant determination*

If the concentration of singlet particles is in excess, Equation 6.1 can be rewritten as a pseudo-first order expression depending on the particle volume fraction:

$$\frac{dS}{dt} = -k'S \qquad (6.8)$$

where $k' = (3\phi/2\pi a^3)k$ and $\phi$ is the volume fraction of particles. The use of the pseudo-first order approximation requires $S/(S_0-S) \gg 1$, where $S_0$ is the initial concentration of singlet particles. The linearized expression given by Equation 6.8 has the advantage of leading to an integral rate expression that depends on the relative concentration of singlet particles (see Equation 6.9). As noted above, the relative concentration of singlets was estimated from the experimental data rather than the absolute singlet concentration since the relative concentration could be determined more accurately.

In a closed system, the particle volume fraction is a constant and Equation 6.8 can be integrated subject to the initial condition that when t = 0, S = $S_0$.

$$\ln\left(\frac{S}{S_0}\right) = -k't \qquad (6.9)$$

A plot of $\ln(S/S_0)$ against time should yield a straight line with the slope being proportional to the rate constant, $k'$.

Since the above rate expression is predicated on doublet formation being the only coagulation process occurring, data collection must stop once the formation of larger order aggregates becomes significant. Aggregates made by the collision of a doublet and a singlet (i.e., a triplet) are most likely to form next. A simple estimate for the importance of triplet formation can be obtained by taking the ratio of the doublet to triplet coagulation rates. Denoting doublet concentration with D and triplet concentration with T, this ratio is given by:

$$\frac{dD/dt}{dT/dt} = \frac{\alpha k^0 S^2}{\alpha_3 k_3^0 SD} \qquad (6.10)$$

where the numerical subscripts indicate the number of primary particles in the aggregate. If $\alpha$ and $k^0$ are not strong functions of aggregate size, Equation 6.10 reduces to:

$$\frac{dD/dt}{dT/dt} \approx 2\frac{S}{S_0 - S} \qquad (6.11)$$

where a particle balance was used to relate D to S, assuming the concentration of higher order aggregates is negligible, i.e., D = ½(S$_0$-S). To within an order one constant, this is the same criterion that was established for using the pseudo-first order approximation in Equation 6.8.

Aggregate breakup can also alter the rate of singlet depletion. Breakup is characterized by a decrease in the observed coagulation rate until the system reaches steady state. In other words, at steady state the formation of doublets is balanced by breakup of doublets and the effective coagulation rate becomes equal to zero. In the following investigations aggregate break up was significant at the higher turbulent shear rates. Doublet breakup was modeled explicitly by including a term in the rate equation for the singlet concentration dependent on the doublet concentration. Thus, Equation 6.8 becomes:

$$\frac{dS}{dt} = -k_T' S + 2bD \tag{6.12}$$

where b is the unknown doublet break up rate constant that is conjectured to depend on the turbulence intensity (McCave, 1984). After substituting D = ½(S$_0$ - S) for the doublet concentration, Equation 6.12 can be integrated to obtain:

$$\frac{S}{S_0} = \frac{b + k_T' \exp[-(b + k_T')t]}{b + k_T'} \tag{6.13}$$

In cases where doublet breakup was experimentally observed, non-linear regression of the experimental data using Equation 6.13 was used to estimate the coagulation rate constant and the break up rate constant. For the data at the highest turbulent shear rate, the transition to equilibrium was very sharp, so use of the explicit breakup model was unnecessary. Instead, the linear regime (see Equation 6.9) dominated by doublet formation was isolated statistically by monitoring the coefficient of determination ($r^2$) of a linear regression as additional data at longer times was included in the regression. Inclusion of data at times when the model given by Equation 6.9 was valid improved the coefficient of determination while inclusion of data that deviated because of significant break up decreased the value of $r^2$. The rate constant obtained at the maximum $r^2$ was used to approximate k for the highest shear case.

## 6.4 Estimation of the Hamaker constant

The Hamaker constant ($A_H$) provides a measure of the strength of the van der Waals attraction between colloidal particles. It was necessary to estimate its value for the 3.9 µm diameter polystyrene beads used in these experiments before the turbulent coagulation experiment and simulation results could be compared. Previous experimental estimates for $A_H$ obtained from Brownian coagulation experiments range from $0.7k_bT$ to $1.9k_bT$ for polystyrene particles (Russel et al., 1989), where $k_b$ is the Boltzmann constant and T is the absolute temperature. Most of the variation in the estimated Hamaker constants is attributed to the weak

dependence of the Brownian collision efficiency on the Hamaker constant (Russel et al., 1989).

The Hamaker constant was obtained by fitting theoretical predictions for the Brownian coagulation rate constant to experimental data. Besides providing an estimate for $A_H$, agreement of the experimentally determined value of $A_H$ with previous estimates furnishes evidence that the extents of coagulation measured with the Coulter Multisizer are reasonable.

### 6.4.1 *Data analysis and procedure*

The initial rate of Brownian coagulation is second order in the singlet concentration and its kinetic expression is given by Equation 6.1, where $k = k_B = \alpha_B 8 k_b T / 3\mu$ is the Brownian diffusion coagulation kernel (Russel et al., 1989) and $\alpha_B$ is the Brownian coagulation collision efficiency incorporating the effects particle interactions.

The Brownian coagulation collision efficiency has been computed for particles influenced by hydrodynamic interactions, van der Waals attraction and electrostatic double layer repulsion (Spielman, 1970; Valioulis & List, 1984). Spielman (1970) considered Brownian coagulation for particles influenced by a non-retarded van der Waals potential, while Valioulis & List (1984) extended the calculations to include the effects of van der Waals retardation. Unfortunately, numerical results were only provided for particles smaller than 1 µm diameter.

The equation for $\alpha_B$ can be derived from the steady state radial pair diffusion equation valid for a particle influenced by Brownian motion, hydrodynamic interactions and an interparticle potential. In agreement

with others (Russel et al., 1989; Spielman, 1970; Valioulis & List, 1984) the following result was obtained for equal sized particles:

$$\frac{1}{\alpha_B} = 2\int_2^\infty \frac{\exp(\Phi/k_bT)}{G(r)} \frac{ds}{s^2} \qquad (6.14)$$

where $\Phi$ is the interparticle potential, $s = r/a$ is the particle separation distance scaled by the particle radius and $G(r)$ is the radial relative mobility for two hydrodynamically interacting Brownian particles (Batchelor, 1976). The solution of Equation 6.14 was obtained using a 5th order Runge-Kutta algorithm with adaptive step control (Press et al., 1992). The van der Waals potential reported by Schenkel & Kitchener (1960) was used for $\Phi$ and values of $G(r)$ were taken from Kim & Karilla (1991). Additional details on the integration method and the form of $\Phi$ may be found in Chapter 3 (see also Brunk et al., 1997a). In Figure 6.2 the solid line shows the model prediction for the Brownian coagulation collision efficiency versus $A_H/kT$.

Brownian coagulation experiments were conducted in the density-matched saline solution. Double layer interactions were assumed to be negligible due to the high ionic strength of the suspending medium, so only hydrodynamic interactions and van der Waals forces affected the experimentally determined Brownian coagulation rate.

The coagulation rate was calculated by the methods outlined in Section 6.3. In the Brownian coagulation experiments doublet breakup was not important so the integral rate expression given by Equation 6.9 was used in the data analysis. Experiments were conducted in particle-free
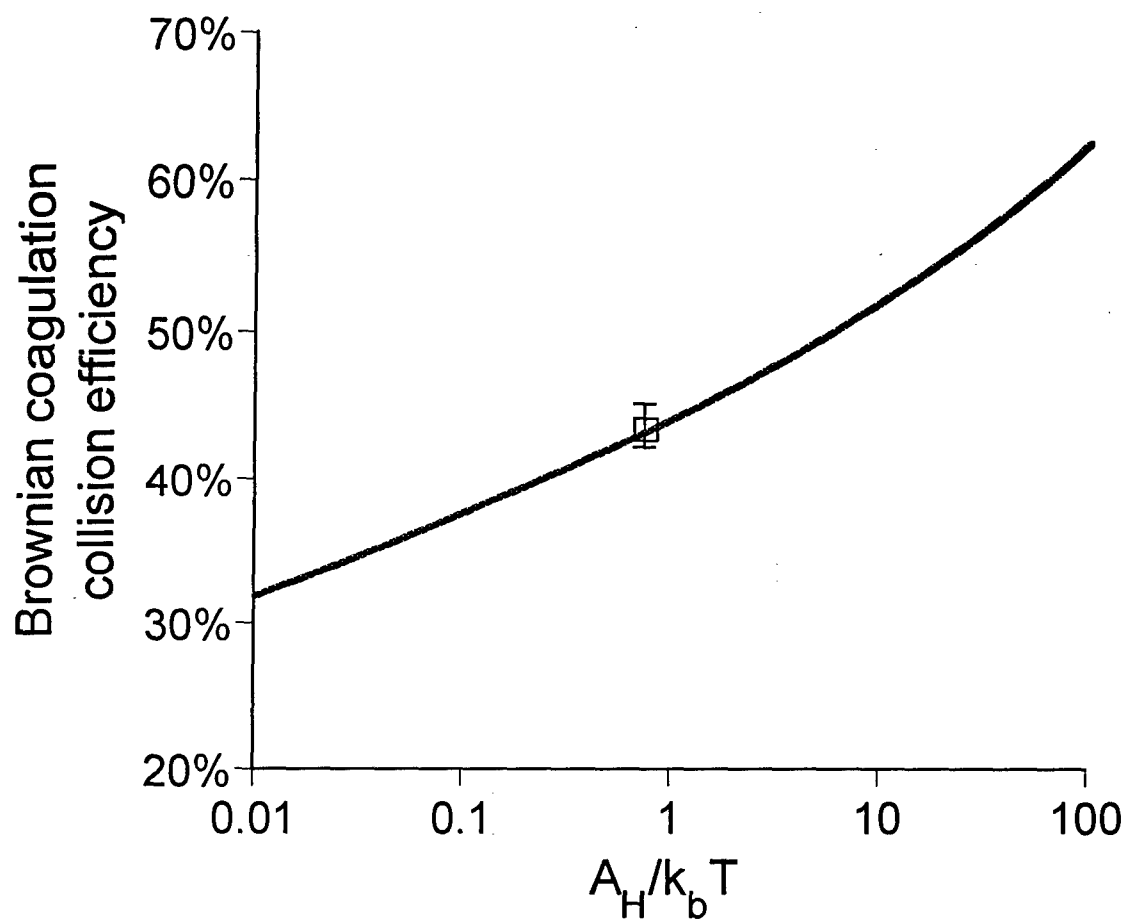
**Figure 6.2**: Model predictions for the Brownian coagulation collision efficiency against the Hamaker constant for 3.9 μm diameter monodisperse polystyrene spherical particles. The square represents the experimentally determined $\alpha_B$ for the 3.9 μm latex particles used in this manuscript. Error bars are 60% confidence intervals.

plastic vials containing approximately 22 ml of solution. A reaction half-life of about 90 minutes was chosen for the experiments which meant that the initial bead concentration in the vials had to be about $9.5 \times 10^6$ particles/ml. Initially, each vial was filled with 2 ml of filtered distilled deionized water. Enough beads were added so that when diluted to 22 ml the vial would contain the correct number concentration of singlets. The 2 ml suspension of beads was placed in a sonicating bath for three minutes to break up any doublets. Then, 20 ml of saline solution was quickly poured into the vial to mix the beads and "start" Brownian coagulation. Fluid motions caused by pouring were allowed to subside. After waiting 5 minutes, samples of the suspension were taken every 5 minutes over 45 minutes. At each sampling time, 52 $\mu$l were removed and diluted 1:400 in previously tared vials containing density-matched glucose solution. Sample dilution quenched the Brownian coagulation reaction and provided the correct concentration levels for accurate analysis in the Coulter Multisizer. Samples were taken using an Eppendorf automatic pipette with the plastic pipette tip enlarged to 1-2 mm diameter. The larger diameter pipette tip was used to minimize particle breakup due to shear caused by sampling (Gibbs, 1982).

### 6.4.2 *Brownian coagulation experimental results*

For each Brownian coagulation experiment a mass balance was computed as a function of elapsed time. Examination of the volumetric concentration evolution data showed that the system was well mixed and temporal trends caused by particle losses/gains were not apparent.

The evolution of the singlet concentration for a representative experiment is shown in Figure 6.3 along with a best fit line through the data using Equation 6.9. For this experiment, $k_B = 4.72$ +/- $0.28$ $\mu m^3/s$ with an $r^2$ of 94%. Error bars are 95% confidence intervals based on Poisson statistics.

The average Brownian coagulation rate constant was obtained from 5 independent experiments and the average rate was normalized by the Brownian coagulation rate without interparticle interactions to yield $\alpha_b = 43.7\%$ with 60% confidence intervals of +/- 1.5%. Using this collision efficiency with Figure 6.2 yields an average $A_H/k_bT = 0.75$ shown as the open square on the graph. The collision efficiency is insensitive to the value of the Hamaker constant; thus, the 60% confidence interval of $A_H$ is wide ($0.5kT$ to $1.3kT$). The best estimate for $A_H/k_bT$, however, compares favorably to estimates summarized in Russel et al. (1989).

## 6.5 Turbulent coagulation experimental results

Experimental measurements of the turbulent coagulation rate are presented below and compared with the computer simulations of turbulent coagulation. Experiments were conducted in the spatially decaying, isotropic turbulence created by an oscillating grid device. First, the technique for measuring the Kolmogorov shear rate in the reactor is presented. Measurements of the turbulent coagulation rate are then correlated with the spatially averaged Kolmogorov shear rate. Finally, the coagulation rate as a function of average Kolmogorov shear rate in the reactor is compared with the turbulent coagulation model summarized
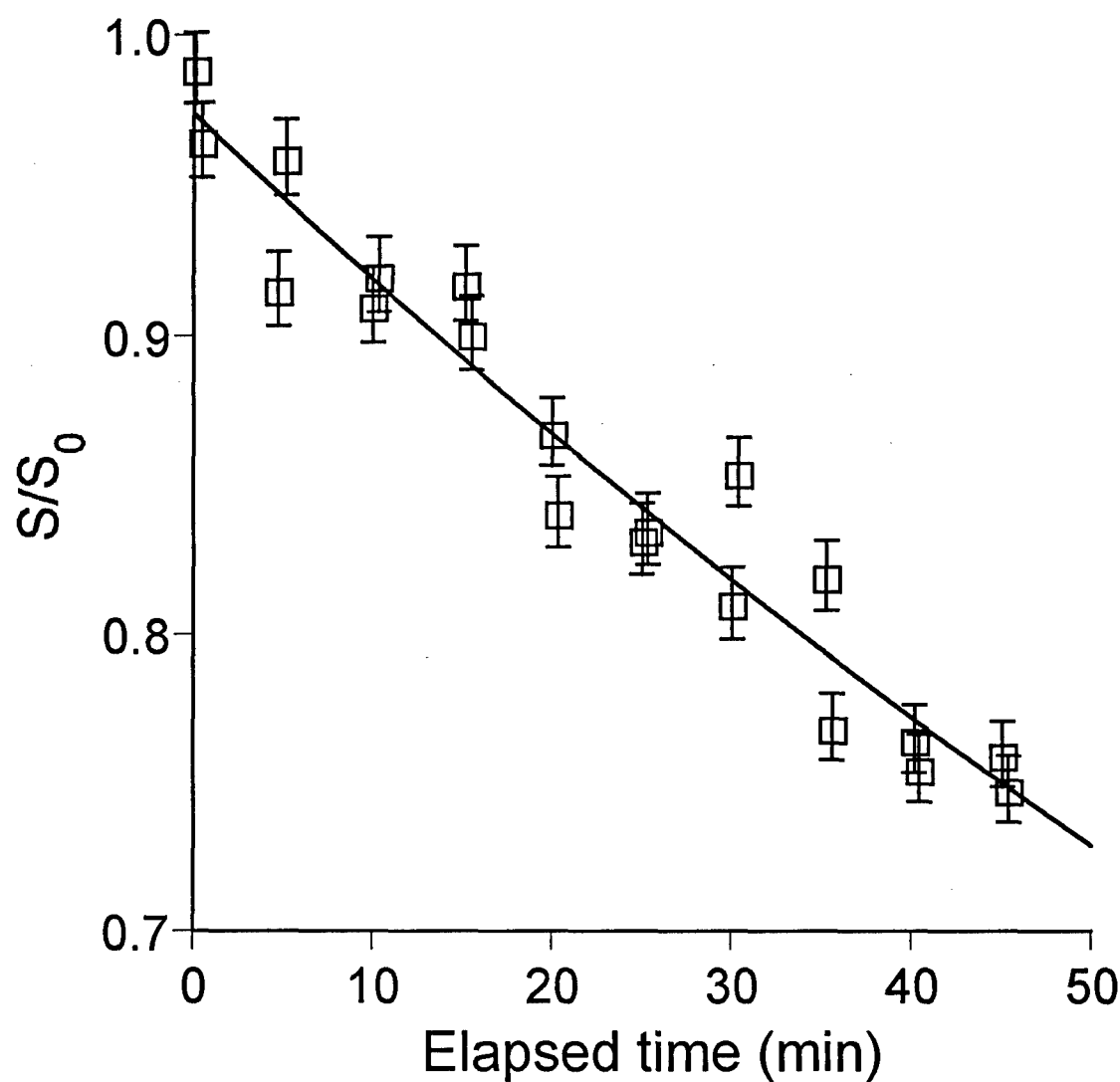
**Figure 6.3**: Linearized singlet concentration evolution data obtained in a Brownian coagulation experiment. The solid line is a best fit through the experimental data and the error bars are 95% confidence intervals based on Poisson statistics.

above (see Section 6.2). The comparison between simulation and experiment also illustrates the importance of correctly relating the model predictions to the local turbulent conditions of the reactor. Comparison is also made between the computer simulations and the turbulent pipe flow coagulation experiments conducted by Delichatsios & Probstein (1975).

### 6.5.1 *Turbulent coagulation materials and methods*

Experiments were conducted in an oscillating grid reactor system that was originally designed to simulate the vertical distribution of turbulence typical for natural aquatic systems. The reactor has been shown to produce well-defined homogeneous, isotropic turbulence that follows established grid-stirred turbulence scaling laws (Chapter 5; Brunk et al., 1996) and it has been used in stratified flow (Jensen, 1997) and sediment transport studies (Chapter 5; Brunk et al., 1996).

The 100 x 40 x 20 cm reactor contains five vertically spaced, independently oscillating, 20 x 40 cm turbulence generating grids. Each stainless steel grid is woven from 2.67 mm rods to form a grid with a mesh spacing of 1.27 cm and a solidity of 37.6%. The center of the grid stroke is located 4 cm from the back of the reactor. Each grid can be independently operated at frequencies ranging from 0 to 8 Hz with a grid stroke (twice the oscillation amplitude) of 0.5 to 4 cm in 0.5 cm increments. Sample ports spaced in 5 cm intervals down the center of the column can be moved to any horizontal distance into the reactor providing gravity-fed *in situ* sampling of the water column.

The intensity of the turbulence created in the reactor can be varied by changing the oscillating frequency and the stroke length of each grid. An

acoustic Doppler velocimeter (ADV) was used to measure three components of the turbulent velocity. The velocimeter samples a cylindrical volume 3 mm in radius and 3-9 mm high at a rate of 25 Hz. The sample volume location is 5 cm below the signal transducers to minimize the effect of the probe on the acquired velocity data (Lohrman et al., 1994). Additional details about the construction and operation of the grid-stirred reactor may be found in Chapter 5 (see also Brunk et al., 1996).

For this work, experiments were conducted with a single oscillating grid in the bottom 1/5th of the reactor to minimize the number of polystyrene beads used in a single experiment. A diagram of the reactor system is shown in Figure 6.4. The control volume consisted of a glass and stainless steel chamber 20 cm wide, 40 cm deep and 25 cm high. The tank was filled with pre-filtered density-matched saline solution through the baffled fill/drain port. For each experiment the reactor contained approximately 20 L of a particle suspension. Samples taken from the reactor before addition of the polystyrene beads indicated that particle contamination was indistinguishable from background noise. After filling with the filtered saline solution, the oscillating grid was set at the desired frequency and the reactor was allowed to reach hydrodynamic steady state.

Using Equation 6.4 in Equation 6.9 and published estimates for $\beta$ and $\alpha_T$ ($\beta \approx 10.4$, $\alpha_T = 1$; Saffman & Turner, 1956), the particle concentration needed to obtain a coagulation half-life of 40 minutes was computed. For this calculation, the characteristic Kolmogorov shear rate was approximated using the methods outlined below in Section 6.5.2. For each turbulent coagulation experiment, the required number of beads was

oscillating
grid

sample ports

25 cm

baffled
fill/drain port

10 cm

40 cm

2.5 cm

5 cm

16 cm

20 cm
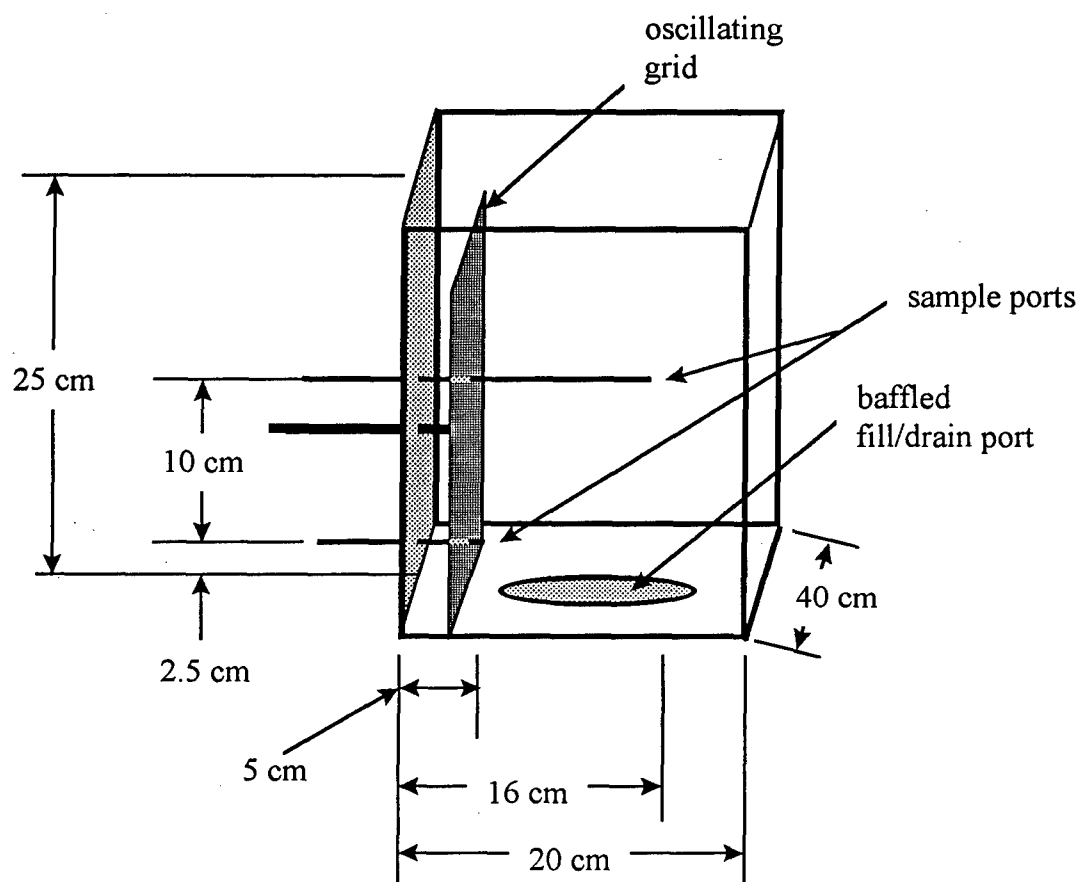
**Figure 6.4**: Diagram of the bottom of the grid-stirred apparatus used for the turbulent coagulation experiments. The schematic shows the location of sampling ports (5 cm and 16 cm from the back wall of the apparatus) and the dimensions of the coagulation experiment control volume. The center of the grid stroke is located 4 cm from the back of the reactor.

diluted in 100 ml of filtered distilled water and sonicated for several minutes. Afterwards the stock solution was distributed rapidly and equally over the water surface. The system was allowed to mix for 30 seconds before sampling began. Samples were taken from the two ports shown in Figure 6.4, placed 2.5 cm from the bottom and 5 cm from the back of the reactor and 12.5 cm from the bottom and 16 cm from the back of the reactor. Aliquots of approximately 1 ml were taken from the reactor periodically and placed in previously tared, particle-free vials containing the density-matched glucose solution. The coagulating suspension was diluted by approximately a factor of 20 in the sample vial to quench the coagulation reaction and lower the particle number concentration to a range suitable for analysis on the Coulter Multisizer.

### 6.5.2 *Characterization of oscillating grid turbulence*

Turbulence generated in an oscillating grid system decays rapidly with distance from the grid (Hopfinger & Toly, 1976); thus, coagulating particles will experience a spatially varying distribution of Kolmogorov shear rate as they migrate throughout the reactor. If the system is well-mixed, aggregating particles will sample the entire reactor space during coagulation; therefore, it would be reasonable to expect the observed coagulation rate measured at a single point to be related to the spatial distribution of shear rates (and hence the distribution of local coagulation rates) within the reactor.

In this section, estimates for the Kolmogorov shear rate are provided as a function of the oscillating grid frequency and distance from the grid. The local estimates for $\Gamma$ are subsequently used to relate the experimental

coagulation rate constant to the volumetrically-averaged shear rate in the reactor.

The assumption that the reactor is well mixed can be evaluated by comparing the characteristic time for coagulation to the reactor mixing time. An estimate for the characteristic coagulation time is $\tau_c = 1/k'$. A conservative estimate for the reactor mixing time is given by the turbulent diffusion time scale, $\tau_i = H^2/u'L$ where H is the reactor height (25 cm), L is the integral length scale (i.e., the length scale of the largest turbulent eddies) and u' is the root mean square velocity. Taking the ratio of $\tau_c$ and $\tau_i$ and simplifying yields:

$$\frac{\tau_c}{\tau_i} \approx \frac{1}{\phi Re^{1/2}}\left(\frac{L}{H}\right)^2 \tag{6.15}$$

where $u'/L\Gamma \approx Re^{-1/2}$ (Tennekes & Lumley, 1972) and $Re = u'L/\nu$ is the turbulent Reynolds number. Measurements of steady state sediment transport in the experimental apparatus suggest that H/L ~ 3 (Chapter 5; Brunk et al., 1996). The highest particle volume fraction used in the turbulent coagulation experiments was $\phi = 10^{-5}$, indicating that the Reynolds number would have to be at least $10^8$ for the well-mixed assumption to be poor. The turbulent Reynolds numbers generated in the apparatus were considerably lower than $10^8$ (see Table 6.1); thus, the assumption that the coagulating particles sample the entire reactor was justified.

Comparison between experimental coagulation rates obtained in the oscillating grid reactor and model calculations are predicated on obtaining

**Table 6.1**: Measured and estimated parameters for the oscillating grid turbulence apparatus. $\langle\Gamma\rangle$ is the Kolmogorov shear rate spatially averaged over the grid-stirred reactor. $\eta_{MIN}$ is the smallest local Kolmogorov length scale in the grid-stirred reactor. The smallest $\eta$ will be located in the region of highest turbulence, $-2$ cm $< x < 2$ cm. $\langle\eta\rangle$ is the spatially averaged Kolmogorov length scale. Re $= u'l/\nu$ is the turbulent Reynolds number. $Re_\lambda = u'\lambda/\nu$ is the Taylor-scale Reynolds number where $\lambda \approx 4Re^{1/4}\eta$ is the Taylor scale. $\langle Pe\rangle = \Gamma a^2/D$ is the spatially averaged Peclet number where D is the Brownian diffusivity of the 3.9 $\mu$m diameter particles.

| Grid Frequency (Hz): | 1 | 3 | 4 | 6 | 8 |
|---|---|---|---|---|---|
| $\langle\Gamma\rangle$ (1/s) | 3.7 | 19.3 | 29.6 | 54.3 | 83.6 |
| $\eta_{MIN}$ ($\mu$m) | 240 | 105 | 85 | 63 | 50 |
| $\langle\eta\rangle$ ($\mu$m) | 520 | 228 | 184 | 135 | 109 |
| Re | 71 | 214 | 286 | 428 | 572 |
| $Re_\lambda$ | 39 | 67.5 | 78 | 95 | 110 |
| $\langle Pe\rangle$ | 79 | 410 | 632 | 1162 | 1789 |

an accurate estimate for the Kolmogorov shear rate distribution within the reactor. As described above (Section 6.2.1), the Kolmogorov shear rate can be found through scaling arguments by balancing the turbulent dissipation rate, $\epsilon$, with the viscous dissipation to obtain Equation 6.3. The difficulty in using this relation lies in obtaining an accurate estimate for the turbulent dissipation rate. There are two main techniques that can be employed to accomplish this: direct measurement of $\epsilon$ and scaling arguments. The dissipation rate is a small scale quantity that depends on the mean square fluctuating velocity gradient tensor (Tennekes & Lumley, 1972). Since the power spectrum for the velocity derivative peaks in the dissipation subrange of turbulence (i.e., at Kolmogorov length scales) a direct measurement of $\epsilon$ would require a velocity probe with spatial and temporal resolution that is comparable to the Kolmogorov scales (e.g., $\eta \sim$ 0.5 mm ). The acoustic Doppler velocimeter used in this study had a limited sampling resolution of about 3 mm that was unable to resolve the fine scales of turbulence. For instance, turbulent kinetic energy power spectra obtained with the instrument showed only a small portion of the inertial ranges of turbulence. Consequently, an indirect measure was used for estimating the turbulent dissipation rate.

The turbulent dissipation rate can be related to the turbulent energy input at the large scales by (Tennekes & Lumley, 1972):

$$\epsilon \approx \gamma \frac{u'^3}{L} \qquad\qquad (6.16)$$

where $\gamma$ is an order one constant typically taken to be 0.8 (Townsend, 1976). Considerable empirical evidence suggests that this scaling relationship provides a robust estimate for $\epsilon$ (Tennekes & Lumley, 1972). For convenience, Equation 6.16 is recast in terms of the turbulent kinetic energy (E), where $1/2E = (3u')^2$, and substituted into Equation 6.3. After manipulation, an expression relating the Kolmogorov shear rate to the turbulent kinetic energy and the integral length scale is obtained:

$$\Gamma \approx \left[ \frac{\gamma \left( \frac{2}{3} E \right)^{3/2}}{L \nu} \right]^{1/2} \tag{6.17}$$

The variation of the integral length scale (L) with distance from the oscillating grid (x) has been investigated previously (Hopfinger & Toly, 1976; Brumley & Jirka, 1987; E & Hopfinger, 1986). Hopfinger & Toly (1976) found that L was proportional to x with the proportionality constant, B, ranging from 0.1 to 0.35 depending on the grid stroke (St) and grid mesh spacing (M). Further investigations by E and Hopfinger (1986) indicated that B is larger for large St/M. The ratio of stroke to mesh size is large in the reactor; therefore, a value of B = 0.35 was chosen for this study. In the near field the integral length scale was set at the mesh spacing since this length was expected to dominate in the oscillating grid region. The integral scale was made a piecewise continuous function of distance from the oscillating grid by setting L to the mesh size, 1.27 cm for x < 3.63 cm, and allowing it to vary linearly with distance in the far field (x > 3.63 cm).

At distances far from the oscillating grid, the integral scale velocity decays with distance from the oscillating grid and is well represented by the scaling relation developed by Hopfinger & Toly (1976):

$$u'/fSt = C_{HT}(St^{1/2}M^{1/2}/x)$$ (6.18)

where f is the grid frequency (Hz), St is the grid stroke (4 cm for these experiments), M is the center-to-center mesh spacing (1.27 cm for these experiments), x is the horizontal distance from the center of the operating grid stroke and $C_{HT}$ is a constant found to be about 0.25 (Hopfinger & Toly, 1976), although values of $C_{HT}$ ranging from 0.22 to 0.27 (De Silva & Fernando, 1992) have been reported. This scaling relationship has been subsequently verified by a number of other researchers (De Silva & Fernando, 1992; Brumley & Jirka, 1987; Fernando & Long, 1985).

The isotropy of grid-generated turbulence may be used to rewrite Equation 6.18 in terms of E (Chapter 5; Brunk et al., 1996):

$$E = \frac{3}{2}C_{HT}^2\frac{f^2St^3M}{x^2}$$ (6.19)

Estimates for the range over which Equations 6.18 and 6.19 are applicable vary from x > 4St (De Silva & Fernando, 1992) to x > 2M (Atkinson et al., 1987). As shown below, the Atkinson et al. (1987) estimate of x > 2M held well for the grid parameters used in these experiments.

For this work, the turbulent kinetic energy distribution in the near and far field of the grid were both required to estimate the spatial distribution of $\Gamma$ using Equation 6.17. To that end, turbulence

measurements were made as a function of distance from the oscillating grid. The stroke was held constant at 4 cm and f was varied from 0 to 8 Hz giving turbulent Re as high as 572 for f = 8 Hz. The turbulence parameters obtained for the reactor are summarized as a function of oscillating grid frequency in Table 6.1. Three-component velocity data were obtained for different reactor operating conditions using the *in situ* ADV probe (Sontek Inc., CA) at a data rate of 25 Hz for at least 300 seconds. At each grid frequency, velocity samples were taken at several vertical and horizontal positions in the plane a distance x from the oscillating grid and the velocity data were combined for the ensuing analysis.

The scaling law for E depends only on distances parallel to the grid motion, implying that grid-stirred turbulence is homogeneous in planes perpendicular to the grid motion. Detailed mappings of the turbulent kinetic energy variation over a plane parallel to an oscillating grid showed an absence of long range structure and a relatively narrow variance relative to the average E (Chapter 5; Brunk et al., 1996). Both results suggest that the apparatus produced nearly homogeneous turbulence.

For each grid frequency, the turbulent kinetic energy data obtained in the far field (i.e., x > 2M) was plotted against the right-hand side of Equation 6.19 to verify the scaling relation in the reactor and obtain an estimate for $C_{HT}$. The scaling law fit the experimental data with $r^2$ ranging from 61 to 92% and the predicted $C_{HT}$ varied from 0.22 to 0.24 in agreement with the work of others (Hopfinger & Toly, 1976; De Silva & Fernando, 1992). In Figure 6.5 the data sets for various grid frequencies
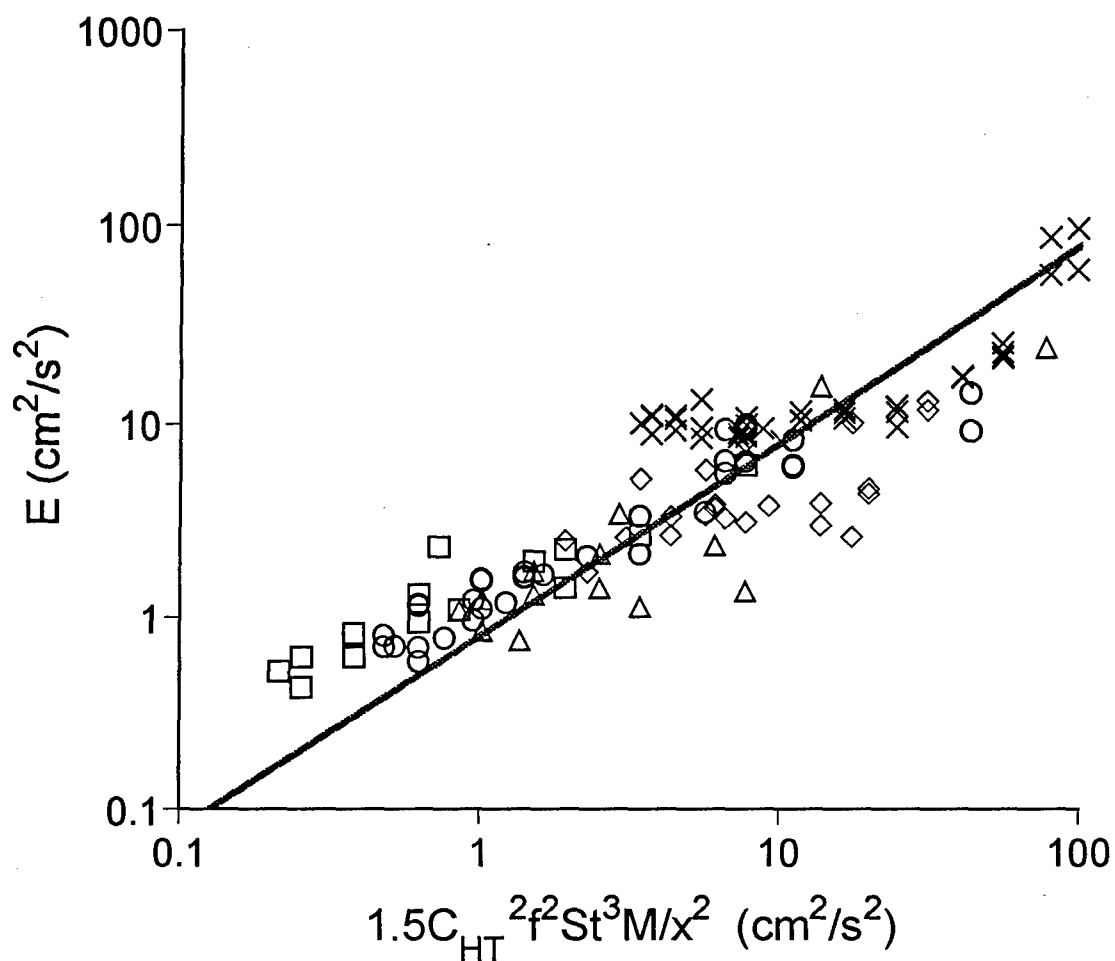
**Figure 6.5**: Comparison of the measured turbulent kinetic energy in the far field with the grid scaling relation for the turbulent kinetic energy (Hopfinger & Toly, 1976). For the experiments, St = 4 cm and f = 2 Hz (squares), 3 Hz (circles), 4 Hz (triangles), 6 Hz (diamonds) and 8 Hz (crosses).

are combined and compared with the scaling law using the frequency-averaged value of $C_{HT} = 0.225$.

Figure 6.6 summarizes the near field results obtained by plotting the measured E versus distance from the oscillating grid center for frequencies ranging from 3 to 8 Hz. The error bars are standard deviations from independent experiments when available. The turbulent intensity displayed no systematic dependence on position for distances less than 2 cm and therefore the near field was represented as a constant value, shown by the solid horizontal lines in Figure 6.6. A plot of the average turbulent kinetic energy in the near field versus grid frequency (Figure 6.7) exhibits the expected $f^2$ dependence. The symbols are averages of the E measurements made in the oscillating grid region at each frequency and the error bars represent 95% confidence intervals. The correlation, $E = 2.93f^2$, fit the data with an $r^2 = 99\%$. Here, E has units of $cm^2/s^2$ and f is in Hz.

By combining the turbulent kinetic energy scaling relations valid for the inner and outer regions, a piece-wise continuous approximation to the experimental data was obtained when $x = 1.45$ cm was used to separate the near and far field results. The calculated E profile obtained for $f = 8$ Hz is shown in Figure 6.8 along with the experimental data. At distances greater than about 1.45 cm from the grid, the turbulence followed the Hopfinger & Toly (1976) decay law shown as the solid line. Near the grid, turbulence intensity was assumed to be constant as illustrated with the dashed line in Figure 6.8.

The average Kolmogorov shear rate at each operating condition was obtained by taking the volumetric average of the measured $\Gamma$ distributions
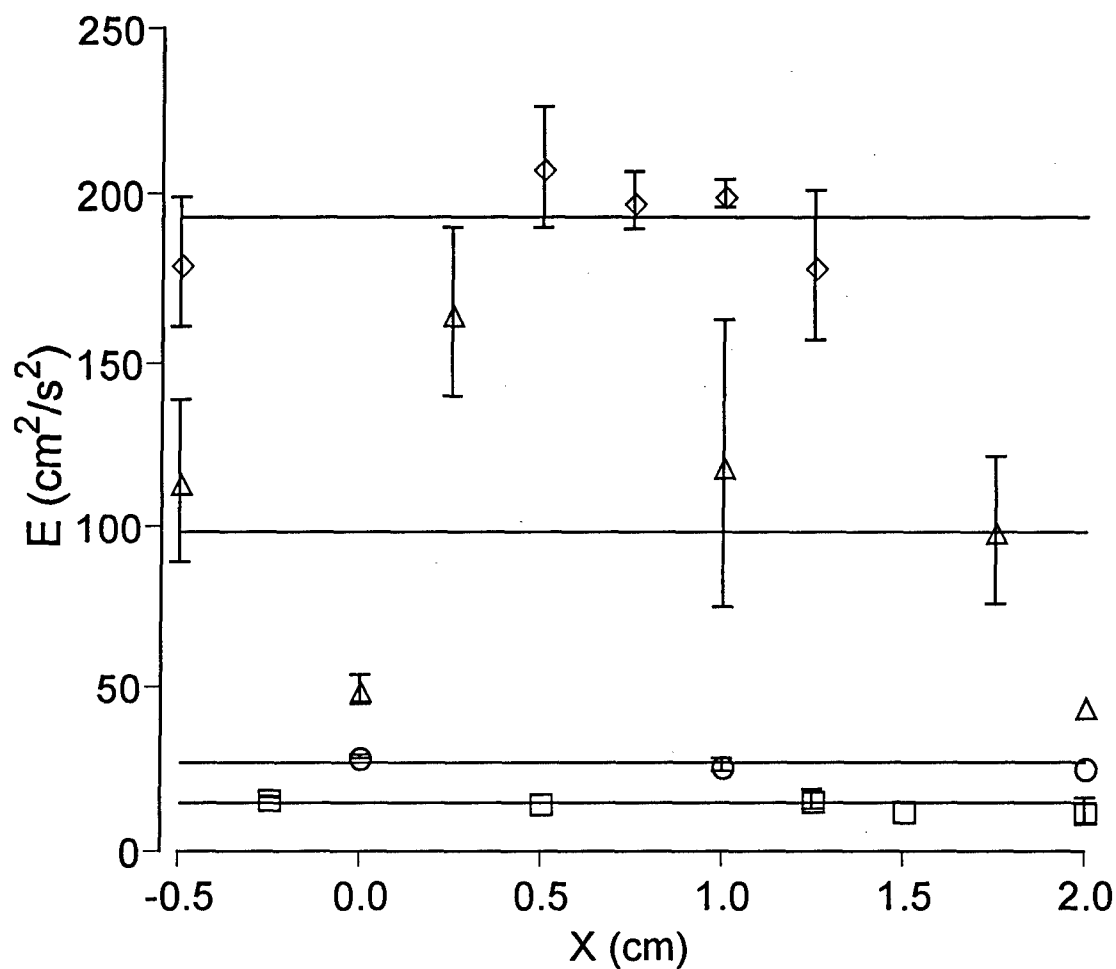
**Figure 6.6**: Spatial distribution of turbulent kinetic energy in the grid region when St = 4 cm and f = 3 Hz (squares), 4 Hz (circles), 6 Hz (triangles) and 8 Hz (diamonds). The horizontal lines are averages for each grid frequency and the error bars are +/- one standard deviation from the mean when available.
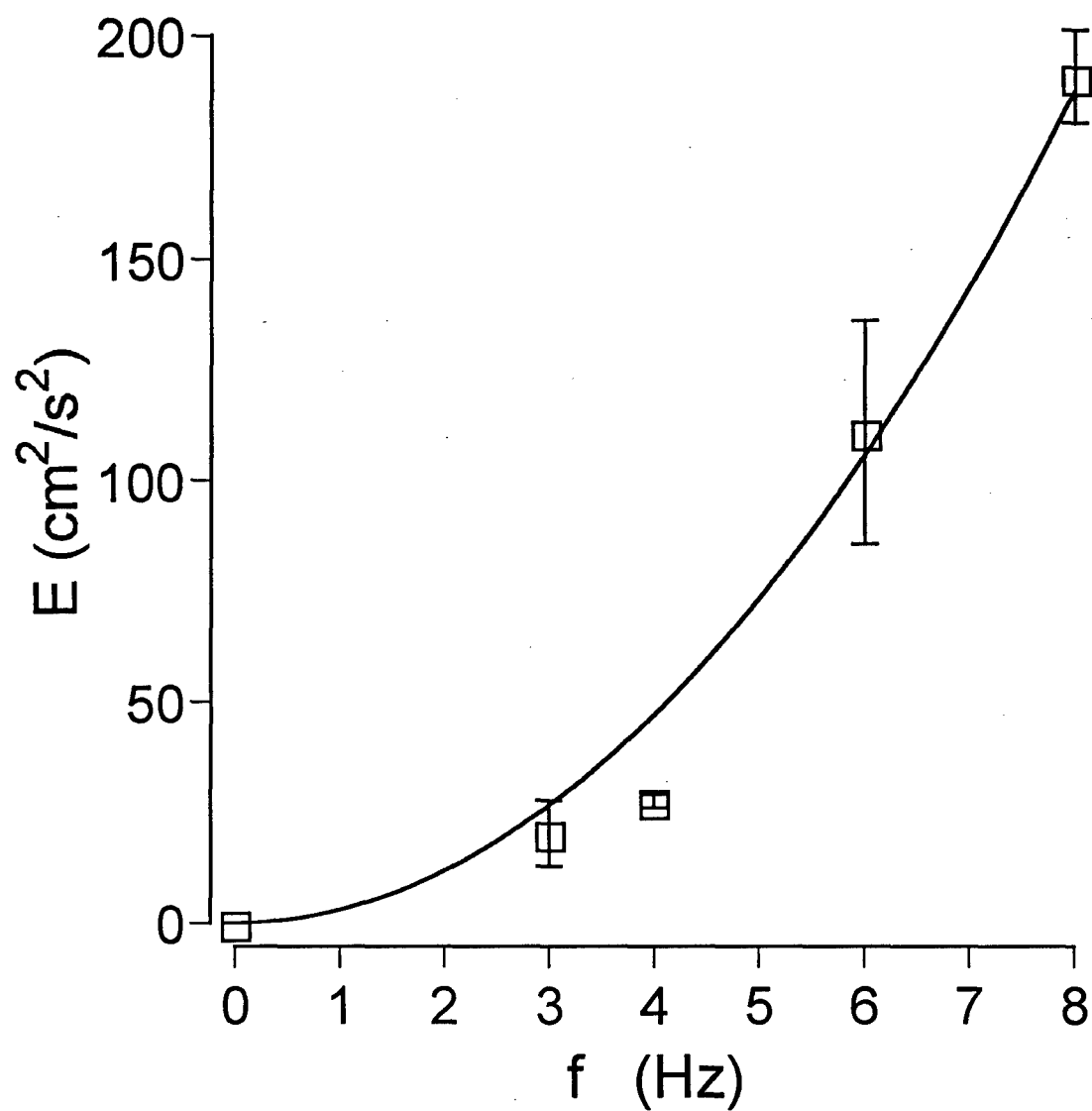
**Figure 6.7**: The average turbulent kinetic energy in the grid region versus the grid frequency. The solid line is a best-fit to the experimental data and error bars are 95% confidence intervals.
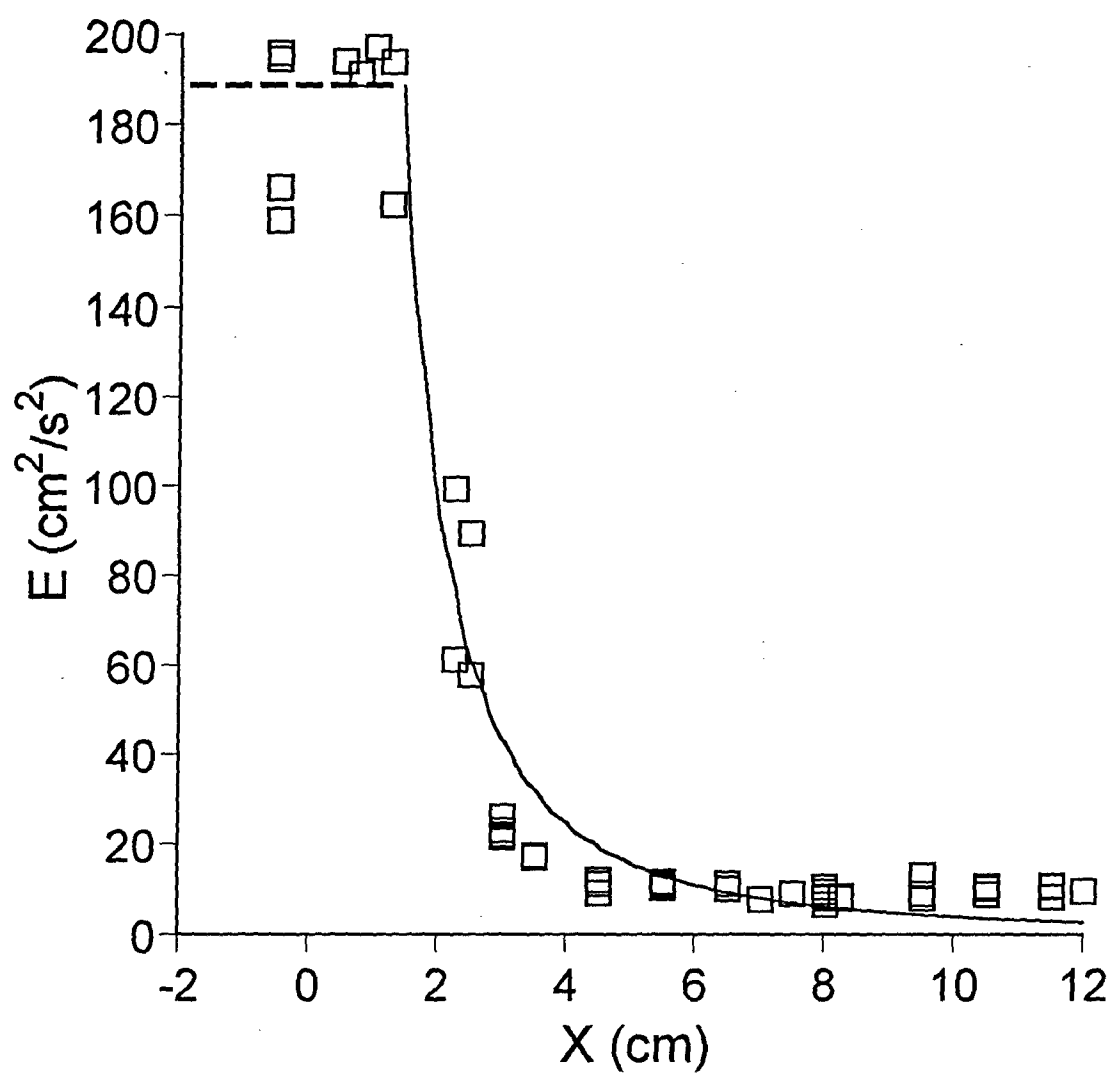
**Figure 6.8**: The spatial distribution of turbulent kinetic energy (E) as a function of horizontal distance from the oscillating grid. Results are shown for St = 4 cm and f = 8 Hz. The solid line represents the expected far field E distribution and the dashed line is an average of the measurements made in the oscillating grid region.

assuming homogeneity in planes perpendicular to the grid motion as indicated by Equation 6.19. Table 6.1 lists the computed spatially averaged Kolmogorov shear rates, $<\Gamma>$, which range from 3.7 $s^{-1}$ at $f = 1$ Hz to 83.6 $s^{-1}$ at $f = 8$ Hz. The average Kolmogorov length scale varied from 520 to 109 $\mu$m as the grid frequency was changed from 1 to 8 Hz. The estimate for $\eta$ in the most turbulent regions of the tank ($x = 0$ cm) was found always to be above 50 $\mu$m (see Table 6.1); therefore, the assumption that the particle diameters (3.9 $\mu$m) were much smaller than the Kolmogorov length scale applied for all the operating conditions used in the coagulation experiments.

### 6.5.3 *Analysis of turbulent coagulation measurements*

Turbulent coagulation experiments were conducted using the procedure outlined in Section 6.3. Four to 6 independent experiments were performed for each oscillating grid frequency. Figure 6.9 shows the mass balance as a function of time for an experiment conducted at $f = 6$ Hz. Shown are symbols for the two sampling ports as well as a solid line indicating the average mass in the system and dashed lines denoting +/-10% of the mean. The error bars show 95% confidence intervals in the calculated concentrations based on Poisson statistics. Particle losses were not observed over the lifetime of the experiment and no statistically significant trend with sampling port was observed. These conditions also hold for the other turbulent coagulation experiments reported here. In addition, this mass balance illustrates how incomplete mixing was detected during an experiment. The +/- 10% boundaries were used to flag outlying samples exhibiting incomplete mixing and the aberrant samples were
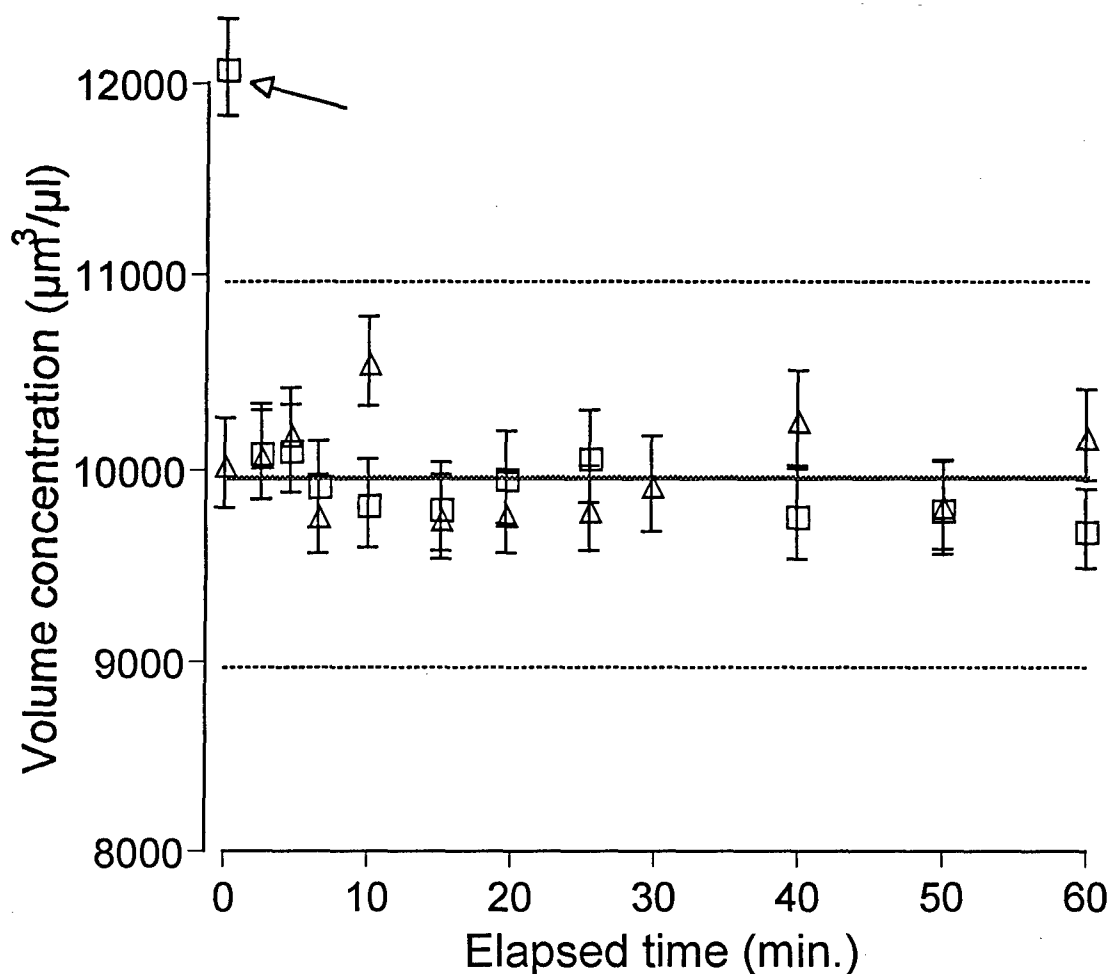
**Figure 6.9**: Volume concentration of particles as a function of time for a turbulent coagulation experiment when the grid was oscillating at 6 Hz. Shown are symbols for the two sampling positions. The solid line is the time average volume concentration and the error bars are 95% confidence intervals based on Poisson statistics. The dashed lines demarcate +/- 10% of the mean and were used to identify data (marked with the arrow) inadvertently collected before the reactor was completely mixed.

removed from the analysis. In the experiment depicted in Figure 6.9, the first sample taken (marked with the arrow in Figure 6.9) had an abnormally high concentration indicative of incomplete mixing in the reactor and it was dropped from further analysis.

The evolution of the singlet concentration for the same $f = 6$ Hz experiment is plotted in Figure 6.10. Shown are different symbols for the two sample ports. The error bars denote 95% confidence intervals based on Poisson statistics. The incomplete mixing point tagged using Figure 6.9 is marked with an arrow on Figure 6.10. The solid line is a regression through the data using the explicit break up model, Equation 6.13, in the region where triplet formation was negligible. Triplet formation was considered significant when the triplet formation rate was calculated to be greater than 20% of the doublet formation rate. Equation 6.11 shows that triplet formation became significant for $S/S_0 < 0.78$. This corresponded to data taken after 25 minutes and the boundary for significant triplet formation is shown by the vertical dotted line in Figure 6.10. When triplet formation is significant, the singlet concentration should decrease faster than the model predictions based on doublet formation alone. The data in Figure 6.10 does not show a deviation from the model prediction that ignores triplet formation — in fact, the effect of triplet formation was not observed for any of the experiments conducted. Since break up would be expected to affect triplets more than doublets, perhaps it was instrumental in keeping the number of triplets in the system low. The fit of the regressed equation led to an estimate of $k_T = 431$ $\mu m^3/s$. Similar analyses were performed for additional experiments at $f = 0, 1, 3, 4, 6,$ and 8 Hz.
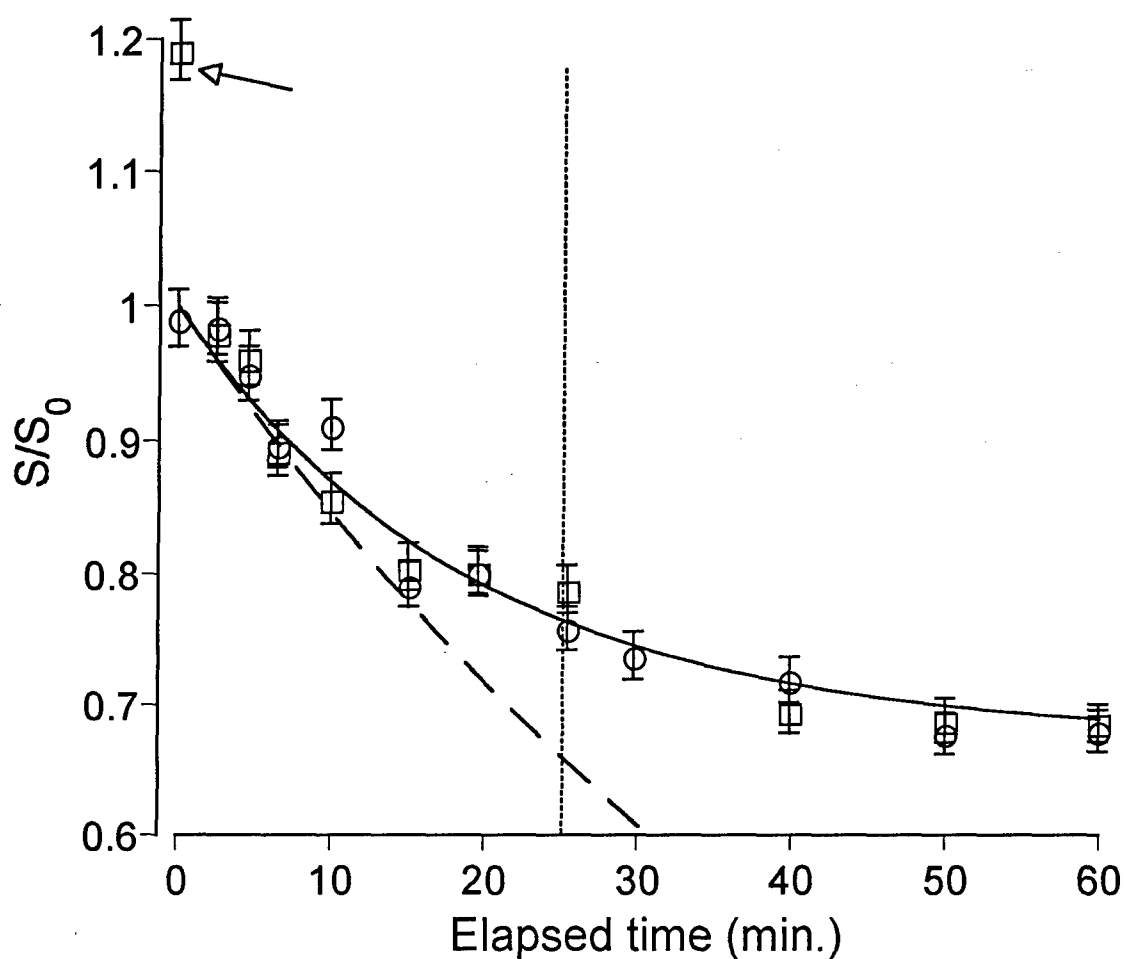
**Figure 6.10**: Coagulation rate data plotted for an experiment conducted with f = 6 Hz. Non-linear regression using the integral rate expression with break up (solid line) was used to estimate the coagulation rate constant. The dashed line is the expected behavior if doublet break up is neglected. The symbols represent the two sample ports and error bars are 95% confidence intervals based on Poisson statistics. Data to the right of the vertical dotted line was expected to have significant triplet formation based on (3.4) and was not included in the regression. The arrow marks the data collected before mixing was complete.

The importance of particle breakup may be seen by comparing the model prediction that includes particle break up with the prediction obtained when break up is neglected, Equation 6.9. The dashed line in Figure 6.10 shows the model prediction when break up is ignored. It can be seen that break up is manifested by a deviation from the model prediction that neglects break up (dashed line) at times greater than about 20 minutes.

A summary of the flocculation rate data obtained is shown in Figure 6.11, where the coagulation rate constant is plotted against average Kolmogorov shear rate. The symbols represent the average of independent experiments (4 to 6 runs for each grid frequency) and the error bars show 95% confidence intervals. A power law fit of the data (not shown in Figure 6.11) indicates that $k_T = 2.1a^3\Gamma^{0.84}$ with an $r^2$ of 99.9%. Here the units on $\Gamma$ are $s^{-1}$.

The analysis of the experimental data given in Section 6.3 assumes the effect of Brownian coagulation is negligible. Peclet numbers based upon the Kolmogorov scales and the particle radius (shown in Table 6.1) are larger than 79 for all turbulent coagulation experiments suggesting that Brownian motion did not influence the results. However, Feke & Schowalter (1983, 1985) have shown that Brownian motion can affect the coagulation rate in simple shear or uniaxial extension at Pe values of 150 or higher. In steady flows at infinite Pe, large concentration gradients develop at the boundaries between streamlines that lead to coagulation and those that do not. Therefore, even at large Pe, Brownian motion allows particles to diffuse across these boundaries, thus measurably affecting the predicted
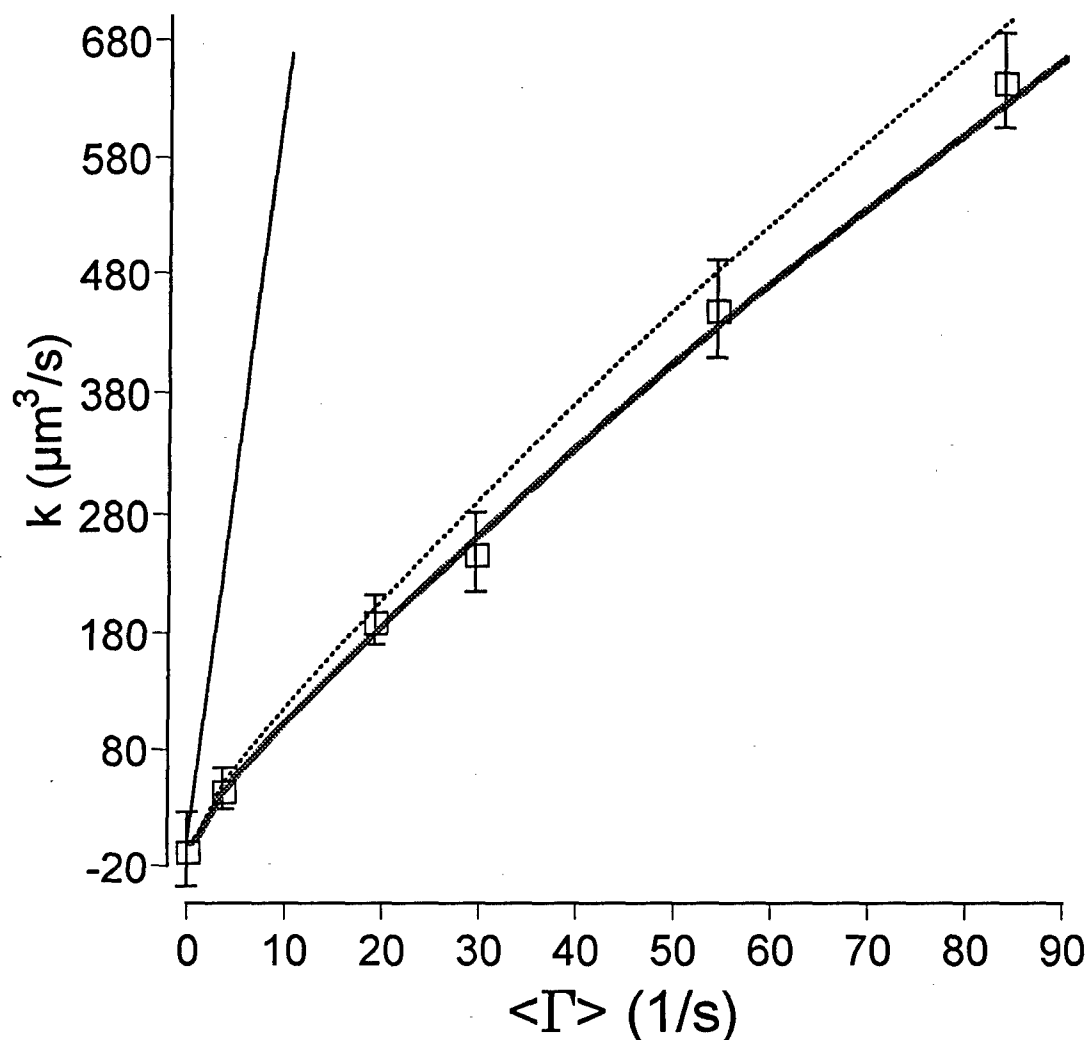
**Figure 6.11**: Summary of the experimentally determined coagulation rate constant as a function of average Kolmogorov shear rate. Shown are the averages with 95% confidence intervals for experiments conducted at several grid frequencies. The thin line is the prediction obtained when interparticle interactions are not included. Including van der Waals attraction and hydrodynamic interactions leads to the model prediction shown by the thick solid line when the coagulation rate constant is obtained by averaging over the local coagulation rates in the reactor. When the predicted coagulation rate is calculated using the average Kolmogorov shear rate, the curve presented as the dotted line results.

coagulation rate (Feke & Schowalter, 1983). In contrast, for a temporally varying linear flow, large concentration gradients do not persist because the fluctuating motion of the fluid acts to disperse particles. From a theoretical calculation of coagulation in a randomly varying flow field with small total strain, the author found that Brownian motion was unimportant for Pe values much beyond 1 (Chapter 3; Brunk et al., 1997a).

Turbulence has an intermediate total strain; thus, Brownian motion can be anticipated to be more important than predicted at the small total strain limit but less important than the analysis of Feke & Schowalter (1983) suggests. Although the effects of Brownian motion for isotropic turbulence have not been explicitly modeled, the excellent agreement between the model simulations and experiments (to be discussed below) suggests the influence of Brownian diffusion was insignificant for the Peclet numbers used in these coagulation experiments.

### 6.5.4 Comparison with model predictions

The thin solid line in Figure 6.11 is the predicted coagulation rate based on the model simulations Equation 6.6 described in Section 6.2 for *non-interacting* particles ($\alpha_T = 1$). The thin solid line is also representative of the coagulation rate that is predicted from the asymptotic limits of large and small strain. Comparing the experimental data in Figure 6.11 with the thin solid line shows that the actual coagulation rate increases more slowly with shear rate than predicted by the non-interacting particle model. The results that neglect particle interactions consistently overestimate the actual rate of coagulation and the error is exacerbated at larger shear rates because of differences in the power law dependence of k on $\langle \Gamma \rangle$.

Predictions based on the model calculations that include interparticle interactions are shown in Figure 6.11 as the thick solid line. The computer simulations predict $k_T = 2.05a^3<\Gamma>^{0.84}$, in close agreement with the best fit of the experimental data and yielding only a slightly lower $r^2 = 99.8\%$. It should be emphasized that no fitting parameters were used in this model prediction and, as described previously, estimates for the Hamaker constant and spatial Kolmogorov shear rate distribution were obtained in independent experiments.

The reader is cautioned that the model predictions relating the coagulation rate constant to the spatially averaged Kolmogorov shear rate are system specific. Although the predicted power law dependence on $\Gamma$ should remain the same, the preexponential factor will depend on the spatial distribution of turbulence within a particular system. The model prediction shown as the thick solid line on Figure 6.11 was obtained by spatially averaging the turbulent coagulation rate constant, i.e.,

$$<k_T> = \frac{1}{20\ cm} \int_{-4\ cm}^{16\ cm} k_T(\Gamma(x))dx \qquad (6.20)$$

where spatial homogeneity in the plane perpendicular to the grid motion was assumed, $k_T(\Gamma)$ was given by Equation 6.6 and $\alpha(\Gamma)$ in Equation 6.6 was given by Equation 6.7. Based on Equation 6.20 and the measured $\Gamma$ distribution, approximately 45% of the total coagulation occurred in the far field regions of the tank.

To illustrate the importance of accounting for local variations in $\Gamma$ throughout the reactor, consider the proposal to characterize the turbulence

with the average Kolmogorov velocity gradient: $<\Gamma>$. The model prediction based upon $k_T(<\Gamma>)$, shown as the dotted line on Figure 6.11, overestimated the experimentally measured coagulation rate constants by about 11%.

The only turbulent coagulation data by other investigators that is amenable to comparison with the computer simulations is that published by Delichatsios & Probstein (1975). These investigators measured the coagulation rate of 0.6 μm diameter polystyrene particles in turbulent pipe flow having Reynolds numbers ranging from 15,000 to 50,000 based upon the pipe diameter and mean velocity. A summary of their results and a comparison to our model predictions is shown in Table 6.2. Average Kolmogorov shear rates ranged from 89 $s^{-1}$ to 377 $s^{-1}$ and measured coagulation rate constants varied from 4.9 $\mu m^3/s$ to 17.7 $\mu m^3/s$ for the most destabilized systems reported. Error bars provided for the $\Gamma = 221$ $s^{-1}$ experiments indicate a coefficient of variation of about 25% and the same relative error was assumed for the other two experimental conditions.

Estimates of the coagulation rate assuming non-interacting particles overestimate the coagulation rates observed by Delichatsios & Probstein (1975) by factors of 4 to 5. The model predictions using the Hamaker constant found in this work and an extrapolation of Equation 6.7 to 0.6 μm diameter particles overestimated the coagulation rate by 22 to 37% when the average Kolmogorov shear rate in the core region was used to characterize the turbulence within the pipe.

It is difficult to judge the accuracy of Delichatsios & Probstein's experiments. This prior work did not consider particle break up, triplet

**Table 6.2**: Comparison of model prediction with the turbulent coagulation data collected by Delichatsios & Probstein (1975) in pipe flow. Model prediction uses the Hamaker constant obtained in this work and assumes a constant Kolmogorov shear rate in the turbulent pipe. Superscripts in the table stand for experimental measurements (exp), model prediction with interparticle forces (pred) and model prediction for non-interacting particles (0). The uncertainty interval in the experimental data corresponds to a 25% coefficient of variation using results summarized for the $\Gamma = 221$ s$^{-1}$ data set.

| $<\Gamma>$ (1/s) | $k_T^{exp}$ ($\mu m^3/s$) | $k_T^{pred}$ ($\mu m^3/s$) | % Difference | $k_T^0$ ($\mu m^3/s$) |
|---|---|---|---|---|
| 89 | 4.9±1.2 | 6.8 | 37% | 20.7 |
| 221 | 11.9±3.0 | 14.5 | 22% | 51.4 |
| 377 | 17.7±4.4 | 22.7 | 28% | 87.7 |

formation, or whether the implicit assumption of excess singlets was satisfied. This model prediction is considerably better than estimates based on non-interacting particles and deviations from the experiments can at least partly be explained by experimental accuracy. The trend of the experimental data was well represented by a power law correlation of the form: $k = 4.52a^3\Gamma^{0.84}$ ($r^2 = 99.5\%$), where the units on $\Gamma$ are $s^{-1}$. Thus, the turbulent pipe experimental coagulation data shows the same power law trend as that predicted by the computer simulations. The Peclet number of the turbulent pipe flow experiments were 5 to 23, about an order of magnitude lower than the Pe for the experiments reported in this paper. Therefore, it is likely that Brownian diffusion affected the results of Delichatsios & Probstein's work. Brownian motion increased the coagulation rate in Feke & Schowalter's (1984) analysis of simple shear coagulation and in the author's pair diffusion approximation for coagulation in a random linear flow (Chapter 3; Brunk et al., 1997a). This expectation is in opposition to the discrepancy between the experimental data of Delichatsios & Probstein and the non-Brownian model predictions presented in Table 6.2. The spatial variation of turbulent shear rates in the pipe flow was ignored in the analysis of Delichatsios & Probstein's experimental data and this could partially explain the difference between experiment and simulation. For grid-stirred turbulence, the constant Kolmogorov shear rate approximation led to model predictions that overestimated the experimental results. Except very near the pipe wall, turbulence in pipe flow is nearly homogeneous (Delichatsios & Probstein, 1975). While it is likely that spatial heterogenities in the turbulent shear

rates caused some of the error in the model predictions for Delichatsios & Probstein's coagulation experiments, preliminary analysis suggests that the relatively small turbulent boundary layer in pipe flow is unlikely to drastically alter the model prediction summarized in Table 6.2. Doublet break up due to the high Kolmogorov shears rates in the pipe flow is another possible cause for the differences between the model and experimental data of Delichatsios & Probstein (1975). An inspection of the experimental singlet evolution data in the turbulent pipe flow coagulation experiments does not show deviations from linearity, indicating that break up was probably unimportant. In light of these concerns, the simulations with interparticle forces reproduce the coagulation experiments conducted by Delichatsios & Probstein (1975) remarkably well and are able to predict the correct dependence on Kolmogorov shear rate.

## 6.6 Summary and conclusions

Experimental measurements of turbulent coagulation were made in an oscillating grid reactor and compared with model predictions that included viscous effects and van der Waals attraction. An initially monodisperse suspension of 3.9 $\mu$m diameter polystyrene beads was placed in the reactor and the loss of singlets over time was measured as a function of turbulence intensity in the apparatus. The particles were smaller than the Kolmogorov length scale so that turbulent shear rates at the Kolmogorov scale controlled the coagulation rate while differential settling and particle inertia effects were minimized by running the experiments in density matched fluids.

Grid-stirred devices produce a well characterized, nearly isotropic turbulence that decays rapidly with distance from the oscillating grid. Considerable effort was expended to measure the spatial distribution of turbulence within the reactor so the experimentally observed average coagulation rate constant could be related to an average of the local coagulation rates within the reactor. Grid scaling laws developed and verified by others (Hopfinger & Toly, 1976; De Silva & Fernando, 1992; Brumley & Jirka, 1987; Fernando & Long, 1988) were found to represent the turbulent kinetic energy at distances greater than about 2M from the oscillating grid. Within the grid region (x < 2 cm), the turbulent kinetic energy showed no systematic variations with position and was, therefore, represented as a constant. A scaling law was used to relate the measured E profiles to the dissipation rate in the reactor and then through Kolmogorov's similarity hypothesis to the Kolmogorov shear rate, $\Gamma$.

The experimental coagulation rate constant was found to be proportional to $<\Gamma>^{0.84}$, in agreement with the model predictions. For comparison, analytical (such as Saffman & Turner, 1956 or Chapter 3, Brunk et al., 1997a) and model (Chapter 4; Brunk et al., 1997b) predictions that neglect particle interactions suggest that $k \propto \Gamma$. These results, summarized in Figure 6.11, indicate that interparticle interactions play an important role in controlling the rate of turbulent coagulation. Model predictions incorporating particle interactions were obtained by averaging over the local coagulation rate constants in the reactor. These simulation results agreed with experiment ($r^2 = 99.8\%$) without use of adjustable parameters. The spatial variation of turbulence within a coagulating system

was shown to influence the model prediction. For instance, characterizing the turbulence in the tank with <Γ> led to a prediction that overestimated the experimental data by 11%.

Comparison of the model and experimental turbulent coagulation rate constant predictions required knowledge of the Hamaker constant for the coagulating polystyrene beads. The Hamaker constant was obtained through Brownian coagulation experiments. A Hamaker constant of $0.75k_bT$, consistent with other investigations (Russel et al., 1989), resulted in agreement between the experimental and theoretical Brownian coagulation rate.

To the author's knowledge, no previous attempt has been made to quantify the importance of particle interactions in turbulent coagulation of interacting particles, either theoretically or experimentally. Numerous studies have, however, been conducted for steady linear flows (see Greene et al., 1994 for a review of past work.). Trajectory calculations for coagulation in simple shear and uniaxial extension that include hydrodynamic and van der Waals forces show a similar dependence on the shear rate as that obtained in this paper. Feke & Schowalter (1983) found that $k \propto \Gamma^{0.77}$ for simple shear and Zeichner & Schowalter (1977) obtained $k \propto \Gamma^{0.89}$ for uniaxial extension, both are similar to the $k \propto \Gamma^{0.84}$ dependence measured for turbulent coagulation in this work.

Considerable empirical evidence garnered from flocculation studies of natural sediments indicate that collision efficiencies near 10% are typical for destabilized colloidal particles (O'Melia, 1995). The turbulent shear rates and particle sizes used in this research are within the range of typical

values expected for natural aquatic environments such as estuaries (Krone, 1970; McCave, 1984) and so collision efficiencies calculated for the data reported here are amenable to comparison with field measurements. The collision efficiency for the experimental data in Figure 6.11 can be estimated by dividing the flocculation rate obtained experimentally with that predicted by the non-interacting model given by Equation 6.6 with $\alpha_T = 1$. The calculated collision efficiencies fall from 15% at the low shear rates to 9% at the highest shear rate examined in these experiments, in qualitative agreement with field measurements (O'Melia, 1995).

The similarity of the theoretical predictions and the experimental measurements is remarkable considering the expected errors associated with using scaling arguments to calculate $\Gamma$. While the absolute values of the Kolmogorov shear rate in the reactor may be suspect, the predicted $k \propto <\Gamma>^{0.84}$ power law remains robust. Therefore the computer simulations of coagulation in isotropic turbulence at finite total strain (Chapter 4; Brunk et al., 1997b) capture the essential physics of turbulent coagulation. For neutrally buoyant particles with diameters smaller than the length scales of turbulence, the rate of coagulation is dominated by the Kolmogorov scales of turbulence. Relative particle motion on length scales comparable to the particle radius is the rate limiting step for turbulent shear coagulation and consideration of particle interactions is necessary to explain experimental observations. Since isotropy at the small scales is universally seen for turbulent flows, the turbulent coagulation simulations validated in this thesis should have wide application to other engineered and naturally occurring turbulent systems.

# REFERENCES

ATKINSON, J. F., DAMIANI, L. & HARLEMAN, D. R. F. 1987 A comparison of velocity measurements using a laser anemometer and a hot-film probe, with applications to grid-stirring entrainment experiments. *Phys. Fluids* **30**, 3290.

APPIAH, A. & O'MELIA, C. R. 1990 *Coagulation Processes: Destabilization, Mixing and Flocculation* in *Water Quality and Treatment.* Pontius, Frederick W. (Ed.), McGraw-Hill, New York.

BATCHELOR, G. K. 1976 Brownian diffusion of particles with hydrodynamic interactions. *J. Fluid Mech.* **74**, 1.

BRUMLEY, B. H. & JIRKA, G. H. 1987 Near-surface turbulence in a grid-stirred tank. *J. Fluid Mech.* **183**, 235.

BRUNK, B., WEBER-SHIRK, M., JENSEN, A., JIRKA, G., & LION, L. W. 1996 Modeling natural hydrodynamic systems with a differential-turbulence column. *J. Hydr. Eng.* **122**, 373-380.

BRUNK, B. K., KOCH, D. L., & LION, L. W. 1997a Hydrodynamic pair diffusion in isotropic random velocity fields with application to turbulent coagulation. *Accepted by Phys. Fluids.*

BRUNK, B. K., KOCH, D. L., & LION, L. W. 1997b Turbulent coagulation of colloidal particles. *Submitted to J. Fluid Mech.*

CAMP, T. R., & STEIN, P. C. 1943 Velocity gradients and internal work in fluid motion. *J. Bost. Soc. Civil Eng.* **30**, 219-237.

CASSON, L. W., & LAWLER, D. F. 1990 Flocculation in turbulent flow: measurement and modeling of particle size distributions. *AWWA J.* **8**, 54-68.

CLARK, M. M. 1985 Critique of Camp and Stein's RMS velocity gradient. *J. Env. Eng.* **222**, 741-754.

DELICHATSIOS, M. A. & PROBSTEIN, R. F. 1975 Coagulation in turbulent flow: theory and experiment. *J. Coll. & Int. Sci.* **51**, 394-405.

DE SILVA, I. P. D. & FERNANDO, H. J. S. 1992 Some aspects on mixing in a stratified turbulent patch. *J. Fluid Mech.* **240**, 601.

E, XUEQUAN & HOPFINGER, E. J. 1986 On mixing across an interface in stably stratified fluid. *J. Fluid Mech.* **166**, 227.

ELIMELECH, M., GREGORY, J., JIA, X. & WILLIAMS, R. 1995 *Particle deposition & aggregation measurement modeling and simulation.* pp. 180-188. Butterworth-Heinemann, Boston, MA.

FEKE, D. L., & SCHOWALTER, W. R. 1983 The effect of Brownian diffusion on shear-induced coagulation of colloidal dispersions. *J. Fluid Mech.* **133**, 17-35.

FEKE, D. L. & SCHOWALTER, W. R. 1985 The influence of Brownian diffusion on binary flow-induced collision rates in colloidal dispersions. *J. Coll. Int. Sci.* **106**, 203-214.

FERNANDO, H. J. S. & LONG, R. R. 1985 On the nature of the entrainment interface of a two-layer fluid subjected to zero-mean-shear turbulence. *J. Fluid Mech.* **151**, 21.

GIBBS, R. J. 1982 Floc stability during Coulter-Counter size analysis. *J. Sed. Petrol.* **52**, 657-660.

GIRIMAJI, S. S. & POPE, S. B. 1990 A diffusion model for velocity gradients in turbulence. *Phys. Fluids A* **2**, 242-256.

GREENE, M. R., HAMMER, D. A. & OLBRICHT, W. L. 1994 The effect of hydrodynamic flow field on colloidal stability. *J. Coll. Int. Sci.* **167**, 232-246.

HOPFINGER, E. J. & TOLY, J. A. 1976 Spatially decaying turbulence and its relation to mixing across density interfaces. *J. Fluid Mech.* **78**, 155-175.

JENSEN, A. 1997 *Experiments and modeling of turbulence, salinity and sediment concentration interactions in a simulated estuarine water column.* MS Thesis. School of Civil & Environmental Engineering. Cornell University.

KIM, S. & KARRILA, S. J. 1991 *Microhydrodynamics: principles and selected applications*, Butterworth-Heinemann, Boston, MA.

Krone, R. B. 1978 *Estuarine Transport Processes*, (ed. B. Kferfve). University of South Carolina Press.

LOHRMAN, A., CABRERA, R. & KRAUS, N. C. 1994 *Proceedings, Symposium on fundamentals and advancements in hydrodynamic measurements and experimentation* (ed. C.A. Pugh), ASCE, New York, 351.

McCAVE, I. N. 1984 Size spectra and aggregation of suspended particles in the deep ocean. *Deep-Sea Res.* **31(4)**, 329-352.

O'MELIA, C. R. 1980 Aquasols: the behavior of small particles in aquatic systems. *Environ. Sci. Technol.* **14(9)**, 1052-1060.

O'MELIA, C. R. 1995 *From Algae to Aquifers* in *Aquatic Chemistry Interfacial and Interspecies Processes.* (eds. C. P. Huang, C. R. O'Melia, & J. J. Morgan), ACS, Washington, DC.

PEARSON, H. J., VALIOULIS, I. A. & LIST, E. J. 1984 Monte Carlo simulation of coagulation in discrete particle-size distributions. Part 1. Brownian motion and fluid shearing. *J. Fluid Mech.* **143**, 367.

POPE, S. B. 1990 Lagrangian microscales of turbulence. *Phil. Trans. R. Soc. Lond.* **333**, 309-319.

PRESS, W. H., TEUKOLSKY, S. A., VETTERLING, W. T. & FLANNERY, B. P. 1992 *Numerical Recipes in C*, Cambridge U.P., New York.

RUSSEL, W. B., SAVILLE, D. A. & SCHOWALTER, W. R. 1989 *Colloidal Dispersions*, Cambridge U.P., Cambridge, MA.

SAFFMAN, P. G. & TURNER, J. S. 1956 On the collision of drops in turbulent clouds. *J. Fluid Mech.* **1**, 16-30.

SCHENKEL, J. H. & KITCHENER, J. A. 1960 A test of the Derjaguin-Verwey-Overbeek theory with a colloidal suspension. *Trans. Faraday Soc.* **56**, 161.

SPIELMAN, L. A. 1970 Viscous interactions in Brownian coagulation. *J. Coll. Int. Sci.* **33**(4), 562-571.

STUMM, W. & MORGAN, J. J 1981. *Aquatic Chemistry: An Introduction Emphasizing Chemical Equilibrium in Natural Waters.* Wiley, New York.

TENNEKES, H. & LUMLEY, J. L. 1972 *A First Course in Turbulence*, MIT Press, Cambridge, MA.

TOWNSEND, A. A. 1976 *The Structure of Turbulent Shear Flow*, 2nd Ed., Cambridge Univ. Press.

VALIOULIS, I. A. & LIST, E. J. 1984 Collision efficiencies of diffusing spherical particles: hydrodynamic, van der Waals and electrostatic forces. *Adv. Coll. Int. Sci.* **20**, 1.

ZEICHNER, G. R. & SCHOWALTER, W. R. 1977 Use of trajectory analysis to study stability of colloidal dispersions in flow fields. *AIChE J.* **23**, 243-254.

# CHAPTER 7:
# CONCLUSIONS

Equilibrium sorption of phenanthrene in a simulated estuarine water column and turbulent shear-induced coagulation of monodisperse spherical particles was investigated in this thesis. In the two sections below important conclusions garnered from this research are summarized and directions for future research are discussed.

## 7.1 Sorption

Extensive pollutant sorption to settling suspended particulates has often been invoked to explain the observed pollutant trapping behavior of estuaries. Equilibrium sorptive interactions were studied for a model estuarine system consisting of phenanthrene, two clays and several recalcitrant dissolved organic compounds as a function of salinity. The experimental sorption coefficients were used to ascertain the extent to which sorption can explain pollutant phase distribution in estuaries.

The sorptive interactions between phenanthrene, a bacterial extracellular polymer and kaolinite clay were combined into an equilibrium sorption model for the overall sorption coefficient for phenanthrene. Increasing the ionic strength from fresh to marine levels causes a 55% increase in the overall sorption coefficient. Contrary to expectations, sorption of phenanthrene to the clays is not significantly enhanced by the presence of DOM in the system. For example, in the phenanthrene,

309

kaolinite clay and bacterial extracellular polymer system, DOM increases the sorption of phenanthrene to the clay by about 9% at all salinities. In contrast, at very low ionic strengths, small increases in ionic strength have been observed to strongly influence DOM sorption to inorganic sorbents (Tipping, 1981; Tipping & Heaton, 1983; Dempsey & O'Melia, 1983). Results from this study suggest that the effect of ionic strength on DOM sorption becomes saturated at ionic strengths lower than those typically seen in the estuary.

Field measurements of phenanthrene concentrations in sediment and their associated pore waters suggest that greater than 90% of the total phenanthrene in an estuary is trapped within the sediments. Results from the author's investigations of phenanthrene sorption indicate that in the water column only 0.1% of the phenanthrene would partition to the sediments. A similar analysis carried out with other pollutant/sorbent systems also shows phenanthrene trapping of less than 50%. These experiments and model calculations indicate that equilibrium sorption is not sufficient to fully explain the elevated levels of phenanthrene (or other hydrophobic pollutants with comparable sorptive properties) found on the bottom estuarine sediments.

### 7.1.1 *Comments and future work*

The unexpectedly high distribution coefficients for phenanthrene measured in estuarine sediments have also been the foci of other research (McGroddy et al., 1996; Gustafsson et al., 1997). It has been proposed that atmospheric deposition of PAH laden soot particles may be the origin of the high sediment PAH concentrations (McGroddy & Farrington, 1995;

McGroddy et al., 1996). Recently, Gustafsson et al. (1997) have successfully predicted the apparent partitioning of phenanthrene in the pore waters by characterizing the sediment in terms of its soot content and by using a surrogate for the phenanthrene/soot sorption coefficient. Their contention is that the extremely high solid phase PAH concentrations measured on estuarine sediment is the result of this high affinity soot.

Extending Gustafsson et al.'s (1997) calculations further by considering the expected behavior of soot particles as they fall through the estuarine water column is worthwhile. Simcik et al. (1996) estimated atmospheric soot fluxes to Lake Michigan to range from 600 to 800 $mg/m^2/year$. The steady state soot concentration in the water column can be estimated by dividing the flux by the settling velocity of the soot in the water. The settling velocity was calculated with the Stokes settling velocity equation assuming 4 μm diameter soot particles (Maruya et al., 1996) and by assuming the soot density was equal to that for graphite.

Based on the above assumptions, the water column soot concentration was expected to be about 3 $mg/m^3$. In the subsequent calculations a conservative suspended soot concentration of 10 $mg/m^3$ was used and a phenanthrene/soot partition coefficient of $\log K_{sc} = 7.1$ was taken from Gustafsson et al. (1997). The fraction of phenanthrene calculated to be sorbed to sediment was 11% — much lower than the 90% trapping level obtained from direct measurements of phenanthrene in the aqueous and sediment phases (McGroddy & Farrington, 1995). This discrepancy may be attributable to slow desorption of phenanthrene introduced into the water column along with the soot; however, since

residence times in the water column are on the order of days (Bates et al., 1987) and the soot particles are so small, mass transport limitations would be minor. To see this assume an aqueous diffusivity for phenanthrene of D $= 10^{-6}$ cm$^2$/s. The effective diffusivity accounting for hindered diffusion through the soot particle due to sorption would be $D_e = D/K_{sc} = 10^{-13}$ cm$^2$/s. An estimate of the characteristic time for phenanthrene to diffuse out of the soot particle is proportional to $t_D = a^2/D_e$ where a is the particle radius. For the 4 μm diameter particles considered earlier, this results in $t_D = 4.6$ days which is comparable to water column residence times in the estuary (albeit this estimate would increase if tortuosity was significant.). If this characteristic diffusion time applies, significant desorption would have been expected to occur.

As a result of these order of magnitude calculations, the prognosis for sorption as a mechanism to explain the observed trapping of hydrophobic pollutants is doubtful. Furthermore, these calculations bring into question the assertion that soot-bound PAH results from a sorptive process. It would therefore be interesting to conduct additional investigations of PAH/soot interactions.

Some areas for further research include:

- Recent work by Gustafsson et al. (1997) suggests that PAHs are sorbed to soot. The kinetics of PAH sorption to and desorption from soot could be characterized and used to estimate PAH losses while the soot is resident in the water column. The results could also be used to find if all of the PAH in the soot is available for equilibrium phase partitioning.

- Soot is commonly presumed to be composed of highly aromatic carbon (Simcik et al., 1996). While measuring the PAH content of soot artifacts may be introduced because of the aromaticity of the soot matrix itself. That is, protocols for measuring PAHs on solids often involve heating and other harsh conditions that may inadvertently cause further combustion of the soot particle and possibly additional PAH generation. Further research is needed to investigate errors associated with quantifying PAH concentrations on soot.

- The sorption work described in this thesis focused on sorptive interactions of an organic pollutant in the water column. Heavy metals are another important class of aquatic pollutant. Since heavy metals are strongly sorbed, it would be interesting to extend the analyses and experiments described in Chapter 2 to estimate extents of trapping for heavy metals.

## 7.2 Turbulent coagulation

Saffman and Turner (1956) predicted the aggregation rate of small particles in a turbulent flow under the assumptions that the turbulent strain is persistent and the hydrodynamic and colloidal interactions between the particles can be neglected. In this work, the effects of interparticle forces on the coagulation rate are considered, and the influence of the finite Lagrangian strain rate correlation time on coagulation is obtained.

The relative motion of two particles with diameters smaller than the Kolmogorov length scale is expressed as a locally linear flow field with a

temporally varying velocity gradient. The Reynolds number based on the particle diameter and the local shear rate is assumed to be small and, if the suspending fluid is a liquid, the particle inertia is assumed negligible.

The local flow field is characterized in terms of the root-mean-squares of the strain and rotation rates and their correlation times. Saffman and Turner's analysis applies when the product of the root-mean-square strain rate with the strain rate correlation time is very large. In Chapter 3 the relative motion of the interacting particles is treated as hydrodynamic pair diffusion in the opposite limit of very short correlation time. This limit facilitates the inclusion of hydrodynamic and colloidal interactions in semi-analytic predictions of the coagulation rate. Under these conditions colloid stability is found to increase with increasing particle size and turbulent shear rate because of high hydrodynamic resistance to particle collision. For similar shear rates and particle sizes, colloids are less stable in the randomly varying flow than in steady linear flows such as simple shear. This behavior is attributed to the presence of hydrodynamic drift which leads to the accumulation of close pairs and therefore acts like an additional attractive force when calculating the coagulation rate.

Direct numerical simulations (DNS) of turbulent flows indicate that the strain rate correlation is intermediate between the two limits noted above (Pope, 1990). To determine the coagulation rate in an actual turbulent flow, numerical simulations of the relative motion of particles in an isotropic, Gaussian, random velocity field with the same temporal covariance of strain rate and vorticity observed in DNS were conducted (see Chapter 4). In the absence of interparticle interactions the simulated

coagulation rate is significantly different from the large (Saffman & Turner, 1956) and small (pair diffusion approximation, this thesis) total strain asymptotic limits. For isotropic turbulence the simulations predicted a coagulation rate constant of $8.62\Gamma a^3$, where $\Gamma$ is the Kolmogorov shear rate and a is the particle radius.

Simulations run at large total strain are about 5% lower than Saffman & Turner's (1956) prediction that neglect fluid rotation. When the effects of rotation are turned off in the simulation, Saffman & Turner's results are attained. The rotation rate is found to decrease the observed rate of coagulation and this shows that the effects of strain and rotation cannot be separated when considering coagulation. The addition of rotation leads to the formation of closed trajectories that leave and subsequently return to the collision radius. These closed trajectories do not give a net contribution to the overall coagulation rate. In addition, the importance of rotation depends on its correlation time. For long rotation rate correlation times, closed trajectories persist and are thus important in lowering the overall coagulation rate. Conversely, for short rotation rate time scales, the location of closed trajectories fluctuates rapidly so particles can escape the closed trajectories before returning to the collision radius.

The effect of Kolmogorov shear rate on the coagulation of spherical particles is experimentally investigated using an oscillating grid reactor. As discussed in Chapter 5, the apparatus is designed and built to simulate the vertical variations of turbulence levels in natural hydrodynamic systems such as rivers and stratified estuaries. As such, it offers excellent capabilities for simultaneous control of solution chemistry, mass transport

and hydrodynamics. The reactor contains five vertically spaced, independently oscillating turbulence generating grids. Measurements of the turbulent kinetic energy (TKE) in front of an oscillating grid indicate that the instrument can produce nearly homogeneous turbulence. The TKE decays with distance from the oscillating grid and a scaling law based on grid parameters fit the data well. Further investigations focused on simulating steady state vertical turbulence and sediment loading distributions expected for open channel and homogeneous flow conditions. Sediment loading in homogeneous turbulence was fit using a sediment transport equation that balances turbulent diffusion and particle settling. From the results, a characteristic turbulent length scale of 8.9 cm is obtained. Open channel flow turbulence and sediment loading distributions are in good agreement with previously published relations. The experimental program described in Chapter 5 indicates that the apparatus can reproducibly simulate a variety of hydrodynamic and sediment loading conditions.

The initial coagulation rate of monodisperse particles was measured as a function of the turbulent shear rate within the reactor. The average Kolmogorov shear rate for a given grid frequency was estimated by measuring the turbulent kinetic energy as a function of position from the grid and relating it to the Kolmogorov shear rate using scaling arguments valid in the inertial subrange. The initial coagulation rate of particles (diameter = $3.9\mu m$ +/- $0.3\mu m$) was monitored as a function of grid frequency. The coagulation rate increased with average Kolmogorov shear at a rate less than that predicted from coagulation rate laws that ignore

hydrodynamic interactions and interparticle forces. From Brownian coagulation experiments a Hamaker constant of 0.75kT was found for the polystyrene test beads. Using the experimentally obtained Hamaker constant and the distribution of Kolmogorov shear rates in the reactor, the model predictions based on Chapter 4 were compared with the experimental data using no adjustable parameters. The excellent agreement between the model and experiments indicates that the simulations capture the physics of turbulent coagulation.

### 7.2.1 *Future work*

At this point a relatively robust model for computing the coagulation rate of spherical, monodisperse particles in turbulent flows has been obtained. While the results described in the previous chapters can be used to gain a qualitative understanding of turbulent coagulation for complex systems, several avenues need to be explored before the results can be used to obtain a quantitative picture of turbulent flocculation in natural systems where particles are inhomogenous, non-spherical and large multiple-particle aggregates can form. Some areas for further research include the following:

- The existing turbulent coagulation computer simulation can be extended by adding the effects of electrostatic double layer repulsion. Of particular challenge is investigating secondary minimum flocculation and being able to predict when salt destabilization of colloidal particles will occur.

- Brownian motion has been investigated in the pair diffusion approximation described in Chapter 3 and for steady linear flows

(Feke & Schowalter, 1983, 1985). Simultaneous Brownian motion and turbulent coagulation could be computed. Understanding coagulation rates when both Brownian motion and turbulent coagulation are significant would be important if the simulations presented in Chapter 4 are to be extended to smaller particle sizes.

- While coagulation of single particles in the presence of interparticle forces has been well-characterized, additional work needs to be done on coagulation of multiple-particle aggregates. In this case the particles are no longer spherical — they may be highly porous and have fractal geometries that vary with time.

- The differential turbulence column has been successfully used to simulate a variety of natural aquatic systems as well as measure turbulent coagulation rates of polystyrene beads. The next logical step might be to use this device to measure and model coagulation rates in selected natural aquatic environments.

# REFERENCES

BATES, T. S., MURPHY, P. P., CURL, H. C. JR. & FEELY, R. A. 1987 Hydrocarbon distributions and transport in an urban estuary. *Env. Sci. & Tech.* **21**, 193-198.

DEMPSEY, B. A. & O'MELIA, C. R. 1983 Proton and calcium complexation of four fulvic acid fractions. In *Aquatic and Terrestrial Humic Materials* (eds. R.F. Christman & C.R. O'Melia.). Ann Arbor Sci.

FEKE, D. L. & SCHOWALTER, W. R. 1983 The effect of Brownian diffusion on shear-induced coagulation of colloidal dispersions. *J. Fluid Mech.* **133**, 17-35.

FEKE, D. L. & SCHOWALTER, W. R. 1985 The influence of Brownian diffusion on binary floc-induced collision rates in colloidal dispersions. *J. Coll. Int. Sci.* **106**(1), 203-214.

GUSTAFSSON, O., HAGHSETA, F., CHAN, C., MACFARLANE, J. & GSCHWEND, P. M. 1997 Quantification of the dilute sedimentary soot phase: implications for PAH speciation and bioavailability. *Env. Sci. & Tech.* **31**, 203-209.

McGRODDY, S. E. & FARRINGTON, J. W. 1995 Sediment porewater partitioning of polycyclic aromatic hydrocarbons in three cores from Boston Harbor Massachusetts. *Env. Sci. & Tech.* **29**, 1542-1550.

McGRODDY, S. E., FARRINGTON, J. W. & GSCHWEND, P. M. 1996 Comparison of the in situ and desorption sediment-water partitioning of polycyclic aromatic hydrocarbons and polychlorinated biphenyls. *Env. Sci. & Tech.* **30**, 172-177.

POPE, S. B. 1990 Lagrangian microscales in turbulence. *Phil. Trans. R. Soc. Lond. A* **333**, 309-319.

SAFFMAN, P. G. & TURNER, J. S.  1956 On the collision of drops in turbulent clouds.  *J. Fluid Mech.*  **1**, 16-30.

SIMCIK, M. F., EISENREICH, S. J., GOLDEN, K. A., LIU, S.-P., LIPIATOU, E., SWACKHAMER, D. L. & LONG, D. T.  1996 Atmospheric loading of polycyclic aromatic hydrocarbons to Lake Michigan as recorded in the sediments.  *Env. Sci. & Tech.*  **30**, 3039-3046.

TIPPING, E.  1981 Adsorption by geothite (alpha-FeOOH) of humic substances from three different lakes.  *Chem. Geo.*  **33**, 81-89.

TIPPING, E. & HEATON, M. J.  1983 The adsorption of aquatic humic substances by two oxides of manganese.  *Geochim. et Cosmochim. Acta.*  **47**, 1393-1397.

# APPENDIX A:

# SUPPLEMENTAL REFERENCES

A.1 <u>Selected bibliography</u>

The following textbooks are considered to be good resources for understanding the concepts and terminology employed in this thesis:

*General fluid dynamics*
BIRD, R. B., STEWART, W. E. & LIGHTFOOT, E. N. 1960 *Transport Phenomena*. Wiley.

*Turbulence*
TENNEKES, H. & LUMLEY, J. L. 1994 *A First Course in Turbulence*. MIT Press.

*Colloids and hydrodynamic interactions*
RUSSEL, W. B., SAVILLE, D. A. AND SCHOWALTER, W. R. 1989 *Colloidal Dispersions*. Cambridge University Press.

*Colloids and equilibrium sorption*
STUMM, W. & MORGAN, J. J. 1981 *Aquatic Chemistry*, 2nd ed. Wiley.

*Estuaries and hydraulics*
FISCHER, H. B., LIST, E. J., KOH, R. C. Y., IMBERGER, J. & BROOKS, N. H. 1979 *Mixing in Inland and Coastal Waters*. Academic Press.

## A.2 <u>Definition of selected terms</u>

The following definitions are provided to aid the non-fluid mechanician reader:

*correlation time*: time interval over which a random variable is related to another random variable; mathematically, the time integral of the autocorrelation function.

*rotation rate*: the anti-symmetric component of the velocity gradient; leads to a solid body rotation in which fluid particles follow circular trajectories around the origin; all stream lines are closed; rate at which two fluid particles revolve about the origin.

*shear*: general term for the velocity gradient.

*simple shear*: a unidirectional flow in which the velocity in the x-direction depends on the y-direction, i.e., $u = \gamma y$ where u is the velocity in the x-direction and $\gamma$ is the shear rate.

*strain rate*: the symmetric component of the velocity gradient tensor; in a linear straining flow, all streamlines go to infinity (also known as extensional or stagnation point flow); rate at which two fluid particles are separated.

*turbulent dissipation rate*: rate at which turbulent energy is transferred from the energy containing large scale eddies to the smallest scales of turbulence; units are length$^2$/time$^3$; rate at which turbulent energy is lost to heat via viscous effects.

*velocity gradient*: the spatial derivative of the velocity, i.e., $du/dx$.

# APPENDIX B:

# SUPPLEMENTARY MATERIAL ON EQUILIBRIUM SORPTION OF PHENANTHRENE AND POLLUTANT TRAPPING CALCULATIONS

## B.1 Materials and Methods

### B.1.1 *Materials*

Table B.1 lists additional information about the materials used as surrogates for the hydrophobic pollutant, dissolved organic matter (DOM) and suspended sediment.

### B.1.1.1 Dialysis technique

A modified dialysis technique (Carter & Suffet, 1982; Allen-King et al., 1995) was used to obtain the distribution coefficient for phenanthrene onto kaolinite clay. This procedure eliminated the difficulty of separating the kaolinite clay from the aqueous solution and hence circumvented what has been termed the "solids effect" (Gschwend & Wu, 1985). A dialysis membrane 6-8,000 MWCO was filled with an aqueous solution of desired salinity and then sealed using nichrome wire. The bag was placed into a 30 ml amber hypo-vial (Wheaton, Milwaukee, WI) along with additional aqueous solution, a known weight of clay (0.1 to 1.0 g) and an aliquot of radiolabeled $^{14}$C-phenanthrene. The vial was crimp-capped using a Teflon® backed septum and placed on a rotating drum mixer in the dark at 25°C for 6 days. A series of long term experiments performed over 18

**Table B.1**: Properties of estuarine model surrogates

*Properties of Mineral Sorbents*

|  | Kaolinite | Bentonite |
|---|---|---|
| Density[a,b] (g/ml) | 2.58 | 2.80 |
| Average diameter[a,b] ($\mu$m) | 1.5 | 1.5 |
| Specific surface area[b] ($m^2$/g) | 8.0 | n/a |
| Organic content[c] (%) | 0.076 | 2.03 |
| CEC[c] (cmol/kg) | 11.08 | 76.13 |

*Properties of Phenanthrene*

| Formula | Structure | MW | Solubility[d] ($\mu$g/L) | log $K_{OW}$[d] | Henry's law constant[e] |
|---|---|---|---|---|---|
| $C_{14}H_{10}$ |  | 178.2 | 960 | 4.5 | 0.582 |

*Properties of 9702-M4 extracellular polymer[a]*

| Constituents | Molar ratio relative to glucuronic acid |
|---|---|
| glucose | 1.62 |
| galactose | 1.39 |
| glucuronic acid | 1.00 |

% Carbon by weight = 40.2
Molecular weight[f] $\approx$ 500,000 Daltons

[a]verified in the Cornell Environmental Engineering laboratory, Cornell University, Ithaca, NY. [b]from manufacturers specifications. [c]measured by the Cornell Nutrient Analysis Laboratory, Cornell University, Ithaca, NY. [d] Chin & Gschwend, 1992. [e]1990 CRC Handbook. [f]Dohse & Lion, 1994.

days showed that a 6 day equilibration time was more than sufficient to reach stable phenanthrene concentrations. After equilibration, samples of solution inside and outside the dialysis membrane were each mixed 1:10 with scintillation cocktail (Ecoscint, National Diagnostics, Atlanta, GA) and counted on a Beckman LS9800 liquid scintillation counter (Irvine, CA). The presence of clay slurry within the counting samples did not affect the scintillation results. All counting results were corrected for quench and background levels of radioactivity. Assuming all phenanthrene sinks were at equilibrium, the relative concentration difference of phenanthrene between the aqueous phase inside the dialysis bag and the clay slurry led to the sorption coefficient. A mass balance on the phenanthrene in the slurry phase yielded:

$$[PAH]_s = K_s^{PAH}[PAH]_a = \frac{[PAH]_{sl}V_{sl} - [PAH]_a V_{sla}}{W_k} \qquad \text{(B.1)}$$

where $[PAH]_{sl}$ is the concentration of phenanthrene in the slurry phase, $V_{sl}$ is the slurry volume, $V_{sla}$ is the liquid volume in the slurry and $W_k$ is the weight of kaolinite added to the slurry.

B.1.1.2 Centrifugation technique

The dialysis procedure could not be used in experiments that included the extracellular polymer because the molecular weight cutoff of the dialysis tubing was too small to allow the polymer to pass freely. Particle separation by centrifugation offered an alternative, albeit a possibly inaccurate one due to incomplete solid/aqueous phase separation

(Gschwend & Wu, 1985). This method was used to ascertain the equilibrium distribution coefficient for extracellular polymer sorbing to kaolinite clay and to observe sorption of phenanthrene to clay in the presence of DOM surrogates. Glass microreaction V-Vials (5 ml nominal volume, Wheaton, Milwaukee, WI) were filled with approximately 0.3g of kaolinite clay, 4,000 to 30,000 DPM (disintegrations per minute) of radiolabeled sorbate and approximately 5 ml of saline solution. The vials were crimp capped with Teflon® faced septa and allowed to equilibrate at 25°C on a rotating drum mixer. Samples were mixed for 48 hours and then centrifuged at 2250g for 30 minutes in a Hermle ZK510 swing bucket centrifuge (Germany). Aliquots of the aqueous phase were counted on the Beckman LS9800 liquid scintillation counter. Slow desorption of the phenanthrene from the polymer was found to affect the isotope levels measured by the scintillation counter; therefore, liquid scintillation counting was repeated daily until the phenanthrene activity remained constant between successive measurements. The equilibrium sorption coefficient was obtained from a mass balance equation which was modified to include corrections for sorptive bottle losses (Lion et al., 1990).

$$[Sorbate]_s = K_d[Sorbate]_a = \frac{M_s - (K_b^s + V_a)[Sorbate]_a}{W_k} \quad \text{(B.2)}$$

where $M_s$ is the mass of sorbate added to the bottles (DPM), $K_b^s$ is the distribution coefficient for the sorption of sorbate to the bottle (ml/bottle) and $V_a$ is the aqueous phase volume (ml).

B.1.1.3 Fluorescence quenching

Fluorescence quenching experiments (Backhus & Gschwend, 1990; Gauthier et al., 1986) were used to elucidate the distribution coefficient between phenanthrene and the extracellular polymer. For each experiment two acid and base washed 1 x 1 x 4 cm quartz cuvettes were used. One cuvette was filled with 2 ml of an aqueous phenanthrene solution at the desired salinity and was employed to determine phenanthrene sorption to the extracellular polymer. The other cuvette, used to correct for fluorescence caused by the extracellular polymer, was filled with 2 ml of saline solution. The cuvettes were allowed to equilibrate for several minutes and the initial fluorescence was recorded using an SLM Aminco 8000 spectrofluorimeter with excitation and emission wavelengths of 288 nm and 364 nm, respectively. Incremental 100 $\mu$l aliquots of an extracellular polymer stock solution were added to the cuvettes. Equilibration was observed to occur very rapidly; however, the vials were allowed to mix 2 minutes before the fluorescence intensity was measured again. Between measurements, care was taken to close the shutter of the spectrofluorimeter to prevent photodegradation of the phenanthrene. Preliminary experiments suggested that even after 30 minutes of continuous exposure to the excitation wavelength, photodegradation was undetectable. Polymer addition, solution equilibration, and fluorescence measurement were repeated 6 more times until a total of 700 $\mu$l of polymer stock solution had been added to each vial.

The protocol of Gauthier et al. (1986) was followed to obtain correction factors for apparent quenching or "inner filter effects." Apparent quenching was quantified with absorbance experiments using a Hewlett Packard 8457A diode array spectrophotometer (Wilmington, DE). Quartz cuvettes identical to those described in the fluorescence phase of the experiment were used and the absorbance of the emission and excitation wavelengths was measured as a function of extracellular polymer concentration and salinity. Changes in salinity were not observed to affect the absorbance measurements; however, correction factors due to the polymer ranged from 0 to 30% as the concentration of extracellular polymer increased.

The fluorescence intensity measurements were adjusted for background fluorescence and "inner filter effects" before data analysis. Significant loss of phenanthrene to container walls was not observed and significant volatilization of the phenanthrene was not expected over the time frame of the analysis since the cuvettes were fitted with Teflon® caps. The Stern-Volmer equation was used to relate the ratio of the fluorescence intensity to the distribution coefficient for phenanthrene sorbing to extracellular polymer (Gauthier et al., 1986):

$$\frac{F_0}{F} = K_{DOM}^{PAH}[DOM]_a + 1 \qquad \textbf{(B.3)}$$

where $F_0$ and $F$ are the fluorescence intensity before and after the addition of extracellular polymer, respectively.

## B.2 Evidence for enhanced sorption due to DOM coatings

Figures B.1, B.2 and B.3 show the experimental evidence for enhanced sorption of phenanthrene caused by increased DOM coating at high salinities for different clay:DOM weight ratios. The normalized distribution coefficient is the ratio of the distribution coefficient at 30 ppt to the value at 0 ppt salinity. This ratio is then normalized with the ratio at a clay:DOM value of $\infty$ to remove phenanthrene "salt effects" from the results. Normalized distribution coefficients greater than 1 indicate that DOM coatings enhanced sorption, while values less than 1 mean the DOM prevented the phenanthrene from sorbing strongly to the clay when the salinity was increased. The sorption coefficients obtained in this analysis are tabulated in Table B.2.

## B.3 Literature review of typical sorption coefficients

The level of pollutant trapping for a model system of phenanthrene, humic acid and kaolinite clay was evaluated using literature values for the sorption coefficients characterizing the interactions between the three components. Table B.3 summarizes the list of sources consulted in this analysis.
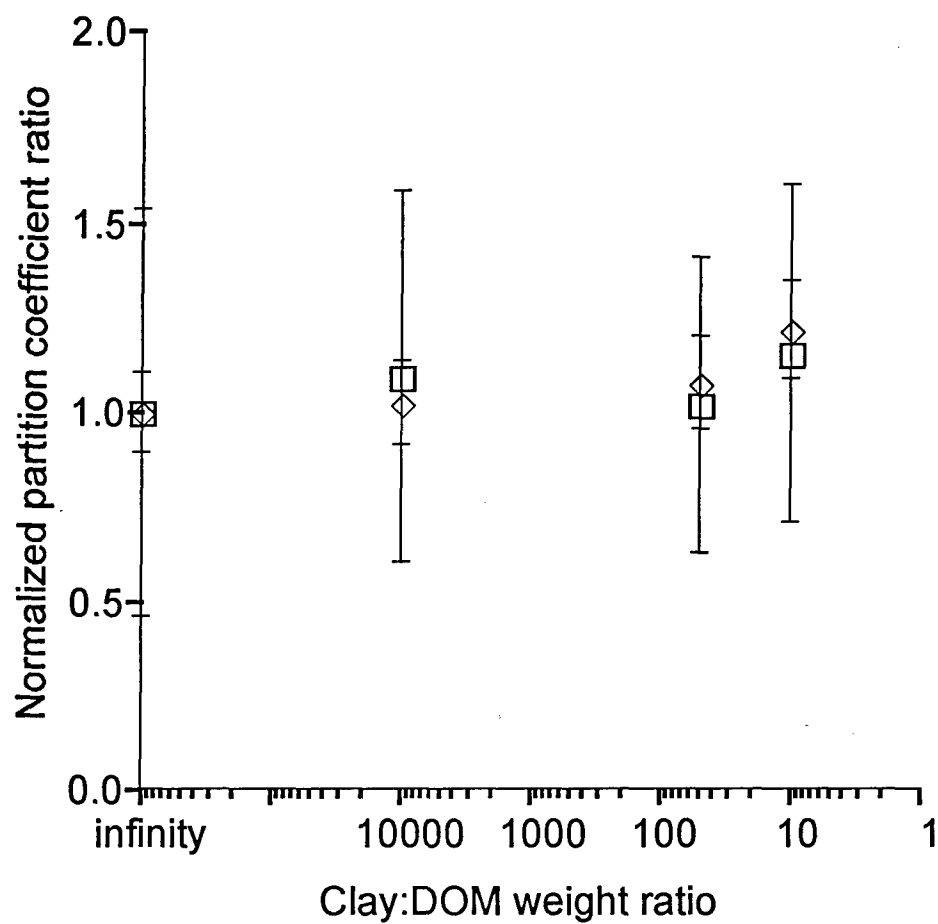
**Figure B.1**: Phenanthrene sorption with alginic acid/kaolinite (□) and alginic acid/bentonite (◇). Error bars are +/- one standard deviation from the mean.
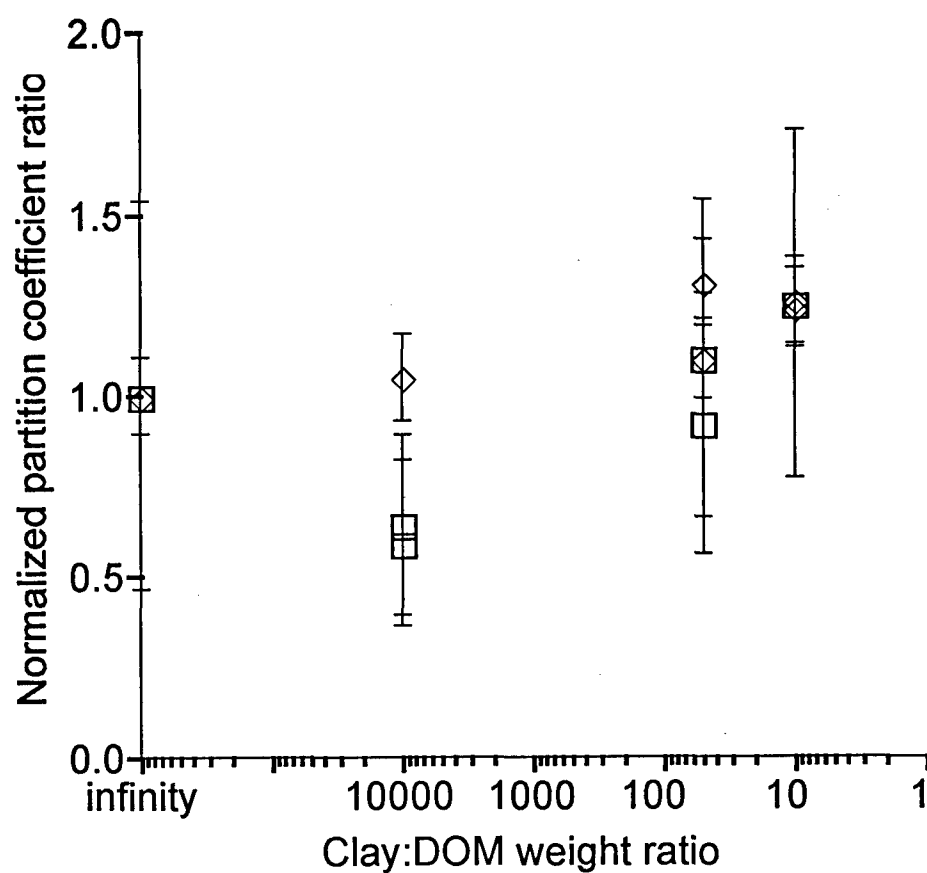
**Figure B.2**: Phenanthrene sorption with tannic acid/kaolinite (□) and tannic acid/bentonite (◇). Error bars are +/- one standard deviation from the mean.
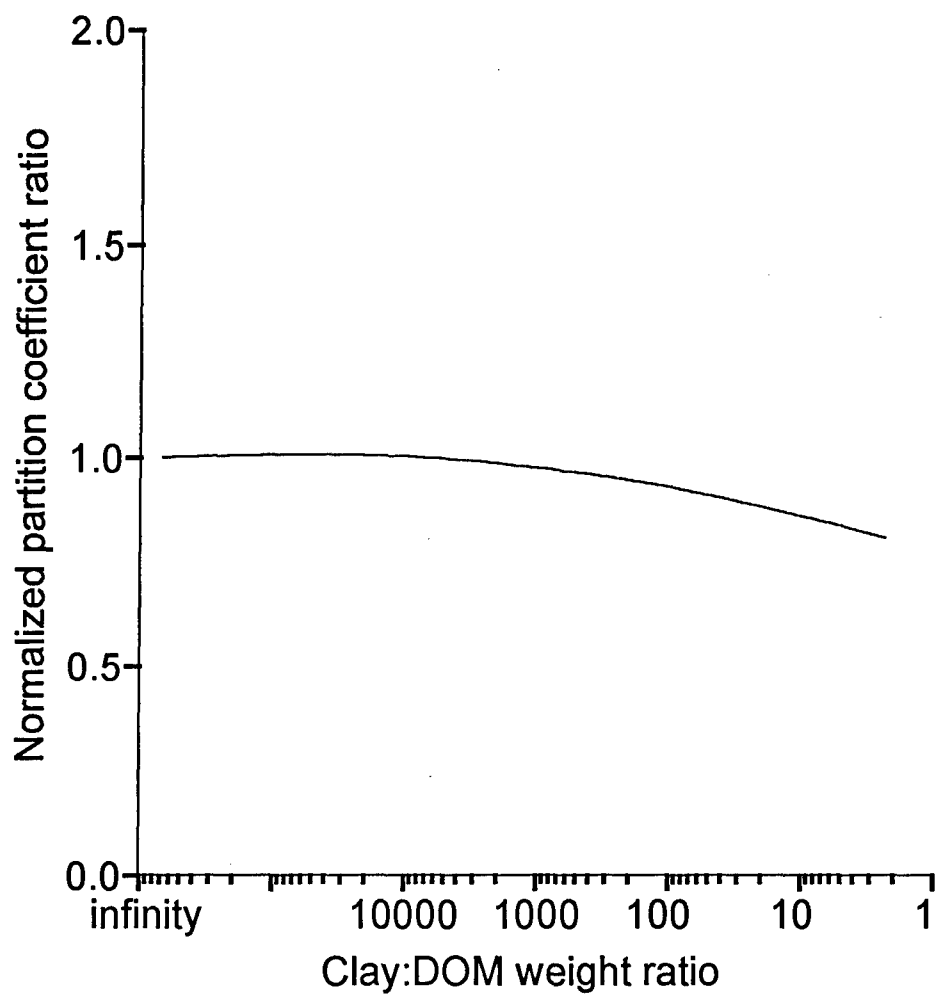
**Figure B.3**: Model calculations for phenanthrene sorption with extracellular polymer/kaolinite.

| Sediment | Kaolinite | | | | Bentonite | | | |
|---|---|---|---|---|---|---|---|---|
| DOM | Alginic acid | | Tannic acid | | Alginic acid | | Tannic acid | |
| Salinity (ppt) | 0 | 30 | 0 | 30 | 0 | 30 | 0 | 30 |
| sediment:DOM weight ratio | Overall Sorption coefficient: $K_0$ (ml/g) | | | | | | | |
| ∞ | 1.56 | 2.23 | 1.56 | 2.23 | 1070 | 1060 | 1070 | 1060 |
| 10,000 | 2.54 | 4.01 | 7.03 | 6.23 | 1010 | 1030 | 684 | 764 |
| 50 | 14.5 | 21.1 | 8.44 | 12.4 | 745 | 798 | 473 | 570 |
| 10 | 40.6 | 67.7 | 7.29 | 13.0 | 640 | 779 | 352 | 437 |

**Table B.2**: Summary of sorption coefficients obtained for phenanthrene sorption to kaolinite and bentonite in the presence of varying amounts of DOM represented by alginic acid and tannic acid.

| Sorbate | Sorbent | $K_d$ (ml/g) | pH | Salinity | Ref. |
|---|---|---|---|---|---|
| *Phenanthrene sorption to humic acid* | | | | | |
| Anthracene | natural humic acid | 14100 | 7.99 | fresh $H_2O$ | Liljestrand & Shimizu, 1991 |
| Anthracene | IHSS[a] humic acid | 10400 | 7.00 | fresh $H_2O$ | Schlautman & Morgan, 1993 |
| Phenanthrene | natural humic acid | 13500 | 8.00 | fresh $H_2O$ | Gauthier et al., 1986 |
| *Humic acid sorption to kaolinite* | | | | | |
| Aldrich humic acid | montmorillonite | 572[b] | 7.0 | fresh $H_2O$ | Liljestrand & Shimizu, 1992 |
| natural humic acid | kaolinite | 124 | 7.0 | fresh $H_2O$ | Murphy et al., 1994 |
| natural humic acid | kaolinite | 250 | 7.0 | 5 ppt | Murphy et al., 1994 |

[a]International Humic Substances Society. [b]Result was scaled to reflect the ratio of the specific surface areas of kaolinite and montmorillonite.

**Table B.3**: Literature values for sorption between phenanthrene, humic acid and kaolinite for $[DOM]_a = 10$ mg/L

REFERENCES

ALLEN-KING, R. M., GROENEVELT, H. & MACKAY, D. M. 1995 Analytical method for sorption of hydrophobic organic pollutants in clay-rich materials. *Env. Sci. Tech.* **29**, 148-153.

BACKHUS, D. A. & GSCHWEND, P. M. 1990 Fluorescent polycyclic aromatic hydrocarbons as probes for studying the impact of colloids on pollutant transport in groundwater. *Env. Sci. & Tech.* **24**, 1214-1223.

CARTER, C. W. & SUFFET, I. H. 1982 Binding of DDT to dissolved humic materials. *Env. Sci. & Tech.* **16**, 735-740.

GAUTHIER, T. D., SHANE, E. C., GUERIN, W. F., SELTZ, W. R. & GRANT, C. L. 1986 Fluorescence quenching method for determining equilibrium constants for polycyclic aromatic hydrocarbons binding to dissolved humic materials. *Env. Sci. & Tech.* **20**, 1162-1166.

GSCHWEND, P. M. & WU, S.-C. 1985 On the constancy of sediment-water partition coefficients of hydrophobic organic pollutants. *Env. Sci. & Tech.* **19**, 90-96.

LION, L. W., STAUFFER, T. B. & MACINTYRE, W. G. 1990 Sorption of hydrophobic compounds in aquifer materials: analysis methods and the effects of organic carbon. *J. Cont. Hydr.* **5**, 215-234.

LILJESTRAND, H. M.; LO, M.-C.; SHIMIZU, Y. 1992 Sorption of humic materials onto inorganic surfaces for the mitigation of facilitated pollutant transport processes. *Wat. Sci. Tech.* **26**, 1221-1228.

LILJESTRAND, H. M. & SHIMIZU, Y. 1991 Sorption of organic pollutants onto natural solid components in aquatic environments. In *Water Pollution: Modelling, Measuring and Prediction* (eds. L.C. Wrobel and C.A. Brebbia.). Computational Mechanics Publications.

LIU, H., AMY, G. 1993 Modeling partitioning and transport interactions between natural organic matter and polynuclear armomatic hydrocarbons in groundwater. *Env. Sci. & Tech.* **27**, 1553-1562.

MURPHY, E. M., ZACHARA, J. M., SMITH, S. C., PHILLIPS, J. L. & WIETSMA, T. W. 1994 Interaction of hydrophobic organic compounds with mineral-bound humic substances. *Env. Sci. & Tech.* **28**, 1291-1299.

SCHLAUTMAN, M. A. & MORGAN, J. J. 1993 Effects of aqueous chemistry on the binding of polycyclic aromatic hydrocarbons by dissolved humic materials. *Env. Sci. & Tech.* **27**, 961-969.

# APPENDIX C:
# ALTERNATIVE DERIVATION OF THE DRIFT VELOCITY AND PAIR DIFFUSION COEFFICIENT IN A RANDOM LINEAR FLOW WITH SMALL TOTAL STRAIN

## C.1 Objective

In Chapter 3 theory is developed for describing particle transport and coagulation in a random linear flow with small total strain. Here we examine the pair probability equation derived in Chapter 3 and by considering the moment equations show that the conservation equation should include a drift term leading to a non-uniform pair probability distribution biased toward small particle separations.

## C.2 Pair probability conservation equation

As discussed in Chapter 3, the flow field is assumed to be linear on scales comparable to the particle radius and statistically stationary in time with separate strain and rotation rate time scales. The analysis is restricted to flows where the product of the characteristic strain (rotation) rate and its correlation time is small. By considering particle movement over times long compared with the flow field correlation times, the pair probability responds as a diffusive process.

For simplicity, the pair probability equation in the absence of Brownian motion and interparticle potentials (i.e., van der Waals attraction

and electrostatic double layer repulsion) will be considered. The pair probability conservation equation for a diffusive process is (Pope, 1985):

$$\frac{\partial P}{\partial t} + \frac{\partial}{\partial r_i}\left[V_i^f P - D_{ij}^f \frac{\partial P}{\partial r_j}\right] = 0 \qquad \textbf{(C.1)}$$

where P is the pair probability distribution function, $r_i$ is the relative position vector connecting the centers of two particles, $V_i^f$ is the drift velocity and $D_{ij}^f$ is the pair diffusion coefficient. The drift velocity is included in the above expression with the expectation that it is non-zero. Equations for the drift velocity and diffusion tensor are found by computing the first and second moments of Equation C.1 with respect to the particle separation.

C.2.1 *First Moment Equation*

Multiplying Equation C.1 by $r_k$ and ensemble averaging over all possible particle separation vectors leads to:

$$\int_r \left\{ r_k \frac{\partial P}{\partial t} + r_k \frac{\partial}{\partial r_i}\left[V_i^f P - D_{ij}^f \frac{\partial P}{\partial r_j}\right] = 0 \right\} d\mathbf{r} \qquad \textbf{(C.2)}$$

Consider Equation C.2 term-by-term. The first term reduces to the average particle velocity. That is,

$$\int_r r_k \frac{\partial P}{\partial t} d\mathbf{r} = \frac{\partial <r_k>}{\partial t} \qquad \textbf{(C.3)}$$

where the angled brackets indicate ensemble averaging over all possible spatial configurations of the two particles. Given an initial starting position of the particle pair, the pair probability is assumed to remain localized in that area. This means that the spatial averaging employed to obtain Equation C.3 does not introduce spatial smoothing of the terms in brackets. Using the product rule, the second term in Equation C.2 can be rewritten as:

$$\int_r \left\{ \frac{\partial}{\partial r_i} \left[ r_k V_i^f P - r_k D_{ij}^f \frac{\partial P}{\partial r_j} \right] - \delta_{ik} \left[ V_i^f P - D_{ij}^f \frac{\partial P}{\partial r_j} \right] \right\} dr \qquad \text{(C.4)}$$

where use has been made of the fact that $\partial r_k / \partial r_i = \delta_{ik}$ and $\delta_{ik}$ is the identity tensor. The divergence theorem allows the first term in Equation C.4 to be rewritten as a flux integral over a spherical surface of radius r:

$$\int_r \frac{\partial}{\partial r_i} \left[ r_k V_i^f P - r_k D_{ij}^f \frac{\partial P}{\partial r_j} \right] dr = \int_{\delta r} \frac{r_i}{r} \left[ r_k V_i^f P - r_k D_{ij}^f \frac{\partial P}{\partial r_j} \right] dr \qquad \text{(C.5)}$$

where r is the magnitude of $r_i$ and $\delta r$ refers to an integration over the surface of a spherical volume with radius r. Letting $r \to \infty$, the pair probability and its spatial derivative decay to zero, so Equation C.5 is zero.

The second term in Equation C.4 simplifies to:

$$\int_r - \delta_{ik} \left[ V_i^f P - D_{ij}^f \frac{\partial P}{\partial r_j} \right] dr = -\langle V_k^f \rangle - \frac{\partial \langle D_{kj}^f \rangle}{\partial r_j} \qquad \text{(C.6)}$$

after an application of the divergence theorem to the diffusive flux part of the equation.

Combining the results from Equations C.3 and C.6 the evolution equation for the average particle separation distance is obtained as:

$$\frac{\partial <r_k>}{\partial t} - <V_k^f> - \left\langle \frac{\partial D_{kj}^f}{\partial r_j} \right\rangle = 0 \qquad (C.7)$$

Equation C.7 shows that unless the time derivative of the particle separation vector exactly balances the divergence of the diffusion coefficient, the drift velocity will have a non-zero value. In Section C.2.3 an explicit expression for the drift velocity is obtained which matches that obtained in Chapter 3 using an alternative derivation.

C.2.2 *Second moment equation*

Multiplying Equation C.1 by $r_k r_l$ and averaging over all particle separation vectors, **r**, gives:

$$\int_r \left\{ r_k r_l \frac{\partial P}{\partial t} + r_k r_l \frac{\partial}{\partial r_i} \left[ V_i^f P - D_{ij}^f \frac{\partial P}{\partial r_j} \right] = 0 \right\} dr \qquad (C.8)$$

Using the divergence theorem repeatedly and assuming the pair probability goes to zero at large separations yields:

$$<D_{kl}^f> = \frac{1}{2} \frac{\partial <r_k r_l>}{\partial t} \qquad (C.9)$$

As expected, the pair diffusivity tensor is related to the time derivative of the mean square displacement (Russel et al., 1989). Equation C.9 can be re-expressed in terms of the two-time velocity autocorrelation function.

First, writing the particle position as a time integral over the particle velocity yields:

$$r_k = r_k(0) + \int_0^t \dot{r}_k(t')dt' \qquad \text{(C.10)}$$

where the overdot indicates a time derivative. Equation C.9 is simplified by taking the time derivative inside the ensemble average and substituting in Equation C.10. As a result, Equation C.9 becomes:

$$D_{kl}^f = \int_0^t \left\langle \dot{r}_k(t') \dot{r}_l(t) \right\rangle dt' \qquad \text{(C.11)}$$

where the overdot indicates a time derivative and terms dependent on the initial particle separation are eliminated because of the assumed spatial homogeneity of the particle number density. Equation C.11 is identical to the expression derived for the diffusion tensor in Chapter 3 (see Equation 3.13).

### C.2.3 *Drift velocity*

The drift velocity given by Equation C.7 is the difference between the average relative particle velocity and the divergence of the pair diffusivity. A compact form for the drift velocity can be obtained in terms

of the two-time velocity/acceleration correlation. First the mean particle velocity is expanded as a linear function of position:

$$\frac{\partial <r_k>}{\partial t} = <\dot{r}_k> = \left\langle r_l(t) L_{kl}(r(t)) \right\rangle \qquad \text{(C.12)}$$

where $L_{kl}$ is defined in Equation 3.21. Substituting Equation C.10 into Equation C.12 and keeping terms of order $(\tau_s \Gamma)^2$ yields:

$$<\dot{r}_k> = \left\langle r_j(0) L_{kj}(r(t)) \right\rangle + \int_0^t \left\langle \dot{r}_j(t') L_{kj}(r(t)) \right\rangle dt' \qquad \text{(C.13)}$$

The first term in Equation C.13 is zero because $r_j(0)$ is constant and the mean particle velocity gradient is zero. Assuming t is much greater than the correlation times of the flow, the lower limit of integration can be replaced with $-\infty$ giving,

$$<\dot{r}_k> = \int_{-\infty}^t \left\langle \dot{r}_j(t') L_{kj}(r(t)) \right\rangle dt' \qquad \text{(C.14)}$$

Taking the divergence of Equation C.11 gives,

$$\frac{\partial D_{jk}^f}{\partial r_j} = \int_{-\infty}^t \left\{ \left\langle \dot{r}_k(t) L_{jj}(r(t')) \right\rangle + \left\langle \dot{r}_j(t') L_{kj}(r(t)) \right\rangle \right\} dt' \qquad \text{(C.15)}$$

Finally, subtracting Equation C.15 from C.14 gives the final expression for the drift velocity:

$$V_k^f = -\int_{-\infty}^{t} \left\langle \dot{r}_k(t) L_{jj}\left(r(t')\right) \right\rangle dt' \qquad \text{(C.16)}$$

Equation C.16 is identical to the drift velocity given by Equation 3.12 in Chapter 3.

# REFERENCES

POPE, S. B. 1985 PDF methods for turbulent reactive flows. *Prog. Energy Combust. Sci.* **11**, 119-192.

RUSSEL, W. B., SAVILLE, D. A. & SCHOWALTER, W. R. 1989 *Colloidal Dispersions*, Cambridge U.P., Cambridge, MA.

# APPENDIX D:

# THE SECOND ORDER STATISTICS OF $\Gamma_{ij}(t)$

An isotropic fluctuating velocity gradient characterized by separate strain and rotation rate correlation times is assumed. Mean flow is ignored so that the expectation of $\Gamma_{ij}(t)$ is zero, where $\Gamma_{ij}(t)$ is the fluctuating velocity gradient tensor. The velocity gradient tensor is separated into its symmetric and antisymmetric parts so that the strain and rotation rates are decoupled along with their time scales:

$$\Gamma_{ij}(t) = S_{ij}(t) + R_{ij}(t) \tag{D.1}$$

where $S_{ij}(t)$ is the strain rate tensor and $R_{ij}(t)$ is the rotation rate tensor.

In the following analysis all times and velocity gradients have been scaled with their Kolmogorov values. Assuming stationary turbulence, the two-time correlation for $\Gamma_{ij}(t)$ is written as:

$$\langle \Gamma_{ik}(0)\Gamma_{jl}(t)\rangle = \langle S_{ik}(0)S_{jl}(t)\rangle + \langle R_{ik}(0)R_{il}(t)\rangle \tag{D.2}$$

where the cross-correlation terms, such as $\langle S_{ik}(0)R_{jl}(t)\rangle$, are zero due to isotropy. Angle brackets, $\langle\rangle$, denote ensemble averaging over the sample space of the random variable.

Velocity gradient autocorrelation data obtained from direct numerical simulations of turbulence (DNS; Girimaji & Pope, 1990) and the properties of isotropic fourth order tensors are used to deduce relationships for the strain and rotation rate autocorrelation functions. The strain rate

345

correlation function decays exponentially with a characteristic decay time, $\tau_S$, of $2.3\tau_\eta$ (Girimaji & Pope, 1990):

$$<S_{ik}(0)S_{jl}(t)> = S_{ikjl}\exp\left(\frac{-t}{\tau_S}\right) \tag{D.3}$$

where the fourth order tensor $S_{ikjl}$ is the covariance of the strain rate and $\tau_\eta$ is the Kolmogorov time scale (characteristic time of the smallest turbulent eddies). Non-linear regression of Girimaji & Pope's simulation data (1990) shows that the exponential form given in Equation D.3 fits the data with an $r^2 = 99.6\%$. $S_{ikjl}$ is written as a fourth order isotropic tensor that depends on three scalar coefficients. The numerical coefficients are obtained by applying symmetry, $S_{ikjl} = S_{kijl}$, continuity, $S_{iijl} = S_{ikjj} = 0$, and dissipation rate, $S_{ijij} = 0.5$. The final form for the strain rate covariance is:

$$S_{ikjl} = \frac{1}{20}\left[\delta_{ij}\delta_{kl} + \delta_{il}\delta_{jk} - \frac{2}{3}\delta_{ik}\delta_{jl}\right] \tag{D.4}$$

The rotation rate correlation function is obtained using a similar analysis to yield:

$$<R_{ik}(0)R_{jl}(t)> = R_{ikjl}\exp\left(\frac{-t}{\tau_R}\right) \tag{D.5}$$

where:

$$R_{ikjl} = \frac{1}{12}\left[\delta_{ij}\delta_{kl} - \delta_{il}\delta_{jk}\right] \tag{D.6}$$

and $\tau_R$ is the rotation rate correlation time with a value estimated to be about $7.2\tau_\eta$ (Girimaji & Pope, 1990). The exponential form for the autocorrelation function fits the DNS data with an $r^2$ of 95%. The form of Equation D.6 is set by applying antisymmetry $R_{ikjl} = -R_{kijl}$, continuity, $R_{iijl}$ $= R_{ikjj} = 0$, and dissipation rate, $R_{ijij} = 0.5$. The last statement comes from the evolution equation for the mean square vorticity fluctuations and is valid for large Reynolds numbers (Tennekes & Lumley, 1972).

The complete expression for the autocorrelation function of the velocity gradient tensor is

$$<\Gamma_{ik}(0)\Gamma_{jl}(t)> = S_{ikjl}\exp\left(\frac{-t}{\tau_S}\right) + R_{ikjl}\exp\left(\frac{-t}{\tau_R}\right) \qquad \textbf{(D.7)}$$

# REFERENCES

GIRIMAJI, S. S. & POPE, S. B. 1990 A diffusion model for velocity gradients in turbulence. *Phys. Fluids A.* **2**, 242-256.

TENNEKES H. & LUMLEY, J. L. 1972 *A first course in turbulence.* MIT Press, Cambridge, MA.

# APPENDIX E:
# PROGRAM LISTINGS

A description of computer programs used to calculate colloidal stability in the random linear flow field (Chapter 3) and dynamic simulations of coagulation in Gaussian isotropic turbulence (Chapter 4) follow.

## E.1 Stability factor for coagulation in a random linear flow field (Chapter 3)

The program for calculating the stability factor, termed WCALC.EXE, has been written for a DOS or Windows based computer. The user is prompted for the non-dimensional parameters governing the system (see Table 3.2). One parameter of the users choosing can be interated over a user specified range. Output in the form of a comma-delimited file is placed in a user specified data file.

### E.1.1 *Execution instructions*

WCALC is executed by typing *wcalc.exe* at the DOS command prompt and hitting the Enter key on the keyboard. The program first prompts the user for the name of an output data file. A valid 8 character file name should be typed in followed by Enter. (The program will append the file extension *.txt*). This comma delimited output file is stored in the subdirectory DATA. Next, the user is prompted to enter the desired values for the non-dimensional parameters listed in Table 3.1. In order as listed in the program, these include: $N_L$, $N_F$, $N_R$, $\kappa'$, and $N_D$, where $N_D$ is 1/Pe. The

program allows the user to vary one of the above parameters during execution. The next prompt lets the user pick the parameter to be varied. Following that, the maximum (it can also be the minimum) value of the varied parameter to input. The number of intervals between the minimum and maximum for the varied parameter may be selected as well as whether to use logrithmic or linear intervals.

Once the parameters have been input, the program integrates the numerical data. Intermediate results are summarized on the screen (all results are placed in the user specified data file).

E.1.2 *Output data file structure*

A sample data file is listed in Table E.1. The first two lines provide information identifying the program, author, revision data and version number of the program. Line three lists the headings for the remaining columns of numerical data, including: P2, the value of the integrating factor at the secondary minimum; W2, the stability factor at the secondary minimum; Alpha2, the collision efficiency at the secondary minimum; Pmin, the integrating factor at the primary minimum; Wmin, the stability factor at the primary minimum; and, Alpha_min, the collision efficiency at the primary minimum. The remaining lines list numerical data for each specified value of the non-dimensional parameters.

E.1.3 *Implementation of the hydrodynamic interactions*

Hydrodynamic interactions are obtained from the tables provided by Kim & Karrila (1991). They provide series solutions to the hydrodynamic interactions in the near and far field. The coefficients in the series

```
"RANDOM LINEAR FLOW STABILITY FACTOR"

"Brett Brunk","January 1, 1997","Version 9.0"

"N1","Beta","Nf","Nr","Khat","Nd","P2","W2","Alpha2","Pmin","Wmin","Alpha_min"
10000.000000,1.000000,1.000000e+00,0.000000,0.000000,,0.0001,4.671132,0.214081
...
10000.000000,1.000000,1.000000e+09,0.000000,0.000000,,0.0000,56.662947,0.017648
```

**Table E.1:** Sample output data file for WCALC.EXE

expansions are a function of the particle radius and WCALC uses spline interpolation to obtain the correct coefficients for the user specified particle radius ratio. These tables of coefficients have been pre-processed by the routine *spline* in MODEL60.CPP (see Section E.1.2 below and Press et al., 1992 for details on the spline interpolation method used in this work).

E.1.4 *Directory locations*

As written WCALC.EXE assumes specific directory locations for the tabulated hydrodynamic interaction functions and output data files. If "." denotes the directory containing WCALC.EXE and ".." denotes the parent directory, then output data files are placed in ./data with a default file extension of *.txt*. The program assumes that the tabulated hydrodynamic interaction functions can be found in ../interp~1/hydrodat.

E.1.5 *Description of code modules used to build WCALC.EXE*

The following C++ files make up the code required to compute the stability factor integral presented in Chapter 3.

**WCALC9.CPP** calculates the stability factor for particles in a random linear flow. It includes subroutines for the integrating factor and stability factor given by Equations 3.45 and 3.47, respectively.

**MODEL60.CPP** contains subroutines used in the main program, WCALC9.CPP. Among the algorithms included are routines for opening data files, a generic 5$^{th}$ order Runge-Kutta routine and a spline interpolation algorithm.

**MODEL50.H** is the header file for MODEL60.CPP containing definitions of constants and subroutines found in MODEL60.CPP. A

detailed listing of subroutines and their usage may be found in MODEL50.H.

**INTFOR3.CPP** contains subroutines related to calculating interparticle forces, interparticle potentials and hydrodynamic mobility functions.

**INTFOR3.H** is the header file for INTFOR3.CPP containing definitions of constants and subroutines found in INTFOR3.CPP.

## E.2 Dynamic simulation of coagulation in Gaussian isotropic turbulence without interparticle forces

The program for calculating the coagulation rate in Gaussian isotropic turbulence in the absence of interparticle forces, termed FLOCSIM.EXE, has been written for a DOS or Windows based computer. The user is prompted for the name of a configuration file and output data file. Output in the form of a comma-delimited file is placed in a user specified data file. In addition, the program gives the option of storing the position of one particle during the simulation.

### E.2.1 *Execution instructions*

FLOCSIM is run by typing *FLOCSIM.EXE* at the DOS prompt and pressing the Enter key on the keyboard. Optionally the program can be written with command line parameters: *FLOCSIM.EXE {CONFIGURATION FILE: \*.CFG} {NUMBER OF REALIZATION: #} {OUTPUT DATA ON PARTICLE POSITIONS: Y/N}*. If these items are not specified on the command line the program will prompt the user for

them. The configuration file is assumed to be in the DATA subdirectory. An output comma delimited text file is created (or appended) with the same name as the configuration file but with a *.txt* file extension. Output data on particle positions is stored similarly but the file extension is *.pos*. The content of the configuration file is detailed below.

Once the configuration file is successfully read the program begins simulating a realization of the flow. Intermediate results are shown on the screen (more detailed results are placed in the output file).

### E.2.2 *Output data file structure*

A sample output file is shown in Table E.2 The first two lines provide information about the program, author and version number. Line three shows the configuration file used to obtain the simulation results tabulated in the rest of the file.

Lines three and four summarize the material present in the configuration file, including: Rcutoff, the location of the outer simulation boundary; Fmax, the maximum normalized flux used to calculate the probability of creating a new particle; N, the number of Fourier modes in the representation of the velocity field; Realization, irrelevant in this version; Max Timestep, irrelevant in this version; seed1 and seed2, irrelevant in this version; Tcutoff, characteristic time for a particle to travel from the outer to inner computational boundary; Tstrain, value of the total strain; Trotation, value of the total rotation. Next, column headings for the

```
"Pair diffusion simulation"

"Brett Brunk","Version",5.30

"Config:","post1k.cfg"

"Rcutoff",10.000000,"Fmax",0.270000,"N",250,"Realization",1,"Max Timestep",0.000000

"seed1",1885360906,"seed2",779012232"Tcutoff",4.407627,"Tstrain",1000.000000,"Trotation",1000.000000

"time","<Qo>","<Qr>","k","%Surv","MaxDT","Nannilated","t_avg","tr_avg","t_max","seed1","seed2",2.,10.
1.00,0.81444,0.7892,11.0533,1.00,0.1000,93.00,3.6537,3.6537,8.7999,2128560802,232298532,0.0297,0.033
...
4.00,0.90614,0.7443,12.2979,1.00,0.1000,25.00,2.8521,2.8521,3.5000,442038164, 731162732,0.0000,0.014
```

**Table E.2**: Sample output data file for FLOCSIM.EXE

realizations are given. These headers include: time, the realization that is being summarized; <Qo>, average particle flow rate at the outer simulation boundary; <Qr>, average particle flow rate at the inner simulation boundary; k, computed coagulation rate constant; %Survive, percentage of particles that coagulate with the test sphere; Max DT, maximum time step used in the realization; Nannilated, number of particles that escape to the outer simulation boundary; t avg, average time that a particle lasts in the computer simulation; tr avg, average time it takes for a particle to traverse the simulation domain; t max, maximum lifetime of a particle in the simulation; seed1, value of the first random number generator seed at the end of the realization; seed2, value of the second random number generator seed at the end of the realization. Following seed2, the numbers of the mid-points of intervals used to calculate the average concentration in the realization are listed.

Results from each realization are tabulated below the column headings.

### E.2.3 *Directory locations*

As written, FLOCSIM.EXE assumes specific directory locations for the tabulated hydrodynamic interaction functions and output data files. If "." denotes the directory containing FLOCSIM.EXE and ".." denotes the parent directory, then output data files are placed in ./data with a default file extension of *.txt*. Configuration files are located in ./data.

E.2.4 *Sample configuration file*

Configuration files for FLOCSIM.EXE have a file extension of *.cfg* and have the following form:

| Line# | File contents |
|---|---|
| 1 | flocsim 5.30 |
| 2 | post1k.cfg : configuration file for flocsim.cpp |
| 3 | 1000.000000 |
| 4 | Rate of strain correlation time |
| 5 | 1000.000000 |
| 6 | Rate of rotation correlation time |
| 7 | 10.000000 |
| 8 | Cutoff radius in units of particle diameter |
| 9 | 250 |
| 10 | Number of elements in Fourier series |
| 11 | 0.270000 |
| 12 | Maximum volumetric flux (i.e., UiNi) |
| 13 | 4 |
| 14 | Current realization of simulation |
| 15 | 442038164 |
| 16 | Seed1 for the random number generators |
| 17 | 731162732 |
| 18 | Seed2 for the random number generators |
| 19 | 50 |
| 20 | Number of bins in concentration profile |

E.2.5 *Description of code modules used to build FLOCSIM.EXE*

The C++ files listed below constitute the code required to run the simulations of coagulation in turbulence detailed in Chapter 4.

**FWIF53.CPP** is the main program for computing turbulent coagulation with interparticle forces. It contains the code for generating a Gaussian random linear flow with separate strain and rotation rate correlation times. Also included in the program are subroutines for moving particles, maintaining a constant concentration boundary condition at the outer simulation boundary, computing the pair probability distribution and calculating the flux of particles incident on the test sphere.

**RANDOM.CPP** contains subroutines for generating uniform and Gaussian random numbers. In addition, an algorithm for determining a random vector on the unit sphere is included.

**RANDOM.H** is the header file for RANDOM.CPP containing function declarations and definitions of routines found in RANDOM.CPP.

The following files contain routines and support programs for generating random numbers using algorithms compiled by NETLIB (program listings and a description of the algorithms can be found on NETLIB, www.att.com): COM.CPP, LINPACK.CPP, RANLIB.CPP, RANLIB.H. Subroutines in RANLIB.CPP were used to generate uniform random numbers using two user chosen seed values. As these are public domain programs, they are not reproduced in this thesis.

The C++ files, MODEL50.CPP, MODEL40.H, INTFOR3.CPP and INTFOR3.H described in Section E.1 were also used in the computer simulation of coagulation in Gaussian isotropic turbulence.

## E.3 Dynamic simulation of coagulation in Gaussian isotropic turbulence with interparticle forces

The program for calculating the coagulation rate in Gaussian isotropic turbulence in the absence of interparticle forces, termed FWIF.EXE, has been written for a DOS or Windows based computer. The program is almost idential to FLOCSIM.EXE. The user is prompted for the name of a configuration file and output data file. Output in the form of a comma-delimited file is placed in a user specified data file. In addition the program gives the option of outputing the position of one particle during the simulation.

### E.3.1 *Program execution*

The program is run by typing FWIF.EXE at the DOS command prompt and pressing Enter on the keyboard. Command line prompts are identical to those used in FLOCSIM.EXE. Output is placed in a comma deliminated data file with the same file name as the configuration file but with a *.txt* file extension.

### E.3.2 *Output data file structure*

The data file has the same structure as that used for FLOCSIM.EXE.

E.3.3 *Warning*

The user should be aware of two problems with the current version of the program. First, the code is using an old version of the non-dimensional parameters. Before compiling FWIF with the current versions of MODEL50.CPP, MODEL40.H, INTFOR3.CPP and INTFOR3.H the formulas used to compute the relative particle velocity should be validated. In addition, the program currently takes $N_F$, not $N_S$, as input for the ratio of viscous forces to van der Waals forces where the total strain in $N_F$ is taken to be 2.3. It is recommended that these two issues be fixed before further simulations are conducted.

E.3.4 *Directory locations*

As written FWIF.EXE assumes specific directory locations for the tabulated hydrodynamic interaction functions and output data files. If "." denotes the directory containing FWIF.EXE and ".." denotes the parent directory, then output data files are placed in ./data with a default file extension of *.txt*. The program assumes that the tabulated hydrodynamic interaction functions can be found in ../interp~1/hydrodat. Configuration files are located in ./data.

E.3.5 *Sample configuration file*

Configuration files for FWIF.EXE have a file extension of *.cfg* and have the following form:

| Line# | File contents |
|---|---|
| 1 | flocwif 2.00 |
| 2 | 4ns8.cfg : configuration file for flocwif.cpp |

| 3  | 2.300000                                                           |
|----|--------------------------------------------------------------------|
| 4  | Rate of strain correlation time                                    |
| 5  | 7.200000                                                           |
| 6  | Rate of rotation correlation time                                  |
| 7  | 5.000000                                                           |
| 8  | Cutoff radius in units of particle diameter                        |
| 9  | 200                                                                |
| 10 | Number of elements in Fourier series                               |
| 11 | 0.270000                                                           |
| 12 | Maximum volumetric flux (i.e., UiNi)                               |
| 13 | 253.000000                                                         |
| 14 | Nl: ratio of particle radius to London retardation wavelength      |
| 15 | 1.000000                                                           |
| 16 | lambda: particle radius ratio                                      |
| 17 | 0.000076                                                           |
| 18 | Nf: ratio of hydrodynamic repulsion to vdw attraction              |
| 19 | 0.000000                                                           |
| 20 | Nr: Electrostatic repulsion to vdw attraction                      |
| 21 | 1.000000                                                           |
| 22 | Khat: London wavelength to Debye length                            |
| 23 | 101                                                                |
| 24 | Current realization of simulation                                  |
| 25 | 85859375                                                           |
| 26 | Seed1 for the random number generators                             |

| | |
|---|---|
| 27 | 1172590394 |
| 28 | Seed2 for the random number generators |
| 29 | 50 |
| 30 | Number of bins in concentration profile |

### E.3.6 *Description of code modules used to build FLOCSIM.EXE*

The same C++ files used to build FLOCSIM.EXE are used for FWIF.EXE except that FWIF.53.CPP is replaced with FWIF20.C.

**FWIF.H** is the header file for FWIF53.CPP containing function definitions and revision history.

# REFERENCES

KIM, S. & KARRILA, S. J. 1991 *Microhydrodynamics: principles and selected applications.* Butterworld-Heinemann, Boston, MA.

PRESS, W. H., TEUKOLKSY, S. A., VETTERLING, W. T. & FLANNERY, B. P. 1992 *Numerical Recipes for C.* Cambridge U.P., Cambridge, MA.